

# **Ice nucleation under cirrus cloud conditions**

**Theodore William Wilson**

Submitted in accordance with the requirements for the degree of Doctor of Philosophy

**The University of Leeds**

**School of Chemistry**

**School of Earth and Environment**

**September 2012**

The candidate confirms that the work submitted is his/her own, except where work which has formed part of jointly-authored publications has been included. The contribution of the candidate and the other authors to specific chapters of this work has been explicitly indicated overleaf. The candidate confirms that appropriate credit has been given within the thesis where reference has been made to the work of others.

This copy has been supplied on the understanding that it is copyright material and that no quotation from the thesis may be published without proper acknowledgement

© 2012 The University of Leeds and Theodore William Wilson

The right of Theodore William Wilson to be identified as Author of this work has been asserted by him in accordance with the Copyright, Designs and Patents Act 1988.

## Summary of the author's contribution to published work

(Chapter 4) B. J. Murray, T. W. Wilson, S. Dobbie, Z. Cui, S. M. R. K. Al-Jumur, O. Möhler, M. Schnaiter, R. Wagner, S. Benz, M. Niemand, H. Saathoff, V. Ebert, S. Wagner & B. Kärcher, *Heterogeneous nucleation of ice particles on glassy aerosols under cirrus conditions*, Nature Geoscience, 3, 233-237, 2010, doi:10.1038/ngeo817.

TWW assisted with experiments at the AIDA chamber, analysed the data provided by the AIDA team and processed, analysed and helped interpret modelling data provided by SD. BJM oversaw the study, sought financial support for it and wrote the manuscript. SD led the modelling aspects in collaboration with SMRKA and BK. OM led the AIDA team, which included MS, RW, SB, MN and HS, who operated the AIDA chamber and associated equipment. BJM and ZC assisted with the AIDA experiments. VE and SW processed the AIDA water vapour data prior to analysis.

(Chapters 2 and 5) T.W. Wilson, B. J. Murray, R. Wagner, O. Möhler, H. Saathoff, M. Schnaiter, J. Skrotzki, H. C. Price, T. L. Malkin, S. Dobbie, S. M. R. K. Al-Jumur, *Glassy aerosols with a range of compositions nucleate ice heterogeneously at cirrus temperature*, Atmos. Chem. Phys., 12, 8611-8632, 2012 doi:10.5194/acp-12-8611-2012.

TWW wrote the manuscript, planned and directed experiments and analysed data in collaboration with RW and BJM. TWW also helped write a successful proposal to EUROCHAMP 2 to fund this work. BJM oversaw the study and sought financial support for. RW oversaw the operation of the AIDA chamber, directed experiments and processed and analysed data in collaboration with TWW and BJM. OM led the AIDA team, which included HS, MS, JS who operated the AIDA chamber and associated equipment. HCP assisted in the analysis of experimental data. TLM, SD and SMRKA assisted in experiments at AIDA.

(Chapter 6) R. Wagner, O. Möhler, H. Saathoff, M. Schnaiter, J. Skrotzki, T. Leisner, T. W. Wilson, T. L. Malkin and B.J. Murray, *Ice cloud processing of ultra-viscous/glassy aerosol particles leads to enhanced ice nucleation ability*, Atmos. Chem. Phys., 12, 8589-8610, 2012, doi:10.5194/acp-12-8589-2012.

TWW directed experiments and analysed results in collaboration with RW and BJM. TWW also helped write a successful proposal to EUROCHAMP 2 to fund this work. RW oversaw the operation of the AIDA chamber, directed experiments and processed and analysed data and wrote the manuscript in collaboration with TWW and BJM. TLM provided additional x-ray diffraction data in collaboration with TWW. BJM oversaw the study and sought financial support. OM and TL led the AIDA team, which included HS, MS, JS and who operated the AIDA chamber and associated equipment.

## Acknowledgements

I would like to personally thank my supervisors Benjamin Murray and Steven Dobbie for their guidance and support during this project. I would also like to thank Robert Wagner in particular and the rest of the AIDA team for everything they have contributed to this project (see previous page and chapter text for details of specific contributions). I also express my gratitude to the following people who have helped during the experimental and writing phases of the project: Tamsin Malkin, Jim Atkinson, Kelly Baustian, Daniel O'Sullivan, Hannah Price, Sarah Broadley, Ross Herbert, Ravi Kumar, Nsikanabasi Umo, Thomas Whale, Paul Seakins, Trevor Ingham, Mark Bart, Dave Fogarty, Colin Kilner, Andy Goddard and everyone in the Mechanical and Electronic workshops in the Schools of Chemistry and Earth and Environment.

I thank my parents for the bottomless supplies of love, support and money they have provided, and without which I wouldn't have started or finished this project. Special thanks go to Danielle Miles, Katie Marriot, Seb Sikora, Aaron O'Leary, Lawrie Morgan and Jon Glahome for providing me with minimally mouldy housing during the unfunded final year of my degree. Danielle deserves particular recognition for making me learn to Lindy Hop, the hobby that keeps on giving.

I'd like to unreservedly thank everyone who has put up with me during the ups and the downs that I have encountered during this project. They have been subjected to moaning, poor humour, erratic decision making and occasional bouts of emotional despair. It hasn't been an easy four years and I couldn't have done it without patient people like Sam Peppe, Christina Barfoot, Ruth Townend and Bethan White.

Finally, I gratefully acknowledge financial assistance provided by the Charles Brotherton Trust, The School of Chemistry (University of Leeds), the European Research Council and the Aerosol Society as well as the financial support during the ICE01 and ICE02 campaigns from ACCENT, the Helmholtz-Gemeinschaft Deutscher Forschungszentren and EUROCHAMP-2.



# Abstract

Cirrus are thin upper tropospheric clouds that are composed entirely of ice particles. Due to their extensive coverage of the Earth's surface, they have a significant impact on the Earth's radiative balance. In the absence of a foreign surface, cirrus ice particles can form via homogeneous ice nucleation in liquid aqueous solution aerosol droplets. Ice can also nucleate heterogeneously when catalysed by the presence of solid particles, which can affect the physical properties of the cloud, potentially resulting in high in-cloud humidity and low optical depth. In order to better quantify the impact of cirrus on future climate it is vital to understand the microphysical processes that lead to their formation. This project focuses on the investigation of heterogeneous ice nucleation in the deposition mode under cirrus conditions. It can be divided into two sections:

- 1) The investigation of the ice nucleation behaviour of glassy aerosols. Atmospheric secondary organic aerosol (SOA) is likely to exist in a semi-solid or glassy state, particularly at low temperatures and humidities. Over the course of two experimental campaigns at the AIDA (Aerosol Interactions and Dynamics in the Atmosphere) cloud simulation chamber, the ice nucleation properties of aerosols of five different glass forming compositions (citric acid, raffinose, 4-hydroxy-3-methoxy-mandelic acid (HMMA), levoglucosan, and a mixture – raffinose/M5AS) were studied. These organic compounds have similar functionality to oxidised organic material found in atmospheric aerosol and have estimated temperature/humidity induced glass transition thresholds that fall within the range predicted for atmospheric SOA. A small fraction of aerosol particles of all compositions were found to nucleate ice heterogeneously in the deposition mode at temperatures  $< 200$  K, which is relevant to the tropical tropopause layer (TTL). Raffinose and HMMA, which form glasses at higher temperatures, nucleated ice heterogeneously at temperatures as high as 214.6 and 218.5 K respectively. Using a 1D cirrus model, it was shown that nucleation on glassy aerosols may explain low ice crystal numbers and high in-cloud humidity in the TTL. It was also found that the ice nucleation efficiency of glassy aerosol particles became enhanced after having been frozen homogeneously at temperatures close to their glass transition thresholds.
- 2) The design and development of a benchtop instrument for the study of deposition mode ice nucleation. After characterisation, the deposition mode chamber was used to investigate ice nucleation by a natural sample of kaolinite clay mineral dust (KGa-1b, Clay Minerals Society). The surface area of kaolinite present was found to affect the onset humidity of ice nucleation. Evidence was also found for the enhancement of kaolinite particles as ice nuclei after they had nucleated ice in an initial experiment.

# Contents

Summary of the author's contribution to published work .....	iii
Acknowledgements .....	iv
Abstract .....	v
Contents .....	vi
List of tables .....	xi
List of figures .....	xii
List of abbreviations .....	xxiv
Chapter 1: Introduction .....	1
1.1    Earth's atmosphere .....	1
1.1.1    Atmospheric structure .....	1
1.1.2    Atmospheric Aerosol .....	2
1.1.3    Clouds and the climate .....	3
1.1.3.1    Cirrus clouds .....	5
1.2    Project objectives .....	6
1.3    Thesis overview .....	7
1.4    Project background .....	7
1.4.1    Ice nucleation in the atmosphere .....	7
1.4.2    Homogeneous ice nucleation .....	7
1.4.2.1    Classical nucleation theory (CNT) .....	8
1.4.2.2    The role of water activity in homogenous ice nucleation .....	11
1.4.3    Heterogeneous ice nucleation .....	13
1.4.3.1    Modes of heterogeneous ice nucleation .....	14
1.4.3.2    Parameterising heterogeneous ice nucleation using CNT .....	16
1.4.3.2.1    The heterogeneous nucleation rate coefficient .....	17
1.4.3.3    Parameterising heterogeneous ice nucleation using the deterministic model .....	19

1.4.3.4	Atmospheric heterogeneous IN .....	20
1.4.4	Which aerosol particles form cirrus? .....	22
1.4.4.1	The composition of upper tropospheric aerosol .....	22
1.4.4.2	The composition of mid-latitude cirrus ice particle residues.....	25
1.4.4.3	The case for studying ice nucleation by natural mineral dust samples.. .....	27
1.4.4.4	The composition of subvisible cirrus ice particles in the tropical tropopause layer .....	28
1.4.4.5	The saturation problem: High in cloud and clear sky humidity .....	30
1.4.4.5.1	Possible causes of high in cloud humidity at TTL temperatures...	33
1.4.5	Evidence for solid amorphous atmospheric aerosol.....	34
1.4.5.1	Glass formation in proxies of atmospheric aerosol .....	35
1.5	Summary .....	39
Chapter 2:	Experimental for AIDA chamber campaigns.....	41
2.1	Preface.....	41
2.2	The AIDA chamber.....	41
2.3	Materials.....	46
2.4	Aerosol phase diagrams .....	47
2.5	Avoidance of aerosol pre-activation during ICE02 campaign.....	51
Chapter 3:	Development of the deposition mode chamber (DMC).....	53
3.1	Generating relative humidities with respect to ice.....	53
3.2	Chamber concept.....	57
3.3	Description of the DMC.....	57
3.3.1	Chamber body .....	57
3.3.2	Temperature control .....	58
3.3.3	Temperature controlled ice surface.....	61
3.3.4	Sample holder.....	62
3.3.5	Sample microscopy .....	63

3.3.6	LabView control and logging software.....	64
3.3.7	Uncertainty in temperature measurements.....	67
3.4	DMC experimental methodology.....	67
3.4.1	Materials.....	67
3.4.2	Slide preparation .....	68
3.4.3	Depositing samples for investigation.....	68
3.4.3.1	Ammonium sulphate.....	68
3.4.3.2	Kaolinite (KGa-1b).....	68
3.4.3.3	Nebulisation.....	68
3.4.3.4	Single droplet evaporation.....	69
3.4.4	Depositing the ice film.....	70
3.4.5	Equilibration and the first experimental run .....	72
Chapter 4:	ICE01 campaign: Heterogeneous ice nucleation by glassy citric acid aerosol .....	73
4.1	Citric acid as a proxy oxygenated organic material in the atmosphere.....	74
4.1.1	The citric acid/water aerosol phase diagram.....	74
4.2	Results and discussion .....	76
4.2.1	Homogeneous ice nucleation in liquid aerosol vs. heterogeneous ice nucleation by glassy aerosol .....	79
4.2.2	Experiments using aerosol injected at temperatures below $T_g'$ .....	81
4.2.3	Why do glassy aerosol particles act as ice nuclei?.....	82
4.2.4	Could homogenous ice nucleation have enhanced the IN ability of the aerosol used during the ICE01 experiments?.....	82
4.2.5	Evidence for ice nucleation by glassy aerosol in the TTL.....	83
4.3	Modelling the impact of glassy aerosol on TTL cirrus .....	84
4.3.1	Modelling methodology.....	84
4.3.2	Modelling results.....	86
4.3.2.1	Heterogeneous vs. Homogeneous freezing.....	88

4.3.2.2	Prolonged supersaturation.....	89
4.3.2.3	The effect of varying model updraft rate .....	90
4.3.2.4	Changing the model temperature .....	94
4.3.2.5	Changing the fraction of aerosol particles which are glassy .....	95
4.4	Summary and conclusions .....	96
Chapter 5:	ICE02 Campaign: Heterogeneous ice nucleation by other glassy aerosols ..	
	.....	98
5.1	Aerosols chosen for study during ICE02 .....	98
5.2	Did aerosols crystallise in experiments during ICE02? .....	101
5.3	Results and discussion .....	105
5.3.1	Expansion with a liquid aerosol .....	105
5.3.2	Expansions with glassy aerosol.....	108
5.3.3	Heterogeneous ice nucleation: a general property of glassy aerosols.....	110
5.3.4	Does glassy SOA nucleate ice heterogeneously?.....	113
5.3.5	Iso-humid experiments to probe ice nucleation above $RH_g$ .....	114
5.3.6	Parameterising ice nucleation by glassy aerosol.....	119
5.3.6.1	Parameterisations based on the fraction activated to ice ( $f_{ice}$ ) .....	120
5.3.6.2	Parameterisations based on the ice active surface site density ( $n_s$ ) ..	120
5.3.7	The impact of glassy aerosol on cirrus formation outside the TTL .....	124
5.4	Summary and conclusions .....	125
Chapter 6:	ICE02 campaign: Enhanced ice nucleation by ice processed glassy	
aerosols	.....	127
6.1	Aerosols chosen for study .....	127
6.2	Results .....	128
6.2.1	HMMA .....	128
6.2.2	Raffinose .....	131
6.2.2.1	Pre-activation in a repetitive series of expansions.....	131

6.2.2.2	Conservation of pre-activation for long time periods under subsaturated conditions .....	135
6.2.3	Raffinose/M5AS .....	138
6.3	Summary of results .....	143
6.4	Discussion .....	144
6.4.1	Could homogeneously nucleated ice catalyse the crystallisation of solute crystals that then nucleate ice heterogeneously?.....	144
6.4.2	The relationship between pre-activation and glass formation.....	147
6.4.3	Atmospheric implications .....	149
6.5	Summary and Conclusions.....	149
Chapter 7:	Characterisation and first results from the DMC .....	151
7.1	Chamber humidity characterisation .....	151
7.1.1	The ice sublimation point.....	151
7.1.2	Deliquescence point of ammonium sulphate .....	156
7.2	Does the hydrophobic sample substrate nucleate ice? .....	157
7.3	Deposition mode ice nucleation by kaolinite (KGa-1b) .....	158
7.3.1	Does repeated ice nucleation by KGa-1b particles enhance their ability to act as IN?.....	159
7.3.2	Effect of KGa-1b surface area on ice onset $RH_i$ .....	165
7.3.3	Nucleation rates and contact angles .....	171
7.4	Summary and conclusions .....	173
Chapter 8:	Summary and conclusions .....	175
8.1	Ice nucleation by glassy aerosols under cirrus conditions .....	175
8.2	The deposition mode chamber .....	179
Appendix – Pictures from the ICE campaigns .....		181
References .....		186

## List of tables

<b>Table 5.1</b> Molecular structures of the glass forming components of the four aqueous aerosols examined in this study with associated $T_g'$ and uncertainties (Zobrist et al., 2008). The molecular structure and $T_g'$ of citric acid, a component of the glassy aerosol that was used for the experiments described in Chapter 4 has been included for comparison (note that no uncertainties in $T_g'$ were available for citric acid). The percentages next to the components of raffinose/M5AS aerosol indicate the individual species contribution by mass to the mixture. ....	100
<b>Table 5.2</b> Parameters for the linear fits to $n_s$ shown in Figure 5.9 and Figure. 5.10 as a function of $RH_i$ . Also included is $n_s$ for glassy citric acid aerosol, calculated based on the parameterisation of $f_{ice}$ vs. $RH_i$ (Figure 4.7). Note that each fit is only valid for the range of $RH_i$ shown in the rightmost column of the table. ....	123
<b>Table 7.1</b> Temperature and $RH_i$ at the onset of ice nucleation for experiments with varying surface areas of KGa-1b present. Note that the ice onset for the 110927-KGa1b experiment (marked in red) is for an ice crystal that could have nucleated either on the glass substrate or on a clay particle. ....	165
<b>Table 7.2</b> The heterogeneous nucleation rate ( $J_{het}$ ) and contact angles at the onset of ice nucleation for experiments 110921-KGa1b and 110929-KGa1b. ....	172

## List of figures

<b>Figure 1.1</b> An example atmospheric temperature profile up to 100 km, adapted from Brasseur et al. (1999). .....	2
<b>Figure 1.2</b> Radiative forcing of climate between 1750 and 2005 from mechanisms and agents discussed in Chapter 2 of the IPCC Fourth Assessment Report: Climate Change 2007, Working Group I: The Physical Science Basis (Solomon et al., 2007). The diagram also includes the associated level of scientific understanding (LOSU) and spatial scales of the effects. ....	4
<b>Figure 1.3</b> The variation of $\Delta G_s$ , $\Delta G_b$ and $\Delta G_c$ with radius ( $r$ ). The critical radius, $r_c$ , is also indicated. Adapted from Mullin (2001). ....	10
<b>Figure 1.4</b> a) Melting (squares) and freezing (circles) temperatures for a variety of aqueous solutions versus solution molality. b) Freezing data shown as a function of water activity. The melting threshold is shown as a dashed line and the freezing threshold a solid line. Taken from Koop et al. (2000). ....	11
<b>Figure 1.5</b> The different modes of heterogeneous ice nucleation. ....	15
<b>Figure 1.6</b> Exponential decay of unfrozen water droplets containing kaolinite and silver iodide with time. Taken from Murray et al. (2012a). ....	18
<b>Figure 1.7</b> Example of the variation in heterogeneous ice nucleation onset temperature and humidity (displayed as ice saturation ( $S_i$ ) = $RH_i/100$ ) for IN of various compositions (see legend) in the deposition, condensation and immersion modes. The black solid line is the water saturation threshold and the dashed black line is the homogeneous ice nucleation threshold (Koop et al., 2000). Figure taken from Hoose and Möhler (2012). ....	22
<b>Figure 1.8</b> Typical negative ion single-particle mass spectra of stratospheric aerosol (A) and the upper troposphere (B), taken from Murphy et al. (1998). It can be seen that the stratosphere is dominated by sulphate species whereas the upper tropospheric aerosol also contained organic species ( <i>e.g.</i> C <sub>2</sub> H <sub>2</sub> <sup>-</sup> fragment) including organic acids ( <i>e.g.</i> CH <sub>3</sub> CO <sub>2</sub> <sup>-</sup> fragment), as well as some sulphate species. ....	23
<b>Figure 1.9</b> Altitude vs. latitude cross section adapted from Murphy et al. (2006) showing the variation of aerosol composition between pure sulphates in the stratosphere and internally mixed sulphate-organic aerosol in the upper troposphere. Note the abundance of aerosols containing large fractions of organic material at tropical latitudes ~23°N. ....	24



**Figure 1.10** A) The composition of background aerosol (left hand chart) and the residues of ice particles nucleated heterogeneously and homogeneously (middle chart) and solely heterogeneously (right hand chart) from natural aerosol at cirrus temperatures (adapted from Demott et al. (2003)). B) Ice crystal residues from anvil cirrus at 12 – 14 km at tropical and sub-tropical latitudes (adapted from Froyd et al. (2010), sub-tropical data from Cziczo et al. (2004)). Anvil cirrus ice crystal residues contained disproportionately more mineral dust and sea salt compared to the background aerosol. ....26

**Figure 1.11** Average composition of atmospheric mineral dust (Atkinson and Murray, 2012) based on dust compositions from seven *in situ* studies (see text).....27

**Figure 1.12** The layer of subvisible cirrus (SVC) as seen from the cockpit of NASA WB-57F during the CRAVE campaign (Costa Rica Aura Validation Experiment). Photograph credited to CPI. J. H. Bain of NASA Johnson Space Center and adapted from Lawson et al. (2008).....29

**Figure 1.13** A comparison of the composition of unfrozen background aerosol particles in the TTL (left hand chart) with the residue of ice crystals from SVC sampled *in situ* in the TTL. Adapted from Froyd et al. (Froyd et al., 2010).....30

**Figure 1.14** Quality checked clear sky (A) and in cloud (B) humidities collected during 28 flights. Adapted from Krämer et al. (2009).....32

**Figure 1.15** A schematic comparing the viscosities of some common liquids, semi-solids and solids. Adapted from Koop et al. (2011).....36

**Figure 1.16** A schematic of the change in enthalpy and entropy and isobaric heat capacity that occurs during crystallisation and at the glass transition. Reproduced from Zobrist et al. (2008).....37

**Figure 1.17** The behaviour of ‘shattered’ ultra-viscous or glassy iodine acid droplets on increasing humidity. Taken from Murray et al. (2012b).....38

**Figure 1.18** The effect of changing the surrounding humidity on an amorphous solid. Mass is equivalent to hygroscopic growth factor, which is equal to the ratio of the aerosol particle radius at a given RH and the aerosol particle’s dry radius. Adapted from Koop et al.(2011). ....39

**Figure 2.1** A schematic diagram of the AIDA chamber and its associated instrumentation. Adapted from Wagner et al. (2012b). ....42

**Figure 2.2** Particle diameter (D, top panel) and inferred ice particle number concentration ( $N_{ice}$ , bottom panel) observed by optical particle counters WELAS 1

(blue) and WELAS 2 (black) during an ice nucleation event (start of ice nucleation inferred using SIMONE and marked by vertical dashed black line). .....	46
<b>Figure 2.3.</b> The phase diagram of levoglucosan solution aerosol and the idealised trajectory of an aerosol during typical experiments at AIDA. The black line is the ice liquid equilibrium line, the dashed red line is the homogeneous freezing threshold based on the water activity homogeneous freezing criteria (Koop et al., 2000) and the green solid line is the humidity induced glass transition threshold ( $RH_g$ ) for levoglucosan solution aerosol, with associated upper and lower uncertainties (dashed green lines) based on uncertainties in the parameters used in the Gordon-Taylor equation (Equation 2.1) (Zobrist et al., 2008). The orange arrows represent idealised temperature/humidity trajectories. The ice-liquid equilibrium and homogeneous freezing lines are common to all solutions used in this study, but $RH_g$ is unique to each solution system. ....	49
<b>Figure 3.1</b> The partial pressure of water vapour as a function of temperature at 100% $RH_i$ . Plotted using a parameterisation of the saturation vapour pressure of water vapour over an hexagonal ice surface (Murphy and Koop, 2005). .....	54
<b>Figure 3.2</b> The body of the chamber, made from PEEK polymer. A shows it without the sample holder in place. B shows the chamber in position on the bottom plate, with the sample holder in place. Note also the fan and four ports, one of which the power cables for the fan exit through.....	58
<b>Figure 3.3</b> Cross sectional diagram of the deposition mode chamber showing the position of the temperature controlled ice surface and sample holder. The chamber's associated temperatures controllers, thermometer, microscope and microscope stand have been omitted for clarity.....	60
<b>Figure 3.4</b> A) The aluminium surface the ice layer is deposited upon sits on top of a Peltier element and both are surrounded by an insulating plastic ring. B) This whole assembly is attached to the surface of the top plate with a thin layer of thermal paste. .	61
<b>Figure 3.5</b> The sample holder is designed to ensure a good thermal contact between the end of the copper rod and the underside of the glass coverslip the sample is deposited onto.....	63
<b>Figure 3.6</b> A screen shot from the LabView program written to display and record images and temperatures from the chamber. It works in conjunction with a USB camera connected to the microscope and a HS1560 thermometer connected via an RS232 serial port. The program also continuously calculates and displays the humidity using the measured temperatures and Equation 3.1.....	65

<b>Figure 3.7</b> The LabView block diagram for the program written for use with the chamber during experiments (see description in text). .....	66
<b>Figure 3.8</b> A comparison of the results of depositing KGa-1b mineral dust using a nebuliser (panel a) and by evaporating a single droplet of suspended clay (panel b).....	69
<b>Figure 3.9</b> The DMC and associated experimental apparatus.....	71
<b>Figure 4.1</b> Citric acid (2-hydroxypropane-1,2,3-tricarboxylic acid) was used as a proxy for atmospheric oxygenated organic material. ....	74
<b>Figure 4.2</b> a) Phase diagram for aqueous citric acid aerosol particle as a function of temperature and citric acid wt%, with idealised experimental trajectories for expansions 1 – 5 shown as black arrows. The dashed arrows represent trajectories where the concentration of the aerosol is uncertain due to expansions starting below the glass transition ( $RH_g$ ) (cyan dot dash line). Also shown are the homogeneous ice nucleation threshold based on data from Murray et al. (2008b) and the ice liquid equilibrium line (Koop et al., 2000). b) shows the phase diagram as a function of $RH_{liq}$ . Above $RH_g$ the aerosol concentration was in equilibrium with the chamber humidity, therefore $a_w = RH_{liq}/100$ . The ice liquid equilibrium threshold is shown as a solid black line and the homogeneous freezing threshold (Koop et al., 2000) is shown as a dashed red line.....	76
<b>Figure 4.3</b> SMPS size distribution for citric acid solution aerosol particles taken immediately prior to run 3. The red line is a log normal fit to the distribution. ....	77
<b>Figure 4.4</b> A summary of the results of expansion experiments during ICE01. Fits to experimental $RH_i$ /temperature trajectories are shown as dashed black lines. Depolarisation thresholds are indicated on each experimental trajectory by orange triangles. For clarity, only the depolarisation thresholds have been shown (blue diamond and star respectively) for experiments six and seven, which used different citric acid aerosols from that used in runs 1 – 5 (see Section 4.2.2). The size/colour of the overlaid bubbles shows the fraction of aerosol frozen ( $f_{ice}$ ) during the course of experiments 1- 5. The $RH_g$ threshold for citric acid solution aerosol (Maltini et al., 1997;Murray, 2008b) is shown as a dot-dash cyan line. ....	78
<b>Figure 4.5</b> Comparison of an expansion in which homogeneous nucleation occurred (Run 4, panels A and B) with an expansion in which the glassy citric acid aerosol nucleated ice heterogeneously (Run 3, Panels C and D). Panels A and C show the temperature and $RH_i$ (black and blue solid lines respectively), the $RH_g$ threshold (cyan dot-dot-dash line) and the homogeneous freezing threshold based on liquid $H_2SO_4$ aerosol freezing at AIDA (Möhler et al., 2003) (blue dot-dash line). Panels B and D	

show  $N_{ice}$  measured using the WELAS 2 instrument. Grey dashed lines mark the onset of ice nucleation in each case, based on  $\delta$ ..... 80

**Figure 4.6** Temperature, pressure,  $RH_i$  and  $H_2O$  mixing ratios used in the initialisation of APSCm-1-D. All values are within the range of TTL in situ measurements (Peter et al., 2003;Jensen et al., 2008). ..... 85

**Figure 4.7** The parameterisation of heterogeneous ice nucleation by glassy aerosol used in the cirrus modelling. It is a linear fit to  $f_{ice}$  as a function of  $RH_i$  from run 3. The fit has the equation  $f_{ice} = 7.7211 \times 10^{-5} RH_i(\%) - 9.2688 \times 10^{-3}$ . It is valid for  $RH_i$  from 121 to 170%. When  $RH_i < 121\%$ ,  $f_{ice} = 0$ . ..... 86

**Figure 4.8** Example model results for  $S_i$ ,  $N_{ice}$ ,  $R$  and IWC. Plots on the left are from runs using only liquid aerosol, right hand plots used a 50/50 mix of liquid and glassy aerosol. All runs used a cooling rate of  $0.76 \text{ K hr}^{-1}$ ,  $100 \text{ cm}^{-3}$  aerosol concentration and were initialised using the profiles in Figure 4.6..... 87

**Figure 4.9** A comparison of modelling results averaged between 17.25 and 17.35 km. Both runs were initialised using the profiles shown in Figure 4.6, used a cooling rate of  $0.76 \text{ K hr}^{-1}$  (equivalent to  $3 \text{ cm s}^{-1}$  updraft rate) and had a total aerosol number concentration of  $100 \text{ cm}^{-3}$ . Panel a) shows the results from a run in which only liquid aerosol were present. Panel b) shows a run in which 50% of the aerosol were liquid and 50% were in the glassy state. .... 88

**Figure 4.10** The effect of changing the cooling rate on  $N_{ice}$  and  $RH_i$  for runs that had a total aerosol concentration of  $100 \text{ cm}^{-3}$  that was split 50/50 between glassy and liquid aerosol. For comparison, a run that used only liquid aerosol and a cooling rate of  $0.76 \text{ k hr}^{-1}$  is included (dashed red line). All runs were initialised using the profiles in Figure 4.6. The solid grey bar represents the observed range of  $N_{ice}$  in the TTL (Jensen et al., 2010). ..... 91

**Figure 4.11** The effective surface area of ice ( $SA_{eff}$ ), effective radius ( $R$ ),  $N_{ice}$  and  $RH_i$  for runs with varying cooling rates. The horizontal lines mark peak  $N_{ice}$  in each case. All runs used  $100 \text{ cm}^{-3}$  aerosol concentration and a 50/50 mix of glassy and liquid particles. Also shown is the homogeneous run at  $0.76 \text{ K hr}^{-1}$ . Colours correspond to those in Figure 4.10. .... 93

**Figure 4.12** A comparison of the effective ice surface area ( $SA_{eff}$ ) at peak  $N_{ice}$  for the heterogeneous runs and the homogeneous run shown in Figure 4.10 (blue squares) and for the sensitivity tests shown in Figure 4.13 ( $SA_{eff}$  at peak  $N_{ice}$  for runs which took

place at higher (green diamond) and lower (black diamond) temperatures, and with a smaller fraction of glassy particles (open red diamond)).....94

**Figure 4.13** Sensitivity tests to establish the effects on  $R$ , IWC,  $N_{ice}$  and  $RH_i$  of both increasing the initial model temperature by 10 K (green lines) and decreasing the initial model temperature by 5 K (black lines). These runs used  $100\text{ cm}^{-3}$  total aerosol concentration split 50/50 between glassy and liquid aerosol. The effect of reducing the ratio of glassy to liquid aerosol to 1:9 was also investigated (red lines). In this run the model was initialised using the original temperature profile and kept a total aerosol concentration of  $100\text{ cm}^{-3}$ . All runs used a cooling rate of  $0.76\text{ k hr}^{-1}$ .....95

**Figure 5.1** An aerosol phase diagram comparing the estimated range of the relative humidity induced glass transition threshold ( $RH_g$ ) for atmospheric SOA (grey area) (Koop et al., 2011) and the  $RH_g$  thresholds (Zobrist et al., 2008) for the aerosols investigated in this study. The solid black line is the ice-liquid equilibrium and the dashed red line is the homogeneous freezing threshold for liquid solution droplets (Koop et al., 2000). For a more detailed explanation of aerosol phase diagrams see Chapter 2. ....99

**Figure 5.2** Panel A shows the experimental temperature/time series for raffinose aerosol cooled to 217.5 K then warmed up to 229 K at which point an expansion was performed. The top section of panel B shows the temperature and  $RH_i$  (solid black and blue lines respectively) as well as the temperature dependent threshold humidity at which homogeneous ice nucleation is expected to occur, based on AIDA experiments using liquid aqueous  $\text{H}_2\text{SO}_4$  aerosol (Möhler et al., 2003) (dotted blue line). Homogeneous ice nucleation was observed at the predicted humidity, indicating that the aerosol had liquefied on exposure to increasing humidity, which would not have occurred had it crystallised..... 104

**Figure 5.3** A typical expansion experiment at the AIDA chamber using liquid aqueous raffinose/M5AS aerosol. Panel A shows the temperature and  $RH_i$  (solid black and blue lines) as well as the expected homogeneous freezing  $RH_i$  (dash-dot blue line), based on AIDA homogeneous freezing data from liquid aqueous  $\text{H}_2\text{SO}_4$  aerosol (Möhler et al., 2003). Panel B shows the pressure and total aerosol concentration (orange and burgundy lines). The ice particle number concentration from WELAS 1 and the fraction of aerosol that froze are shown in Panel C (black and red lines). In panel D, the onset of ice

nucleation is seen as the sharp rise in  $\delta$  (cyan line). The time/humidity at the onset of freezing is marked with dashed black lines..... 107

**Figure 5.4** A comparison of the behaviour of aqueous HMMA solution in expansion runs B and C. Panel A shows the temperature profile of the experimental series. The bottom panels show experimental data for runs B (started at 220.7 K) and C (started at 232.1 K). Panels B1 and C1 show in each case the experimental temperature and humidity (black and blue solid lines respectively). Panels B2 and C2 show the ice particle number concentration ( $N_{ice}$ , black line) and the fraction of the aerosol frozen ( $f_{ice}$ , red line). The AIDA homogeneous ice nucleation threshold (Möhler et al., 2003) is indicated in B1 and C1 by dash-dot blue lines. The ice nucleation onsets were observed as an increase of at least 1% in the backscattering linear depolarisation ratio,  $\delta$ , and are marked with dashed black lines. .... 109

**Figure. 5.5** The experimental temperature – RH<sub>i</sub> trajectories for the expansion experiments for each aerosol type (solid black lines). Associated with each trajectory is an ice nucleation onset determined using the depolarisation measurement (defined by a change in the depolarisation ratio of at least 1% – for example see Figure 5.3), with orange triangles representing homogeneous ice nucleation onsets and blue stars representing heterogeneous ice nucleation onsets. The figures also show the aerosol RH<sub>g</sub> thresholds (dashed red lines) and their associated uncertainties (shaded blue areas) based on parameterisations from Zobrist et al. (2008). The point at which RH<sub>g</sub> crosses the marked 100% RH<sub>i</sub> line (dotted black line) is equal to  $T_g'$  for that aerosol type. Also shown is the water saturation line (cyan dot-dot-dash line, shows where RH<sub>liq</sub> is equal to 100%) and the expected homogeneous freezing threshold (blue dot-dash line), based on the homogeneous freezing of sulphuric acid solution aerosol in the AIDA chamber (Möhler et al., 2003)..... 111

**Figure. 5.6** The fraction of aerosol that froze heterogeneously at temperatures above 198 K during the expansion experiments shown in Figure. 5.5. At temperatures below 198 K, the ice crystals were too small to allow  $N_{ice}$  to be inferred accurately from the WELAS data using a size threshold, preventing the calculation of  $f_{ice}$  for those experiments. See figure legend for details. Bracketed numbers in legend indicate the temperature at which the onset of ice nucleation occurred in each case. The solid cyan line is the linear fit ( $f_{ice} = 7.7211 \times 10^{-5} (\%RH_i) - 9.2688 \times 10^{-3}$  for RH<sub>i</sub>=121 - 170% and  $f_{ice} = 0$  when RH<sub>i</sub><121%) used to parameterise heterogeneous ice nucleation by glassy

citric acid solution aerosol (see Chapter 4). Due to scatter in the ice particle concentration data, a certain amount of noise is present. The shaded region represents a region of uncertainty in which the signal to noise ratio is too low for an accurate estimation of the fraction frozen. .... 114

**Figure 5.7** Time series for ice production runs using raffinose/M5AS solution aerosol (Panels A1 and A2) and raffinose solution aerosol (Panels B1 and B2). The temperature trajectories are shown as solid black lines in panels A1 and B1. In these panels the RH<sub>i</sub> trajectories are displayed as colour mapped time series, the colour maps correspond to the estimated time taken for water molecules in the aerosol particles to diffuse 85 nm (the average radius of particles in this study). The humidity at which homogeneous ice nucleation is expected is shown in both cases as a dash-dot blue line. RH<sub>g</sub> is shown as red dot-dot-dash lines. The ice particle number concentration ( $N_{ice}$ ) and fraction frozen ( $f_{ice}$ ) are shown as black and red lines respectively. The onset of ice nucleation is represented in each case by black dashed lines. .... 116

**Figure 5.8** A comparison of combined SMPS and APS size distributions of aerosols taken immediately prior to experiments shown in Figure 5.5. The size distributions of the aerosols used in ICE02 were found to be consistent with size distributions measured for citric acid aerosol during the ICE01 campaign (Figure 4.3). The average of the mean volume-equivalent sphere diameters ( $d_p$ ) of the aerosols was  $0.170 \pm 0.027 \mu\text{m}$ . .... 121

**Figure 5.9** The ice active surface site densities ( $n_s$ ) for glassy aerosols which nucleated ice heterogeneously (see Figure 5.5). Linear fits to each dataset are shown in the corresponding colour. The solid cyan line is  $n_s$  for glassy citric acid aerosol calculated using the fraction frozen parameterisation from Chapter 4 (shown in Figure 5.6 and Figure 4.11) and the size distribution for the aerosol used in the experiment upon which the parameterisation is based. Table 5.2 contains equations for linear fits to  $n_s$  for aerosols from this study and glassy citric acid aerosol. .... 122

**Figure 5.10** A comparison of  $n_s$  for glassy aerosols from this study and other IN species (see Figure 5.6 legend for symbol details). Glassy citric acid aerosol  $n_s$  is also shown (solid cyan line, see Figure 5.9 caption for details). Linear fits to the data from this study are shown in the corresponding colour. Volcanic dust at ~225 K, (grey circles) (Steinke et al., 2011), Arizona test dust (ATD) at 238 – 248 K (grey downwards pointing triangles) (Connolly et al., 2009) (note that these are revised figures for ATD, based on a re-analysis by Niemand et al. (Niemand et al., 2012b)) and a

parameterisation of  $n_s$  for iron oxide nanoparticles at 190 K (grey dashed line) (Saunders et al., 2010) are shown. The parameters to the fits to  $n_s$  vs.  $RH_i$  for all of the glassy aerosols shown in this figure (solid lines) are included in Table 5.2..... 124

**Figure 6.1** Panel A shows the experimental temperature time series for expansion runs (1 – 5) that used HMMA aerosol. Panel B shows the approximate starting points for expansions 1 – 5 in the HMMA solution state diagram. See text for details..... 129

**Figure 6.2** Experimental results for runs 3 and 4 (Figure 6.1A) that used HMMA aerosol. In run 3, homogeneous nucleation occurred at the AIDA homogeneous nucleation threshold (Green solid line). This caused enhancement of the aerosol’s ice nucleation ability in the following run in which ice nucleated very close to ice saturation (red horizontal line second panel down) at 105%  $RH_i$ . The  $RH_g$  threshold is also shown (solid blue line, second panel down) (Zobrist et al. (2008)) and in each panel data colour is coordinated to the colour of the corresponding axis label. Particle diameter (third panel down) and  $N_{ice}$  (fourth panel down) data from the WELAS 1 and WELAS 2 OPC’s are displayed in blue and black respectively. Vertical black dashed lines indicate the onset of ice nucleation based on the change in the backscattering linear depolarisation ratio  $\delta$  in the bottom panel, which also shows the backscattered intensity parallel to the incident polarisation state of the laser light,  $I_{back,par}$ . ..... 130

**Figure 6.3** Temperature profile for an expansion series using raffinose aerosol. The four expansion experiments are labelled ‘H’ or ‘A’ to indicate the presence of homogeneous ice nucleation or pre-activation behaviour during the expansion. .... 132

**Figure 6.4** Results for the experimental series of expansions shown in Figure 6.3 after ~35000 s. Note that the second panel down which shows the chamber humidity (black solid line) also includes the AIDA homogeneous ice nucleation threshold (green line) and the  $RH_g$  threshold (blue line) (Zobrist et al., 2008). The vertical black dashed lines mark the time at which the chamber humidity passed 100%  $RH_i$ . ..... 134

**Figure 6.5** Temperature profile experiments using raffinose aerosol. Pre-activation was observed in run 3 after homogeneous nucleation in run 2, despite ~2.5 hours at ~70%  $RH_i$ . ..... 136

**Figure 6.6** Experimental data for runs 2 and 3 which used raffinose aerosol. Early onset ice nucleation consistent with pre-activation was observed in run 3 after homogeneous ice nucleation in run 2. This was despite the aerosol being exposed to humidities between 70 and 80%  $RH_i$  for 2.5 hours between the two runs. See Figure 6.2 caption for full details of each panels contents..... 137



<b>Figure 6.7</b> Temperature profile for an experimental series using raffinose/M5AS aerosol. Early onset ice nucleation consistent with pre-activation was observed in runs 1D and 1E after homogeneous ice nucleation in the run 1C.....	138
<b>Figure 6.8</b> Run 1B of the series of expansions shown in the temperature profile in Figure 6.7. Ice nucleation starting at 120% RH <sub>i</sub> is most likely heterogeneous. See Figure 6.2 caption for details of the contents of each panel. ....	139
<b>Figure 6.9</b> Experimental data for runs 1C and 1D from the expansion series shown in Figure 6.7. An early ice mode at with an onset at 130% RH <sub>i</sub> was observed in 1D (first vertical dashed black line right hand panel, second vertical line marks start of homogeneous mode). This followed homogeneous ice nucleation in run 1C. See caption of Figure 6.2 for details of the measurements shown in each panel. ....	141
<b>Figure 6.10</b> Experimental temperature profile for another series of expansions using raffinose/M5AS aerosol. ....	142
<b>Figure 6.11</b> Experimental data for expansion runs 2B and 2C of the experimental series shown in Figure 6.10. No early ice mode was observed in run 2C despite homogeneous freezing in the preceding expansion (run 2B) and the expansion starting at a temperature close to run 1D in which an early mode was observed. This appears to be due to 2B taking place at a higher temperature. For details of the measurements shown in each panel see Figure 6.2.....	143
<b>Figure 6.12</b> Powder X-ray diffraction patterns captured during a freezing experiment using an emulsion of 15 wt% aqueous raffinose solution in oil (A – D). These patterns are consistent with those of stacking disordered ice (Isd) found by Malkin et al. (2012) (E). Also shown are the diffraction patterns for 2 wt% crystalline raffinose pentahydrate in oil (F) and crystalline raffinose pentahydrate. ....	146
<b>Figure 7.1</b> The rate of change in RH <sub>i</sub> at ice saturation for a sample changing in temperature at 0.1 K min <sup>-1</sup> . ....	152
<b>Figure 7.2</b> Parts of large ice crystals (panel A) which were not in good thermal contact with the glass substrate were found to sublime at higher calculated humidities. Smaller crystals like those shown in panel B sublimated uniformly.....	153
<b>Figure 7.3</b> The humidities generated by the DMC were tested by observing the point at which ice crystals began sublimating as they were heated at 0.1 K min <sup>-1</sup> . There was found to be an offset between RH <sub>i</sub> calculated using Equation 3.1, based on the temperatures of the sample support and the ice film, and the actual chamber RH <sub>i</sub> at	

saturation. The offset was significantly larger for thermocouple 1 (TC 1, blue triangle) than it was for thermocouple 2 (TC 2, red squares)..... 154

**Figure 7.4** The calculated temperature offset for the TC1 thermocouple based on the linear fit to the sublimation offsets shown in Figure 7.3. The fit was converted from a  $RH_i$  offset to a temperature offset and re-fitted using a second order polynomial - (Offset =  $-0.00015448918T^2 + 0.063085882T - 5.1732499$ ). ..... 155

**Figure 7.5** Still images taken from a DMC experimental video which show the initial restructuring and then dissolution of ammonium sulphate crystals on crossing the deliquescence threshold. .... 157

**Figure 7.6** Deliquescence  $RH_i$  onsets for ammonium sulphate crystals tested in the DMC at a range of temperatures (red stars). Also shown are experimentally derived deliquescence onsets from the literature (grey symbols, see figure legend and text for details) and the deliquescence threshold predicted using the E-AIM model (Wexler and Clegg, 2002)...... 157

**Figure 7.7** Ice nucleation onsets for two cleaned, silanised glass slides of the type used to support samples in the DMC..... 158

**Figure 7.8** Sample 110929-KGa1b (pictured) was deposited by evaporating a single large droplet of an aqueous suspension of Kga-1b. Rather than one big particle, this image shows a collection of smaller particles..... 160

**Figure 7.9** Time series for experimental runs 1- 4 which used sample 110929-KGa1b. The top panel shows the measured Peltier temperature and the sample temperature corrected based on the temperature offset for TC 2 at 240 K. The bottom panel shows  $RH_i$  calculated with the corrected sample temperature using Equation 3.1. For each experiment, the onset time of ice nucleation is marked with a vertical dashed black line and the time at which all visible ice particles had sublimated is marked with a vertical dash-dot-dot red line. The run 1  $RH_i$  ice onset and the average onset found in runs 2 – 4 are shown as black and green horizontal dashed lines respectively..... 161

**Figure 7.10** Stills from the videos of runs 1 – 4 taken after ice nucleation had occurred. The distribution and number of ice particles that nucleated on the sample was greatly reduced in runs 2 and 4 (Panels C and D), in which ice nucleation was enhanced. .... 163

**Figure 7.11** A comparison of  $\Delta RH_i$  for KGa-1b calculated from the ice onsets for runs 1 and 2 with  $\Delta RH_i$  for a different kaolinite sample (Roberts and Hallett, 1968) and Arizona Test Dust (ATD) (Knopf and Koop, 2006). ..... 164

**Figure 7.12** Images before (left hand column) and after (right hand column) ice nucleation in experiments using KGa-1b kaolinite (clay minerals society) particles of known surface area. For a summary of results see Table 7.1. .... 167

**Figure 7.13** The variation of ice onset  $RH_i$  with the surface area of kaolinite mineral dust. Ice onsets from DMC experiments at ~238 K which used KGa-1b kaolinite (red diamonds) are shown. They are compared with an ice onset for KGa-1b at 233 K (Kanji et al., 2008) (grey diamond) and average ice onsets for Fluka kaolinite at temperatures between 242 and 239 K (Wheeler and Bertram, 2012) (black squares). .... 169

**Figure 7.14** A comparison of ice onset  $RH_i$  as a function of sample surface area for a variety of atmospherically relevant mineral dusts. Ice nucleation onsets are shown for KGa-1b sample tested in the DMC at ~238 K alongside ice onsets for kaolinite (Fluka) and Illite (IMt-1, Clay Minerals Society) at 242 and 239 K and a selection of minerals dusts (including KGa-1b) tested by Kanji et al. (2008) at 233 K. .... 170

## List of abbreviations

AIDA	Aerosol Interactions and Dynamics in the Atmosphere
$a_w$	Water activity
CNT	Classical nucleation theory
CPC	Condensation particle counter
DMC	Deposition Mode Chamber
HMMA	hydroxy-3-methoxy-mandelic acid
IN	Ice nuclei
Kga-1b	Natural Kaolinite sample from the clay minerals society
$N_{ice}$	Ice particle number concentration
OPC	Optical Particle Counter
M5AS	A mixture of malonic acid, malic acid, maleic acid, glutaric acid, methylsuccinic acid and ammonium sulphate
RH	Relative Humidity
$RH_g$	The relative humidity induced glass transition
$RH_i$	Relative Humidity with respect to Ice
$RH_{liq}$	Relative Humidity with respect to liquid water
SOA	Secondary Organic Aerosol
SVC	Subvisible cirrus
$T$	Temperature
$T_g$	Glass transition temperature
$T_g'$	Glass transition temperature at ice saturation (100% $RH_i$ )
TTL	Tropical Tropopause Layer
UT	upper troposphere
$\delta$	The backscattering linear depolarisation ratio

# Chapter 1: Introduction

## 1.1 Earth's atmosphere

Earth is surrounded by a layer of gases that are retained by the action of gravity. The atmosphere protects the Earth from ultraviolet radiation emitted by the Sun, warms the surface of the planet via the greenhouse effect and acts as a buffer against extreme temperature changes during the diurnal cycle. These properties allowed the evolution of terrestrial life forms and continue to support a habitable environment at the Earth's surface.

The atmosphere is mainly composed of nitrogen (78.08%), oxygen (20.95%), argon (0.93%) and carbon dioxide (0.039%), plus traces of other gases including ozone and methane. It also has the largest percentage abundance of water vapour of all the planetary atmospheres in the solar system; containing ~0.4% water vapour averaged across the whole atmosphere (Wayne, 2000). The chemical composition of the atmosphere is maintained on geological timescales by the biosphere (*i.e.* by photosynthesis), by release from and uptake to the material of the Earth's crust and by degassing of the planet's interior (Seinfeld and Pandis, 2006). The release of anthropogenic pollutants since the industrial revolution has been shown to have had a concerning affect on the Earth's atmosphere. A clear example of this is the release of trace gases such as chlorofluorocarbons (Wayne, 2000), which catalytically destroy stratospheric ozone causing a hole in the Earth's ozone layer. There is also a large body of evidence that shows increased emissions of the greenhouse gas CO<sub>2</sub> from fossil fuel burning by a growing world population is causing an increase in global temperatures (Solomon et al., 2007).

### 1.1.1 Atmospheric structure

The atmosphere is divided into a series of layers based on the inversions that occur in its temperature profile as altitude increases (Figure 1.1). The lowest layer, the troposphere, extends ~10 km in height at the poles and ~17 km at the equator. It makes up 90% of the mass of the atmosphere and contains the vast majority of its water vapour and aerosols (Wayne, 2000). The troposphere is heated primarily at ground level by solar radiation and its temperature decreases as altitude increases. The tropopause is the

coldest point of the troposphere and marks the temperature inversion that occurs at the transition to the stratosphere. This inversion is due to heating associated with the presence of ozone in the stratosphere (Wayne, 2000).

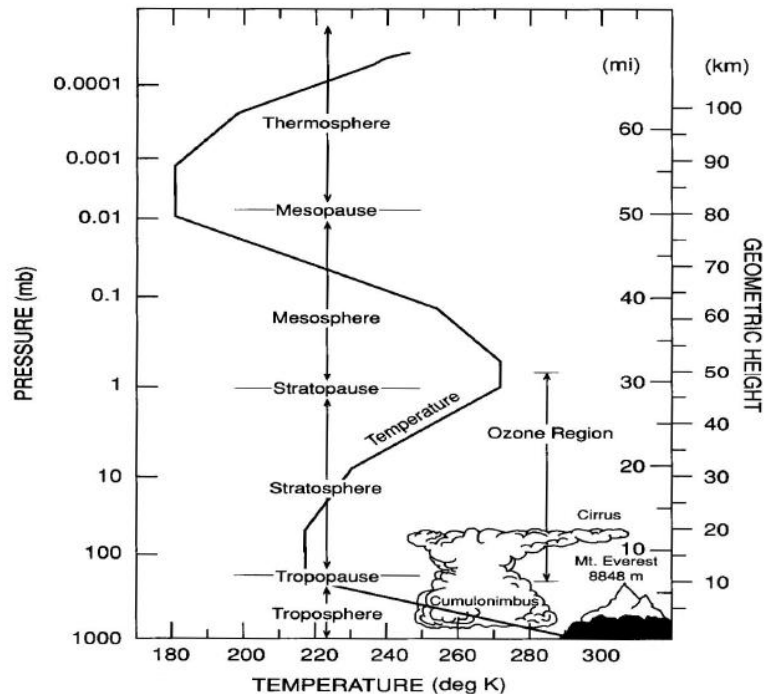


**Figure 1.1** An example atmospheric temperature profile up to 100 km, adapted from Brasseur et al. (1999).

### 1.1.2 Atmospheric Aerosol

Atmospheric aerosol is ubiquitous and is the precursor to liquid and ice cloud formation. Aerosols are suspensions of fine solid particles or liquid droplets in a gas. Generally atmospheric aerosol particles are considered to exist in a range of sizes from tens of micrometres to a few nanometres (Seinfeld and Pandis, 2006). They originate from the surface of the earth (primary atmospheric aerosol) and are also generated *in situ* (secondary atmospheric aerosol). Primary aerosol is emitted directly from both anthropogenic and natural sources such as the soot from the combustion of fossil fuels and biomass burning (*i.e.* natural wildfires) or mineral dust from desert regions blown into the atmosphere by storms (Koren et al., 2006). Secondary organic aerosol (SOA) is formed by gas phase organic species (often emitted by plants) condensing and/or reacting (Seinfeld and Pandis, 2006). The chemical composition of SOA is dependent upon its source region, its chemical precursors and how old it is. As SOA ages, the

uptake of gas phase species by the aerosol continues as does oxidation of the aerosol components by reactive species such as the OH radical.

Aerosol has both direct and indirect effects on climate. Aerosol particles directly affect the global radiation budget by scattering and absorbing incoming solar radiation. The indirect aerosol effect is more complex and is concerned with aerosol-cloud interactions. This includes the modification of the radiative properties of existing clouds by aerosol particles and the formation of new clouds (Twomey, 1974; Forster et al., 2007; Albrecht, 1989; Baker, 1997; Rosenfeld, 2000; Ramanathan et al., 2001; Baker and Peter, 2008). Insoluble particulates such as mineral dusts provide catalytic surfaces for liquid water to condense upon and soluble particles can take up water and become liquid droplets. Aerosols acting in these ways are described as cloud condensation nuclei (CCN). Liquid aerosol droplets can freeze homogeneously, *i.e.* in the absence of any foreign surfaces. Solid particles can heterogeneously catalyse the formation of ice either from within liquid droplets or directly from the vapour phase, thereby acting as ice nuclei (IN).

Aerosol-cloud interactions are one of the largest uncertainties when predicting change in the future climate (Forster et al., 2007) (see Figure 1.2). There is an increasing understanding of the impact of CCN on climate (Forster et al., 2007; Ramanathan et al., 2001; Lohmann and Feichter, 2005; McFiggans et al., 2006), but the role of IN in the indirect aerosol effect is still poorly understood (Forster et al., 2007; Baker, 1997; Cantrell and Heymsfield, 2005; Baker and Peter, 2008).

### **1.1.3 Clouds and the climate**

Only 0.001% of the Earth's water is in the atmosphere at any one time, the rest is in the oceans (97%), polar ice caps (2.4%) and lakes and rivers (0.6%) (Wayne, 2000). The atmosphere contains water in all three phases - as a vapour, as liquid droplets and as ice crystals. Clouds can contain both liquid droplets and ice particles at the same time (mixed phase clouds) or exist in entirely liquid or glaciated states (single phase clouds).

Clouds have a dual effect on Earth's climate as they simultaneously trap heat from the surface and reflect solar radiation back into space. The balance between these two effects is strongly dependent on the number, size and phase of cloud particles, which are directly influenced by the physical properties of the aerosol from which

clouds nucleate. There is no consensus on whether clouds will have a net cooling or warming feedback in response to an increase in anthropogenic CO<sub>2</sub>. It has been stated that this is the main cause of uncertainty in the magnitude of global warming when CO<sub>2</sub> is doubled (Lohmann and Feichter, 2005). Figure 1.2 summarises the estimated global average radiative forcing of climate (the difference between radiant energy received by the earth and energy re-radiated to space) between 1750 and 2005 associated with mechanisms and agents discussed in Chapter 2 of the IPCC Fourth Assessment Report (Solomon et al., 2007). The effect of CCN on the radiative properties of liquid clouds is considered to be well enough understood that it is included as the ‘cloud albedo effect’ forcing. In contrast, the effect of ice nucleation on cloud properties and formation is so poorly understood that its impact on the climate could not even be estimated (Solomon et al., 2007).

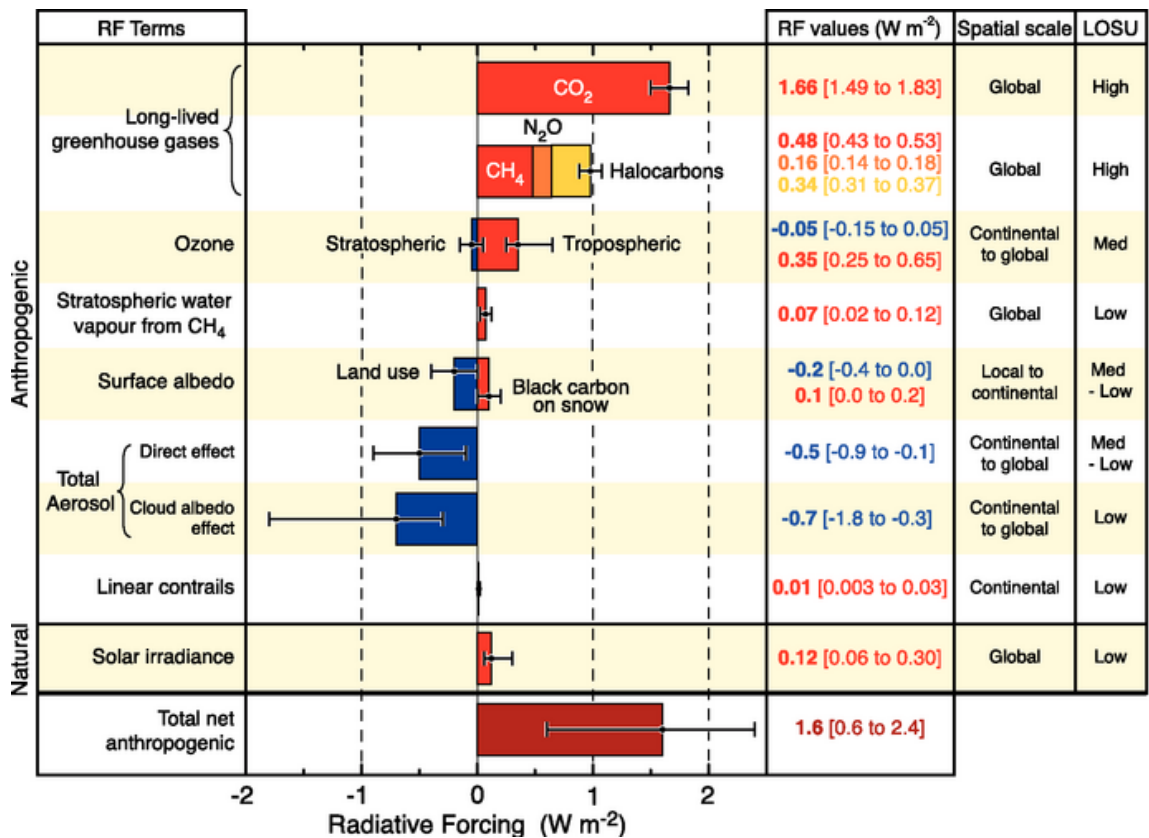


**Figure 1.2** Radiative forcing of climate between 1750 and 2005 from mechanisms and agents discussed in Chapter 2 of the IPCC Fourth Assessment Report: Climate Change 2007, Working Group I: The Physical Science Basis (Solomon et al., 2007). The diagram also includes the associated level of scientific understanding (LOSU) and spatial scales of the effects.



Clouds also have the potential to become a key asset in the mitigation of anthropogenic climate change; by either dispersing or ‘whitening’ them, it may be possible to adjust the Earth’s radiative balance (Latham et al., 2008; Mitchell and Finnegan, 2009).

### 1.1.3.1 Cirrus clouds

In recent years, cirrus clouds have been the focus of an increasing amount of research due to the large impact that changes in their coverage and microphysics have on model climates (Heintzenberg and Charlson, 2009). The World Meteorological Organisation defines cirrus clouds based on their day-time visible morphology as being “Detached clouds in the form of white delicate filaments or white/mostly white patches or narrow bands. These clouds have fibrous (hair-like) appearance, or a silky sheen, or both” (Lynch et al., 2002). The name cirrus is derived from the Latin meaning ‘a lock or ringlet of hair’. More generally, they are considered simply as cold, high clouds made entirely of ice particles. This definition allows the inclusion of the ubiquitous very high altitude, thin, featureless clouds commonly found in the tropics (Lynch, 1996).

Cirrus clouds exist below the homogeneous freezing point of liquid water (~236 K) (Pruppacher and Klett, 1997) and at altitudes above 6 km (Baran, 2009) but below the tropopause. Cirrus can also be divided into three broad sub-categories based on how they form; *in situ cirrus* which are widespread at all latitudes and form by ice nucleation in supercooled droplets or on solid ice nuclei, *anvil cirrus* which are common in the tropics and arise from the outflow at the top of deep convective systems and *contrail cirrus* that are associated with jet aircraft exhausts (Heintzenberg and Charlson, 2009).

Cirrus clouds cover ~30% of the Earth’s surface at any one time and in the tropics coverage is typically ~60 – 70% (Baran, 2009; Wylie and Menzel, 1999; Stubenrauch et al., 2006; Sassen et al., 2008; Nazaryan et al., 2008; Liou and Takano, 1994; Sassen and Comstock, 2001). Due to their ubiquity, they have a significant impact on the Earth’s radiative balance (Baran, 2009; Liou, 1986; Mitchell et al., 1989; Fu, 2007; Zhang et al., 1999), as well as playing important roles in upper tropospheric heat transfer (Ramanathan and Collins, 1991) and the transport of water vapour across the tropopause into the stratosphere (Jensen and Pfister, 2004). The radiative effect of cirrus at the surface is dependent on a number of factors including the clouds geographic location, their geometric thickness, variation in the shape and the

distribution of ice crystals. These factors determine how much infra-red radiation from the surface is trapped versus the amount of shorter wavelength solar radiation that is reflected back into space (Baran, 2009; Lynch et al., 2002). Changing the size of ice particles alone has a massive effect on the net radiative forcing. Modelling by Zhang et al. (1999) found that smaller ice crystals gave a net cooling of approximately  $40 \text{ W m}^{-2}$  compared to larger crystals that resulted in a net warming of about  $+20 \text{ W m}^{-2}$  (Baran, 2009). To be able to better quantify the impact of cirrus on future climate it is vital to better understand the microphysical processes that lead to their formation.

The conditions for cirrus formation (decreasing temperature, increasing humidity) are generated by the cooling of air parcels containing aerosol particles. This cooling can originate from the expansion of rising air parcels during large scale synoptic uplift (Lynch et al., 2002). More rapid temperature fluctuations caused by gravity waves also lead to cirrus formation (Barahona and Nenes, 2011; Lynch et al., 2002). In-situ cirrus nucleates from the background aerosol particles that are present in the cooling air mass. Ice can nucleate homogeneously when soluble aerosol take up water on increasing humidity, dilute and eventually freeze at the homogeneous nucleation threshold (Koop et al., 2000). Nucleation can be catalysed heterogeneously at humidities below the homogeneous threshold by solid IN particles. Nucleation at lower humidities by a small subset of aerosol particles can lead to a significant reduction of the cloud's ice particle number concentration (Jensen et al., 2010), which will also affect radiative properties of the cloud. It is important therefore to be able to identify which particles in an air mass will act as heterogeneous IN, which will take up water and freeze homogeneously and which will merely spectate.

## 1.2 Project objectives

The purpose of this project was to experimentally study the heterogeneous catalysis of ice nucleation by specific types of aerosol particles under conditions relevant to cirrus clouds that form *in situ*. The main objectives were:

- To investigate the ice nucleation behaviour of glassy aerosol particles under cirrus conditions at the AIDA (Aerosol Interactions and Dynamics in the Atmosphere) cloud simulation chamber.
- To develop and characterise a bench top instrument for the investigation of deposition mode ice nucleation.

- To use the new instrument to study the ice nucleation behaviour of a natural clay mineral dust in the deposition mode.

## 1.3 Thesis overview

The methodology and results relating to the investigation of glassy aerosol particles are presented in Chapters 2, 4, 5 and 6. Details of the development, characterisation and the results from the deposition mode chamber (DMC) are given in Chapters 3 and 7. Chapter 8 provides a summary of the project and presents the important conclusions.

The remainder of this chapter gives a general introduction to the theory of atmospheric ice nucleation and the aerosol particles that act as IN. It also introduces the topic of ‘amorphous aerosol’ and presents the rationale for studying the behaviour of glassy aerosol particles and clay minerals.

## 1.4 Project background

### 1.4.1 Ice nucleation in the atmosphere

Ice formation in clouds is a key process in initiating precipitation and is considered for this reason to be of vital importance to life on Earth (DeMott et al., 2010). The production of ice particles can affect the properties and behaviour of low and mid-level mixed phase cloud as well as upper tropospheric ice clouds. In mixed phase clouds, nucleated ice particles can grow larger at the expense of supercooled liquid water droplets (the Bergeron-Findeisen process) and then sediment, reducing the lifetime of the cloud (Pruppacher and Klett, 1997). The release of latent heat from the crystallisation of liquid water can drive clouds to higher altitudes and influence atmospheric dynamics. In upper tropospheric ice clouds (such as cirrus) the number of IN effects the number and size of ice particles, which changes the optical properties of the cloud. More, smaller ice particles result in whiter cirrus, increasing the reflectivity of the cloud (Lynch et al., 2002).

### 1.4.2 Homogeneous ice nucleation

Ice nucleation can occur homogeneously, *i.e.* directly from the liquid phase. This process starts with the formation of a cluster of the new phase. Cluster formation creates a new solid-liquid interface, which costs energy because molecules at the interface do not have all of their bonding interactions satisfied. The formation of new bonds between water

molecules inside the cluster releases energy. Competition between the energetically favourable creation of the bulk ice phase and the unfavourable interface formation results in a barrier to the formation of the new phase. Consequently, clusters of ice have to reach a critical size before they become stable enough to grow rather than just break up. Homogeneous nucleation is a stochastic process as the formation of clusters occurs randomly. For this reason, the probability of forming a stable cluster scales with the volume of the liquid. In larger volumes of water (*e.g.* ml), nucleation is likely to occur close to the melting point of ice, whereas in very small droplets ( $\sim 1 \mu\text{m}$  in diameter) such as those found in the atmosphere, water is able to supercool to  $\sim 236 \text{ K}$  (Stan et al., 2009; Kramer et al., 1999; Demott and Rogers, 1990; Benz et al., 2005; Murray et al., 2010a). This provides a limiting temperature below which pure water droplets in clouds are completely glaciated.

#### 1.4.2.1 Classical nucleation theory (CNT)

Ice nucleation can be described using classical nucleation theory (CNT). In the following example this theory is applied to the homogeneous nucleation of ice from supercooled water. The equations used are in a general form that can be applied to other situations such as the nucleation of ice from a gas supersaturated with water vapour. CNT provides a model for calculating the Gibbs free energy for the formation of a cluster of the new phase containing  $n$  water molecules ( $\Delta G_c$ ) (Mullin, 2001). This quantity is the sum of the Gibbs energy required for the formation of the interface between ice and supercooled water,  $\Delta G_s$  and the energy released by the forming of bonds in the new more thermodynamically stable bulk ice phase,  $\Delta G_b$ .

$$\Delta G_c = \Delta G_s + \Delta G_b$$

Equation 1.1

The energy of formation of the interface of a spherical cluster of  $n$  molecules of radius,  $r_n$ , is expressed as

$$\Delta G_s = 4\pi r_n^2 \gamma_{sl}$$

Equation 1.2

where in the case of homogeneous ice nucleation from liquid water,  $\gamma_{sl}$  (units:  $\text{J cm}^{-2}$ ) is the interfacial tension (or surface energy) between the developing crystalline

surface of ice and supercooled liquid water. The Gibbs free energy for the formation of the bonds in the cluster is given by

$$\Delta G_b = (\mu_s - \mu_l)n$$

Equation 1.3

where  $\mu_s$  and  $\mu_l$  are chemical potentials of the solid and liquid phase respectively. The difference in chemical potentials can be expressed as

$$-(\mu_s - \mu_l) = kT \ln S$$

Equation 1.4

where  $k$  is the Boltzmann constant,  $T$  is the temperature and  $S$  is the saturation of liquid water with respect to ice. The number of molecules in the spherical cluster,  $n$ , can be replaced with the expression

$$n = \frac{4\pi r_n^3}{3v}$$

Equation 1.5

where  $v$  is the molecular volume of water. Substituting Equation 1.2 - Equation 1.5 into Equation 1.1 gives

$$\Delta G_c = 4\pi r_n^2 \gamma_{sl} - \frac{4\pi r_n^3}{3v} kT \ln S$$

Equation 1.6

The two free energy terms have opposite signs and vary with  $r_n$ , causing  $\Delta G_c$  to pass through a maximum once the radius of the cluster reaches a critical size (Figure 1.3). Any cluster greater than or equal to this size is stable and therefore able to grow.

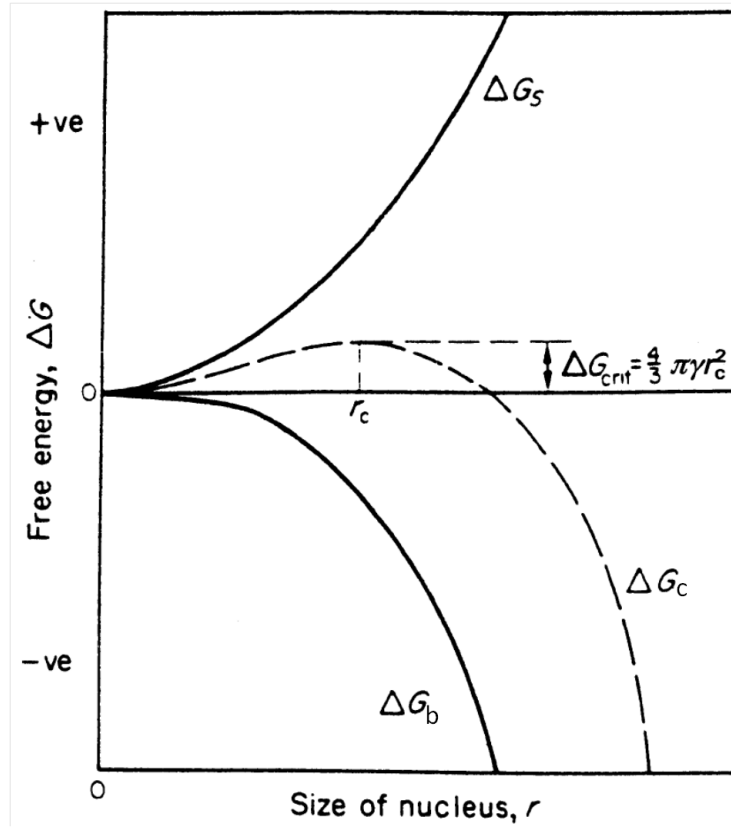


**Figure 1.3** The variation of  $\Delta G_s$ ,  $\Delta G_b$  and  $\Delta G_c$  with radius ( $r$ ). The critical radius,  $r_c$ , is also indicated. Adapted from Mullin (2001).

Differentiating Equation 1.6 with respect to  $r_n$ , setting  $d\Delta G_c/dr_n$  equal to zero and then rearranging for  $r_n$  yields the minimum radius required for a cluster to become stable. This is termed the critical radius,  $r_c$

$$r_c = \frac{2\gamma_{sl}v}{kT \ln S}$$

Equation 1.7

Substituting Equation 1.7 into Equation 1.6 and simplifying gives the free energy of formation of a critically sized cluster of new ice phase,  $\Delta G_{\text{hom}}$

$$\Delta G_{\text{hom}} = \frac{16\pi\gamma_{sl}^3v^2}{3(kT \ln S)^2}$$

Equation 1.8

### 1.4.2.2 The role of water activity in homogenous ice nucleation

Solutes depress the freezing temperature of water, allowing solution droplets to remain liquid at temperatures below the freezing threshold for pure water droplets (~236 K). The homogeneous freezing temperature of solution droplets of the same molality (moles of solute per kg of solution) varies depending on the solute. The offset in freezing temperatures is particularly noticeable at moderate to high solute concentrations. Koop et al. (2000) showed that the homogeneous freezing point for solution droplets was instead dependent on the water activity ( $a_w$ ) of the solution. Water activity provides an ‘effective’ solute concentration as it accounts for the intensity of the colligative effects between the water molecules and dissolved species. Water activity is equal to the ratio of the equilibrium vapour pressure of the solution and the equilibrium vapour pressure of pure water at the same temperature.

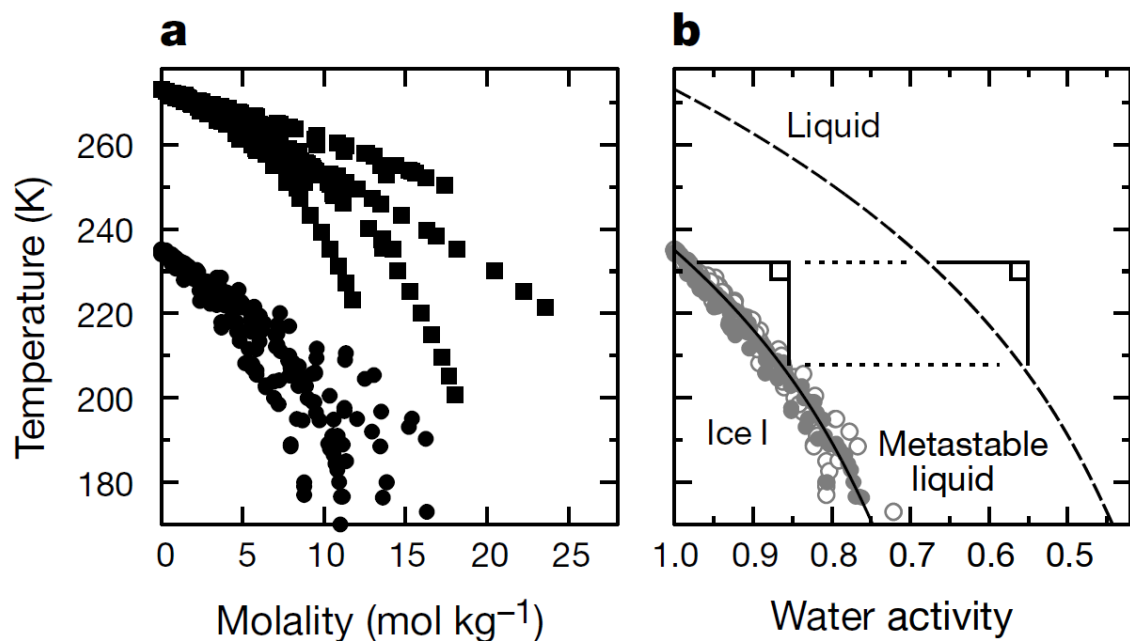


**Figure 1.4** a) Melting (squares) and freezing (circles) temperatures for a variety of aqueous solutions versus solution molality. b) Freezing data shown as a function of water activity. The melting threshold is shown as a dashed line and the freezing threshold a solid line. Taken from Koop et al. (2000).

Figure 1.4 compares the freezing and melting temperatures of solution droplets as a function of molality and water activity. Panel a shows the considerable deviation in freezing and melting points for different solutes at the same molality. When converted to the water activity scale, the freezing and melting points both collapse onto smooth

curves (Panel b). The melting points fall on to one curve because the water activity of the solution when in equilibrium with ice,  $a_w^i$ , is independent of the identity of the solute as it is only a function of temperature ( $T$ ) and pressure ( $p$ )

$$a_w^i(T, p) = e^{\frac{(\mu_w^i(T, p) - \mu_w^0(T, p))}{RT}}$$

Equation 1.9

where  $R$  is the gas constant and  $\mu_w^i(T, p)$  and  $\mu_w^0(T, p)$  are the temperature and pressure dependent chemical potentials in pure ice and pure liquid water respectively (in  $\text{J mol}^{-1}$ ). Koop et al. (2000) established that the freezing threshold (solid line in Figure 1.4b) is identical to the melting curve offset horizontally by a certain ' $\Delta a_w$ '. The freezing curve shown in Figure 1.4b corresponds to  $\Delta a_w = 0.305$

At equilibrium, the water activity of liquid solution droplets is equal to the saturation with respect to liquid water ( $S_{\text{liq}}$ ) of the air that surrounds them (*i.e.*  $a_w = S_{\text{liq}}$ ). At a particular temperature,  $S_{\text{liq}}$  is expressed as the ratio of the partial pressure of water vapour ( $p_{\text{H}_2\text{O}}$ ) and the saturation vapour pressure of water vapour over a flat liquid water surface ( $p_{\text{liq}}^*(T)$ ). The relative humidity with respect to liquid water ( $\text{RH}_{\text{liq}}$ ) is simply  $S_{\text{liq}}$  expressed as a percentage.

$$S_{\text{liq}} = \frac{p_{\text{H}_2\text{O}}}{p_{\text{liq}}^*(T)} = \frac{\text{RH}_{\text{liq}}}{100}$$

Equation 1.10

The relative humidity can also be expressed with respect to hexagonal ice ( $\text{RH}_i$ , this is important for deposition mode heterogeneous ice nucleation, see below). This expression takes the same form as that for liquid water, but with  $p_{\text{liq}}^*(T)$  replaced with the saturation vapour pressure of water vapour over a hexagonal ice surface  $p_{\text{ice}}^*(T)$ . Murphy and Koop (2005) provide parameterisations for  $p_{\text{liq}}^*(T)$  and  $p_{\text{ice}}^*(T)$  for temperatures between 123 and 332 K.

$$S_i = \frac{p_{\text{H}_2\text{O}}}{p_{\text{ice}}^*(T)} = \frac{\text{RH}_i}{100}$$

Equation 1.11



When supercooled concentrated ( $a_w \ll 1$ ) liquid solution droplets are exposed to increasing atmospheric humidity they will dilute and then freeze when their water activity reaches a threshold temperature dependent value of  $RH_{liq}$ . This result simplifies the prediction of the conditions under which homogeneous ice nucleation occurs in atmospheric aerosol droplets devoid of any solid impurities.

### 1.4.3 Heterogeneous ice nucleation

The nucleation of ice can be catalysed by particles in the atmosphere, raising the temperature or lowering the humidity at which it can occur. Ice nuclei (IN) represent a subset of the atmosphere's aerosol population. In general, the fraction of aerosol able to act as IN increases as temperature decreases and  $RH_i$  increases (Pruppacher and Klett, 1997). The absolute number of IN has been found to correlate with the number concentration of aerosol particles larger than 0.5  $\mu\text{m}$  in diameter (DeMott et al., 2010). Typically IN concentrations are found to be seven to nine orders of magnitude lower than the total aerosol concentration (at  $\sim 260$  K) (Szyrmer and Zawadzki, 1997). Pruppacher and Klett (1997) outline some physical characteristics that increase the likelihood of a particle being able to act as an ice nucleus:

- *Insolubility* – particles that dissolve or disintegrate under wet conditions are less likely to be able to act as IN as they would not provide a rigid surface to aid the formation of a critically sized ice germ. It should be noted however that soluble crystalline materials such as ammonium sulphate (Abbatt et al., 2006) do nucleate ice. Hence this characteristic could be defined simply as the ability to act as a surface.
- *Size* – IN need to be similarly sized or bigger than the size of a critical ice germ and are typically found to be  $> 0.1 \mu\text{m}$  in diameter.
- *Chemical bonds* – the type and strength of available chemical bonds between the surface of the IN and the ice germ affect the particle's ability to nucleate ice. Considering that ice is held together by hydrogen bonds of particular polarity and strength, it is assumed that an effective IN would have similar available hydrogen bonding sites at its surface.
- *Crystallography* – the geometric arrangement of bonds at the surface of the IN is at least as important as their chemical nature. An exposed crystal face with molecular or ionic bonding sites arranged in the same geometry as that of the ice

crystal (*e.g.* silver iodide (Vonnegut, 1947)) would be expected to aid the nucleation of a critical germ. Small discrepancies between the geometry of the surface and the ice germ may be compensated for by elastic deformation of the ice lattice and the IN surface.

- *Active sites* – IN may possess ‘active sites’ that are areas of surface pre-disposed to ice nucleation due to specific physical properties. An active site may be a morphological surface inhomogeneity such as a step, crack, pore or cavity or it may be a hydrophilic chemical inhomogeneity that allows lower energy binding of water molecules than elsewhere.

These criteria provide a useful framework for understanding what properties might make certain particles more efficient IN. Currently however it is impossible to accurately predict a materials IN ability based on its physical properties (Hoose and Möhler, 2012).

#### **1.4.3.1 Modes of heterogeneous ice nucleation**

Ice nucleation in the atmosphere occurs by a set of different mechanisms which are commonly referred to as ‘modes’ (Figure 1.5). *Immersion mode* nucleation occurs when an insoluble IN immersed in a supercooled liquid droplet catalyses ice formation. *Deposition mode* nucleation becomes possible above ice saturation (100% RH<sub>i</sub>), with water vapour depositing directly as ice upon the surface of a solid IN. *Contact mode* nucleation occurs when an IN collides with a supercooled liquid water droplet, causing immediate ice nucleation. *Condensation mode* nucleation occurs when liquid water condenses upon on a particle, allowing the particle to act as an IN. If the particle becomes entirely coated in liquid water then any ice nucleation would then be classified as immersion mode. Certain modes of heterogeneous nucleation may dominate, depending on the identities and number concentration of the IN available and the surrounding humidity and temperature.

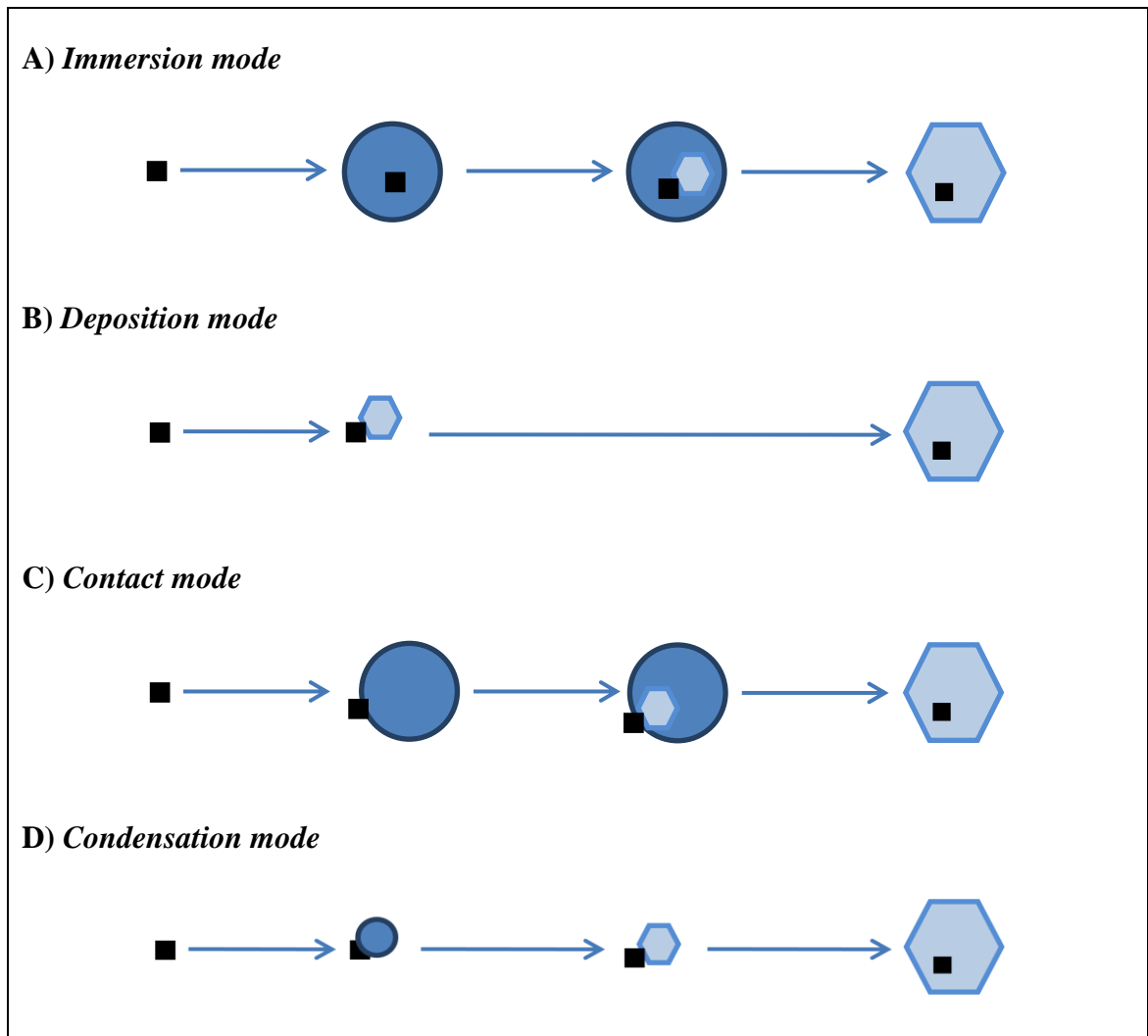


**Figure 1.5** The different modes of heterogeneous ice nucleation.

Cirrus clouds exist at temperatures below the homogenous limit for ice nucleation in pure water droplets ( $\sim 236$  K). Currently, the importance of each mode of ice nucleation for cirrus formation has not been fully evaluated. A key area of knowledge that is required when trying to understand how cirrus clouds form is therefore the reaction of different aerosol types to varying humidity and temperature conditions. If a particle is soluble it can take up water when exposed to increasing humidity and will freeze homogeneously once the humidity reaches the Koop threshold (Koop et al., 2000). Soluble material on the surface of an insoluble IN could also take up water below water saturation and then freeze either as the result of immersion, condensation, contact or even homogeneous mode nucleation. Deposition mode ice nucleation, which is the focus of this study, can only occur at humidities above ice saturation ( $100\% RH_i$ ).

### 1.4.3.2 Parameterising heterogeneous ice nucleation using CNT

As our understanding of the properties of different classes of atmospheric IN improves, there is an increasing requirement to be able to model the effects of different aerosols on cirrus and mixed phase cloud properties. CNT can be used to attempt the parameterisation of ice nucleation by different IN. The presence of an IN lowers the activation barrier to the nucleation of the ice phase. The free energy for the formation of a critically sized cluster of ice on the surface of an IN,  $\Delta G_{\text{het}}$ , is therefore smaller than  $\Delta G_{\text{hom}}$ . This reduction in the free energy required for cluster formation can be expressed by multiplying  $\Delta G_{\text{hom}}$  by a parameter ( $f_{\text{het}}$ ) which has a value between 0 and 1

$$\Delta G_{\text{het}} = \Delta G_{\text{hom}} \times f_{\text{het}}$$

Equation 1.12

Substituting Equation 1.8 into Equation 1.12 gives

$$\Delta G_{\text{het}} = \frac{16\pi\gamma^3 v^2 f_{\text{het}}}{3(kT \ln S)^2}$$

Equation 1.13

When parameterising deposition mode ice nucleation the solid ice/vapour interfacial tension ( $\gamma_{\text{sv}}$ ) is used as is the saturation with respect to ice. In its simplest form, CNT assumes that ice nucleation is stochastic and that it has an equal chance of occurring at any location on the surface of an IN (Fletcher, 1958). It assumes either that all droplets or all particles are uniform (depending on which mode of ice nucleation is being modelled). The value of  $f_{\text{het}}$  is often based on ice clusters having a single, common contact angle ( $\alpha$ ) between all ice embryos and the surface of a particular type of IN (Pruppacher and Klett, 1997). This is referred to as the single- $\alpha$  model (Wheeler and Bertram, 2012). Using this model  $f_{\text{het}}$  is expressed as

$$f_{\text{het}} = \frac{(2 + \cos \alpha)(2 - \cos \alpha)^2}{4}$$

Equation 1.14

The single- $\alpha$  model has been used extensively to parameterise experimental data (*e.g.* Archutela et al. (2005), Eastwood et al. (2008), Wheeler and Bertram (2012), Chernoff and Bertram (2010)) and has also been used to describe heterogeneous ice

nucleation in atmospheric cloud models (*e.g.* Kärcher (1996), Jensen and Toon (1997) Jensen et al. (1998), Hoose et al. (2010a), Hoose et al. (2010b)). As it has been widely used, the values of  $\alpha$  do provide a somewhat useful comparison of different IN. Recent work does however suggest that caution should be taken when using the single- $\alpha$  model as it does not always provide an accurate description of the effect of changing the surface area of an IN that is available (Wheeler and Bertram, 2012). To improve its applicability in some cases, the single- $\alpha$  model has been modified. An example is the probability distribution function- $\alpha$  model (Marcolli et al., 2007; Lüönd et al., 2010), which assume particle-to-particle variation, described by a probability distribution function.

#### 1.4.3.2.1 The heterogeneous nucleation rate coefficient

A commonly used parameter that allows comparison between different experimental measurements is  $J_{\text{het}}$ , the rate coefficient of heterogeneous ice nucleation.  $J_{\text{het}}$  is defined as the number of nucleation events per unit of surface area of material per unit time (*e.g.*  $\text{cm}^{-2} \text{s}^{-1}$ ) (Pruppacher and Klett, 1997). In this section, the nucleation rate by a single, uniform IN type is considered (*i.e.* the single stochastic model). For immersion mode ice nucleation  $J_{\text{het}}$  is just a function of temperature. For deposition mode nucleation,  $J_{\text{het}}$  is a function of both temperature and relative humidity. In both cases it can be expressed as an Arrhenius equation that relates it to  $\Delta G_{\text{het}}$

$$J_{\text{het}} = J_0 e^{-\frac{\Delta G_{\text{het}}}{kT}}$$

Equation 1.15

where  $k$  ( $\text{J K}^{-1}$ ) is the Boltzmann constant,  $T$  is the temperature (K) and  $J_0$  is a pre-exponential factor with units of  $\text{cm}^{-2} \text{s}^{-1}$ . The rate at which particles nucleate ice can be defined as

$$\text{Rate} = \frac{dN}{dt} = -J_{\text{het}} \sigma_s N$$

Equation 1.16

For immersion mode freezing,  $dN$  is the number of ice free liquid droplets containing nucleant with a surface area of  $\sigma_s$  that freeze in time  $dt$  (Wagner et al., 2012a). Between times  $t_1$  and  $t_2$ , the number of unfrozen droplets decreases from  $N_1$  to

$N_2$ . Integrating the left hand side of Equation 1.16 between  $N_2$  and  $N_1$  and the right hand side between  $t_2$  and  $t_1$  gives

$$N_2 = N_1 e^{-J_{\text{het}} \sigma_s \Delta t}$$

Equation 1.17

where  $\Delta t = t_2 - t_1$ . If the decay of the fraction of liquid droplets is approximately exponential, the nucleation rate can be derived from experimental data using this model. Examples of exponential decay are shown for kaolinite and silver iodide containing droplets in Figure 1.6 (Wagner et al., 2012a).

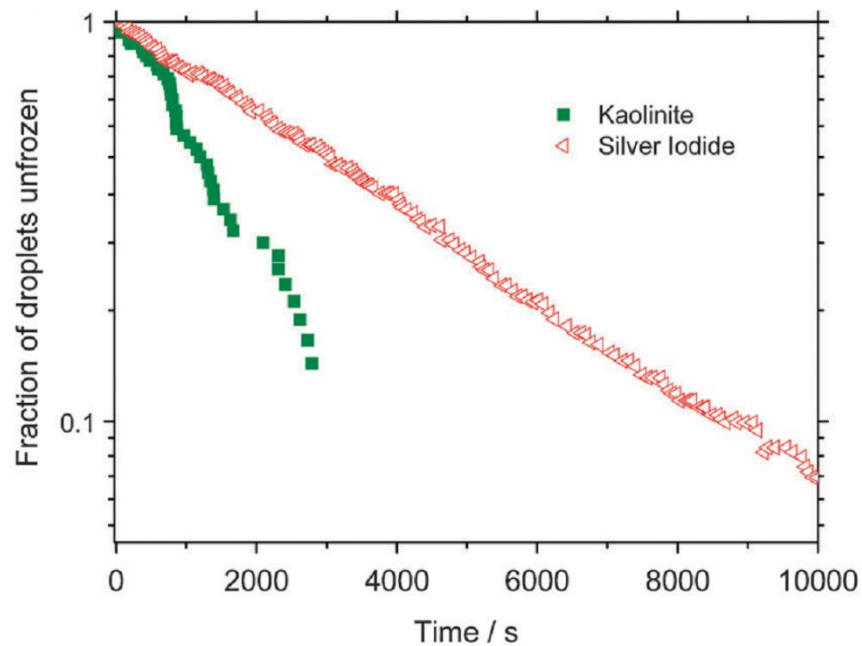


**Figure 1.6** Exponential decay of unfrozen water droplets containing kaolinite and silver iodide with time. Taken from Murray et al. (2012a).

When calculating  $J_{\text{het}}$  for deposition mode data,  $\sigma_s$  is the surface area per ice free particle and  $N$  is the number of ice free particles. As the number of particles that nucleate ice during  $\Delta t$  ( $\Delta N_{\text{ice}}$ ) is equal to  $N_1 - N_2$ , Equation 1.17 can be expressed as

$$\frac{\Delta N_{\text{ice}}}{N_1} = 1 - e^{-J_{\text{het}} \sigma_s \Delta t}$$

Equation 1.18

Re-arranging gives

$$J_{\text{het}} = \frac{-\ln\left(1 - \frac{\Delta N_{\text{ice}}}{N_1}\right)}{\sigma_s t}$$

Equation 1.19

If the total number of particles is unknown (as is the case in experiments performed in Chapter 7), Equation 1.19 can be modified so that only the total surface area needs to be known. The total surface area ( $A_s$ ) is the product of  $\sigma_s$  and  $N_1$ , Hence

$$N_1 = \frac{A_s}{\sigma_s}$$

Equation 1.20

Substituting Equation 1.20 into Equation 1.19 gives

$$J_{\text{het}} = \frac{-\ln\left(1 - \frac{\Delta N_{\text{ice}} \sigma_s}{A_s}\right)}{\sigma_s t}$$

Equation 1.21

When  $\Delta N_{\text{ice}}/N_1$  is less than 0.1 Equation 1.21 can be simplified using an approximation based on the Taylor series *i.e.*

$$\ln(1 - x) = -x$$

$$\text{if } -x < 0.1$$

Giving

$$J_{\text{het}} = \frac{\Delta N_{\text{ice}}}{A_s t}$$

Equation 1.22

### 1.4.3.3 Parameterising heterogeneous ice nucleation using the deterministic model

Nucleation has been shown to be a stochastic process (Vonnegut and Baldwin, 1984; Broadley et al., 2012; Murray et al., 2011), but it has been suggested that the time dependence of nucleation is of secondary importance when compared to particle heterogeneity (Pruppacher and Klett, 1997; Vali, 2008). Neglecting any time dependence allows a simpler approach to parameterising heterogeneous ice nucleation

data that is not based on CNT. This was done previously with the cumulative nucleus spectrum defined by Vali (1971),(1994). A similar time independent quantification that takes into account the surface area dependence of ice nucleation is the ‘ice active surface site density’ or  $n_s$ , which was first defined by DeMott (1995). It has been used more recently in a number of studies to parameterise nucleation by mineral dusts (Connolly et al., 2009; Lüönd et al., 2010; Broadley et al., 2012; Wheeler and Bertram, 2012; Niemand et al., 2012b; Hoose and Möhler, 2012), volcanic ash (Steinke et al., 2011) and marine diatoms (Alpert et al., 2011). This singular parameterisation makes the assumption that IN have localized active sites that are distributed evenly across the surface of the IN. The active sites have specific activation temperatures and/or supersaturations with respect to ice. The ice active surface site density is defined as follows:

$$n_s = -\frac{\ln(1 - f_{ice})}{A_s}$$

Equation 1.23

where  $f_{ice}$ , is the fraction of particles activated to ice at a specific temperature and/or  $S_{ice}$ . It should be noted that when this singular approximation is applied to experiments that use very slow cooling rates, the description may lead to an underestimate of the number of ice nuclei, due to the effects of time dependence (Murray et al., 2011; Vonnegut and Baldwin, 1984).

#### 1.4.3.4 Atmospheric heterogeneous IN

Many atmospheric particles have the potential to act as IN including:

- *Mineral dusts* - a mixture of many different discrete and aggregated mineral types, the composition of which changes as it is transported. Analyses of snowflakes sampled at ground level found the particles at the centre of the flakes to usually be clay minerals (Kumai, 1951, 1961, 1976; Kumai and Francis, 1962; Isono, 1955; Rucklidge.J, 1965).
- *Soot* - the result of combustion such as biomass burning and is a common atmospheric aerosol (Seinfeld and Pandis, 2006). It has been increasing in concentration since industrialisation (Lavanchy et al., 1999), but is found generally to be a less efficient IN than mineral dust (Dymarska et al., 2006;



DeMott et al., 1999; Kanji and Abbatt, 2006), except for more oxidised hydrophilic soot particles (Koehler et al., 2009).

- *Ash* - from volcanic eruptions which is emitted in large quantities globally. A good example is that of the recent eruption of Eyjafjallajökull, the ash from which was found to nucleate ice efficiently (Bingemer et al., 2012; Steinke et al., 2011).
- *Primary biological aerosols* - bacteria, pollens and fungal spores have all been shown to act as IN (Despres et al., 2012). The bacteria *Pseudomonas syringae* has evolved ice nucleating proteins on its surface as an aid to causing frost damage to plants to release nutrients (Maki et al., 1974). It has been found to be a particularly efficient nucleator of ice at temperatures higher than 260 K (Kanji et al., 2011; Hoose and Möhler, 2012).
- *Metallic particles* - have been sampled in ice cloud crystal residues (Heintzenberg et al., 1996; DeMott et al., 2003). Lead compounds have been found to be particularly good ice nuclei, and may be of interest due to the reduction of lead emissions from petrol (Cziczo et al., 2009).
- *Soluble inorganic crystalline particles* - such as ammonium sulphate (Abbatt et al., 2006) and sea salt (Wise et al., 2012) nucleate ice in the deposition mode and are potentially important nuclei for cirrus formation.
- *Organic material* - may also be involved in cirrus ice nucleation (Baustian et al., 2012; DeMott et al., 2003). Studies show that crystalline organic particles such as oxalic (Wagner et al., 2010, 2011) and malonic acids (Shilling et al., 2006) as well non-crystalline humic acid (Wang and Knopf, 2011) nucleate ice heterogeneously.

The efficiency of many IN species was compared in a recent review by Hoose and Möhler (2012). Figure 1.7 is taken from that review and shows the huge variation in the temperature/ $S_{ice}$  of ice nucleation onsets for IN particles even within the same class (*e.g.* mineral dusts). Part of the cause of the variation shown in the figure is due to experiments using samples with different surface areas and particle size distributions. Hoose and Möhler (2012) recommend that to make comparison between different studies easier, authors need to better record the size distributions, surface areas, fraction of particles frozen and cooling rates for experiments.

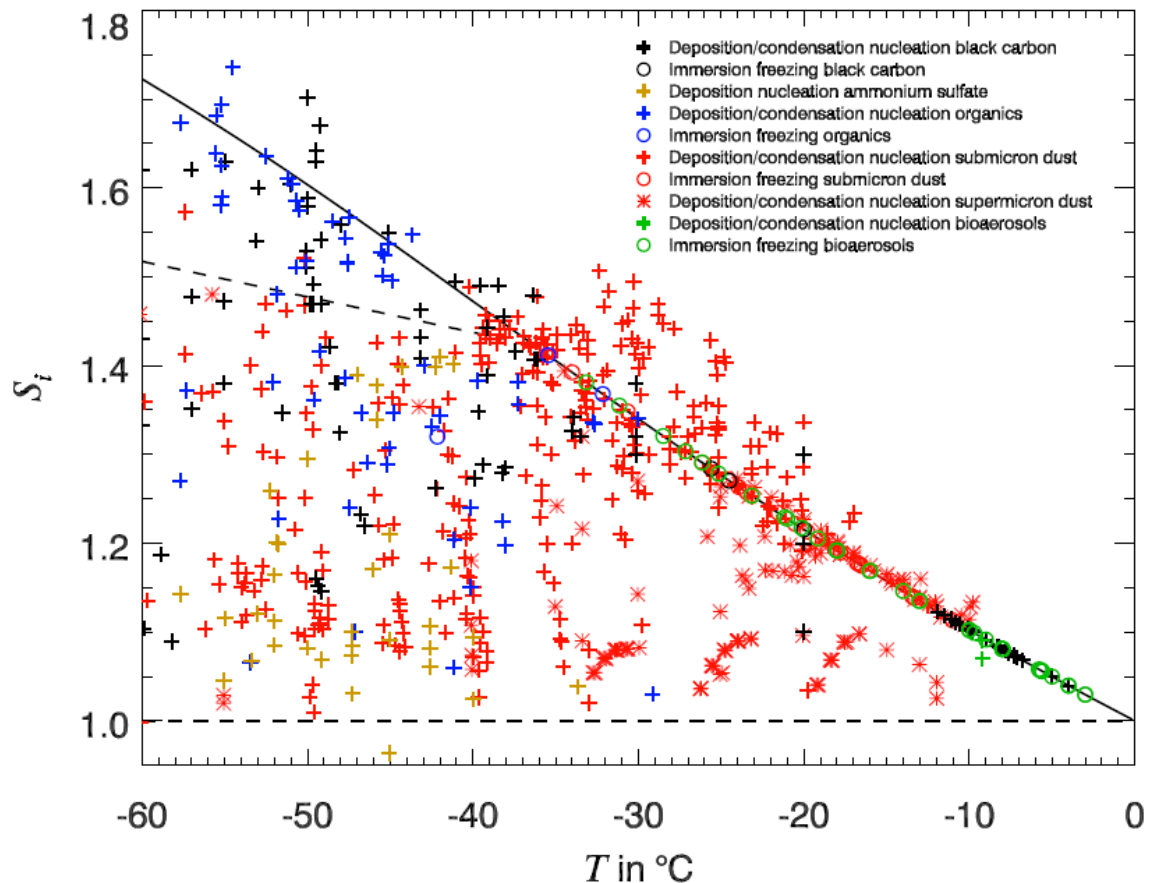


**Figure 1.7** Example of the variation in heterogeneous ice nucleation onset temperature and humidity (displayed as ice saturation ( $S_i$ ) =  $RH_i/100$ ) for IN of various compositions (see legend) in the deposition, condensation and immersion modes. The black solid line is the water saturation threshold and the dashed black line is the homogeneous ice nucleation threshold (Koop et al., 2000). Figure taken from Hoose and Möhler (2012).

#### 1.4.4 Which aerosol particles form cirrus?

The composition of aerosol particles in the upper troposphere varies depending on source region and on how much oxidative chemical aging they have undergone (Froyd et al., 2009b). Due to the increased difficulty of high altitude sampling, measurements of upper tropospheric aerosol composition are less common than those made at lower levels.

##### 1.4.4.1 The composition of upper tropospheric aerosol

*In situ* measurements of the composition of unfrozen background aerosol in the upper troposphere using single particle mass spectrometry find that the most abundant particles are internal mixtures of sulphate and organic species (Murphy et al., 1998).

This is in contrast to the stratosphere (Figure 1.8), where the aerosol mostly consists of concentrated (60 – 80%) aqueous sulphuric acid solution droplets (Shen et al., 1995).

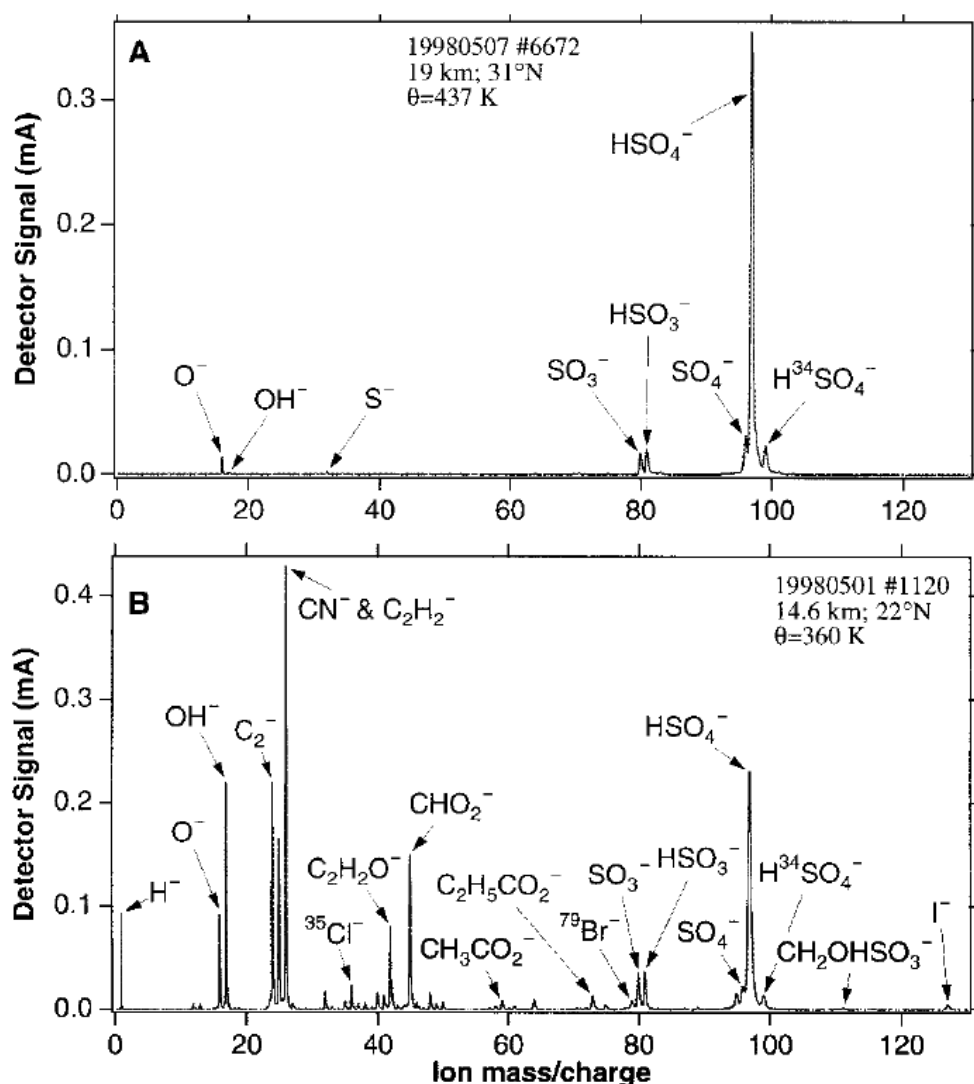


**Figure 1.8** Typical negative ion single-particle mass spectra of stratospheric aerosol (A) and the upper troposphere (B), taken from Murphy et al. (1998). It can be seen that the stratosphere is dominated by sulphate species whereas the upper tropospheric aerosol also contained organic species (*e.g.*  $\text{C}_2\text{H}_2^-$  fragment) including organic acids (*e.g.*  $\text{CH}_3\text{CO}_2^-$  fragment), as well as some sulphate species.

The variation of the fraction of sulphate and organic species as a function of altitude and latitude has also been investigated using single particle mass spectrometry (Murphy et al., 2006). The abundance of organic species in internally mixed organic-sulphate aerosol was higher at northern tropical latitudes ( $\sim 23^\circ\text{N}$ ), compared to regions further from the equator (Figure 1.9). Organic species were found to make up between

30% and 80% of the total aerosol mass in the regions studied. Nitrate ions were found to be almost always present in neutralized sulphate–organic particles, but not in acidic aerosol. Mineral dust or fly ash was identified by the presence of the  $\text{SiO}_3^-$  peak in the mass spectra. Particles  $> 1 \mu\text{m}$  were found to have a  $\text{SiO}_3^-$  peak 9% of the time, compared to particles  $< 1 \mu\text{m}$ , which only had  $\text{SiO}_3^-$  peaks 0.2% of the time. Metallic species such as lead have also been observed in much smaller quantities (Murphy et al., 1998; Murphy et al., 2006).

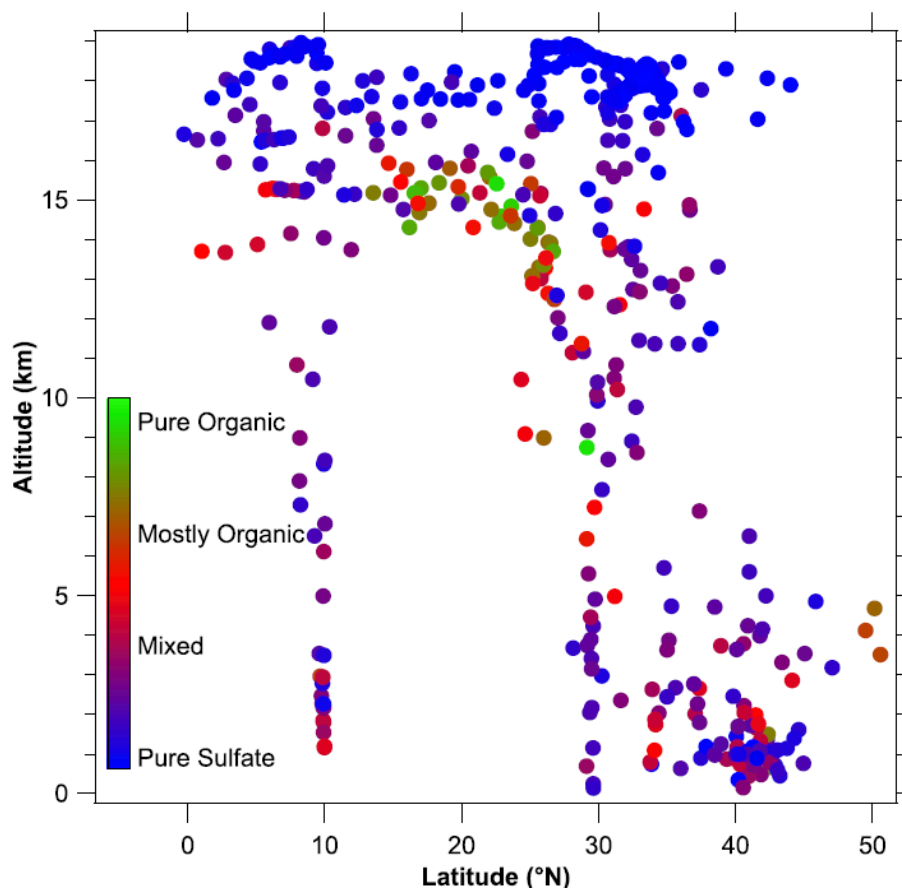


**Figure 1.9** Altitude vs. latitude cross section adapted from Murphy et al. (2006) showing the variation of aerosol composition between pure sulphates in the stratosphere and internally mixed sulphate-organic aerosol in the upper troposphere. Note the abundance of aerosols containing large fractions of organic material at tropical latitudes  $\sim 23^\circ\text{N}$ .

A more specific study of aerosol composition in the tropical upper troposphere and specifically the TTL again using single particle mass spectrometry (Froyd et al., 2009b) found a clear transition at around 12 km (at the bottom of the TTL) from acidic sulphate rich aerosol to neutralized highly oxidised organic rich aerosol. This change coincided with the layers being subject to different convective influences. The lower

layer received aerosol from maritime convection and the upper layer from continental convection. The mass spectra of the organic species found in the TTL were consistent with dicarboxylic acids, most likely formed from the oxidation of the components of biogenic SOA. Mineral dust was found throughout the TTL, but it only made up ~5% of the total observed aerosol particles compared with ~80% for sulphate-organic aerosol on flights in which the TTL was not subject to unusual convective influence. The remaining fraction of aerosol particles was mostly particles originating from biomass burning and also elemental carbon (*i.e.* soot).

#### **1.4.4.2 The composition of mid-latitude cirrus ice particle residues**

Residues from evaporated ice crystals sampled *in situ* show significant chemical differences to the background aerosol from where they were sampled. Heintzenberg et al. (1996) used electron microscopy to analyse ice residues from crystals sampled in thin cirrus at 9 km altitude above the Alps using a counterflow virtual impactor (CVI). The residues showed enrichment in species consistent with mineral dust (*e.g.* Si) and also in heavier elements such as Ti and Cd compared to the background aerosol, which contained more sulphur.

A number of campaigns have used continuous flow diffusion chambers (CFDC) to nucleate ice particles from unfrozen background aerosol, simulating cirrus formation. These instruments expose aerosol particles to constant supersaturations with respect to ice, allowing the ice nucleation to be investigated at a set supersaturation and temperature. Chen et al. (1998) used a CFDC to nucleate ice particles at 110% RH<sub>i</sub> on aerosol in the upper troposphere over Oklahoma, USA, which were then collected on electron microscopy grids and analysed. They also found that silicates were enriched in the ice residues compared to the mostly sulphate type background aerosol, however IN sampling was limited to temperatures above 236 K, preventing investigation of the temperature regime most applicable to cirrus. Using a later version of the same CFDC, Demott et al. (2003) sampled IN at the top of Storm Peak, Colorado, USA and exposed them to cirrus temperatures (233 - 218 K) and supersaturations up to and above the homogeneous freezing limit. A single particle mass spectrometer instrument coupled to the CFDC was used to analyse the residues of the nucleated ice crystals. The unfrozen background aerosol was also sampled and analysed. The resulting spectra were then categorized and compared (Figure 1.10A). Background aerosol particles were largely found to be internal mixtures of sulphate and organic species (86%). Smaller

contributions came from potassium and carbon containing particles (9%, probably from biomass burning), metallic particles (1.6%), mineral dust or fly ash (1%) and also some unidentified material (0.2%). The composition of the sampled heterogeneous IN showed substantial enhancement in mineral dust/fly ash (33%) and in metallic particles (25%).

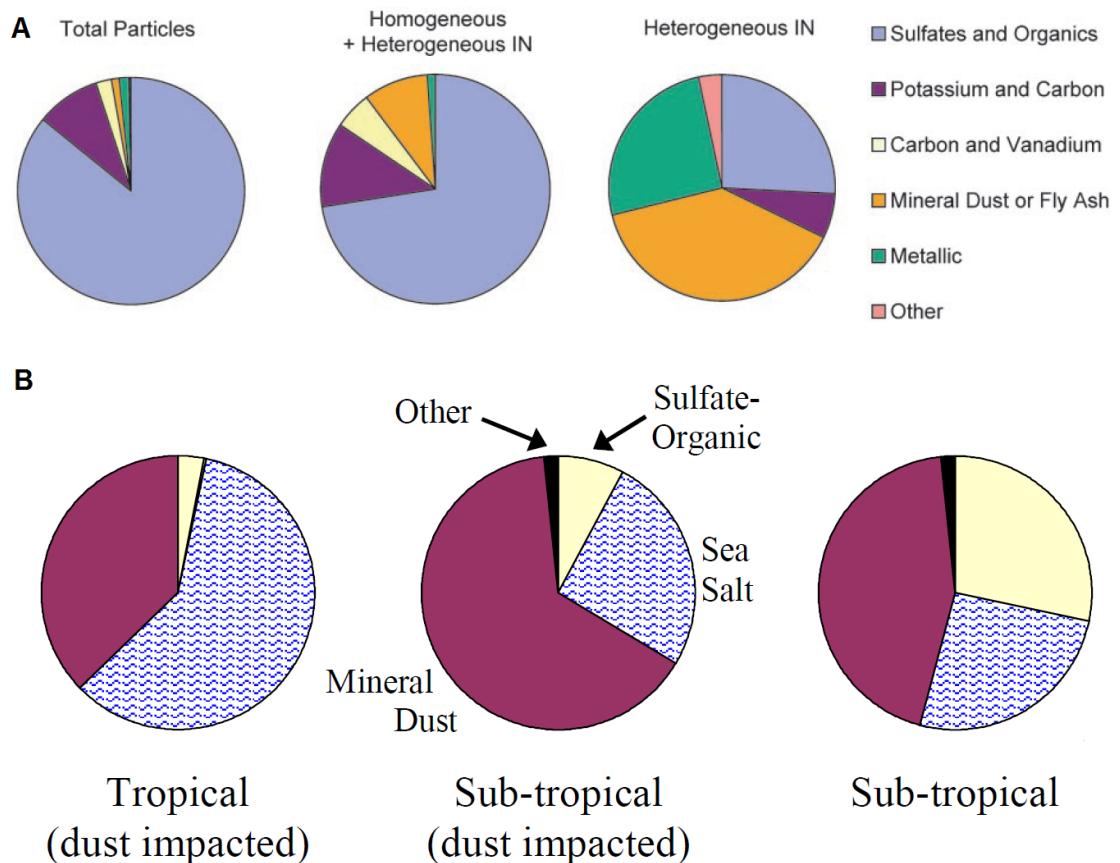


**Figure 1.10** A) The composition of background aerosol (left hand chart) and the residues of ice particles nucleated heterogeneously and homogeneously (middle chart) and solely heterogeneously (right hand chart) from natural aerosol at cirrus temperatures (adapted from Demott et al. (2003)). B) Ice crystal residues from anvil cirrus at 12 – 14 km at tropical and sub-tropical latitudes (adapted from Froyd et al. (2010), sub-tropical data from Cziczo et al. (2004)). Anvil cirrus ice crystal residues contained disproportionately more mineral dust and sea salt compared to the background aerosol.

Combining a CVI and a PALMS instrument, Cziczo et al. (2004) sampled and analysed the residues of ice particles from anvil cirrus *in situ* during the CRYSTAL-FACE field campaign. Measurements were taken at between 5 and 15 km in cirrus over land and ocean at latitudes of 12° to 28° north. After analysis the results were categorized. Once again mineral dust was found to be enhanced in the ice particle residues (Figure 1.10B), particularly in air masses impacted by dust storms in the

Sahara. Sea salt was also a common component of the IN residues in cirrus above the ocean, which would be expected as the aerosol that form anvil cirrus have been lofted by convective systems starting at the surface.

#### 1.4.4.3 The case for studying ice nucleation by natural mineral dust samples

The analysis of mid-latitude cirrus residues shows that mineral dust particles are heavily involved in cirrus formation. Mineral dust is a mixture of many different discrete and aggregated mineral types. The major source of mineral dust in the atmosphere is from arid and semi-arid regions such as the Sahara, with annual total emissions of between 1000 and 3000 Tg (Goudie and Middleton, 2006). A series of studies have investigated the composition of atmospheric mineral dusts after transport from arid regions (Prospero et al., 1981; Kandler et al., 2011; Delany et al., 1967; Glaccum and Prospero, 1980; Kandler et al., 2009; Arnold et al., 1998; Leinen et al., 1994). Figure 1.11 shows the averaged mineralogical composition of mineral dust from those studies (Atkinson and Murray, 2012). The aluminosilicate clay minerals, illite and kaolinite, make up over half the sampled dust particles and quartz is the most abundant non-clay mineral.

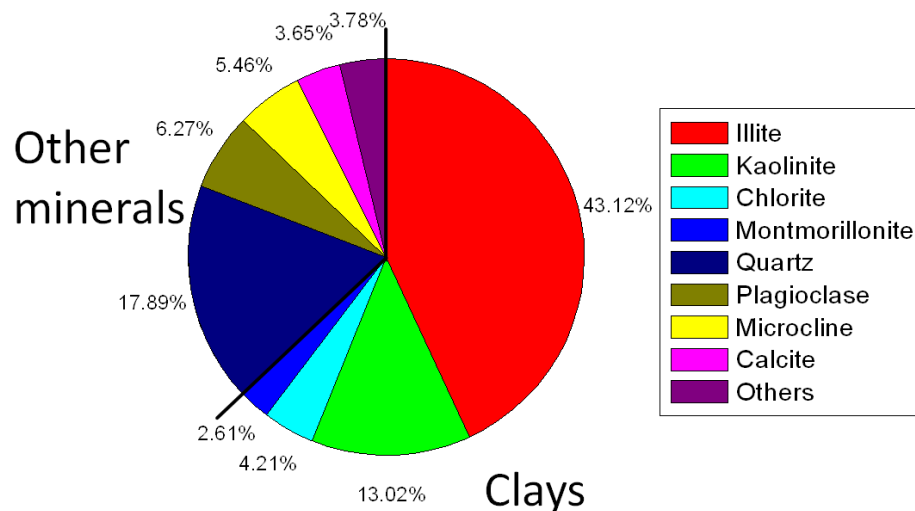


**Figure 1.11** Average composition of atmospheric mineral dust (Atkinson and Murray, 2012) based on dust compositions from seven *in situ* studies (see text).

Ice nucleation by various mineral dusts has been investigated in the deposition, immersion, condensation and contact modes and the available literature is well summarised in the review by Hoose and Möhler (2012). Studies have focussed on

natural desert dust samples (*e.g.* Kulkarni et al. (2010), Connolly et al.(2009)), natural clay mineral samples (*e.g.* Murray et al. (2011), Zimmerman et al. (2008)), so called surrogates for atmospheric dusts such as Arizona Test Dust (ATD) (*e.g.* Marcolli et al. (2007), Archutela et al. (2005)) and also more atmospherically representative dust mixtures (Broadley et al., 2012).

In general, mineral dusts have been found to be good IN below ~260 K in the deposition, immersion and condensation modes. However, as many samples are mixtures of different minerals it is not always clear exactly which minerals are responsible for the observed nucleation (Hoose and Möhler, 2012; Atkinson and Murray, 2012). Particular care should also be taken when considering the behaviour of commercial materials that may not be representative of natural dust. A good example of this is ATD, which is used commercially for grading the efficiency of air filters. ATD is milled to a particular size range and washed, potentially altering its natural surface properties.

A better understanding of the ice nucleation behaviour of the individual components of atmospheric mineral dust will allow the development of more accurate parameterisations for cirrus cloud models. This can be achieved by observing the properties of natural, untreated, single component dusts. In Chapter 7, deposition mode ice nucleation by a well characterised sample of kaolinite dust (KGa-1b, provided by the Clay Minerals Society (Costanzo and Guggenheim, 2001)) was investigated using the newly developed deposition mode chamber.

#### **1.4.4.4 The composition of subvisible cirrus ice particles in the tropical tropopause layer**

The microphysical properties of cirrus in the extremely cold (180 – 200 K) tropical tropopause layer (TTL) have received significant attention in recent years (Peter et al., 2006; Fueglistaler et al., 2009). These cirrus are known to play a critical role in dehydrating air entering the stratosphere (Holton and Gettelman, 2001; Jensen et al., 1996) and may also have a non-negligible radiative impact on the planet (McFarquhar et al., 2000). The TTL is the region between 20°N and 20°S in which the tropopause is at its highest altitudes (14 - 18.5 km) (Fueglistaler et al., 2009). Cirrus clouds which form *in situ* in the TTL, rather than as the product of convective outflow, are extensive (up to 10<sup>5</sup> km<sup>2</sup>), but very thin (200 – 300 m deep) (Lynch et al., 2002) (Figure 1.12). These



clouds have very low particle number densities (Krämer et al., 2009), making them optically thin and as such they are referred to as subvisible or subvisual cirrus (SVC) clouds.

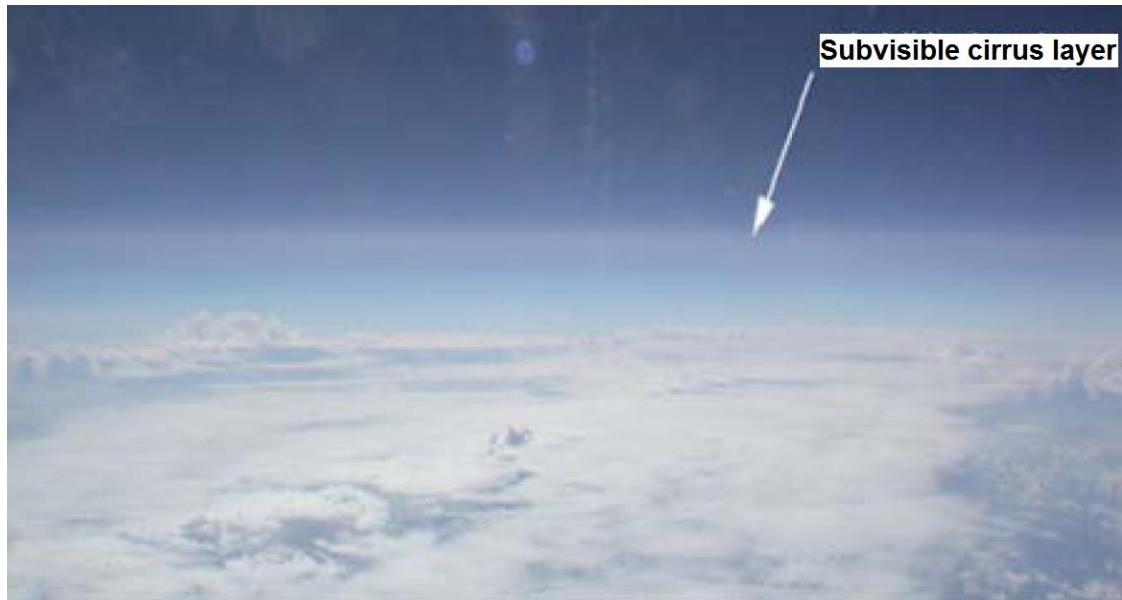


**Figure 1.12** The layer of subvisible cirrus (SVC) as seen from the cockpit of NASA WB-57F during the CRAVE campaign (Costa Rica Aura Validation Experiment). Photograph credited to CPI. J. H. Bain of NASA Johnson Space Center and adapted from Lawson et al. (2008).

The mechanism by which SVC form is currently unclear, because unlike the ice particle residues sampled at lower altitudes, the residues from the TTL did not show enhancement in mineral dust compared to the background aerosol composition (Figure 1.13) (Froyd et al., 2010). Instead the residues of the SVC ice particles were found to be overwhelmingly of neutralized sulphate internally mixed with organic material. This was chemically identical to the majority of the unfrozen background aerosol. The SVC clouds from which crystals were sampled had ice particle number concentrations of between  $0.02$  and  $0.05 \text{ cm}^{-3}$ , this is very low compared to the total unfrozen background aerosol concentration of  $\sim 10 \text{ cm}^{-3}$ . Low ice particle numbers indicate that nucleation may have occurred on a small subset of heterogeneous IN rather than by homogeneous nucleation by a larger fraction of aerosol (see Section 1.4.4.5.1 for more possible explanations for low ice particle number density in cold cirrus). However, due to the lack of ‘traditional’ IN (such as mineral dust) the exact nature of the particles that may have acted as heterogeneous IN was unclear.

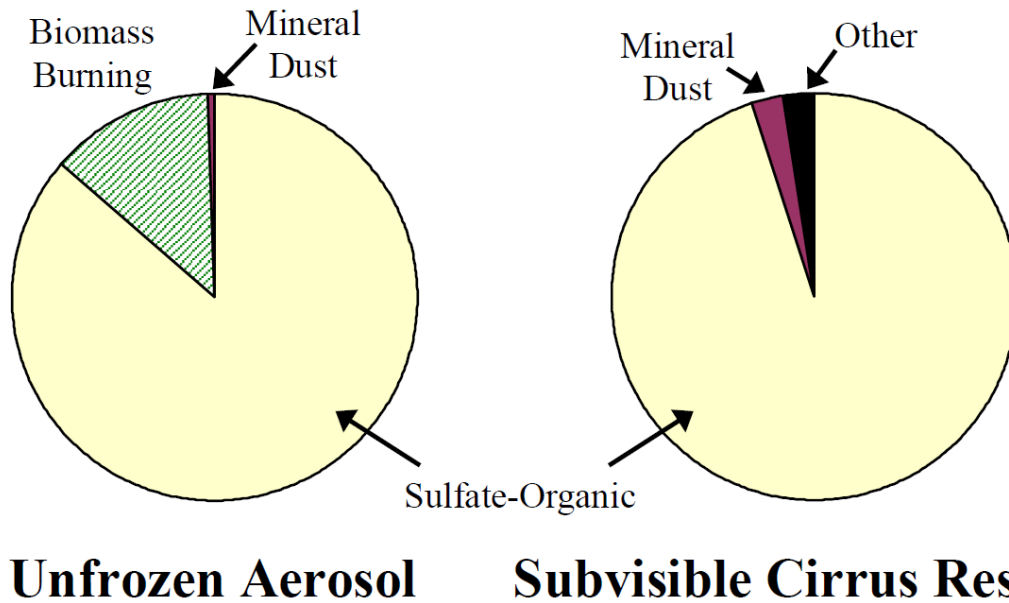


**Figure 1.13** A comparison of the composition of unfrozen background aerosol particles in the TTL (left hand chart) with the residue of ice crystals from SVC sampled *in situ* in the TTL. Adapted from Froyd et al. (Froyd et al., 2010).

#### 1.4.4.5 The saturation problem: High in cloud and clear sky humidity

Some observations of water vapour concentrations in the upper troposphere have found unexpectedly high values of  $RH_i$  both inside cirrus clouds and under clear sky conditions (Peter et al., 2006). Kramer et al. (2009) provide a summary of the existing studies; at temperatures above 200 K, in cloud and out of cloud supersaturations have been observed to often reach the homogeneous freezing threshold (as defined by Koop et al.(2000)) (Heymsfield and LM, 1995; Heymsfield et al., 1998; Jensen et al., 2001; Gierens et al., 1999; Gierens et al., 2000; Gayet et al., 2004; Gayet et al., 2006; Haag et al., 2003; Ovarlez et al., 2002; Spichtinger et al., 2003; Spichtinger et al., 2004; Lee et al., 2004; Comstock et al., 2004; Korolev and Isaac, 2006; Gettelman et al., 2006; Immler et al., 2008). Measurements made *in situ* at higher altitudes (and therefore at temperatures relevant to the TTL) are more challenging in terms of water vapour measurement instrumentation and are made less frequently. Studies that made observations both inside and outside cirrus at temperatures relevant to the TTL (< 200 K) measured  $RH_i$  up to and exceeding the water saturation threshold (Kelly et al., 1993; Gao et al., 2004; Jensen et al., 2005a; Jensen et al., 2005b; MacKenzie et al., 2006; Popp et al., 2007). Lower, persistent supersaturations of ~30% with respect to ice

were also observed in ice clouds and contrails (Gao et al., 2004) for periods of at least one hour (Lee et al., 2004).

Based on the established understanding of ice nucleation microphysics, clear sky humidities would be, in the absence of heterogeneous IN, expected to reach the homogeneous freezing threshold but not exceed it (as the nucleation of ice would be expected to relax the supersaturation). Supersaturations inside ice clouds might be expected for a short period of time between nucleation of the ice and the equilibration of the ice and vapour phases at saturation, depending on the strength of any local updraft. What is not expected however is in cloud supersaturations above the homogeneous and water saturation thresholds and persistent smaller supersaturations over a period of hours.

At face value, the observations suggest that we lack sufficient understanding of the basic processes that underpin ice cloud formation. They also have implications for our understanding of the distribution of water vapour in the upper troposphere (Peter et al., 2006). However, due to the difficulties in measuring the small water vapour concentrations present at low temperatures, it is also reasonable to suspect that the very high observed supersaturations at lower temperatures are the result of instrumental error.

Krämer et al. (2009) present a comprehensive data set of in cloud and clear sky water vapour measurements taken over the course of 28 flights in the arctic, at mid-latitudes and in the tropics. The measurements took place at temperatures between 183 and 240 K. To try and eliminate any possibility of instrumental error, the water vapour data from the Lyman- $\alpha$  'FLASH' instrument and the open path TDL instrument 'OJSTER' were quality checked by referencing the regularly calibrated Lyman- $\alpha$  'FISH' instrument that measured the total water vapour concentration including sampled ice crystals (when in cloud).

The quality checked clear sky data (Figure 1.14A) from these flights showed only a very small number of instances where the humidity was above the homogeneous threshold. The dashed and dot-dashed lines in Figure 1.14A represent RH<sub>i</sub> at constant H<sub>2</sub>O mixing ratios of 1.5 and 3 ppmv respectively. These values represent the typical values near the tropical tropopause. At TTL temperatures the most measured RH<sub>i</sub> values

are contained within these limits, indicating that the data is representative of real clear sky humidity in the TTL.

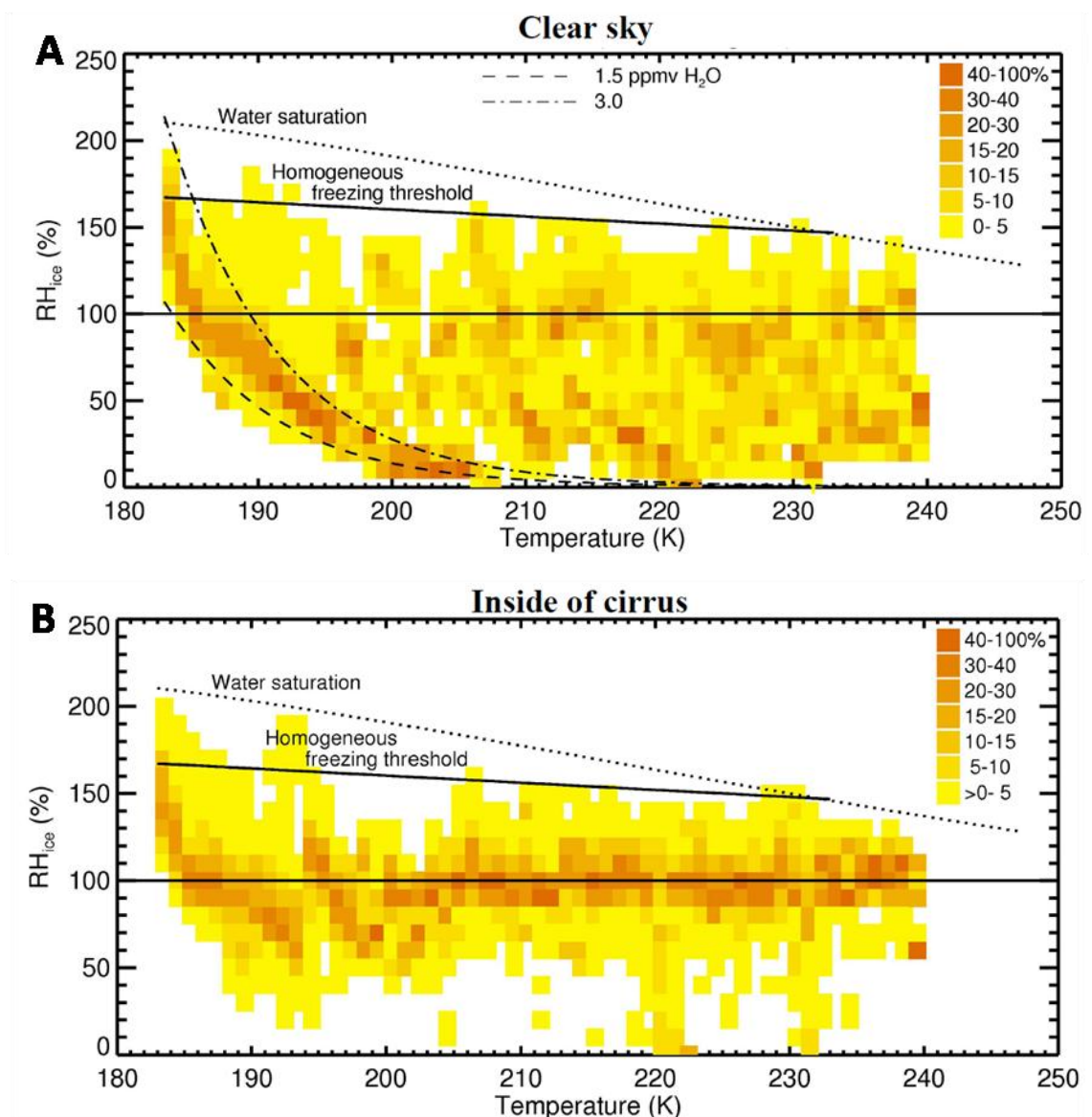


**Figure 1.14** Quality checked clear sky (A) and in cloud (B) humidities collected during 28 flights. Adapted from Krämer et al. (2009).

The in cloud humidity frequency data (Figure 1.14B) above  $\sim 195$  K is clustered around the ice saturation line, as would be expected when the air mass is at or coming into equilibrium with the ice phase. Below 195 K, there is a definite increase in the number of observations of humidity above 100%  $RH_i$ . The trend to higher in cloud humidity rises as the temperature decreases.

The findings of Krämer et al. (2009) indicate that previous measurements of extremely high clear sky and in cloud supersaturations may be the result of experimental artefacts. Their data does however suggest that humidities above ice saturation are commonplace in cirrus clouds at TTL temperatures ( $< 200$  K).

#### **1.4.4.5.1 Possible causes of high in cloud humidity at TTL temperatures**

A number of potential mechanisms for the sustained supersaturations observed inside cold cirrus have been suggested. Laboratory experiments have shown that a metastable phase of ice, originally described as cubic ice, can crystallise from aqueous droplets at TTL temperatures (Murray et al., 2005; Murray and Bertram, 2007; Murray, 2008a; Murray and Bertram, 2008). More recent work has revealed that it is better described as stacking disordered ice (Malkin et al., 2012). This phase of ice has a higher vapour pressure than the stable hexagonal polymorph (Murray et al., 2005; Shilling et al., 2006a) and may allow a Bergeron-Findeisen like process, leading to a low ice number density. Gao et al. (2004) suggested that the adsorption of nitric acid onto ice particles can interfere with the uptake of water vapour, leading to supersaturations. It was also suggested that the uptake of water vapour by ice crystals in the TTL might be slow if the accommodation coefficient of water on ice is very small ( $< 0.0075$ ) (Magee et al., 2006). Recent work has however found that the accommodation coefficient is  $> 0.1$  at temperatures between 190 and 225 K (Skrotzki, 2012). Barahona and Nenes (2011) have suggested that gravity wave activity in the TTL might lead to a ‘dynamic equilibrium’ in which ice production balances sedimentation resulting in low ice number densities and high in-cloud humidity. In their study it was found that dynamic equilibrium was achievable when aerosol droplets froze homogeneously, but it was also found that heterogeneous nucleation by ice nuclei (IN) facilitated the onset of the equilibrium state.

A number of modelling studies show that the heterogeneous nucleation of ice alone can result in low particle densities and correspondingly long relaxation times for humidity (Krämer et al., 2009; Gensch et al., 2008; Khvorostyanov et al., 2006; Spichtinger and Gierens, 2009; Spichtinger and Cziczo, 2010; Jensen et al., 2010; Ren and Mackenzie, 2005; Murray et al., 2010b). As discussed in Section 1.4.4.4, measurements of the composition of unfrozen background aerosol in the TTL and the composition of residues from evaporated SVC ice particles show very low concentrations of species traditionally considered to be effective IN, such as mineral

dusts. Aerosol and ice particle residues are shown instead to be largely composed of neutralised sulphate-organic mixtures, the organic component being highly oxidised (Froyd et al., 2009a; Froyd et al., 2010). DeMott et al (2003) also show that at warmer temperatures (218 - 238 K) 25% of heterogeneously nucleated ice particle residues were composed of sulphate-organic species. This suggest that the TTL cirrus residues may also be from sulphate-organic aerosol that nucleated ice heterogeneously.

Crystalline ammonium sulphate particles have been shown to nucleate ice heterogeneously and it has been suggested that they could influence cirrus formation (Abbatt et al., 2006; Wise et al., 2009; Eastwood et al., 2009; Wise et al., 2010; Jensen et al., 2010). However, a recent study has shown that citric acid, a glass forming organic tri-carboxylic acid, inhibits the efflorescence of ammonium sulphate below 250 K, making it unclear how many crystalline ammonium sulphate particles would exist in the TTL (Bodsworth et al., 2010).

If ammonium sulphate or other species are unable to crystallise from the sulphate-organic aerosol present in the upper troposphere then a question remains about the nature of the aerosol that might be heterogeneously nucleating ice in the TTL. Mikhailov et al. (Mikhailov et al., 2009) suggest that aerosol particles which do not exhibit efflorescence (crystallisation on drying) could exist in a solid or semi-solid amorphous (*i.e.* non-crystalline, lacking long range repeating molecular structure) states such as rubbers, gels or glasses. If TTL aerosol were to exist in a solid amorphous state then it would potentially provide a surface for ice crystals to nucleate on. The following section presents the current evidence for the existence of solid amorphous aerosol particles in the atmosphere.

#### **1.4.5 Evidence for solid amorphous atmospheric aerosol**

Evidence for natural aerosol particles existing in a solid amorphous state has been found in a number of studies; Cappa and Wilson. (2011) found that heating ozone oxidised  $\alpha$ -pinene SOA did not change the aerosol's mass spectra, indicating that the diffusion of molecules out of the aerosol was retarded. Similarly Vaden et al. (2011) found that the rate of evaporation of SOA at room temperature was much slower than predicted by current kinetic models. Both Cappa and Wilson (2011) and Vaden et al. (2011) conclude that their observations are consistent with aerosol existing in an amorphous solid rather than a liquid state. Shiraiwa et al. (2011) found that the chemical aging of

an organic aerosol proxy slows at lower humidity and they attribute this to the aerosol particles becoming semi-solid, which slows diffusion into the interior of the particles, reducing the reactive uptake. Virtanen et al. (2010) show that a large proportion of SOA generated in a plant chamber and aerosol sampled from boreal forest bounced off an impactor, behaviour which is consistent with solid rather than liquid aerosol. They state that the tested SOA was most probably glassy (see Section 1.4.5.1 for definition). Measurements using the a similar technique show that laboratory generated SOA remained solid or semi solid up to at least 50% relative humidity with respect to liquid water. The same study found that the addition of sulphuric acid to the SOA resulted in a reduction in the humidity at which the aerosols liquefied due to their increased hygroscopicity (Saukko et al., 2012).

As discussed by Koop et al. (2011), other atmospheric measurements have also shown that some carbonaceous aerosols emitted during biomass burning exist in amorphous solid or semi-solid states. These spherical particles behave like solids and are referred to as ‘tar balls’ (Posfai et al., 2004; Tivanski et al., 2007; Alexander et al., 2008). The number of tar balls increases as biomass burning plumes age (Adachi and Buseck, 2011), which is likely to be related to ongoing oligomerisation reactions between poly-carboxylic acids that result in heavier molecules, which promote higher viscosities (Zobrist et al., 2008). Tar balls have been found to have much in common with humic-like complex organic acids, which have been shown to have very high glass transition temperatures (Young and Leboeuf, 2000). Anthropogenic aerosol may also exist as an amorphous solid; Roth et al. (2005) suggest that up to 80% of urban organic particulates may be in the glassy state, based on the sorption behaviour of volatile organic compounds. They suggest that this is likely due to the presence of oligomeric species in the aerosol.

#### **1.4.5.1 Glass formation in proxies of atmospheric aerosol**

Aqueous solutions of surrogates for the highly oxidised organic species found in atmospheric aerosol have been shown to become glassy solids at humidities and temperatures relevant to a large part of the Earth’s atmosphere (Murray, 2008b; Zobrist et al., 2008; Mikhailov et al., 2009). Glasses are amorphous solids with extremely high viscosities of  $> 10^{12}$  Pa s (Angell, 1995; Debenedetti and Stillinger, 2001). To put that value into context, Figure 1.15 compares the viscosities of some common liquids, solids and semi-solids.

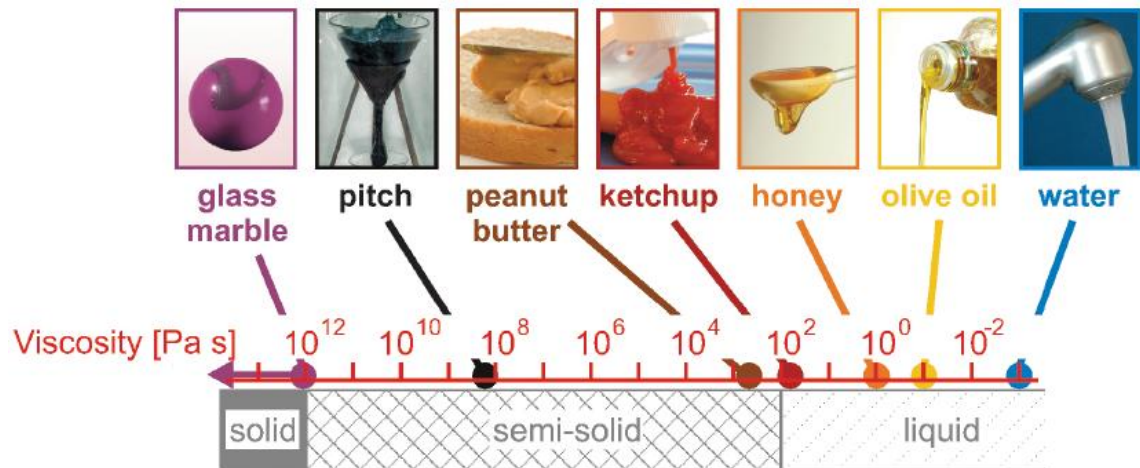


**Figure 1.15** A schematic comparing the viscosities of some common liquids, semi-solids and solids. Adapted from Koop et al. (2011).

The glass transition is a second order phase transition, which differs from first order phase transitions (like crystallisation) in that there is not an abrupt change in the materials enthalpy ( $H$ ) or entropy ( $S$ ). When cooling a crystallisable stable liquid,  $H$  and  $S$  normally decrease continuously (green line, Figure 1.16a). When the equilibrium melting point ( $T_m$ ) is reached, nucleation of the new crystalline phase can occur. Due to the presence of a kinetic energy barrier, crystallisation may not occur immediately on crossing  $T_m$ , causing the liquid to ‘supercool’ to lower temperatures. When the crystallisation does occur, there is a sudden drop in  $H$  and  $S$  (Atkins and De Paula, 2006) (blue line, Figure 1.16a). However, as a liquid is cooled its viscosity increases and this can inhibit the nucleation and growth of the new crystal phase, allowing supercooling to lower temperatures. In some cases it is possible for the viscosity to increase to the point where molecular motion practically ceases, preventing equilibration to the system’s lowest energy state (Debenedetti, 1996; Debenedetti and Stillinger, 2001). This is termed vitrification and occurs at the glass transition temperature ( $T_g$ ). At  $T_g$ , there is a change in the slope of  $H$  and  $S$  on continued cooling below  $T_g$  (red line, Figure 1.16). This is indicative of the glass transition and is due to the molecules translational and re-orientational degrees of freedom being essentially stopped at experimental timescales.



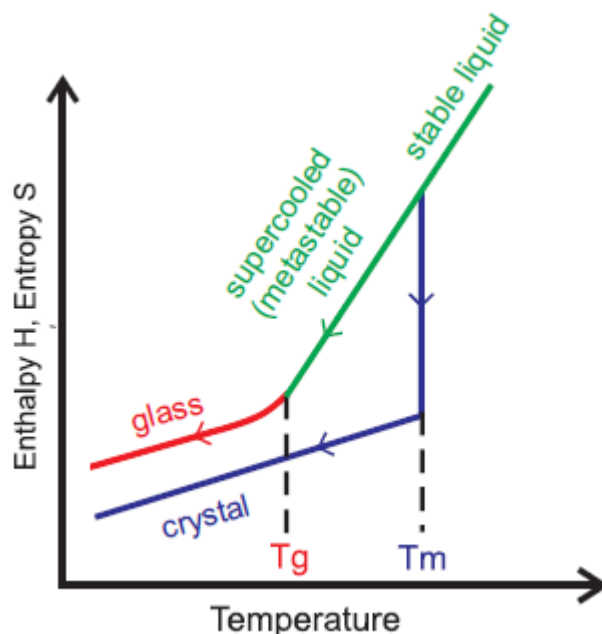


**Figure 1.16** A schematic of the change in enthalpy and entropy and isobaric heat capacity that occurs during crystallisation and at the glass transition. Reproduced from Zobrist et al. (2008).

The  $T_g$  of a liquid depends on its chemical composition. Water has a low glass transition temperature ( $T_g = 136$  K (Kohl et al., 2005)) and will therefore act as a plasticiser when mixed with species with higher  $T_g$ , reducing the  $T_g$  of the resulting mixture. Glass formation can occur therefore by the dehydration of liquid solution droplets, with the glass transition occurring at a characteristic humidity ( $RH_g$ ) (Koop et al., 2011). Murray et al. (2012a) present visual evidence of glass or semi-solid formation in micrometer sized amorphous iodic acid droplets at low humidity. The droplets were subjected to mechanical force and shattered in a manner consistent with a solid. On humidification, the shattered droplets took up water, returned to the liquid phase and reformed into droplets (Figure 1.17).

Lower temperatures, lower humidities (*i.e.* higher solute concentrations) and larger solute molecules capable of hydrogen bonding all serve to increase solution viscosity (Koop et al., 2011; Zobrist et al., 2008). The high mass oxygenated organic compounds found in atmospheric aerosol are therefore likely to increase viscosity and promote glass formation under atmospherically relevant conditions.

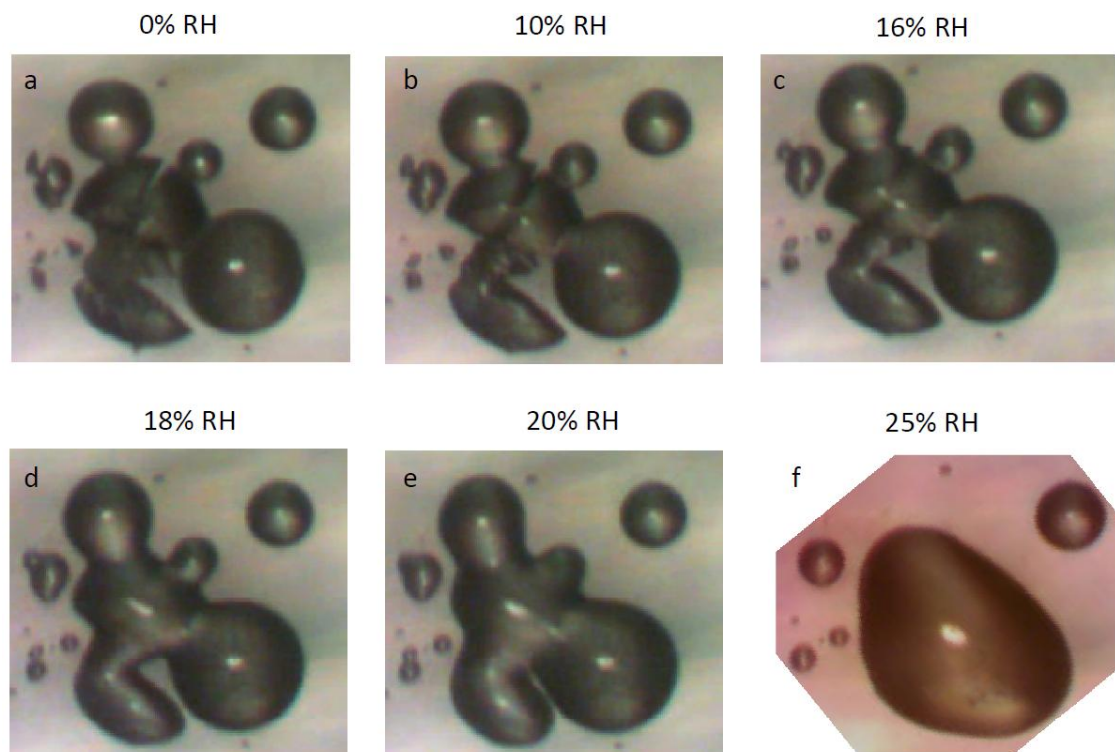


**Figure 1.17** The behaviour of ‘shattered’ ultra-viscous or glassy iodine acid droplets on increasing humidity. Taken from Murray et al. (2012b).

At equilibrium, the water activity ( $a_w$ ) of a liquid aqueous solution droplet is equal to the  $RH_{liq}/100$  (Koop et al., 2000). Water molecules can easily diffuse into and out of liquid solution droplets allowing them to remain in equilibrium with their surroundings. Due to their high viscosity, diffusion of water molecules within glassy or semi-solid materials is extremely slow and gets slower as temperature decreases (Zobrist et al., 2011; Tong et al., 2011; Koop et al., 2011). This makes it difficult for glassy particles to efficiently take up water and dilute on humidification, resulting in a much more gradual deliquescence than a soluble crystalline aerosol (Figure 1.18). The humidity at which they liquefy (or become glassy on drying) ( $RH_g$ ) is dependent on the rate of increase of the surrounding humidity (Zobrist et al., 2011; Bones et al., 2012). A fast increase in humidity results in a higher  $RH_g$  (green line, Figure 1.18c) compared to  $RH_g$  for slower increases in humidity (orange line). Tong et al. (2011) observed that at room temperature, sucrose aerosol particles returned to equilibrium upon crossing  $RH_g$  in 10s – 100s seconds. At lower temperatures, the delay in water uptake may be substantially longer. There is also evidence that concentration gradients occur within solid or semi-solids particles as the result of the effect of high viscosities on the

diffusion of water molecules into and out of amorphous particles (Bones et al., 2012; Zobrist et al., 2011).

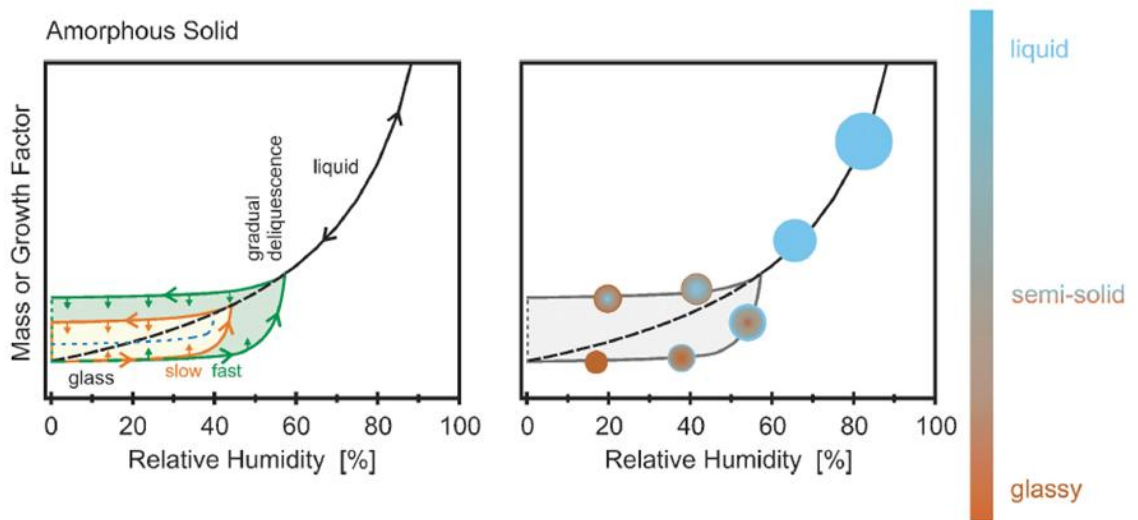


**Figure 1.18** The effect of changing the surrounding humidity on an amorphous solid. Mass is equivalent to hygroscopic growth factor, which is equal to the ratio of the aerosol particle radius at a given RH and the aerosol particle's dry radius. Adapted from Koop et al.(2011).

An aim of this project was to investigate the ice nucleation properties of glassy aerosol particles under cirrus conditions. Chapters 4, 5 and 6 detail experiments that took place using glassy aerosols of a variety of compositions at the AIDA cloud simulation chamber, Karlsruhe.

## 1.5 Summary

Cirrus clouds are ubiquitous upper tropospheric ice clouds that have a significant impact on the radiative balance of the Earth. Currently, the impact of heterogeneous ice nucleation on the physical and optical properties of cirrus clouds is poorly understood. Studies of cirrus ice particle residues at mid-latitudes find that the presence of mineral dust is enhanced compared to the background aerosol, indicating that this species of IN catalyse the production of cirrus ice. Cirrus cloud models provide evidence that the extensive, thin, subvisible cirrus clouds (SVC) that exist in the tropical tropopause layer (TTL) are likely to result from the heterogeneous nucleation of ice. However, SVC ice particle residues have been shown to overwhelmingly consist of sulphate-organic species rather than traditional heterogeneous IN such as mineral dust. Recent measurements have shown that aerosol particles containing large amounts of organic material (such as those found in the TTL) are likely to exist in a semi-solid or solid

amorphous (non-crystalline) state at temperatures relevant to the upper troposphere and TTL (Virtanen et al., 2010; Koop et al., 2011). This thesis reports on investigations into the ice nucleating behaviour of glassy (*i.e.* solid amorphous) aerosol particles under cirrus conditions at a cloud simulation chamber. It also details the development and characterisation of a bench top instrument for deposition mode ice nucleation and its use to study the ice nucleation behaviour of a natural mineral dust.

## **Chapter 2: Experimental for AIDA chamber campaigns**

### **2.1 Preface**

Chapters 4, 5 and 6 of this thesis describe the results from experiments performed at the AIDA (Aerosol Interactions and Dynamics in the Atmosphere) cloud simulation chamber at the Karlsruhe Institute of Technology, Germany. The purpose of the experiments was to study the behaviour of glassy aqueous solution aerosols when exposed to conditions relevant for cirrus clouds in the TTL and the wider upper troposphere. The experiments were performed as parts of the first and second ICE (Inhibition of Crystallisation Experiment) campaigns - ICE01 (Chapter 4) and ICE02 (Chapters 5 and 6). The purpose of this chapter is to describe the AIDA chamber's mode of function during the ICE campaigns and the instrumentation used to observe the 'atmospheric' conditions inside the chamber. It is not intended to provide an exhaustive review of the AIDA chamber's extensive experimental capabilities. Additional detailed information on the AIDA chamber can be found in Möhler et al. (2006) and Wagner et al. (2010). Also discussed in this chapter are aerosol phase diagrams, which were used during the campaigns to predict the phase of aqueous solution aerosols when exposed to particular temperatures and humidities.

### **2.2 The AIDA chamber**

The AIDA chamber is a large (84 m<sup>3</sup>), highly instrumented aerosol and cloud chamber in which temperatures and humidities equivalent to those required for cirrus formation are accessible. A cross sectional schematic of the chamber and associated instrumentation is shown in Figure 2.1.

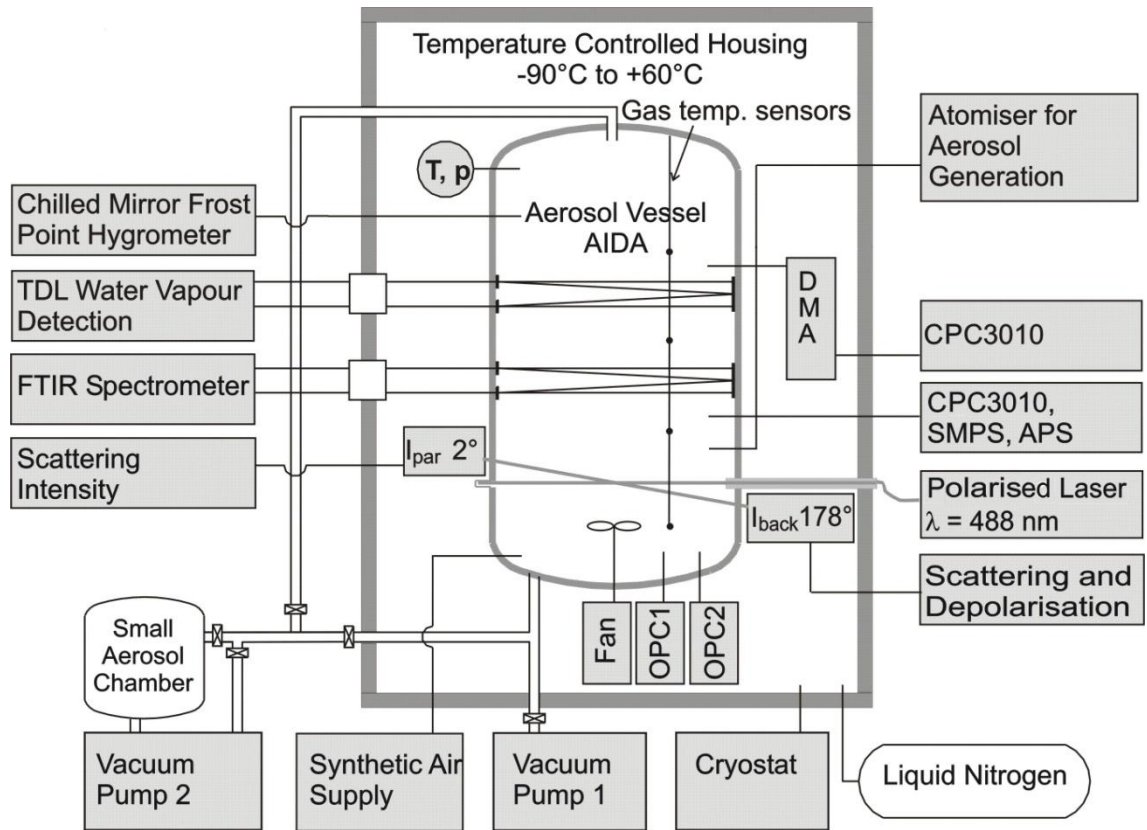


**Figure 2.1** A schematic diagram of the AIDA chamber and its associated instrumentation. Adapted from Wagner et al. (2012b).

The temperature of the aluminium walls of the chamber was controlled between  $\sim 190$  and  $240$  K during the ICE01 and ICE02 campaigns. This was achieved by using liquid nitrogen to cool air within the chamber's thermostated jacket. The gas phase water partial pressure ( $P_{\text{H}_2\text{O}}$ ) in the chamber was controlled by a coating of ice on the vessel walls. The ice layer was deposited after the chamber had been evacuated to  $\sim 0.01$  hPa and then flushed repeatedly with particulate free air to reduce the number of background aerosol particles to  $< 1 \text{ cm}^{-3}$ . Purified water was evaporated into the evacuated chamber, which deposited as an ice layer on the cooled chamber walls. Temperature sensors arranged vertically and horizontally in the chamber determined the average gas temperature and sensors embedded in the aluminium walls determined the average wall temperature. The chamber was continuously stirred by a fan and the measured gas temperatures were typically within  $\pm 0.3$  K (Wagner et al., 2011). The presence of internal sources of heat (heated sampling tubes, the mixing fan etc.) meant that the gas temperature was slightly higher ( $\sim 1$  K) than the wall temperature, giving a relative humidity with respect to hexagonal ice ( $\text{RH}_i = p_{\text{H}_2\text{O}}/p_{\text{ice}}^*(T) \times 100$ , where

$p_{\text{ice}}^*(T)$  is the equilibrium vapour pressure over a flat surface of hexagonal ice) of around 90-95% at equilibrium. The equilibrium vapour pressure over a flat surface of hexagonal ice was calculated from the mean gas temperature using the parameterisation from Murphy and Koop (2005).

In order to produce supersaturated conditions, the pressure in the chamber was reduced by pumping air out of the chamber using a pair of vacuum pumps. Heat conduction from the walls into the chamber was relatively slow and expansions were initially close to adiabatic. This resulted in a decrease in the gas temperature, which caused the  $\text{RH}_i$  to increase. The gas phase water partial pressure ( $p_{\text{H}_2\text{O}}$ ) was determined using absorption measurements from a multipath cell tuneable diode laser (TDL) spectrometer (Wagner et al., 2010). Measurements of  $p_{\text{H}_2\text{O}}$  using this system are found to be within 5% of the actual value (Skrotzki, 2012; Fahey et al., 2009). The total water content (ice and gas phases) was determined using a chilled mirror hygrometer (MBW LX-373) which sampled from the chamber via a heated tube, returning any sampled ice particles to the gas phase (Wagner et al., 2010, 2011; Wagner et al., 2009).

An aqueous aerosol dispersion of the desired composition was introduced into the chamber by nebulising 3 - 3.5 wt% bulk solutions with a compressed-air atomiser (TSI). The aerosol particle concentration reached an almost constant value of about  $15000 \text{ cm}^{-3}$  shortly after nebulising. Aerosol number concentrations were measured using condensation particle counters (CPC, TSI 3010, TSI 3775, TSI 3776). The CPC3010 was used at pressures below ambient, allowing the aerosol number concentration to be measured continuously during expansion experiments. However, during the ICE02 campaign (Chapters 5 and 6) the CPC3010 was unavailable for some experiments; in these cases two other CPC instruments (CPC3775 and CPC3776) were used. These instruments are only able to operate at ambient pressure so just prior to each expansion the aerosol number concentration was measured for a period of time (~200 seconds). The aerosol concentration falls continuously even when not expanding because of sampling losses and deposition of particles to the walls. To account for this, a linear fit to the mean of the CPC3775 and CPC3776 concentration/time data was extrapolated to the time at which the expansion started. This estimated initial aerosol concentration was then scaled with the decreasing chamber pressure during expansion, providing an estimate of the aerosol number concentration during the experiments. This estimate was compared with data from experiments that used CPC3010 and was found

to be accurate to within 3 - 10%. The aerosol concentration during expansion experiments was typically 5000 – 15000 cm<sup>-3</sup>.

The aerosol size distributions were measured using both an aerodynamic particle sizer (APS, TSI, 0.5 – 20 µm) and a scanning mobility particle sizer (SMPS, TSI, 0.01 – 0.9 µm) (Figure 5.8). A particle density of 1.6 g cm<sup>-3</sup> was assumed when converting the aerodynamic diameters measured by the APS into volume-equivalent spherical diameters ( $d_p$ ) (Hinds, 1999). The exact densities of the solution aerosol used in the two campaigns are unknown, however the assumed density is close to that of the crystalline forms of the species investigated. Spherical particles have mobility-equivalent diameters (as measured by the SMPS) that are equal to  $d_p$ .

The onset of ice nucleation was observed *in situ* using the laser scattering and depolarisation instrument SIMONE (Schnaiter et al., 2012). Three photomultipliers mounted outside the chamber's thermal housing receive forward and back scattered light ( $I_{\text{for}}$ ; 2° to the incident beam,  $I_{\text{back}}$ ; 178° to the incident beam). The incident continuous wave laser beam has an emission wavelength of 488 nm and is linearly polarised with its polarisation vector oriented parallel to the scattering plane. Light scattered in the 178° direction is decomposed according to its polarisation state by means of a polarising prism. The intensities of the scattered components having a polarisation parallel to ( $I_{\text{back,par}}$ ) and perpendicular to ( $I_{\text{back,per}}$ ) the scattering plane are measured. The backscattering linear depolarisation ratio,  $\delta$ , is then defined as the ratio of  $I_{\text{back,per}}$  to  $I_{\text{back,par}}$ . The magnitude of  $\delta$  is dependent on particle size and shape; for perfectly spherical particles,  $\delta$  would be zero, in practice the observed  $\delta$  for unfrozen glassy aerosols and liquid aerosols in this study was between 0.02 and 0.03. This small background  $\delta$  was due to a combination of the incident laser light being only 99% linearly polarised to start with, Rayleigh scattering by air molecules and minor optical misalignments. Ice particles are aspherical and cause a clear increase in  $\delta$ . A change of at least 1% was used to infer the onset of ice nucleation (See Chapters 5 and 6 for examples of the change in  $\delta$  during an ice nucleation experiment) (Möhler et al., 2003; Schnaiter et al., 2012).

Two WELAS2000 optical particle counters (OPC) (Palas GmbH) were used to count and size single particles. These instruments are described in detail by (Benz et al., 2005; Wagner et al., 2006). Each instrument measures a different size range for



spherical particles with the refractive index of ice (1.33); WELAS 1 covers 0.7 – 46.0  $\mu\text{m}$  and WELAS 2 covers 5.0 – 240.0  $\mu\text{m}$ . The optical sizes for aspherical particles (*e.g.* ice crystals) were considered approximate as particle asphericity is not considered when relating the scattering intensity to particle diameter. Due to its ability to detect particles down to 0.7  $\mu\text{m}$ , the WELAS 1 OPC is able measure the larger unfrozen background aerosol particles, which are clearly present in the diameters measured by WELAS 1 in Figure 2.2 (top panel). To infer ice particle number concentrations ( $N_{\text{ice}}$ ) from the WELAS 1 total particle number concentration data, it was necessary therefore to apply a threshold size, above which particles were assumed to be ice. In order to differentiate between ice particles and background aerosol the threshold has to be tuned depending on the size of the background aerosol and the rate of growth of the ice particles. At lower temperatures ice particles do not grow as large because of the lower absolute humidity. Consequently it was not possible to apply a size threshold to distinguish ice crystals from the larger of the background aerosol particles. Where possible, WELAS 2 data was used to provide a lower limit for  $N_{\text{ice}}$  in experiments which took place below  $\sim 200$  K. A comparison of  $N_{\text{ice}}$  inferred from WELAS 1 and 2 during an ice nucleation event is shown in Figure 2.2 (bottom panel). It can be seen that WELAS 1 measures marginally higher ice number concentrations due to its larger size range.

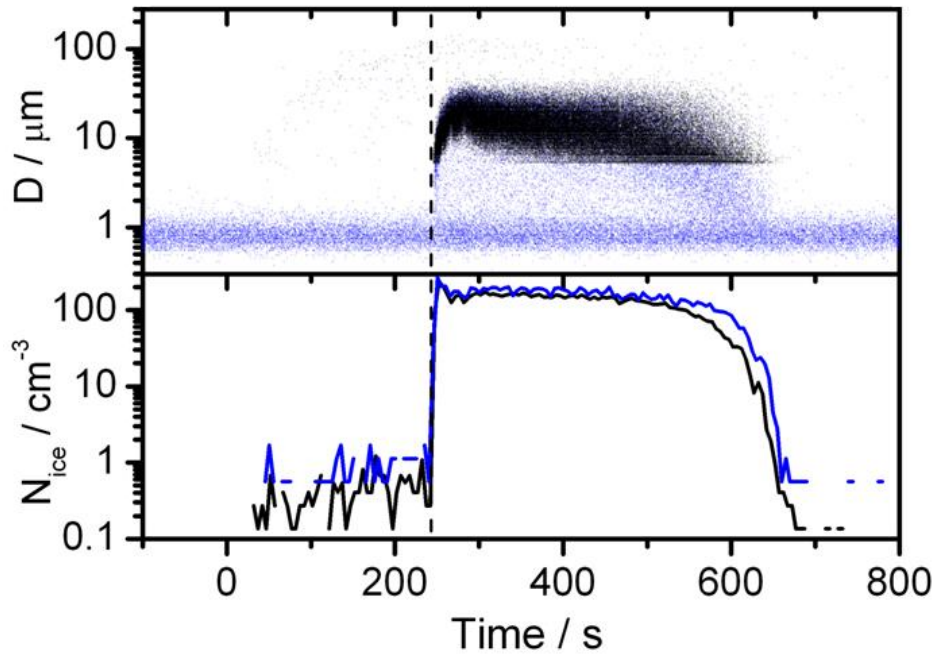


**Figure 2.2** Particle diameter ( $D$ , top panel) and inferred ice particle number concentration ( $N_{ice}$ , bottom panel) observed by optical particle counters WELAS 1 (blue) and WELAS 2 (black) during an ice nucleation event (start of ice nucleation inferred using SIMONE and marked by vertical dashed black line).

## 2.3 Materials

The ICE01 campaign experiments used only aqueous citric acid aerosol. During the ICE02 campaign the following single component aerosols were used: Raffinose (D-(+)-Raffinose pentahydrate,  $\geq 98\%$ , 594.52 g/mol, Sigma-Aldrich), levoglucosan ((-)-1,6-Anhydro- $\beta$ -D-glucopyranose,  $\geq 99\%$ , 162.14 g/mol, Merck Schuchardt) and HMMA (4-Hydroxy-3-methoxy-DL-mandelic acid, 98%, 198.17 g/mol, Alfa Aesar). Experiments in ICE02 also used a multi component aerosol first used by Zobrist et al. (2008), which was a 1:1 mixture of raffinose and M5AS - a mixture of 30.7 wt% malonic acid ( $\geq 99\%$ , 104.06 g/mol, Merck Schuchardt), 14.7 wt% malic acid (DL-Malic acid,  $\geq 99.5\%$ , 134.08 g/mol, Merck), 14.1 wt% maleic acid ( $\geq 99\%$ , 116.07 g/mol, Merck Schuchardt), 17.7 wt% glutaric acid ( $\geq 99\%$ , 132.11 g/mol, Merck Schuchardt), 7.4 wt% methylsuccinic acid (99%, 132.12 g/mol, Sigma-Aldrich) and 15.4 wt% ammonium sulphate ( $\geq 99.5\%$ , 132.14 g/mol, Merck). All solutions in both campaigns were made using 18.5 M $\Omega$  cm water and were passed through a sub-micron (0.45  $\mu\text{m}$ ) filter to remove particulates.

## 2.4 Aerosol phase diagrams

In order to test the difference in behaviour of liquid and glassy aerosols of the same composition, phase diagrams were used to predict the state of aerosol at specific temperatures and humidities. All the aqueous systems that were selected for study in the ICE01 and ICE02 campaigns have been characterised previously and the conditions under which they form glasses have been quantified.

In the ICE01 campaign, citric acid solution aerosol droplets were investigated and the citric acid solution aerosol phase diagram is shown in Chapter 4. The glass transition ( $T_g$ ) threshold for citric acid shown in Figure 4.2 is based on a fit to measurements made by Maltini et al.(1997). That threshold was converted from a function of solute wt% to a function of  $a_w$  using equation A1 in Murray et al. (2008b). The  $T_g$  thresholds for the systems investigated in the ICE02 campaign (raffinose, HMMA, levoglucosan and raffinose/M5AS, see Chapter 5 for details) were investigated in detail by Zobrist et al. (2008). Based on differential scanning calorimetry measurements made on emulsion samples, Zobrist et al. calculated the solute specific constant,  $k$ , from the Gordon-Taylor equation for the glass transition temperature of binary solutions (Equation 2.1) (Gordon and Taylor, 1952; Katkov and Levine, 2004). Using the solute specific value of  $k$  determined by Zobrist et al. (2008) and the glass transition temperatures of the pure form of water ( $T_{g1} = 136$  K (Johari et al., 1987; Kohl et al., 2005)) and the solute ( $T_{g2}$ ), glass transition temperatures were calculated as a function of the weight fraction of the solute ( $w_2$ ) and the weight fraction of water,  $w_1$  ( $w_1 = 1 - w_2$ ). Upper and lower limits of  $T_g$  were also calculated using the estimated uncertainties in  $k$  and  $T_{g2}$  for each solute.

$$T_g(w_2) = \frac{w_1 T_{g1} + \frac{1}{k} w_2 T_{g2}}{w_1 + \frac{1}{k} w_2}$$

Equation 2.1

The solute weight fraction could then be converted to water activity using parameterisations provided by Zobrist et al. (2008), based on vapour pressure measurements taken for solutions of differing concentration at a series of temperatures between 313 and 289 K, which were then extrapolated to lower temperatures. As water

activity is directly equivalent to relative humidity when at equilibrium, the calculated  $T_g$  thresholds can be used to estimate the humidity and temperature at which a liquid aerosol particle would become glassy and vice versa. The  $T_g$  thresholds will be from this point forward referred to as the humidity induced glass transitions,  $RH_g$ , as this is of relevance in our experiments as the aerosol are subject to a more significant change in humidity than temperature during expansions.

An example phase diagram, in this case for aqueous levoglucosan, is shown in Figure 2.3. The glass transition for aqueous levoglucosan solution aerosol as a function of temperature and water activity is shown as a solid green line. Also plotted are the ice-liquid equilibrium threshold (solid black line) and the homogeneous freezing threshold (dashed red line), which are both related directly to water activity (Koop et al., 2000). The advantage of plotting the phase diagram in terms of water activity as opposed to concentration is that at equilibrium, the water activity of liquid solution aerosol is equal to  $RH_{liq}$  (relative humidity with respect to liquid water). Hence, if an aerosol particle is able to come into equilibrium with its surroundings rapidly, then it is possible to estimate the aerosol's solute concentration based on temperature and  $RH_{liq}$ . However, if the aerosol particle is glassy or ultra-viscous, then diffusion of water into or out of the particle will be slow and it may remain out of equilibrium, making the water activity no longer equal to the  $RH_{liq}$  (Zobrist et al., 2011; Tong et al., 2011; Mikhailov et al., 2009; Koop et al., 2011; Bones et al., 2012).

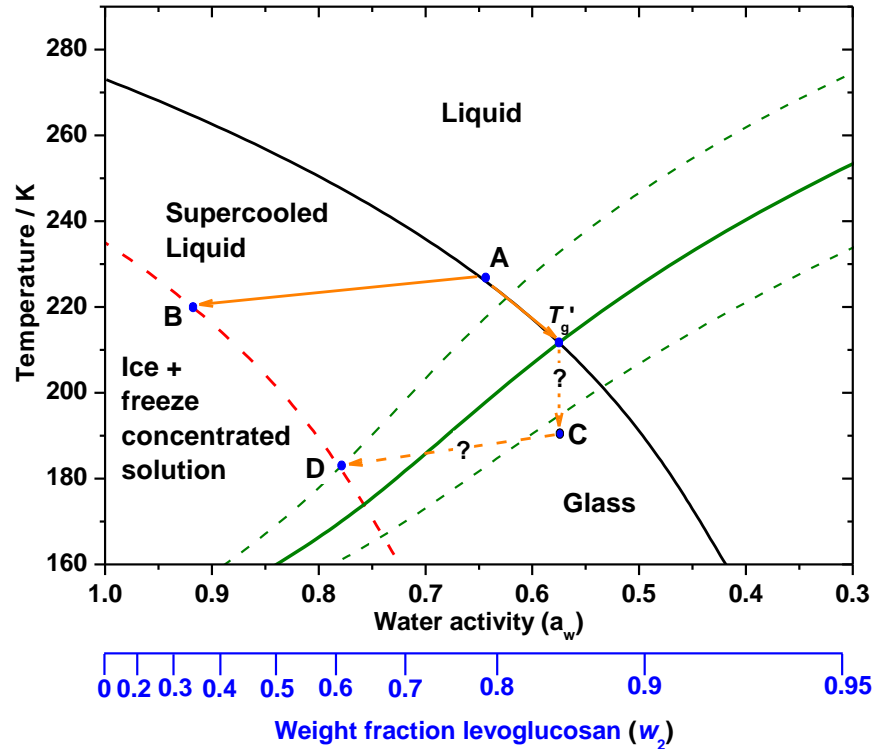


**Figure 2.3.** The phase diagram of levoglucosan solution aerosol and the idealised trajectory of an aerosol during typical experiments at AIDA. The black line is the ice liquid equilibrium line, the dashed red line is the homogeneous freezing threshold based on the water activity homogeneous freezing criteria (Koop et al., 2000) and the green solid line is the humidity induced glass transition threshold ( $RH_g$ ) for levoglucosan solution aerosol, with associated upper and lower uncertainties (dashed green lines) based on uncertainties in the parameters used in the Gordon-Taylor equation (Equation 2.1) (Zobrist et al., 2008). The orange arrows represent idealised temperature/humidity trajectories. The ice-liquid equilibrium and homogeneous freezing lines are common to all solutions used in this study, but  $RH_g$  is unique to each solution system.

Under non-expansion conditions, the chamber water vapour is close to equilibrium with the ice layer on the walls. Consequently, the water activity of aqueous liquid solution aerosols in the chamber, which are in equilibrium with the gas phase, is therefore approximately described by the ice-liquid equilibrium line shown in Figure 2.3. The actual chamber humidity was around 90 - 95%  $RH_i$ , due to the presence of heat sources in the chamber (as discussed above), so the exact water activity of liquid aerosol is to the right (lower water activity) side of the ice-liquid equilibrium line. For simplicity, the trajectory of the change in temperature and water activity of aerosol particles during chamber cooling/heating periods is depicted as being along the ice-

liquid equilibrium line. The point at which  $RH_g$  and the ice-liquid equilibrium line cross ( $T_g'$ ) is a useful indication of the likely phase of aerosol particles before an expansion experiment. Above  $T_g'$ , the aerosol particles are likely to be liquid and below they are likely to be in the glassy state.

For all of the experiments described in Chapters 5 and 6, and for the majority of the experiments shown in Chapter 4 aerosol particles were injected into the chamber when the gas temperature was above  $T_g'$  of the aerosol type being investigated. These liquid solution droplets equilibrated with the water vapour in the chamber. The concentration of liquid levoglucosan solution aerosol injected at  $\sim 237$  K rapidly adjusted to around point A in Figure 2.3. Slow cooling ( $\sim 4$  K  $hr^{-1}$ ) of the chamber walls allowed the water vapour within the chamber to remain equilibrated with the ice film on the walls. The viscosity of liquid near the glass transition increases rapidly with decreasing temperature and decreasing water activity (Angell, 2002; Murray, 2008b; Murray, 2008a). At viscosities above but close to the glass transition the composition of the aerosol is likely cease to remain in equilibrium with the chamber humidity, as diffusion into and out of semi-solid droplets has been shown to be significantly inhibited (Bones et al. 2012). It is likely therefore that the actual aerosol composition will deviate from the trajectory marked between point A and  $T_g'$ . Once the glass transition is arrived at, the aerosol water content will have ceased to respond to changes in the chamber humidity. This is represented tentatively by the vertical dashed arrow in Figure 2.3 between  $T_g'$  and point C. In Chapter 4, two experiments are described in which aerosol was injected well below  $T_g'$ , for details see Section 4.2.2.

The evolution of aerosol composition differs when an expansion is started in the liquid regime compared to the glassy regime. Liquid solution aerosol at point A (Figure 2.3) take up water and dilute as the chamber humidity rises with decreasing temperature (arrow between points A and B). This increases the aerosol particles' water activity until ice nucleates at the homogeneous ice nucleation threshold (point B). The change in water activity on increasing humidity of a glassy aerosol starting at point C (remembering that the composition at point C is already uncertain) is not clear since the uptake of water is dependent on the rate at which water molecules can diffuse into the aerosol particles. The rate of diffusion of water in glassy solids is very slow (Koop et al., 2011; Tong et al., 2011; Zobrist et al., 2011) and once  $RH_g$  is crossed liquefaction of the aerosol particles may be delayed (Mikhailov et al., 2009; Tong et al., 2011). If the

aerosol particles do liquefy then they will freeze at the homogeneous nucleation threshold at point D. Nevertheless, prior to liquefying these aerosol particles will exist in a glassy state while in an ice supersaturated environment.

There is some uncertainty in the conditions under which the aerosol droplets exist in a glassy state and cease to be in equilibrium on slowly cooling the chamber. This is due to uncertainty in the position of the  $RH_g$  line. In addition to the upper and lower uncertainty limits for  $RH_g$ , shown in Figure 2.3 there is also an additional error in  $RH_g$  associated with the conversion of solution concentration to water activity, as it was necessary for Zobrist et al. (2008) to extrapolate measurements of solution water activity to low temperatures. Also, the enhancement of vapour pressure due to surface curvature (the Kelvin effect) can become important for small droplets. However, at 243.15 K a 100 nm pure water droplet would have a vapour pressure only 2.9% higher than that of a flat surface of liquid water, suggesting that the Kelvin effect is of secondary importance. This was calculated using water density of  $983.8 \text{ kg m}^{-3}$  (Wagner and Pruss, 2002). Surface tension was estimated using a parameterisation by Vargaftik et al. (1983) (which is consistent with nucleation data well below the temperatures at which surface tensions have been measured (Murray and Jensen, 2010)) and the saturation vapour pressure for a flat water surface was calculated using the parameterisation provided by Murphy and Koop (2005). Finally, it should also be noted that the conditions under which an aerosol particle will undergo the glass transition and go out of equilibrium with the surrounding atmosphere are time dependent. When given a longer equilibration time, a droplet will remain in equilibrium to lower temperatures and therefore greater concentrations. However, the viscosity of many aqueous solutions increases so strongly with decreasing temperature (because they are fragile liquids, which have much ‘sharper’ glass transitions on cooling (Angell, 2002)) that the glass transition temperature provides a very useful estimate of the conditions under which the dynamic arrest of the solution is expected.

## **2.5 Avoidance of aerosol pre-activation during ICE02 campaign**

In Chapter 6 results are presented that show that the aerosols used in the ICE02 campaign became ‘pre-activated’ under conditions relevant for the results presented in Chapters 4 and 5. Under specific conditions it was observed that aerosol particles which

had already nucleated ice homogeneously would act as ice nuclei at as low as 105% RH<sub>i</sub> in subsequent expansions, even after being held under subsaturated conditions for in excess of 30 minutes between expansion experiments. Pre-activation was only observed in aerosol close to their predicted  $T_g'$ , so it was possible to design experiments in such a way as to avoid the aerosol becoming pre-activated. The results presented in Chapter 5 for heterogeneous ice nucleation in the glassy regime are only for aerosols which had not been frozen homogeneously prior to cooling or for aerosol which had been frozen homogeneously at temperatures too high for pre-activation to occur (which was confirmed by performing a second expansion at the same temperature to look for early ice nucleation). While this reduced the number of experiments that it was possible to perform within the time constraints of the campaign, it was necessary in order to unambiguously avoid experimental artefacts relating to pre-activation. These precautions were not followed during the ICE01 campaign, resulting in the possibility that the pre-activation of aerosols could have occurred in the experiments described in Chapter 4. There is however no clear evidence that pre-activation occurred during ICE01 and this is discussed in detail in Section 4.2.4.



## Chapter 3: Development of the deposition mode chamber (DMC)

An objective of this project was to build an instrument for the direct observation of deposition mode ice nucleation on particles of tens of micrometers in size. The bench top instrument would allow the investigation of the same particles over extended periods of time and under controlled conditions. Data from such an instrument would complement ‘bulk’ ice nucleation measurements possible at large cloud chambers like AIDA, which are effective at observing large quantities small aerosol particles during short expansion experiments, but which cannot maintain particles at constant temperature and humidity for extended periods of time, preventing the calculation of ice nucleation rates at set humidities or temperatures.

*Some components used in the building of the chamber began as parts of an existing instrument built by Gourihar Kulkarni and Steven Dobbie (Kulkarni 2007; Kulkarni et al., 2009; Kulkarni and Dobbie, 2010). This instrument was a thermal gradient diffusion chamber (see below for details) that operated in a refrigerated cold room. This was inconvenient and limited the length of time that it could be operated for during experiments, so it was decided to modify it into liquid N<sub>2</sub> cooled bench top instrument. This modification involved an extensive redesign and completely changed the chamber’s mode of operation, resulting in an essentially new instrument.*

### 3.1 Generating relative humidities with respect to ice

The deposition of ice directly from the vapour phase can occur at temperatures below 273.15 K providing that the humidity is above ice saturation ( $RH_i > 100\%$ ). The precise humidity at which ice nucleation occurs is dependent on the surface properties of the available nuclei. At temperatures above the homogeneous freezing point of pure water droplets (~235 K), it is possible for liquid water to condense if water saturation is reached (where the relative humidity with respect to liquid water = 100%). This occurs when the available surface lacks any suitable sites for deposition mode ice nucleation. As the temperature decreases from 273 K the absolute amount of water vapour at 100%  $RH_i$  decreases sharply (Figure 3.1). At cirrus cloud temperatures (< 235 K (Lynch et al., 2002)) there are orders of magnitude less water vapour at ice saturation than at 270 K.

This makes observing ice nucleation under cirrus conditions challenging, as controlling such small vapour pressures requires a higher degree of precision.

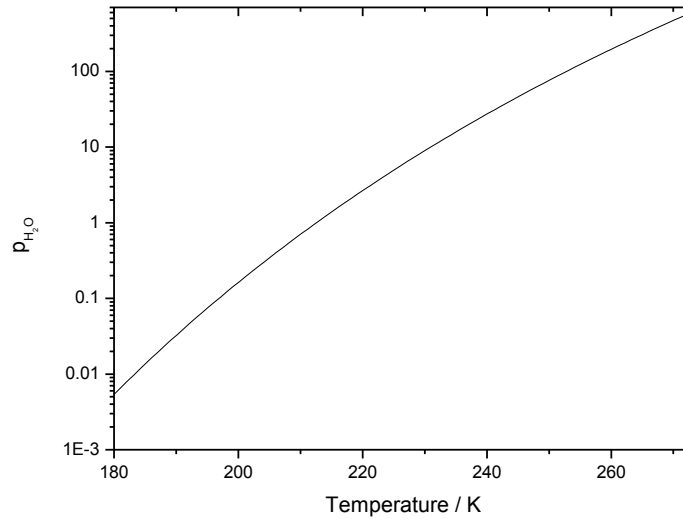


**Figure 3.1** The partial pressure of water vapour as a function of temperature at 100%  $\text{RH}_i$ . Plotted using a parameterisation of the saturation vapour pressure of water vapour over an hexagonal ice surface (Murphy and Koop, 2005).

Chambers for studying deposition mode ice nucleation can be broadly divided into two classes; those which study a flow (*e.g.* Cziczo et al. (2003)) or dispersion of particles (like the AIDA chamber, see below) and those which place particles onto a static non-ice nucleating surface (*e.g.* Dymarska et al. (Dymarska et al., 2006)). In both cases the particles are then exposed to increasing supersaturation with respect to ice, to simulate the processes by which atmospheric ice cloud formation occurs. In general, dispersion and flowing systems allow the analysis of large numbers of particles on relatively short timescales (seconds – minutes), which are then lost, whereas static instruments sample fewer particles, for potentially longer time periods (minutes – hours) and allow samples to be retained for further experimentation. The analysis of large numbers of particles allows more accurate fraction frozen data, which is useful for parameterisations of ice nucleation for cloud models. However, being able to expose potential IN to consistent conditions (*i.e.* constant temperature and supersaturation) for longer periods of time in a static instrument allows the time dependence of ice nucleation to be investigated. This is also of interest when parameterising the behaviour

of IN, as some approaches make the assumption that ice nucleation is time independent (*i.e.* stochastic vs. singular parameterisations, See Section 1.4.3) (Broadley et al., 2012).

An example of a dispersion type instrument is the AIDA chamber, which is described in detail in Chapter 2. AIDA's walls are coated with a thin layer of ice that controls the equilibrium partial pressure of water in the chamber. The pressure within the chamber is reduced, resulting in an initially adiabatic expansion that causes the gas to cool to temperatures below that of the ice deposited on the chamber walls, generating ice supersaturated conditions. Chambers that observe freezing in a flow of aerosol particles use other methods of generating supersaturations; the FINCH (Fast Ice Nucleus Chamber) instrument operates on the mixing principle, whereby a flow of aerosol in cold dry air is exposed to supersaturation when it mixes with warmer, particulate free humid air (Bundke et al., 2008). A more common technique for flowing instruments is the continuous flow diffusion chamber (CFDC). Diffusion chambers generate supersaturations with respect to ice in a region between two ice covered surfaces held at different temperatures. The geometry of CFDCs varies, with some approaches using two concentric cylinders (Archuleta et al., 2005) and others a pair of parallel plates (Hoyle et al., 2011; Friedman et al., 2011). CFDCs are also used to study ice nucleation during field measurements. These instruments take in a flow of *in situ* sampled aerosol, exposing it to supersaturations and can be coupled to single particle mass spectrometers, allowing the composition of ice nuclei to be probed (Cziczo et al., 2003; DeMott et al., 2003). Dispersion and flowing instruments often detect the formation of ice using light scattering/depolarisation methods like that used at AIDA.

Static surface type instruments often use a temperature controlled cold stage to cool particles in an environment containing a known amount of water vapour, hence exposing the particles to ice supersaturation when they reach temperatures below the frost point. Particles are usually observed using visible light microscopy. A common method of generating water vapour is to saturate gas by bubbling it through water and then dilute it with a known quantity of dry gas to reach the desired partial pressure of water vapour. The gas can then be flowed through the cell containing the cold stage and particles (Dymarska et al., 2006; Eastwood et al., 2008; Kanji and Abbatt, 2006; Kanji et al., 2008). Producing accurate humidities using this method at cirrus temperatures requires precision mass flow controllers, a source of very dry carrier gas and a temperature controlled bath to set the temperature of the water in the bubbler.

Another approach is to have a source of water vapour in the chamber itself. This can be achieved in a number of ways; static thermal gradient diffusion chambers (TGDC) produce supersaturations in the same manner as CFDCs but observe particles on a surface within the chamber. The TGDC developed by Kulkarni et al. (Kulkarni et al., 2009) was a static parallel plate instrument, similar to that used by Bailey and Hallett (Bailey and Hallett, 2002). Deposition mode ice nucleation could be investigated by introducing particles sat on the end of a rod into the supersaturated region between its two ice covered plates. By raising their position in the chamber, particles were subjected to increasing temperature and supersaturation (Kulkarni and Dobbie, 2010). TGDCs are limited by not being able to access humidities  $< 100\% RH_i$ , making it difficult to perform repeated ice nucleation experiments upon a sample. This is particularly important when observing whether particles become pre-activated after an initial freezing event (See Chapters 6 and 7 for more detail and experimental results involving pre-activation of glassy and mineral dust aerosol particles).

Another approach to generating water vapour *in situ* is to control the temperature of a single surface of ice sealed within an experimental chamber that will, when at equilibrium, generate a partial pressure of water vapour equal to its saturation vapour pressure at that temperature. The temperature of the sample is independently controlled so it can be cooled to temperatures below that of the ice surface to generate supersaturations and raised to a temperature above that of the ice surface to generate subsaturations. This technique was used by Shaw and Mason (1955), Bryant et al. (Bryant et al., 1959) and Roberts and Hallett (Roberts and Hallett, 1968) to study ice crystal growth and ice nucleation by mineral dusts. Those instruments had internal surfaces coated with ice that were temperature controlled using circulated cooled liquids.

A limitation of static instruments is that once ice has nucleated on a sample particle, the growth of the associated crystal can deplete the nearby environment of water vapour, causing substantial uncertainty in the humidity. This may be less of an issue when using a flow of humidified gas as water vapour is replenished more rapidly, though depending on the rate of diffusion, a local depletion of water vapour may still occur. A technique that avoids this is to conduct experiments at pressures in the Knudsen regime, where the mean free path of molecules is larger than the dimensions of the cell. This has been achieved using low pressure ‘Knudsen cell’ type instruments that

generate water form an ice or water surface (depending on the temperature) (Knopf and Koop, 2006; Klein et al., 2010).

## 3.2 Chamber concept

The decision was made to convert Kulkarni's chamber from a TGDC into a chamber that operates on the same principle as the chamber used by Roberts and Hallett (1968) (see above). This would allow particles to be exposed to humidities below ice saturation, enabling the investigation of IN pre-activation behaviour as well as allowing isothermal and isohumid experiments. The chamber generates a known partial pressure of water vapour *in situ* using a single temperature controlled ice surface. Adjusting the temperature of a sample of potential ice nuclei placed on a hydrophobic surface within the chamber relative to the temperature of the ice surface, exposes that sample to both a known temperature and humidity with respect to ice. The humidity experienced by the sample under investigation,  $RH_i(T_{\text{sample}})$ , is calculated using the following equation:

$$RH_i(T_{\text{sample}}) = \frac{p_{\text{ice}}^*(T_{\text{ice}})}{p_{\text{ice}}^*(T_{\text{sample}})} \times 100$$

Equation 3.1

Where  $p_{\text{ice}}^*(T_{\text{ice}})$  and  $p_{\text{ice}}^*(T_{\text{sample}})$  are the equilibrium vapour pressures of ice at the temperatures of the ice surface and of the sample respectively, both calculated using the parameterisations provided by Murphy and Koop (2005). When the particles are at the same temperature as the ice surface, they experience  $RH_i$  of 100%. Unlike a thermal gradient diffusion chamber, this method of generating humidities allows both super and subsaturations with respect to ice to be generated, depending on whether the sample is at a lower or higher temperature than the ice surface.

## 3.3 Description of the DMC

### 3.3.1 Chamber body

The chamber body has a volume of  $\sim 65 \text{ cm}^3$  and consists of a PEEK (polyether ether ketone) thermoplastic dish (Figure 3.2) sandwiched between two liquid  $\text{N}_2$  cooled plates. The plates are used in the control of the temperatures of the sample and the ice film (Figure 3.3). The top rim of the PEEK dish has an inset EPDM (*ethylene propylene diene monomer*) rubber O-ring that seals against the inner surface of the stainless steel

top plate. The chamber is held together by four machine bolts that run between the two plates. These are tightened to ensure a good seal between the O-ring and the top plate surface. In the centre of the top plate is a viewing port covered with a borosilicate glass window, this is used to view the particles under investigation with a microscope. The chamber is kept well mixed by a continuously functioning 5 V axial fan (Sunon, RS components), mounted in the base of the PEEK dish.

The PEEK dish has four ports, one of which is used to supply the power cables to the chamber mixing fan. The remaining ports were not used during the experiments detailed here, but were included in the design to allow the chamber to also operate as part of a flowing system, if required.

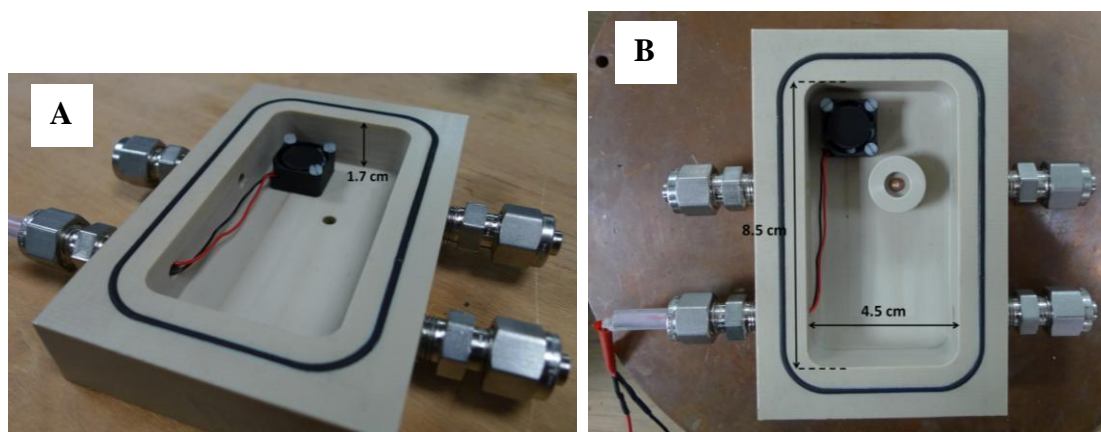


**Figure 3.2** The body of the chamber, made from PEEK polymer. A shows it without the sample holder in place. B shows the chamber in position on the bottom plate, with the sample holder in place. Note also the fan and four ports, one of which the power cables for the fan exit through.

### 3.3.2 Temperature control

Both the top and bottom plates of the chamber incorporate copper elements through which, via two separate solenoid pulse valves, liquid nitrogen is passed as a coolant. The temperature of each plate is controlled using separate Eurotherm 2416 PID (proportional–integral–derivative) temperature controllers linked to PT100 platinum resistance thermometers (PRT), which in the case of the top plate is embedded in its stainless steel layer and in the case of the copper bottom plate is located on its bottom surface as close to the centre as possible. The PID controllers adjust the temperature of their associated plate by opening the relevant pulse valve, allowing liquid N<sub>2</sub> from a pressurised dewar to flow through the plate. Both Eurotherm devices are controlled

remotely by a PC via RS485 communication ports. The PC uses software written in Delphi by Trevor Ingham (Department of Chemistry, University of Leeds) which allows control of the rate at which cooling takes place and also logs temperature data from the controllers.

The top and bottom plates also both incorporate custom made 300 W silicone heating mats (Holroyd, UK), which are controlled using a separate pair of CAL 3300 temperature controllers (CAL Controls, UK). The mats allow rapid heating of the plates when required.

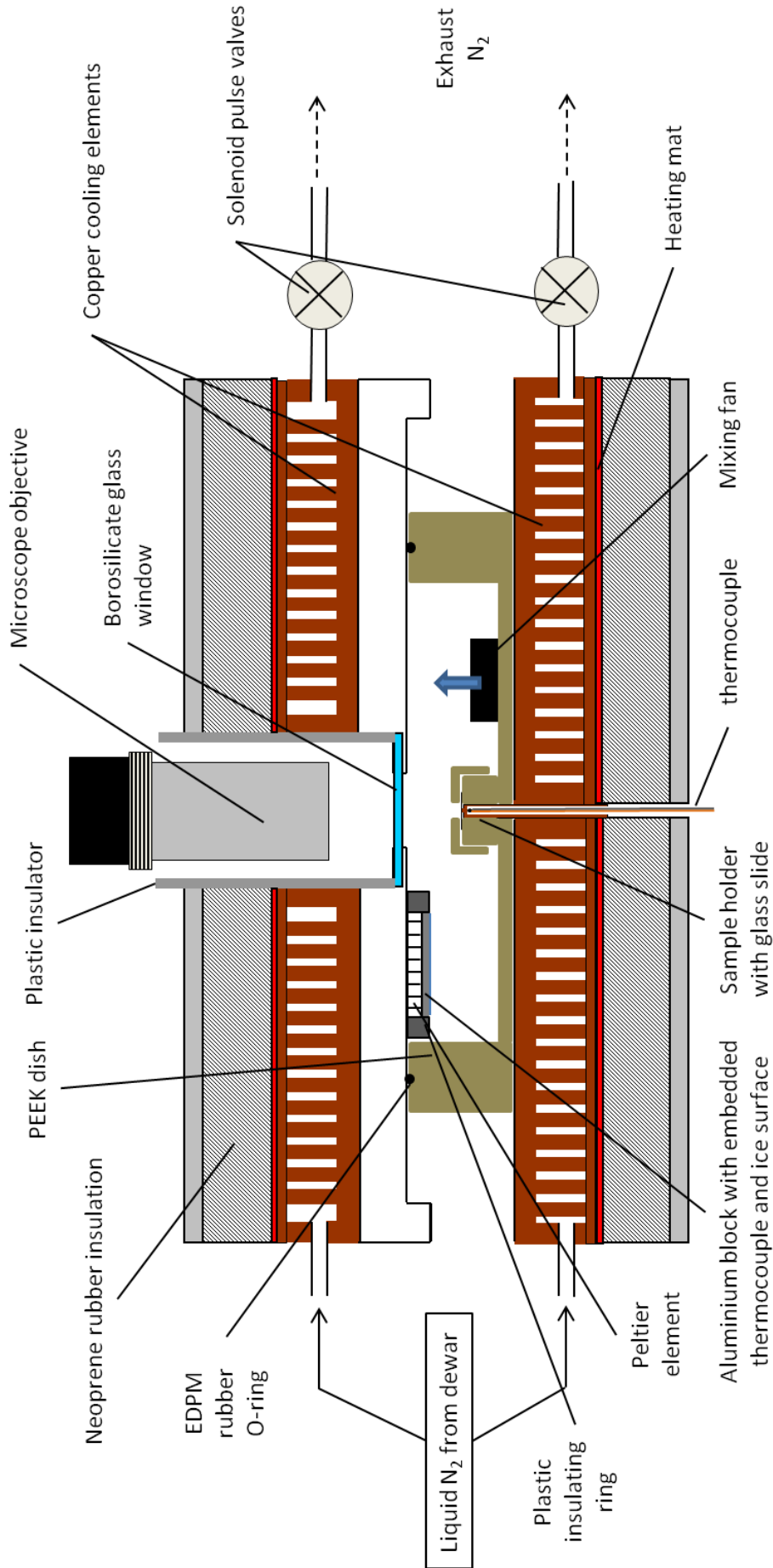


**Figure 3.3** Cross sectional diagram of the deposition mode chamber showing the position of the temperature controlled ice surface and sample holder. The chamber's associated temperatures controllers, thermometer, microscope and microscope stand have been omitted for clarity.



### 3.3.3 Temperature controlled ice surface

In order to generate known partial pressures of water vapour inside the chamber there is a 30 mm square temperature controlled ice surface. Ice is deposited onto a 30 x 30 x 3 mm layer of aluminium which sits upon the ‘cold’ side of a single-stage, 38 W, 30 mm square Peltier element (RS Components). The edges of the Peltier element and aluminium are surrounded by a tight fitting plastic insulating ring, which prevents ice forming anywhere other than the main face of the aluminium. This assembly sits inside the chamber, to one side of the viewing port. It is attached to the stainless steel surface of the top plate using a thin layer of thermally conductive paste applied to the ‘hot’ side of the Peltier element. The aluminium layer includes a ~15 mm deep port into which a narrow gauge, T-type thermocouple with an exposed junction is placed. The temperature from this thermocouple is read using a Hart Scientific HS1560 precision thermometer (supplied by Fluke). As aluminium is thermally conductive, the temperature measured from this thermocouple is used as the ice film temperatures when calculating the in chamber humidity during experiments.

The power cables that supply the Peltier element and the wire from the thermocouple embedded in the aluminium exit the chamber via a hole drilled into the stainless steel layer of the top plate. The hole is sealed using Apiezon sealing compound.

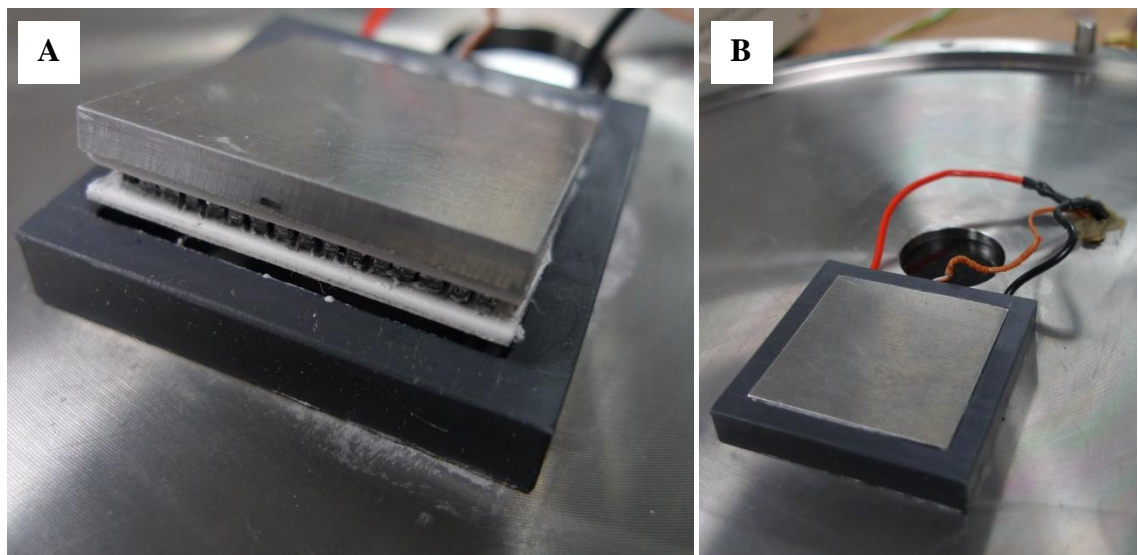


**Figure 3.4** A) The aluminium surface the ice layer is deposited upon sits on top of a Peltier element and both are surrounded by an insulating plastic ring. B) This whole assembly is attached to the surface of the top plate with a thin layer of thermal paste.

The temperature of the ice film is controlled using a combination of the top plate's Eurotherm PID controller and by adjusting the voltage applied to the Peltier element using a bench top variable power supply. When a current is applied to the Peltier device, one side of the element becomes hot and the other side cools down, creating a temperature difference between the top plate and the cold side of the Peltier. By adjusting the voltage, the difference in temperature between the cold side of the Peltier and the top plate can be increased or decreased. During experiments, the temperature difference was always kept  $> 10$  K, ensuring that the ice film is colder than the surface of the plate, therefore preventing ice growth elsewhere.

### 3.3.4 Sample holder

At the centre of the PEEK dish there is a 4 mm hole into which slots the sample holding assembly. This consists of a hollow copper rod, 4 mm diameter, which is open at one end (for inserting temperature probes) and steps down to a 1 mm diameter flat tip at the other (Figure 3.5). The tip is put in contact with the underside of a silanised hydrophobic glass coverslip upon which a sample can be placed. In order to ensure a positive contact between the tip and the underside of the slide, there is a threaded PEEK collar which sits so that the end of the tip extends just beyond it. When a coverslip is placed across the collar, so that the tip is in contact with its centre point, a threaded PEEK cover with a central hole can be screwed down over it. As the tip of the rod is slightly higher than the PEEK collar, the glass coverslip is put under small amount of tension, which holds it against the tip of the rod. To ensure a good thermal contact, prior to putting the coverslip on a very thin layer of thermal paste can be applied to the rod tip. Once assembled the copper rod is inserted into a hole in the centre of the PEEK chamber (Figure 3.2), which lines up with a second hole in the bottom copper cooling plate (Figure 3.3). The rod is engineered to fit snugly and be in good thermal contact with the cooling plate, minimising any lag when the temperature of the plate changes.

The PEEK collar insulates the sides of the copper rod and the glass slide acts as a barrier to water vapour at the top. As discussed in Section 3.1, the sample has to be the coldest available point in the chamber in order to prevent ice nucleating somewhere else and reducing the available water vapour. The coldest point inside this chamber is the area of glass which is in contact with the copper rod. As the glass is silanised (its surface  $-OH$  groups have been replaced with hydrophobic silane groups) it does not

efficiently nucleate ice (for a characterisation of the IN ability of the hydrophobic glass see Chapter 7)

As the bottom cooling element is in direct thermal contact with the sample that is being investigated, the temperature of the sample is controlled using the bottom plate's Eurotherm PID controller. The temperature of the sample is measured separately using the HS1560 precision thermometer connected to an exposed junction T-type thermocouple, which is pushed to the end of the hollow copper sample rod until it is in direct physical contact with the copper at the end of the rod.

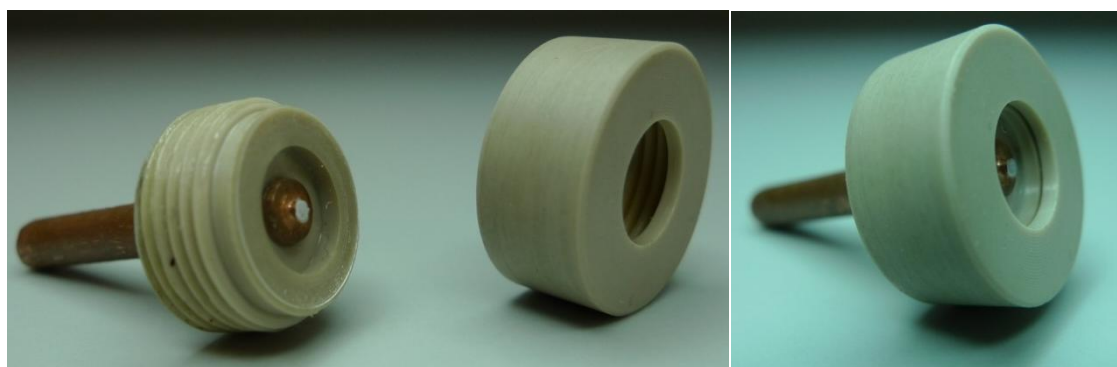


**Figure 3.5** The sample holder is designed to ensure a good thermal contact between the end of the copper rod and the underside of the glass coverslip the sample is deposited onto.

### 3.3.5 Sample microscopy

Samples on the hydrophobic glass coverslip are observed using a modular microscope which consists of a long (33 mm) working range 10x objective (Optem MPlan, 10122) mounted on a dual focus module (Qioptiq, 299084-310), an internal focus module (Best Scientific, BS29-95-91-310), a 7:1 zoom lens (Optem 70XL, 391940), a coaxial illumination module with input for a fibre optic cable (Optem) and a 1.5x mini fixed tube with a camera mount (Optem 299028). The microscope is mounted on a 50 mm vertical translation stage (LT1, Thorlabs) which allows the focus to be adjusted. The tip of the copper rod that is in contact with the glass coverslip has a diameter of 1 mm. The field of view of the microscope is large enough that the whole of the tip can be seen, ensuring that there are no areas where ice could nucleate without being observed. The sample is illuminated by reflected light that is directed through the microscope optics from a light source (Optem VSI 220) via an optical fibre. The light source is fitted with an infra-red filter, preventing any sample heating. The microscope is fitted with a Microsoft LifeCam USB web camera, which has had its focusing lenses removed,

exposing its CCD chip. The webcam modification was based on instructions published by Gary Honis at <http://ghonis2.ho8.com/lifecam/lifecam1.html>.

### 3.3.6 LabView control and logging software

The HS1560 thermometer and microscope USB camera are both controlled via a program written specifically for the DMC using the LabView graphical programming environment. The LabView program switches the thermometer between measurements from the thermocouple in the sample holder and the thermocouple in the aluminium upon which the ice film is deposited, saving the data in an ASCII file. For every pair of measurements from the HS1560 a single frame is captured from the USB camera and saved to an uncompressed .AVI file. It takes ~3 s for the HS1560 to measure from each temperature channel and less than one second to capture a video frame, resulting in up to a 6 s offset between the temperature measurements associated with each frame. This delay results in a negligible temperature offset at the rates of cooling used in the experiments described in this thesis (See Section 3.3.7 for details).

Using Equation 3.1, the program also calculates the  $RH_i$  that the sample is exposed to based on the last measured ice film and sample temperatures. When performing experiments, the measured temperatures and the calculated  $RH_i$  are displayed in a strip chart format along with the last captured video frame (Figure 3.6). A block diagram of the LabView program has also been included (Figure 3.7)

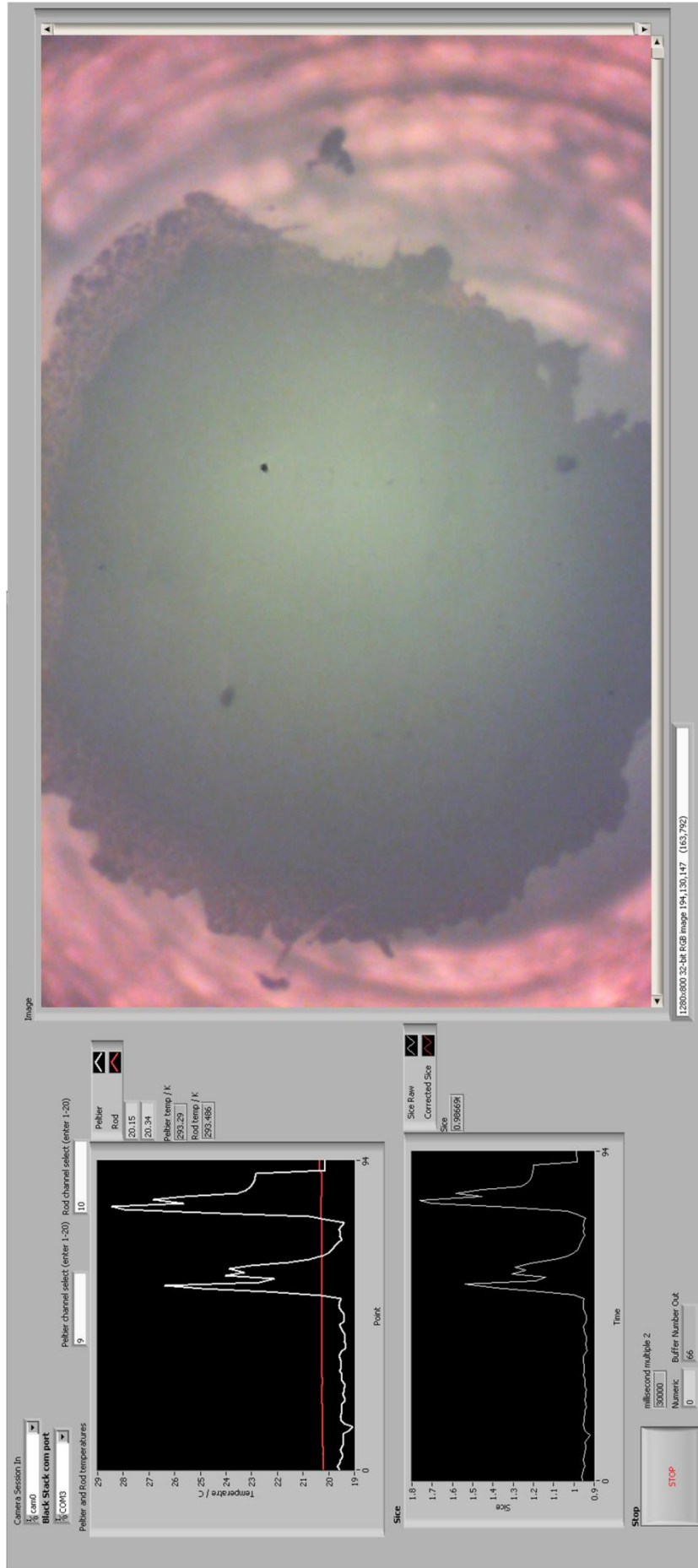


**Figure 3.6** A screen shot from the LabView program written to display and record images and temperatures from the chamber. It works in conjunction with a USB camera connected to the microscope and a HSI560 thermometer connected via an RS232 serial port. The program also continuously calculates and displays the humidity using the measured temperatures and Equation 3.1.



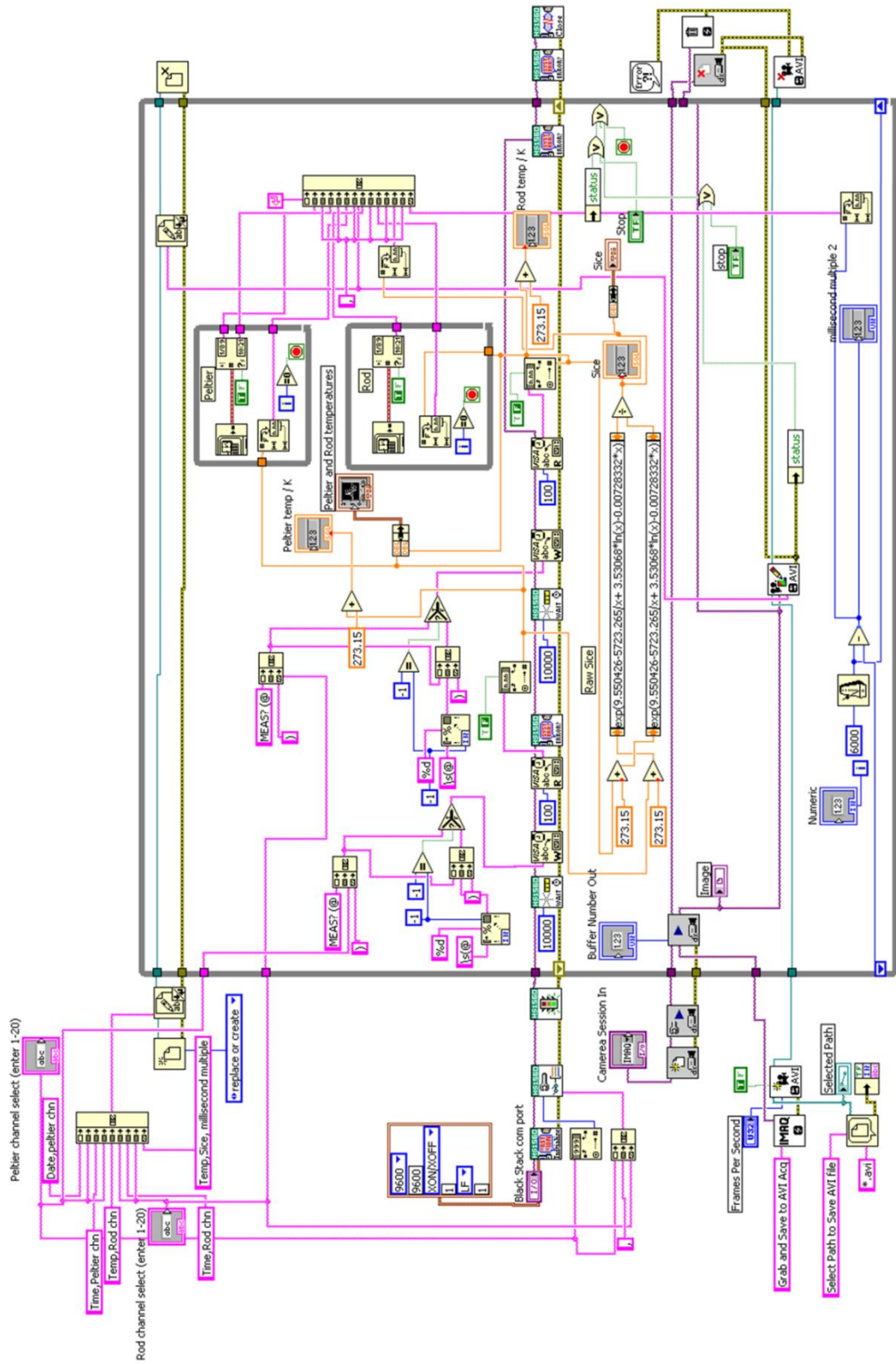


Figure 3.7 The LabView block diagram for the program written for use with the chamber during experiments (see description in text).

### 3.3.7 Uncertainty in temperature measurements

During experiments, the temperature of the ice film is held constant and the temperature of the sample is changed at a rate of  $0.1 \text{ K min}^{-1}$ . Allowing for the maximum 6 second offset between the measurement of the sample temperature and the capture of the associated frame of video, there is a maximum time related offset of 0.01 K between the temperature measured by the HS1560 and the temperature of the sample. This is negligible when compared to the quoted uncertainty of the HS1560 when taking measurements from thermocouples, which is  $\pm 0.5 \text{ K}$ .

Due to their positioning, there is a slight separation between the thermocouples and the ice film/sample. This results in a systematic offset between the temperatures which the thermocouples measure, and the actual temperatures of the sample and the ice film. In both cases the thermocouples are located nearer the source of cooling than either the sample or the ice film. This results in the thermocouples being consistently colder than the sample and the ice film.

The effect of the temperature offsets on the difference between the calculated  $RH_i$  and the humidity/temperature experienced by the sample was found to be dependent upon the type and positioning of the sample thermocouple. This offset was quantified using ice sublimation measurements which are detailed in Chapter 7.

## 3.4 DMC experimental methodology

### 3.4.1 Materials

Ammonium sulphate (99.999%, Puratronic, Alfa Aesar) crystals were used in the characterisation of the chamber humidity and the ice nucleation properties of a natural kaolinite clay dust (KGa-1b, clay minerals society, 96% kaolinite, major impurities anatase, crandallite, mica, illite (Costanzo and Guggenheim, 2001)) were investigated (see Chapter 7).

The surface area of KGa-1b has been well quantified in a number of studies using the Brunauer-Emmett-Teller (BET) gas adsorption method (Dogan et al., 2006; Jaynes et al., 2005; Thompson et al., 1999; Bereznitski et al., 1998; Foster et al., 1998), ethylene glycol monoethyl ether adsorption (Jaynes et al., 2005) and atomic force

microscopy (Bickmore et al., 2002). The mean average of the surface areas found in these studies is  $11.8 \pm 0.8 \text{ m}^2 \text{ g}^{-1}$  (Murray et al., 2011).

### **3.4.2 Slide preparation**

Siliconised hydrophobic coverslips (12 mm diameter, 0.02 mm thick; Hampton Research) were first immersed in chloroform and sonicated in a sonic bath then rinsed in methanol followed by 18.5 M $\Omega$  cm water and allowed to dry before being scoured using a dry ice cleaning gun (SnoGun™ II, Va-Tran Systems).

### **3.4.3 Depositing samples for investigation**

#### **3.4.3.1 Ammonium sulphate**

Finely ground ammonium sulphate was sprinkled onto the centre of a slide that had been fitted into the sample holder and any excess was gently blown off using a stream of zero grade N<sub>2</sub> gas (BOC).

#### **3.4.3.2 Kaolinite (KGa-1b)**

It was necessary to employ more quantitative methods of deposition for kaolinite mineral dust as the available surface area of dust may impact its efficiency as an ice nucleus. Two similar techniques were used using suspensions of KGa-1b in 18.5 M $\Omega$  water with known weight percentages of clay; these are described below.

#### **3.4.3.3 Nebulisation**

Suspensions were nebulised using a homemade nebuliser and humidified chamber. The sample holder, equipped with a freshly cleaned hydrophobic slide, was placed into the mouth of the chamber before activating the nebuliser, which creates a mist of suspension droplets which settled onto the glass slide. In order to prevent the concentration of clay in the mist droplets changing before they settle on the slide, the chamber humidity was maintained at water saturation using a flow of humidified gas from a bubbler kept at the same temperature as the chamber. After ~2 minutes the nebuliser was switched off. The size of the deposited droplets was then recorded using a microscope and attached camera whilst the humidity was maintained at water saturation (the droplets evaporate rapidly at ambient humidity). When calculating their volume, droplets were assumed to be spherical except for the point of contact with the surface. To account for this reduction in spherical volume, a correction was applied based on a 100° contact angle between the droplets and the hydrophobic glass (Broadley et al.,



2012). The mass of clay in the droplets was calculated based on the droplets' corrected volumes and the weight percent of the nebulised suspension. Given the surface area of KGa-1b per gram (Murray et al., 2011) and the mass of clay on the slide, the total surface area of particles under investigation was calculated. The humidified flow was stopped, causing water from the droplets to evaporate. The sample holder and slide were then covered to prevent contamination and transferred to the chamber.

#### 3.4.3.4 Single droplet evaporation

A ~1 mm diameter single droplet of KGa-1b suspension was placed onto the centre of the hydrophobic slide using a micro-syringe. This process was recorded using a microscope and camera so that the diameter of the deposited droplet was known allowing the surface area of clay on the slide to be calculated (See 3.4.3.3). Again, the sample holder and slide were then covered and transferred to the waiting chamber.

Depositing particles using the different techniques had a significant effect on the final distribution of particles on the slide. Nebulising gave a distribution of discreet aggregates of particles, that resulted from the evaporation of many separate droplets (Figure 3.8a). When only a single, larger droplet was deposited and allowed to evaporate, the result was clay particles that covered an area larger than that found for the nebulised particles (Figure 3.8). In both cases the amount of residue that remained depended upon the initial concentration of the clay suspension.

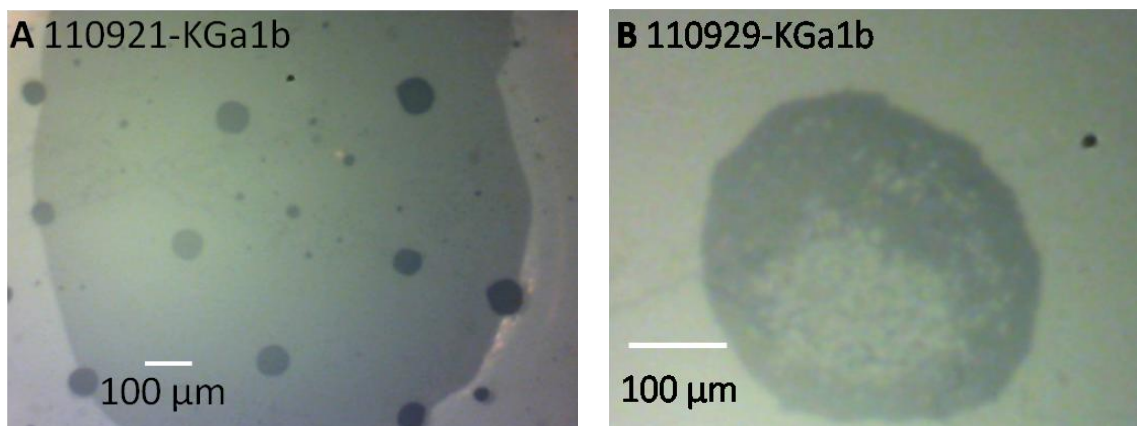


**Figure 3.8** A comparison of the results of depositing KGa-1b mineral dust using a nebuliser (panel a) and by evaporating a single droplet of suspended clay (panel b)

### **3.4.4 Depositing the ice film**

Just prior to the chamber being closed, an ice film was deposited on the aluminium face of the Peltier assembly. This was achieved by cooling the Peltier to  $\sim 260$  K and directing a flow of high purity nitrogen gas that had been bubbled through 18.5 M $\Omega$  cm water at the cooled surface. This caused a very thin layer of ice (no more than 0.1 mm) to rapidly build up on the aluminium. Throughout the process the top plate temperature was kept above the ambient dew point to avoid liquid water from the humidified flow condensing on to its surface. Once a suitable ice layer had been deposited, the chamber was closed quickly and sealed tightly using the machine bolts to prevent any significant increase of the thickness of the ice film from ambient water vapour depositing. The microscope was then positioned in the viewing port and the particles observed. The chamber at this stage of the experiment is pictured in Figure 3.9.

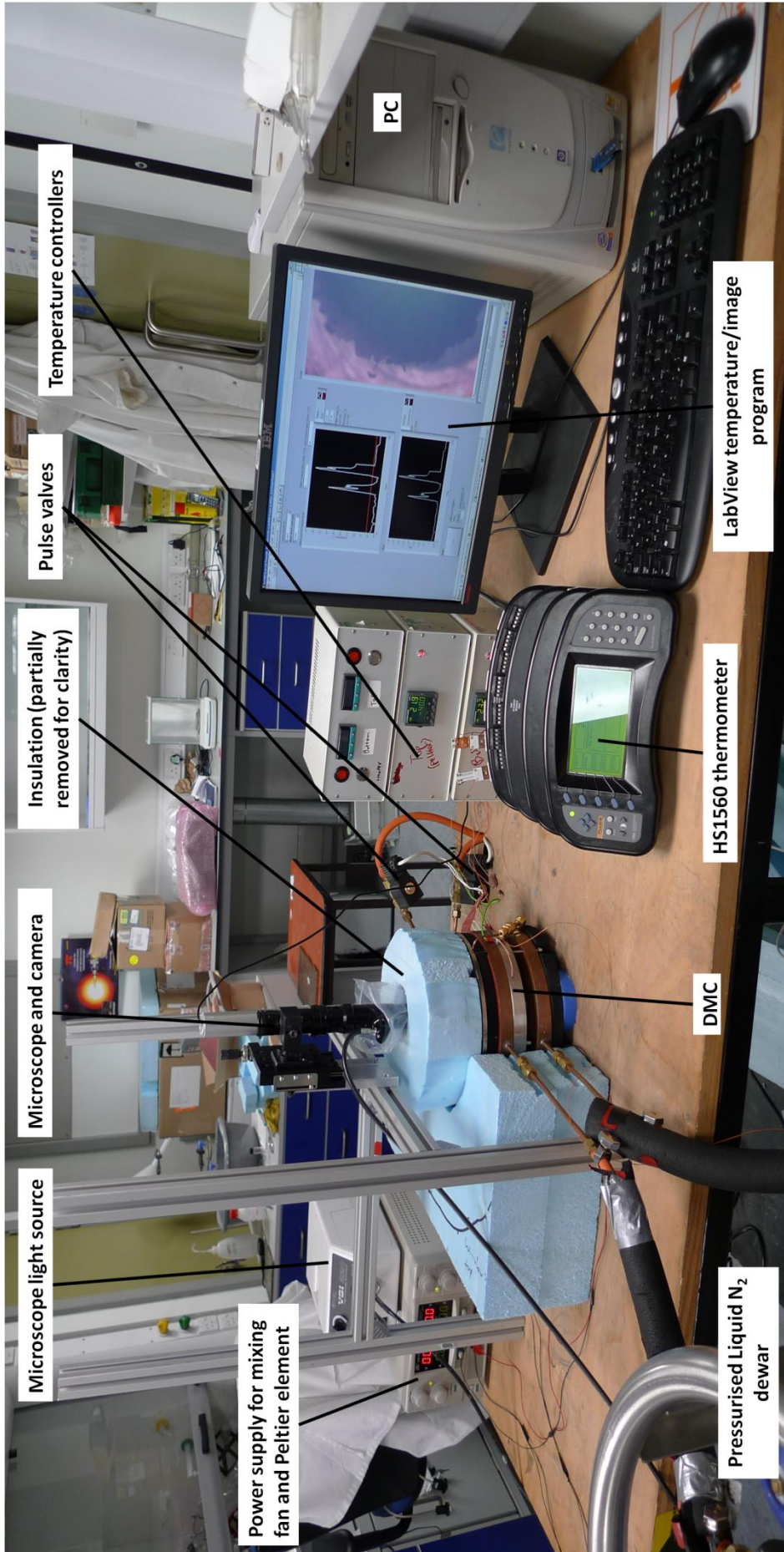


Figure 3.9 The DMC and associated experimental apparatus.

### 3.4.5 Equilibration and the first experimental run

Prior to performing the first experimental run, the ice film was cooled to the desired temperature and the chamber was left to equilibrate with the mixing fan running for at least 30 minutes. To prevent the exposure of the sample under investigation to any supersaturation with respect to ice during this time, the temperature of the sample was kept at least 10 K above that of the ice film.

After equilibration, the sample was cooled to and held at a temperature close to, but still above that of the ice film, resulting in the sample being exposed to a calculated humidity of  $\sim 90\%$  RH<sub>i</sub>. After allowing the temperature of the ice surface to stabilise for  $\sim 30$  minutes, the sample was cooled at a rate of  $0.1 \text{ K min}^{-1}$ , causing the sample to experience increasing humidity, at a rate of about  $1\% \text{ min}^{-1}$  (at  $\sim 240 \text{ K}$ ). Once ice has nucleated, the sample was warmed back up at a rate of  $0.1 \text{ K min}^{-1}$ , allowing the sublimation of the ice to be observed. Once all ice has sublimated the process can be repeated at the same temperature or the ice film can be raised or lowered in temperature before performing another run.

The characterisation of the chamber and ice nucleation results using from an investigation using natural kaolinite dust are presented in Chapter 7.

## Chapter 4: ICE01 campaign: Heterogeneous ice nucleation by glassy citric acid aerosol

Aerosol particles sampled in the TTL and other areas of the upper troposphere contain a large fraction of oxygenated organic species (Froyd et al., 2009b; Froyd et al., 2010). Particles containing oxygenated organic material may exist in a glassy state at temperatures relevant to the TTL (Zobrist et al., 2008; Murray, 2008b; Koop et al., 2011). This chapter presents experiments performed during the ICE01 campaign performed at the AIDA (Aerosol Interactions and Dynamics in the Atmosphere) chamber at the Karlsruhe Institute of Technology, Germany. The AIDA chamber is a large, highly instrumented cloud simulation chamber that is capable of accessing temperatures relevant to the TTL. During ICE01 the behaviour of glassy aqueous citric acid aerosol when exposed to cirrus forming conditions was examined. Evidence for heterogeneous ice nucleation by glassy citric acid aerosol particles at TTL temperatures is presented along with modelling data which shows that heterogeneous ice nucleation by glassy aerosol could be related to observed TTL cirrus properties including high in-cloud supersaturations.

*Experimental and modelling data from this campaign were published as a letter in Nature Geoscience (Murray, B. J., Wilson, T. W., Dobbie, S., Cui, Z. Q., Al-Jumur, S., Mohler, O., Schnaiter, M., Wagner, R., Benz, S., Niemand, M., Saathoff, H., Ebert, V., Wagner, S., and Karcher, B.: Heterogeneous nucleation of ice particles on glassy aerosols under cirrus conditions, Nature Geoscience, 3, 233-237, 10.1038/ngeo817, 2010). TWW assisted with experiments at the AIDA chamber, analysed the data provided by the AIDA team and processed, analysed and helped interpret modelling data provided by SD. BJM oversaw the study, sought financial support for it and wrote the manuscript. SD led the modelling aspects in collaboration with SMRKA and BK. OM led the AIDA team, which included MS, RW, SB, MN and HS, who operated the AIDA chamber and associated equipment. BJM and ZC assisted with the AIDA experiments. VE and SW processed the AIDA water vapour data prior to analysis.*

## 4.1 Citric acid as a proxy oxygenated organic material in the atmosphere

Organic material makes up as much as 70% of the mass of fine aerosol found in the troposphere (McFiggans et al., 2005). This material is often highly oxidised and C=O, OH and COOH groups are ubiquitous (Graber and Rudich, 2006; Saxena and Hildemann, 1996). Highly concentrated aqueous solutions of oxygenated organic species can become semi-solid or glassy at temperatures relevant to cirrus cloud formation (Murray, 2008b; Zobrist et al., 2008; Mikhailov et al., 2009; Koop et al., 2011). The aim of the ICE01 experimental campaign was to investigate whether aerosol in the glassy state affected the formation of ice particles under cirrus conditions. Citric acid (2-hydroxypropane-1,2,3-tricarboxylic acid) was chosen for investigation due to its similar functionality to compounds found in atmospheric aerosol and because its glass forming properties when in an emulsion have been previously studied (Murray, 2008b).

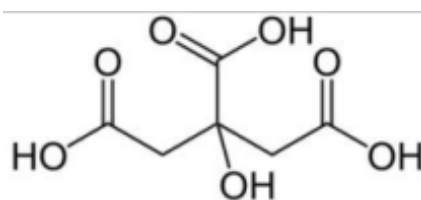


**Figure 4.1** Citric acid (2-hydroxypropane-1,2,3-tricarboxylic acid) was used as a proxy for atmospheric oxygenated organic material.

### 4.1.1 The citric acid/water aerosol phase diagram

The phase diagram of aqueous citric acid solution aerosol is displayed in terms of the citric acid weight percent of the aerosol in Figure 4.2a. The phase diagram shows what phase state aqueous citric acid aerosol would be expected to exist in at a range of temperatures and solution concentrations. It includes the threshold at which ice nucleates homogeneously in citric acid droplets (dashed red line) (Murray, 2008b) and the threshold at which ice and liquid water are in equilibrium (solid black line) (Koop et al., 2000; Murray, 2008b). Between these thresholds the liquid solution aerosol exists in a metastable supercooled state. The  $RH_g$  threshold, based on a fit by Maltini et al. (1997), is marked as a cyan dot-dash line. The citric acid solution aerosol phase diagram is also plotted as a function of relative humidity with respect to liquid water ( $RH_{liq}$ )

(Figure 4.2b). The chamber  $RH_{liq}/100$  is equal to the aerosol water activity ( $a_w$ ) as long as the aerosol droplets are in equilibrium with their surroundings.

Idealised experimental trajectories from five expansions performed on the same aerosol at the AIDA chamber are shown as black arrows. In Figure 4.2a, expansions starting below  $T_g'$  (where the ice-liquid equilibrium threshold and the glass transition cross) are represented by dashed arrows. This is to highlight that the wt% of citric acid in the aerosol droplets is not known accurately as once the glass transition occurs, the aerosol cease to remain in equilibrium with the chamber humidity. When the glass transition is crossed during an expansion, the concentration of the aerosol remains uncertain as the rate of uptake of water and the resulting potential liquefaction of the aerosol may be delayed due to the slow diffusion of water in glasses (Zobrist et al., 2011; Tong et al., 2011; Mikhailov et al., 2009; Koop et al., 2011). In Figure 4.2b the phase diagram is shown in terms of the chamber relative humidity with respect to liquid water ( $RH_{liq}$ ). The arrows are not dashed as they show the trajectory of the chamber humidity during expansions rather than the aerosol composition. To test the effects of the glass transition on ice nucleation, expansion experiments were performed at temperatures above, below and very close to the aerosol droplets' glass transition threshold.

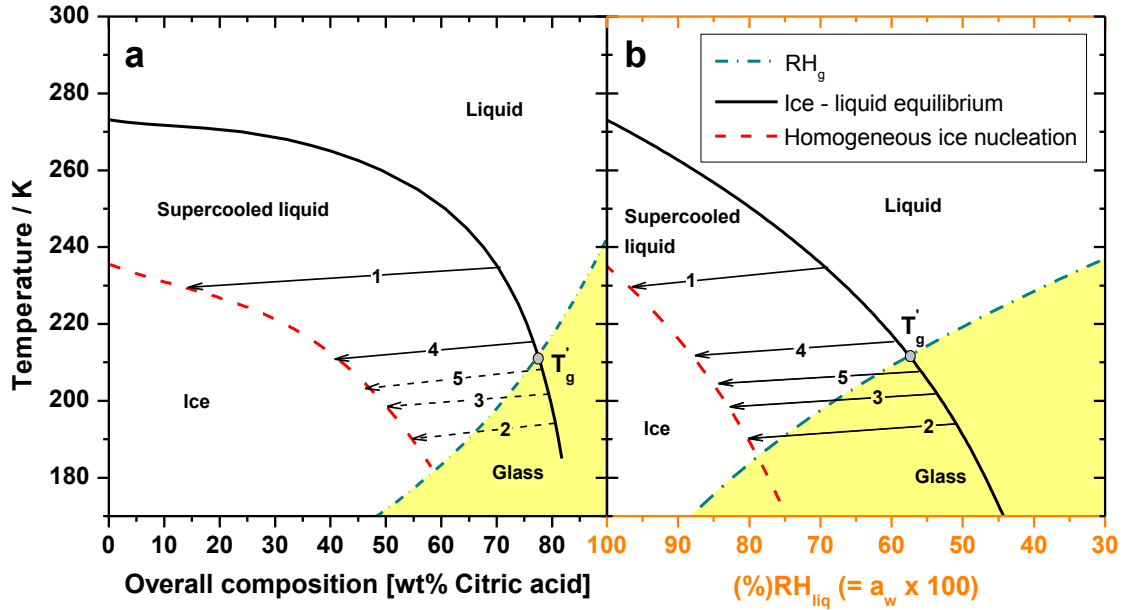


**Figure 4.2** a) Phase diagram for aqueous citric acid aerosol particle as a function of temperature and citric acid wt%, with idealised experimental trajectories for expansions 1 – 5 shown as black arrows. The dashed arrows represent trajectories where the concentration of the aerosol is uncertain due to expansions starting below the glass transition ( $RH_g$ ) (cyan dot dash line). Also shown are the homogeneous ice nucleation threshold based on data from Murray et al. (2008b) and the ice liquid equilibrium line (Koop et al., 2000). b) shows the phase diagram as a function of  $RH_{liq}$ . Above  $RH_g$  the aerosol concentration was in equilibrium with the chamber humidity, therefore  $a_w = RH_{liq}/100$ . The ice liquid equilibrium threshold is shown as a solid black line and the homogeneous freezing threshold (Koop et al., 2000) is shown as a dashed red line.

As discussed in Section 2.4, expansion experiments actually start at humidities just to the right of the ice-liquid equilibrium line due to the chamber  $RH_i$  at equilibrium being 90 – 95%.

## 4.2 Results and discussion

Aerosol was injected into the chamber which was at a temperature of  $\sim 235$  K, well above  $T_g$ . Immediately after injection ceased the aerosol concentration measured by CPC3010 was  $\sim 17500$  cm<sup>-3</sup>. By the start of the first expansion experiment this had dropped due to sampling losses to  $\sim 16000$  cm<sup>-3</sup>. Aerosol was lost during each expansion during pumping and by the continued sampling of chamber air by optical particle counters and other instruments. By run 5, the aerosol concentration at the start of pumping was  $\sim 1000$  cm<sup>-3</sup>. It was necessary therefore to consider the total aerosol concentration when comparing  $N_{ice}$  data from different expansions. To allow more



direct comparison the fraction of aerosol that froze,  $f_{ice}$ , was also calculated ( $f_{ice} = N_{ice}/\text{total aerosol concentration}$ ). A typical size distribution for the citric acid aerosol used in expansion runs described in this chapter is shown Figure 4.3.

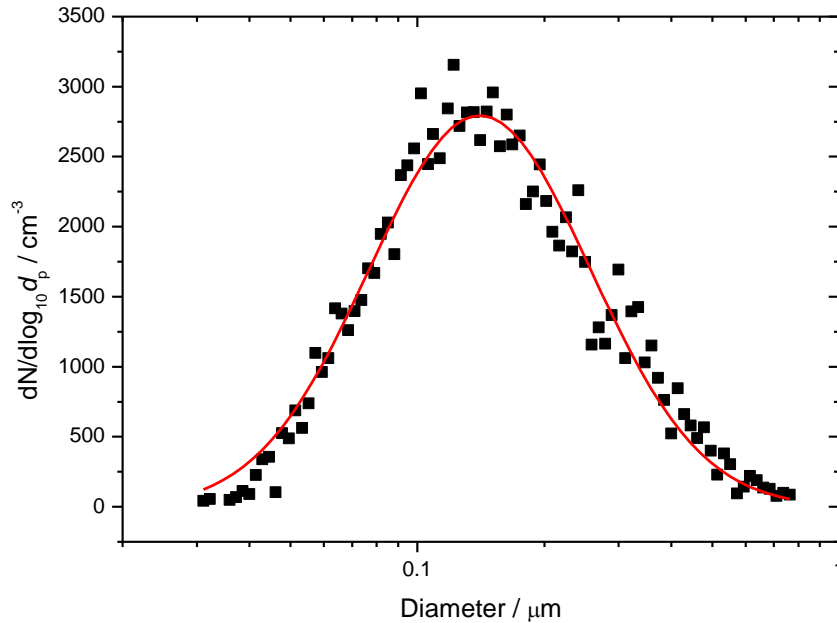


**Figure 4.3** SMPS size distribution for citric acid solution aerosol particles taken immediately prior to run 3. The red line is a log normal fit to the distribution.

The first expansion with the aerosol started at 235 K (well above  $T_g$ ) so the aerosol was expected to be in the liquid state. The onset of ice nucleation was observed as a change in the depolarisation ratio at  $136 \pm 5\%$  RH<sub>i</sub>. This is very close to the threshold at which other liquid solution droplets such as aqueous sulphuric acid aerosol froze homogeneously at the same temperature in previous experiments at the AIDA chamber (solid green line, Figure 4.4) (Möhler et al., 2003) which indicates that the aerosol was indeed in the liquid state. The homogeneous threshold observed at the AIDA is referred to from now on as the ‘AIDA homogeneous threshold’. It should be noted that there is a discrepancy between AIDA homogeneous threshold and the water activity derived homogeneous nucleation threshold’ (Koop et al., 2000). This results in AIDA observing homogeneous ice nucleation at lower humidities than the Koop line at temperatures above  $\sim 210$  K and at higher humidities below 210 K. This was behaviour was observed for all the aerosol compositions investigated during both the ICE01 and ICE02 (see Chapters 6 and 7) campaigns and has also been found for a variety of other liquid solution aerosol (Wagner et al., 2008; Wagner et al., 2011). In this thesis,

homogeneous nucleation by the aerosols tested is always compared against the existing AIDA data for sulphuric acid (Möhler et al., 2003). The issue is going to be addressed directly in a forthcoming paper by the AIDA team.

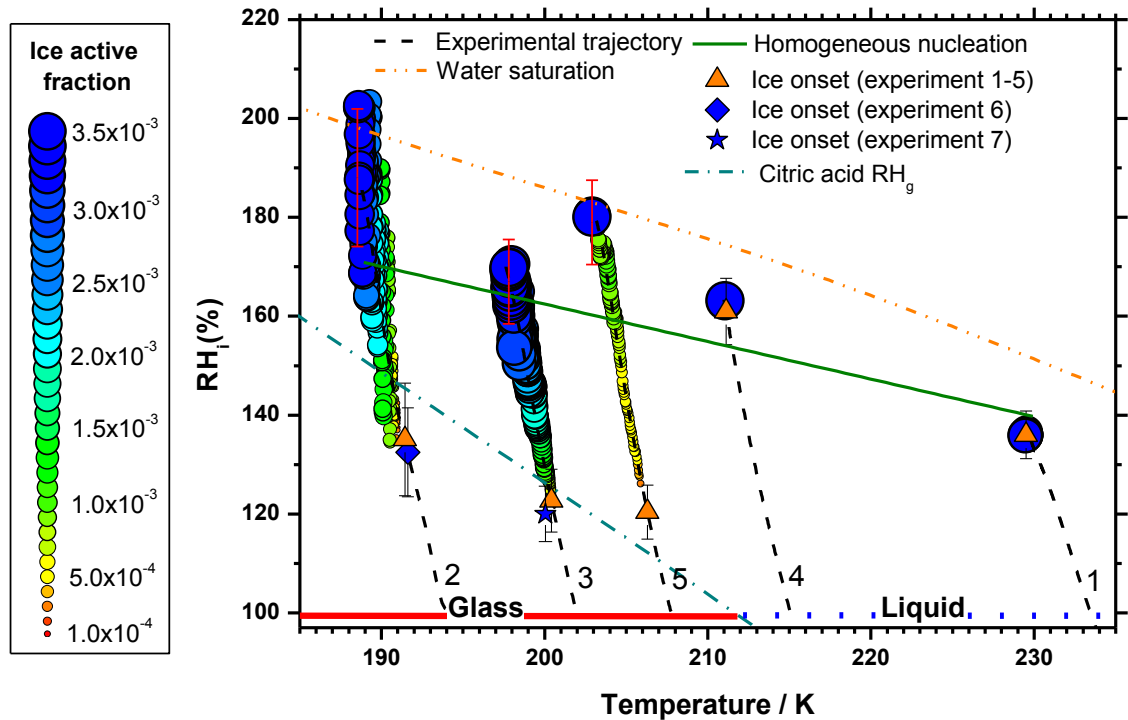


**Figure 4.4** A summary of the results of expansion experiments during ICE01. Fits to experimental  $RH_i$ /temperature trajectories are shown as dashed black lines. Depolarisation thresholds are indicated on each experimental trajectory by orange triangles. For clarity, only the depolarisation thresholds have been shown (blue diamond and star respectively) for experiments six and seven, which used different citric acid aerosols from that used in runs 1 – 5 (see Section 4.2.2). The size/colour of the overlaid bubbles shows the fraction of aerosol frozen ( $f_{ice}$ ) during the course of experiments 1- 5. The  $RH_g$  threshold for citric acid solution aerosol (Maltini et al., 1997; Murray, 2008b) is shown as a dot-dash cyan line.

After pumping finished, the nucleated ice particles were sublimated by refilling the chamber with dry, filtered synthetic air. The chamber was then cooled to 194 K, well below  $T_g'$  and deep into region of the phase diagram in which the aerosol was expected to be glassy. An expansion was performed in which ice nucleation was observed at  $135 \pm 11\%$   $RH_i$ , well below the AIDA homogeneous threshold at this temperature. Ice nucleation below the homogeneous threshold is consistent with the solid glassy aerosol acting as heterogeneous ice nuclei.

In the following runs the temperature was first increased slightly to 202 K, still well within the glassy region (run 3), and heterogeneous ice nucleation was once again observed with the onset of ice nucleation at  $123 \pm 6\%$  RH<sub>i</sub>. The aerosol was then warmed into the liquid part of the phase diagram, and an expansion started at  $\sim 215$  K (run 4). At this temperature the aerosol was observed to nucleate ice only at the predicted AIDA homogeneous freezing threshold, indicating that it had liquefied on crossing RH<sub>g</sub>. The temperature was then reduced again for run 5, to just below  $T_g'$  at 208 K; in this run a very small amount of heterogeneous ice nucleation was observed, with  $\sim 1$  cm<sup>-3</sup> ice particles nucleating from just above  $120 \pm 5\%$  RH<sub>i</sub>.

#### **4.2.1 Homogeneous ice nucleation in liquid aerosol vs. heterogeneous ice nucleation by glassy aerosol**

The differences in the behaviour of the aerosol in expansions which started in the liquid part of the phase diagram (run 4) compared to those in which the aerosol was in the glassy state (run 3) is shown in detail in Figure 4.5. Heterogeneous ice nucleation was found to consistently produce many fewer ice particles than was observed in runs where only homogeneous freezing was observed. In run 3, nucleation starting at  $123 \pm 6\%$  RH<sub>i</sub> only produced 5 cm<sup>-3</sup> ice particles prior to the chamber humidity reaching the AIDA homogeneous threshold. This is small compared to the  $\sim 70$  cm<sup>-3</sup> that nucleated homogeneously (at  $161 \pm 7\%$  RH<sub>i</sub>) in run 4. In homogeneous experiments, the result of rapid ice nucleation and growth was that the supersaturation of water vapour present in the chamber was swiftly quenched, sharply returning RH<sub>i</sub> to near ice saturation. The smaller number of ice particles nucleated heterogeneously by glassy aerosol could not quench supersaturations as efficiently.

The fraction of aerosol that nucleated ice ( $f_{ice}$ ) was calculated by dividing  $N_{ice}$  by the total aerosol concentration data from CPC3010 during each experiment. It is shown as the overlaid bubbles in Figure 4.4. After the onset of heterogeneous ice nucleation in runs 2, 3 and 5,  $f_{ice}$  increased much more gradually prior to homogeneous nucleation. The fraction of aerosol that nucleated ice heterogeneously was small, with  $f_{ice}$  reaching between 3 and  $3.5 \times 10^{-3}$  in runs 2 and 3. The fraction that froze heterogeneously in experiment 5 was even smaller, as many fewer ice particles were nucleated.

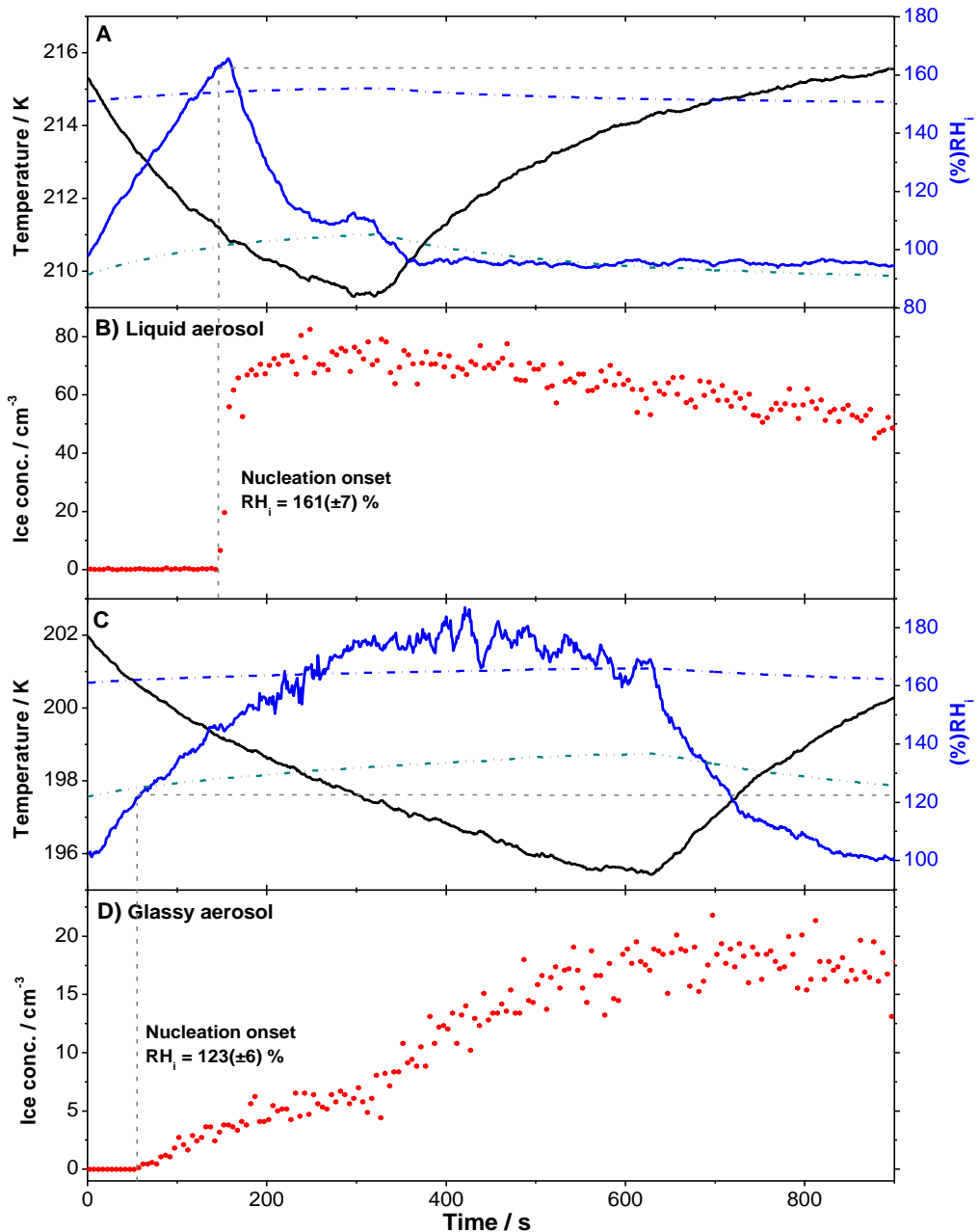


**Figure 4.5** Comparison of an expansion in which homogeneous nucleation occurred (Run 4, panels A and B) with an expansion in which the glassy citric acid aerosol nucleated ice heterogeneously (Run 3, Panels C and D). Panels A and C show the temperature and RH<sub>i</sub> (black and blue solid lines respectively), the RH<sub>g</sub> threshold (cyan dot-dot-dash line) and the homogeneous freezing threshold based on liquid H<sub>2</sub>SO<sub>4</sub> aerosol freezing at AIDA (Möhler et al., 2003) (blue dot-dash line). Panels B and D show  $N_{ice}$  measured using the WELAS 2 instrument. Grey dashed lines mark the onset of ice nucleation in each case, based on  $\delta$ .

In run 3, heterogeneous ice nucleation continued at humidities above RH<sub>g</sub> (cyan dot-dot-dash line in Figure 4.5). This was also observed in runs 2 and 5 (although in the latter case the ice concentration nucleated was very small). The continued nucleation of

ice above  $RH_g$  but below the AIDA homogeneous threshold suggests that the aerosol did not liquefy on crossing  $RH_g$ . This may be due to a delay in the uptake of water by the aerosol, which is consistent with the slow rate of diffusion observed in glassy sucrose droplets (Zobrist et al., 2011). Tong et al. (2011) show that the liquefaction was delayed by 10s – 100s of seconds in supermicron sucrose droplets at room temperature. Nucleation above  $RH_g$  may also be partly the result of uncertainty in the  $RH_g$  threshold, which could exist at a higher humidity.

There is further evidence of delayed water uptake by ultra viscous or glassy aerosol in run 4 where homogeneous ice nucleation occurred ~10%  $RH_i$  above the AIDA homogeneous threshold. This might be the result of slowed water uptake in highly viscous aerosol, delaying the dilution necessary for homogeneous freezing. Similarly in run 3, there was an increase in the rate of ice particle production after the chamber humidity exceeded the AIDA homogeneous threshold. However the increase was not as sudden as the homogeneous nucleation event in run 4. This may indicate that the aerosol was still highly viscous, preventing the equilibration of the aerosol with its surroundings and hence delaying homogeneous nucleation. There is also recent evidence that heterogeneous ice nucleation may occur after initial water uptake (Wang et al., 2012). This is discussed further in Chapter 5 as ice nucleation above  $RH_g$  was also observed in the ICE02 campaign in experiments that used glassy solution aerosol of different chemical compositions.

#### 4.2.2 Experiments using aerosol injected at temperatures below $T_g'$

The aerosol used in runs 1 – 5 was injected into the chamber above  $T_g'$ . Two runs (6 and 7) were performed in which the aerosol was injected below  $T_g'$ , at 194 and 202 K respectively. In both cases expansions were then started at the same temperature. Injecting the aerosol particles below  $T_g'$  subjected them to a significantly different equilibration process. The aerosol used for runs 1 – 5 was cooled in the chamber at a humidity of between 90 and 95%  $RH_i$ , causing the aerosol concentration to roughly follow the ice-liquid equilibrium line (solid blue line, Figure 4.2) until approaching  $T_g'$ , at which point the composition would have ceased to remain in equilibrium with the chamber humidity. The aerosol injected into the chamber at low temperatures would have cooled much more rapidly before hitting the glass transition. This would

potentially affect the concentration of the aerosol, as the rate at which cooling takes place impacts the temperature (and therefore water activity) at which the glass transition occurs. Despite this difference, the ice nucleation onsets for the aerosol injected directly were very similar to those for the aerosol injected above  $T_g'$  (Figure 4.4), as was the observed  $f_{ice}$ , indicating that changing the injection method did not affect the ice nucleation properties of the glassy aerosol.

### 4.2.3 Why do glassy aerosol particles act as ice nuclei?

The results in this chapter provide the first evidence that glassy aerosol particles are able to act as heterogeneous ice nuclei. The mode of ice nucleation occurring is consistent with the definition of deposition mode given by Vali as “*the formation of ice in a supersaturated (vapor) environment*” (Vali, 1985). It is reasonable to suspect that ice nucleation by the glassy aqueous citric acid aerosol is catalysed by water and solute molecules that are arranged in a manner that happens to provide a hydrogen bonding site that matches the crystal lattice of ice. These active sites would occur by chance and may be more or less common in glassy solution aerosol of different composition. To test whether ice nucleation is a general property of glassy aerosols and independent of their composition, a second campaign that used a variety of glassy aerosol compositions was undertaken, the results from which can be found in Chapter 5.

### 4.2.4 Could homogenous ice nucleation have enhanced the IN ability of the aerosol used during the ICE01 experiments?

In experiments performed during the ICE02 campaign the aerosols tested were found to become more efficient heterogeneous IN after having frozen homogeneously close to  $RH_g$ . This phenomenon is dubbed aerosol ‘pre-activation’ and is discussed in detail in Chapter 6. Precautions were taken in the ICE02 campaign to separate ‘normal’ heterogeneous ice nucleation from pre-activated heterogeneous ice nucleation. This was not the case in the first campaign, so it is necessary to re-evaluate the ICE01 data. In run 1, homogeneous nucleation was well away from the  $RH_g$  and in the following run early ice nucleation was not observed, indicating that no aerosol pre-activation occurred. In run 2, despite noise in the TDL humidity data, it is apparent that the AIDA homogeneous nucleation threshold at  $\sim 170\%$   $RH_i$  was reached. However, there does not appear to be any sudden increase in  $N_{ice}$  after the homogeneous threshold was hit. Instead the ice particle concentration continues to increase gradually, suggesting

continued heterogeneous nucleation. Had the aerosol become pre-activated, it would be expected that the ice onset humidity in run 3 would be much closer to ice saturation than is the case. The fraction of aerosol that froze was also consistent with run 2. It is reasonable therefore to assume that the nucleation observed in run 3 was heterogeneous nucleation by glassy aerosol, rather than nucleation by pre-activated aerosol.

Pre-activation might perhaps have been more likely for run 5, as it followed a run in which ice nucleated homogeneously much closer to the glass transition. Only a very small fraction of aerosol nucleated below the homogeneous threshold during this expansion ( $< 1 \text{ cm}^{-3}$ ). It is possible that this was the result of either pre-activation of a small fraction of the aerosol or heterogeneous ice nucleation on glassy aerosol. As the humidity at the onset of nucleation was similar to that found in run 3 it is more likely to be the result of heterogeneous nucleation.

#### **4.2.5 Evidence for ice nucleation by glassy aerosol in the TTL**

The experimental results presented in this chapter show that aqueous citric acid aerosol heterogeneously nucleates ice when in a glassy state at temperatures relevant to the TTL. Cirrus clouds in the TTL have very low ice particle concentrations, which is consistent with them nucleating via heterogeneous ice nucleation on a small fraction of the available aerosol (see Section 1.4.4.5.1). Analysis of the residues of ice crystals from TTL cirrus show that aerosol from which the ice particles nucleated also overwhelmingly consist of internally mixed sulphate and organic species with only a small amplification of the mineral dust fraction (see Figure 1.13).

The dominance of the sulphate organic fraction in the observed SVC ice residues might suggest that the SVC formed homogeneously, by the dilution and freezing of liquid sulphate-organic aerosol. This would not however explain the small ice particle concentrations found in SVC, which are more consistent with heterogeneous ice nucleation (Immler et al., 2008; Krämer et al., 2009; Gensch et al., 2008; Khvorostyanov et al., 2006; Spichtinger and Gierens, 2009; Spichtinger and Cziczo, 2010; Jensen et al., 2010; Ren and Mackenzie, 2005). A possible explanation therefore would be that the sulphate-organic aerosol exist in a glassy state and a small fraction are able to nucleate ice, like the citric acid aerosol tested during ICE01. This would result in low ice number density clouds formed from sulphate-organic aerosol, as observed by

Froyd et al. (2010). In section 4.3, the impact of heterogeneous ice nucleation by glassy aerosol on TTL cirrus cloud is assessed using results from a modelling study.

### **4.3 Modelling the impact of glassy aerosol on TTL cirrus**

In collaboration with Steven Dobbie, Bernd Kärcher, Benjamin Murray and Sardar M.R.K. Al-Jumur a one-dimensional cirrus cloud model was used to assess the effect of heterogeneous ice nucleation by glassy aerosol on cirrus cloud under TTL conditions. I produced a parameterisation for heterogeneous ice nucleation by glassy aerosol based on ICE01 data. I also processed and analysed the model output and contributed to its interpretation.

#### **4.3.1 Modelling methodology**

This study used Kärcher's Advanced Particle Simulation Code (APSCm-1D, (Kärcher, 2005), a one-dimensional column model with Lagrangian tracking of ice crystals in which aerosol microphysics can be explicitly described. The model was initialised using idealised temperature and pressure profiles (Figure 4.6, panels A and B). A layer of cirrus cloud was forced between 17.1 and 17.6 km using a  $RH_i$  step function (panel C). The temperatures, pressures and humidities used in the model were all within the range of measurements made from aircraft in the TTL (Jensen et al., 2008). Advection was simulated in the model by applying a uniform cooling rate to the whole column. A mass accommodation coefficient for water molecules onto ice of 0.5 was applied. Parameterisations for the saturation vapour pressures of liquid water and hexagonal ice were taken from Murphy and Koop (2005).



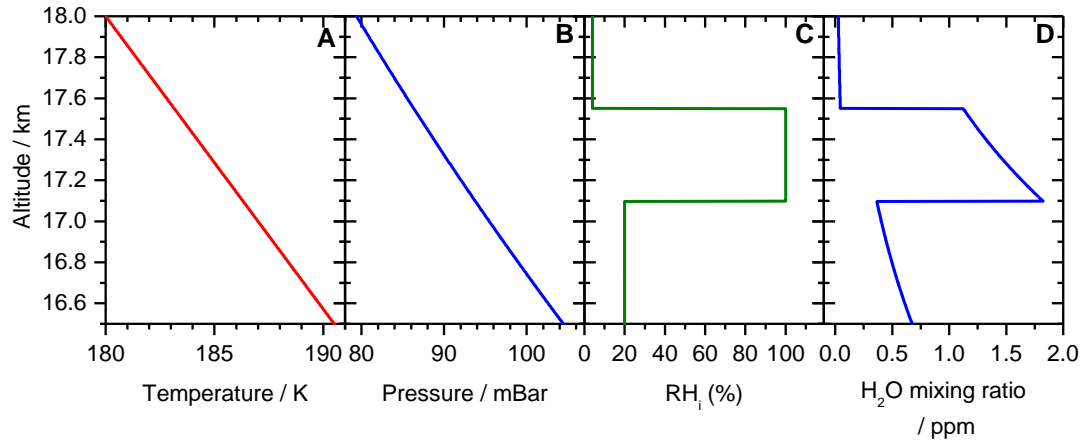


**Figure 4.6** Temperature, pressure,  $RH_i$  and  $H_2O$  mixing ratios used in the initialisation of APSCm-1-D. All values are within the range of TTL in situ measurements (Peter et al., 2003; Jensen et al., 2008).

An aerosol particle number concentration of  $100 \text{ cm}^{-3}$  was used, all with 100 nm diameters. Homogeneous freezing of the liquid aerosol was governed by the water activity freezing criteria for liquid solution droplets found by Koop et al., (2000), *i.e.* the liquid aerosol would freeze if the modelled humidity reached a defined, temperature dependent threshold. Heterogeneous ice nucleation by the glassy aerosol particles was based on a parameterisation of the fraction of glassy citric acid solution aerosol that nucleated ice in the ICE01 experimental campaign. A linear fit was used to describe  $f_{ice}$  as a function of  $RH_i$  from run 3, which started at  $\sim 202 \text{ K}$  (Figure 4.7). For most model runs a 1:1 ratio of glassy to liquid aerosol was used (*i.e.*  $50 \text{ cm}^{-3}$  glassy and  $50 \text{ cm}^{-3}$  liquid). During sensitivity tests (see below) the impact of reducing the fraction of glassy aerosol to 10% was tested. For comparison, runs were also performed in which all the aerosol particles were liquid.

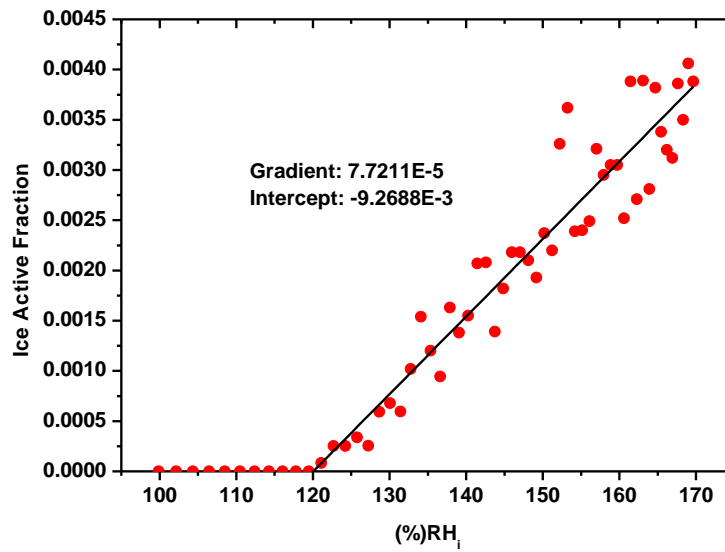


**Figure 4.7** The parameterisation of heterogeneous ice nucleation by glassy aerosol used in the cirrus modelling. It is a linear fit to  $f_{ice}$  as a function of  $RH_i$  from run 3. The fit has the equation  $f_{ice} = 7.7211 \times 10^{-5} RH_i(\%) - 9.2688 \times 10^{-3}$ . It is valid for  $RH_i$  from 121 to 170%. When  $RH_i < 121\%$ ,  $f_{ice} = 0$ .

### 4.3.2 Modelling results

The model output provided  $S_{ice}$  (the ice saturation ratio =  $RH_i/100$ ),  $N_{ice}$ , the mean ice particle effective radius ( $R$ ) and the ice water content (IWC) as a function of altitude and time. These outputs were plotted initially as colour maps on altitude/time axes (Figure 4.8).

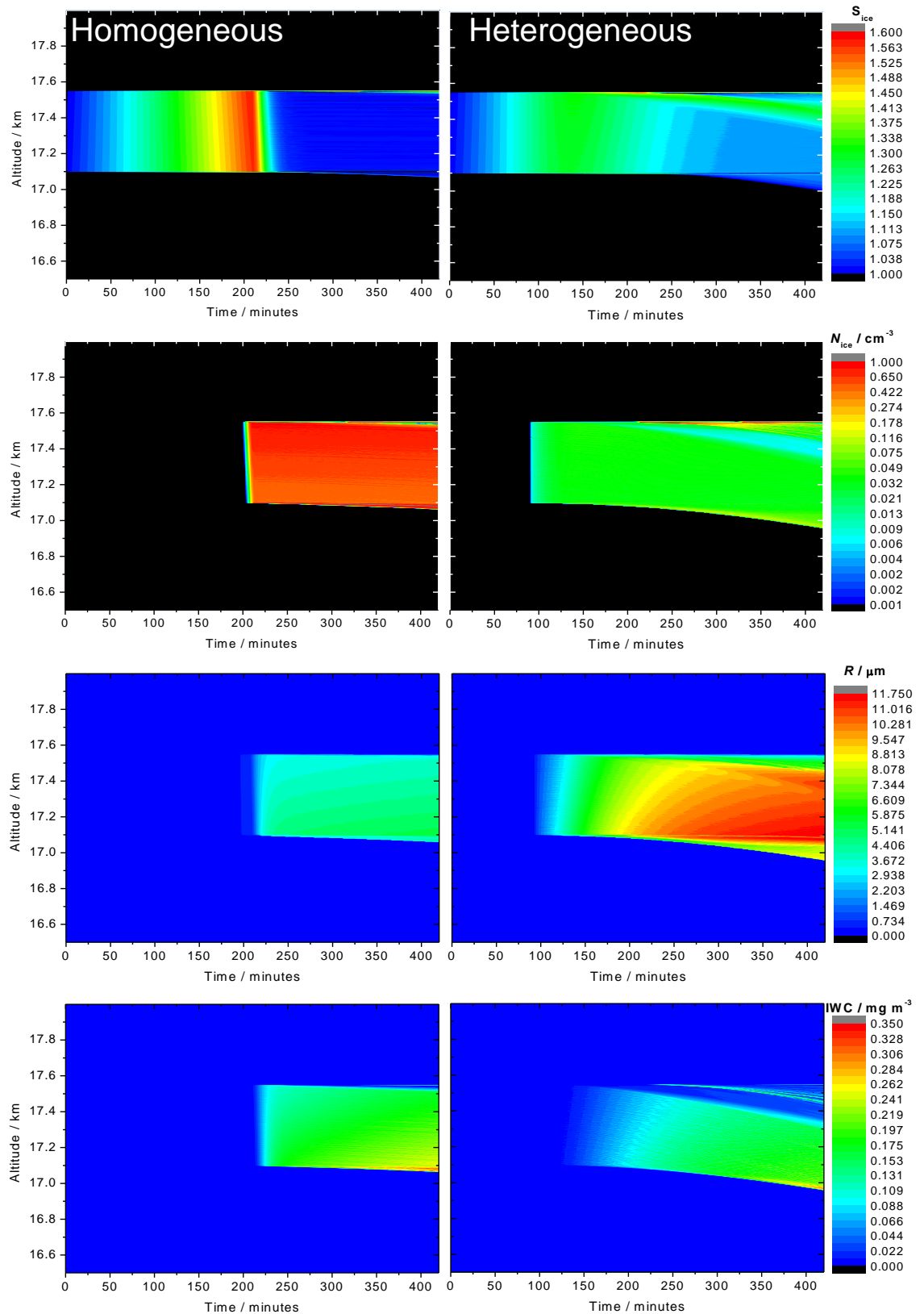


**Figure 4.8** Example model results for  $S_i$ ,  $N_{ice}$ ,  $R$  and IWC. Plots on the left are from runs using only liquid aerosol, right hand plots used a 50/50 mix of liquid and glassy aerosol. All runs used a cooling rate of  $0.76 \text{ K hr}^{-1}$ ,  $100 \text{ cm}^{-3}$  aerosol concentration and were initialised using the profiles in Figure 4.6

### 4.3.2.1 Heterogeneous vs. Homogeneous freezing

The effect of heterogeneous nucleation by glassy aerosol on the properties of cirrus cloud was tested by comparing the results of a run which used only liquid aerosol to a run that used a 50/50 mixture of glassy and liquid aerosol. Both runs were performed at a cooling rate of  $0.76 \text{ K hr}^{-1}$ . The model output from each run (Figure 4.14) shows that cirrus which formed from a mixture of liquid and glassy aerosol had significantly different microphysical properties to that which formed from only liquid aerosol. To make comparison between the model runs easier, the results were averaged for a 100 m layer between 17.25 and 17.35 km. This avoided having to consider the effect of the sedimentation of ice particles, which was clearly occurring in the heterogeneous experiment. The resulting averaged  $RH_i$ ,  $N_{ice}$ ,  $R$  and IWC profiles are shown as a function of time in Figure 4.9.

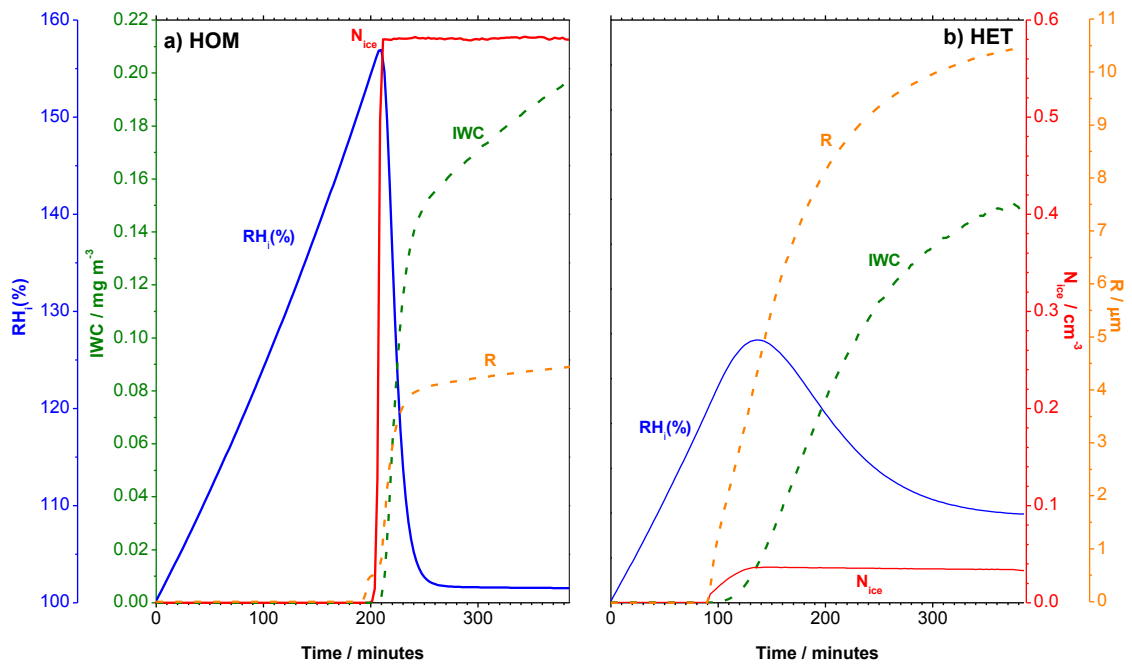


**Figure 4.9** A comparison of modelling results averaged between 17.25 and 17.35 km. Both runs were initialised using the profiles shown in Figure 4.6, used a cooling rate of  $0.76 \text{ K hr}^{-1}$  (equivalent to  $3 \text{ cm s}^{-1}$  updraft rate) and had a total aerosol number concentration of  $100 \text{ cm}^{-3}$ . Panel a) shows the results from a run in which only liquid aerosol were present. Panel b) shows a run in which 50% of the aerosol were liquid and 50% were in the glassy state.

In the liquid aerosol only case,  $RH_i$  reached just over 155%, hitting the homogeneous freezing threshold and allowing the rapid nucleation of many ice particles. An ice particle concentration of  $0.58 \text{ cm}^{-3}$  was reached in  $\sim 10$  s, and the humidity dropped almost immediately back to  $\sim 100\%$   $RH_i$  as water vapour was consumed by the growing ice particles. For the liquid and glassy aerosol run, heterogeneous ice particle production began at 121%  $RH_i$ , as a result of the parameterisation used. This led to the production of a smaller concentration of ice particles ( $0.035 \text{ cm}^{-3}$ ). There was enough uptake of water vapour to prevent the humidity rising above  $\sim 129\%$   $RH_i$ , despite the constant updraft. The small number of ice particles were able to grow to larger sizes from the available water vapour. The particles which nucleated heterogeneously had a mean effective radius ( $R$ ) of more than twice that of those that were nucleated homogeneously. This is significant because the size of ice particles in a cirrus cloud strongly affects its optical properties.

#### 4.3.2.2 Prolonged supersaturation

In all the model simulations  $RH_i$  did not return to 100%  $RH_i$  after ice nucleation. In the case of the homogeneous run shown in Figure 4.9, ice saturation was nearly reached with  $\sim 101\%$   $RH_i$  being reached within 1 hour. In the run including heterogeneous ice nucleation by glassy aerosol it took over 1 hour for  $RH_i$  to fall to 120% and 3.5 hours for it to come to a quasi-steady state of 110%. These quasi steady states are the result of the uptake of water by the ice particles being balanced by the cooling provided by the model's constant updraft. The higher steady state humidity in the heterogeneous run was due to there being approximately 3.4 times less surface area of ice available for water uptake (assuming spherical ice particles and based on  $R$  and  $N_{ice}$  values at 300 minutes).

Prolonged supersaturation in heterogeneously nucleated cloud could be a cause of the high observed in-cloud supersaturations in cold cirrus (Krämer et al., 2009; Peter et al., 2006) (see Section 0). The results presented in this chapter are consistent with those found in other modelling studies that used unspecified heterogeneous ice nuclei (Krämer et al., 2009; Gensch et al., 2008; Khvorostyanov et al., 2006; Spichtinger and Gierens, 2009; Spichtinger and Cziczo, 2010; Jensen et al., 2010; Ren and Mackenzie, 2005).

### 4.3.2.3 The effect of varying model updraft rate

In the TTL cirrus clouds form at a range of cooling rates. To test the effect of different cooling rates on the properties of cirrus nucleated by glassy aerosol the rate of vertical advection was varied in increments between 1 and 15 cm s<sup>-1</sup>. This is equivalent to cooling rates between 0.25 and 3.8 K hr<sup>-1</sup>, when based on the wet adiabat. The rates were chosen as they are representative of those found for slow synoptic scale motions in the TTL (Jensen et al., 2005b) and all cases a 1:1 ratio of glassy to liquid aerosol was used. The model output was averaged in the layer between 17.25 and 17.35 km (Figure 4.10). For comparison the equivalent quantities from the homogeneous run at 0.76 K hr<sup>-1</sup> are also shown. The time series for runs with higher cooling rates were cropped after the point at which sedimentation of larger ice crystals started to effect the profiles *e.g.* when  $N_{ice}$  started dropping.

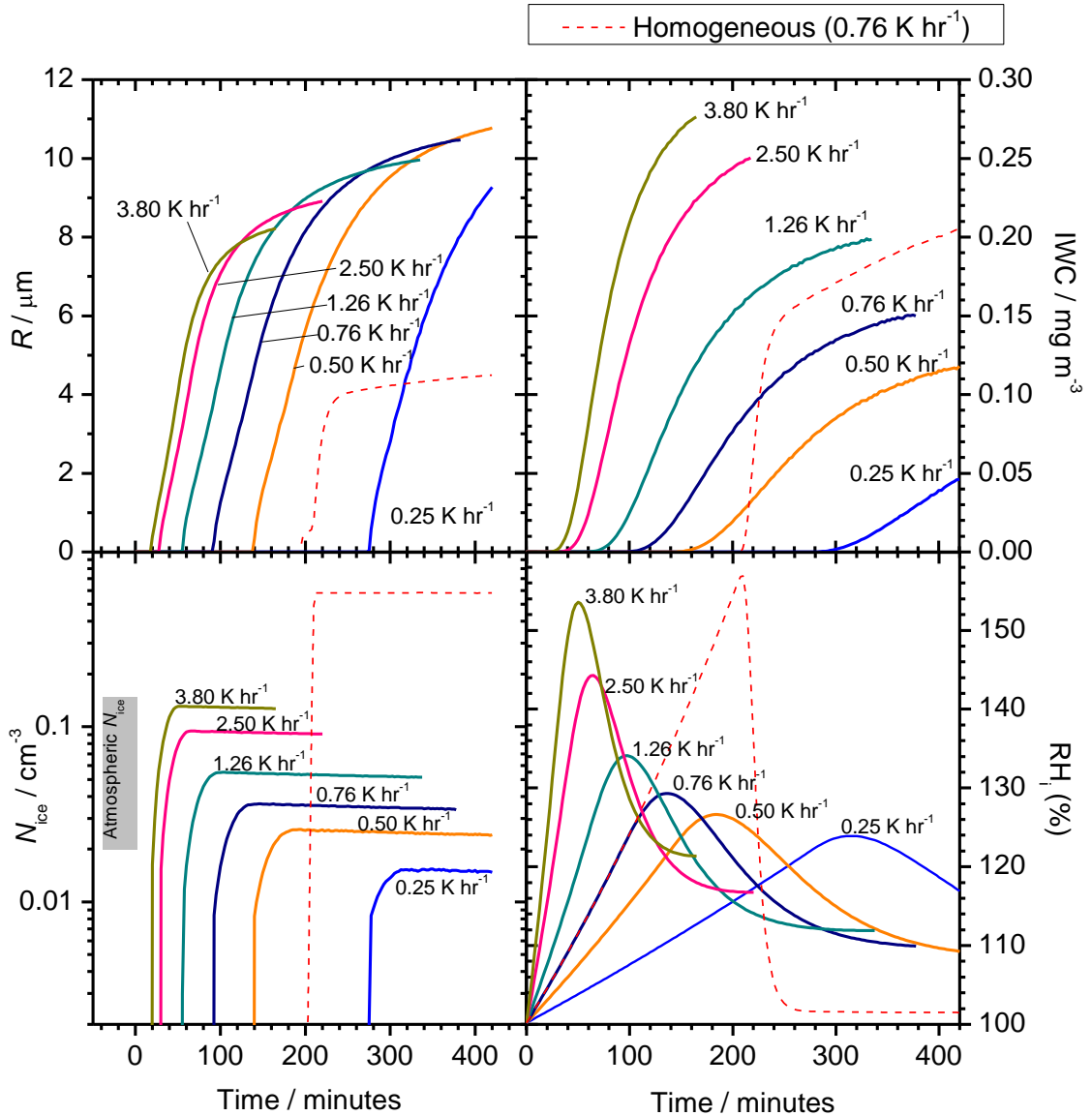


**Figure 4.10** The effect of changing the cooling rate on  $N_{\text{ice}}$  and  $\text{RH}_i$  for runs that had a total aerosol concentration of  $100 \text{ cm}^{-3}$  that was split 50/50 between glassy and liquid aerosol. For comparison, a run that used only liquid aerosol and a cooling rate of  $0.76 \text{ K hr}^{-1}$  is included (dashed red line). All runs were initialised using the profiles in Figure 4.6. The solid grey bar represents the observed range of  $N_{\text{ice}}$  in the TTL (Jensen et al., 2010).

Varying the cooling rate had a significant impact on  $N_{\text{ice}}$ ,  $\text{RH}_i$ ,  $R$  and IWC. At faster updraft rates higher peak  $\text{RH}_i$  was found. This corresponded to a larger IWC but smaller ice crystals. Only heterogeneous nucleation occurred in runs with cooling rates up to  $3.8 \text{ K hr}^{-1}$ , as water uptake by heterogeneously nucleated ice particles stopped the humidity reaching the homogeneous threshold. At ramp rates between  $0.5$  and  $3.8 \text{ K hr}^{-1}$  the modelled cirrus nucleated by glassy aerosol had  $N_{\text{ice}}$  in the range observed for cirrus

in the TTL (Jensen et al., 2010). This range is shown as a solid grey bar in Figure 4.10. Cirrus nucleated homogeneously at a cooling rate of  $0.76 \text{ K hr}^{-1}$  had  $N_{\text{ice}}$  well above the values found in the TTL.

The uptake of water vapour by ice particles controlled the peak humidity that was observed in each model run. In the heterogeneous case a set fraction of the aerosol activated to ice when a particular  $\text{RH}_i$  was reached. In the homogeneous case ice nucleation only occurred when the water activity based homogeneous threshold was reached. This correspondence is shown in Figure 4.11, where the time at which peak  $N_{\text{ice}}$  occurs in each run is marked with a vertical line of the corresponding colour. After peak  $\text{RH}_i$  is reached the ice particles kept growing as the constant updraft provided continued cooling, maintaining  $\text{RH}_i$  above ice saturation. This is seen as a slower ongoing increase in  $R$ .



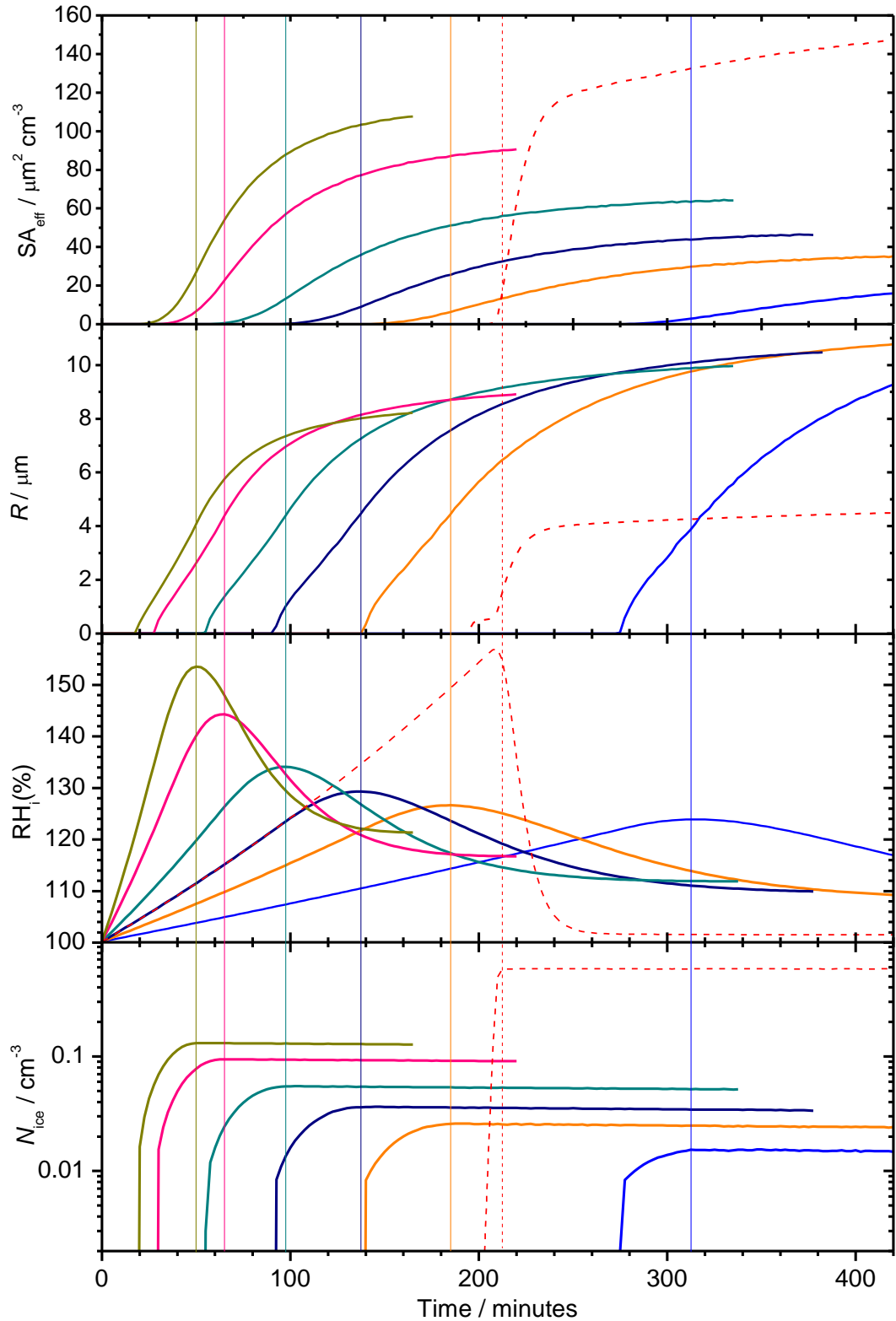


**Figure 4.11** The effective surface area of ice ( $SA_{\text{eff}}$ ), effective radius ( $R$ ),  $N_{\text{ice}}$  and  $RH_i$  for runs with varying cooling rates. The horizontal lines mark peak  $N_{\text{ice}}$  in each case. All runs used  $100 \text{ cm}^{-3}$  aerosol concentration and a 50/50 mix of glassy and liquid particles. Also shown is the homogeneous run at  $0.76 \text{ K hr}^{-1}$ . Colours correspond to those in Figure 4.10.

Using  $N_{\text{ice}}$  and  $R$  and assuming that the aerosol particles were spherical, the total ‘effective’ surface area ( $SA_{\text{eff}}$ ,  $\mu\text{m}^2 \text{cm}^{-3}$ ) of ice was also calculated for each cooling rate (Figure 4.11). As the cooling rate was increased, a larger surface area of ice was required to take up the excess water vapour. This resulted in higher peak  $RH_i$  and therefore  $N_{\text{ice}}$  for runs which used higher cooling rates ( $SA_{\text{eff}}$  at peak  $RH_i$ , blue line, Figure 4.12).

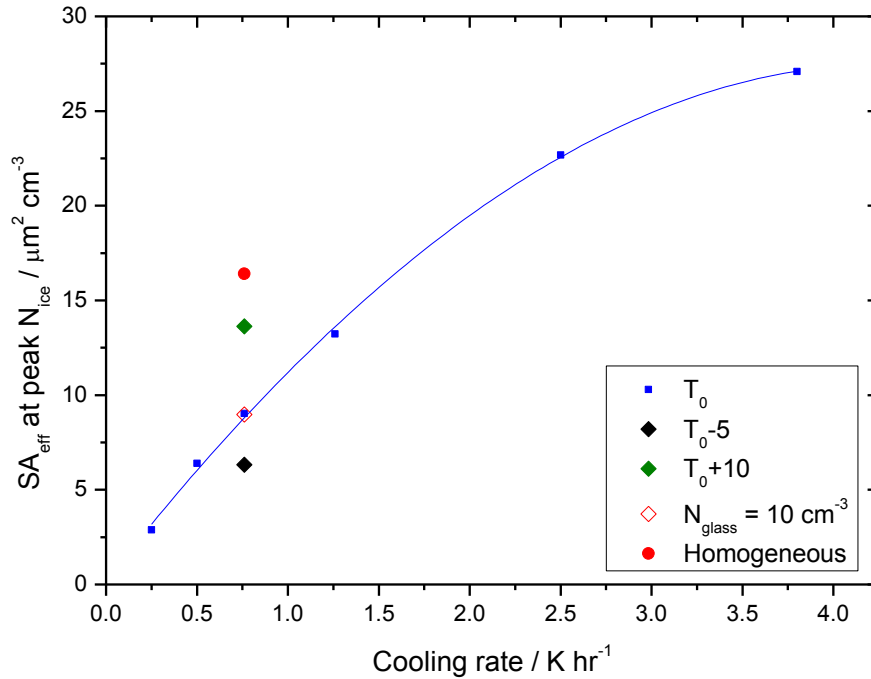


**Figure 4.12** A comparison of the effective ice surface area ( $SA_{\text{eff}}$ ) at peak  $N_{\text{ice}}$  for the heterogeneous runs and the homogeneous run shown in Figure 4.10 (blue squares) and for the sensitivity tests shown in Figure 4.13 ( $SA_{\text{eff}}$  at peak  $N_{\text{ice}}$  for runs which took place at higher (green diamond) and lower (black diamond) temperatures, and with a smaller fraction of glassy particles (open red diamond)).

#### 4.3.2.4 Changing the model temperature

The effect of temperature on the modelled cirrus’ properties was tested by shifting the initial temperature profile ( $T_0$ ) up by 10 K ( $T_0+10$ ) and down by 5 K ( $T_0-5$ ) (green and black lines, Figure 4.13). The mixing ratio of water vapour was adjusted in order to maintain the  $RH_i$  profile shown in Figure 4.6. All of the profiles shown in Figure 4.13 used a cooling rate of  $0.76 \text{ K hr}^{-1}$  and a ratio of 1:1 glassy to liquid aerosol. Due to the larger absolute humidity at the higher temperature, the rate of growth of nucleated ice

crystals was faster, allowing them to grow to larger sizes, causing more rapid sedimentation (notice the immediate decline after peak  $N_{ice}$  in the  $T_0+10$  case) and an increased IWC. The higher rates of ice particle growth at higher temperatures produced a larger effective surface area of ice (Figure 4.12) and a lower peak  $RH_i$ .

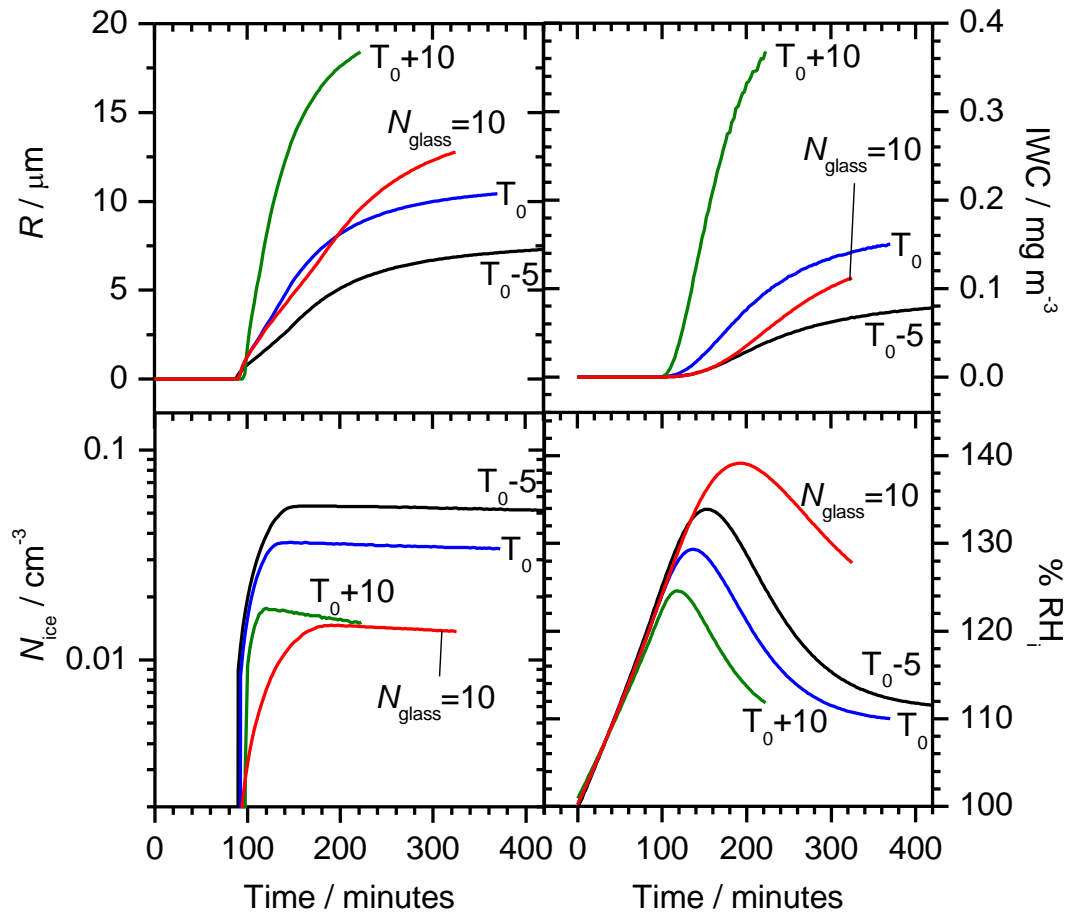


**Figure 4.13** Sensitivity tests to establish the effects on  $R$ , IWC,  $N_{ice}$  and  $RH_i$  of both increasing the initial model temperature by 10 K (green lines) and decreasing the initial model temperature by 5 K (black lines). These runs used  $100 \text{ cm}^{-3}$  total aerosol concentration split 50/50 between glassy and liquid aerosol. The effect of reducing the ratio of glassy to liquid aerosol to 1:9 was also investigated (red lines). In this run the model was initialised using the original temperature profile and kept a total aerosol concentration of  $100 \text{ cm}^{-3}$ . All runs used a cooling rate of  $0.76 \text{ K hr}^{-1}$ .

#### 4.3.2.5 Changing the fraction of aerosol particles which are glassy

To test the effect of reducing the concentration of glassy aerosol in the model, the ratio of glassy to liquid aerosol was reduced to 1:9 (*i.e.* the model used a concentration of

10 cm<sup>-3</sup> glassy and 90 cm<sup>-3</sup> liquid aerosol). This run used the T<sub>0</sub> temperature profile, an updraft rate of 0.76 K hr<sup>-1</sup> and used the same parameterisation for heterogeneous nucleation by glassy aerosol (Figure 4.7) as previous runs. Compared to the equivalent run that used a 1:1 ratio (solid blue line, Figure 4.13), the run with a reduced number of glassy particles (red line) produced fewer but larger ice particles. The ice particles were able to grow larger as the available water vapour was divided between fewer particles. The smaller available surface area of ice for water uptake resulted in a considerably higher peak humidity in the run with fewer glassy aerosol. However, in both the runs the same surface area of ice was reached at peak RH<sub>i</sub> (Figure 4.12).

## **4.4 Summary and conclusions**

In this chapter results from the ICE01 campaign at the AIDA cloud simulation chamber were presented. The aim of the campaign was to assess the ice nucleation behaviour of glassy citric acid aerosol under cirrus conditions. It was found that a fraction ( $\sim 3 \times 10^{-3}$ ) of citric acid aerosol nucleated ice heterogeneously at 120 – 135% RH<sub>i</sub>, below the glass transition temperature for aqueous citric acid aerosol particles (211.8 K). Heterogeneous ice nucleation was not observed when the aerosol was in a liquid state; instead the particles froze at humidities consistent with other liquid aerosol particle such as sulphuric acid. Ice nucleation at the observed temperatures is relevant to the TTL. Heterogeneous ice nucleation by glassy aerosol may be a route to the formation of the sub-visible cirrus clouds that are found in the TTL and potentially explains the lack of traditional IN such as mineral dusts in SVC ice particle residues (Froyd et al., 2010).

A one-dimensional cirrus cloud model was used to investigate the impact of heterogeneous ice nucleation by glassy aerosol on cirrus formed under conditions relevant to the TTL. A parameterisation based on the fraction of glassy citric acid that nucleated ice was used to represent glassy aerosol in the TTL. Modelled cirrus formed from a mixture of glassy and liquid aerosol had ice particle concentrations consistent with those found in the TTL (Jensen et al., 2010). The small surface area of ice particles available for the uptake of water vapour in cirrus formed by glassy aerosol resulted in prolonged supersaturations which continued for hours after the heterogeneous nucleation of ice. This is consistent with in-cloud supersaturations observed in cirrus at TTL temperatures (Krämer et al., 2009). This finding is in agreement with other studies that found heterogeneous ice nucleation by unspecified IN resulted in low ice particle

number density cirrus with high in-cloud humidity. Cirrus clouds in the TTL are involved in the regulation of the amount of water vapour that enters the stratosphere (Fueglistaler et al., 2009). High in-cloud humidities in TTL cirrus are likely to increase the amount of water vapour that enters the stratosphere, which would potentially lead to an increase in the destruction of stratospheric ozone.

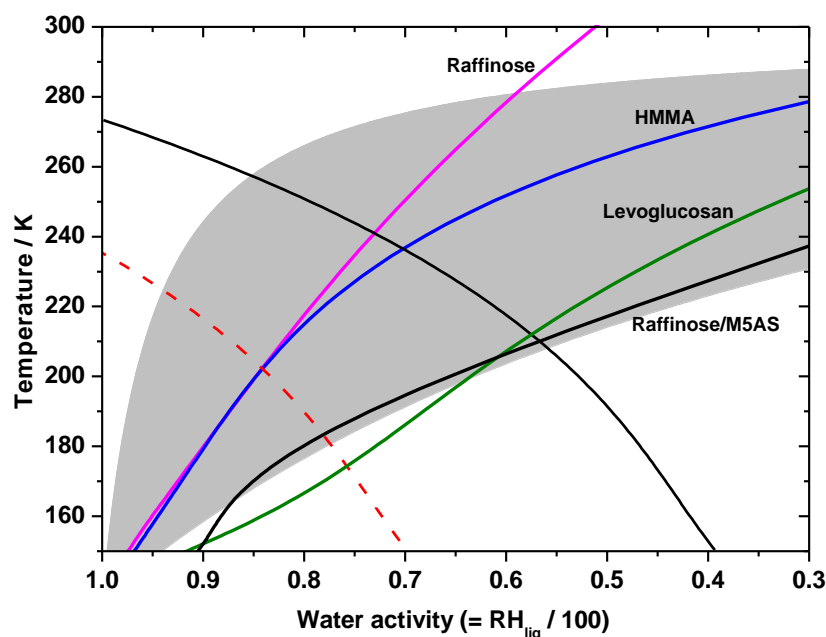
## Chapter 5: ICE02 Campaign: Heterogeneous ice nucleation by other glassy aerosols

Glassy aqueous citric acid aerosol was shown to nucleate ice heterogeneously at temperatures relevant to the TTL in experiments described in Chapter 4. The aim of the experiments presented in this chapter was to test if the ability to nucleate ice heterogeneously is a property common to other glassy aqueous solution aerosols. Experiments were performed at the AIDA cloud simulation chamber as part of the ICE02 campaign.

*Results from this chapter are published in Atmospheric Chemistry and Physics Discussions. (Wilson, T. W., Murray, B. J., Wagner, R., Möhler, O., Saathoff, H., Schnaiter, M., Skrotzki, J., Price, H. C., Malkin, T. L., Dobbie, S., and Al-Jumur, S. M. R. K., Glassy aerosols with a range of compositions nucleate ice heterogeneously at cirrus temperature Atmospheric Chemistry and Physics, 12, 8611 - 8632, 2012 doi:10.5194/acp-12-8611-2012). TWW wrote the manuscript, planned and directed experiments and analysed data in collaboration with RW and BJM. TWW also helped write a successful proposal to EUROCHAMP 2 to fund this work. BJM oversaw the study and sought financial support for it. RW oversaw the operation of the AIDA chamber, directed experiments and processed and analysed data in collaboration with TWW and BJM. OM led the AIDA team, which included HS, MS, JS who operated the AIDA chamber and associated equipment. HCP assisted in the analysis of experimental data. TLM, SD and SMRKA assisted in experiments at AIDA.*

### 5.1 Aerosols chosen for study during ICE02

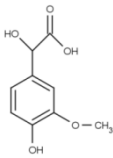
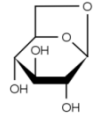
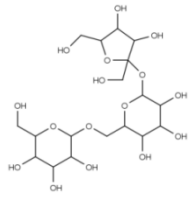
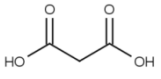
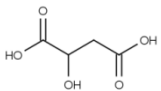
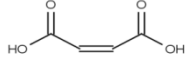
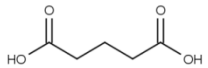
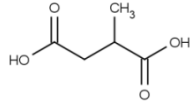
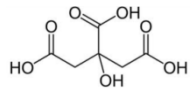
Aerosols with four different chemical compositions were tested to see if they nucleated ice heterogeneously. All of the aerosols that were examined become glassy under upper tropospheric conditions. The substances were chosen for study both because they are broadly representative of organic species found in atmospheric aerosol and because they have well characterised aerosol phase diagrams (Zobrist et al., 2008). The  $T_g$ ' values of the aerosols chosen for study all fall within the range predicted for atmospheric SOA (Figure 5.1) (Koop et al., 2011) based upon the properties of SOA derived from measurements made during the AMAZE-08 campaign (Gunthe et al., 2009).



**Figure 5.1** An aerosol phase diagram comparing the estimated range of the relative humidity induced glass transition threshold ( $RH_g$ ) for atmospheric SOA (grey area) (Koop et al., 2011) and the  $RH_g$  thresholds (Zobrist et al., 2008) for the aerosols investigated in this study. The solid black line is the ice-liquid equilibrium and the dashed red line is the homogeneous freezing threshold for liquid solution droplets (Koop et al., 2000). For a more detailed explanation of aerosol phase diagrams see Chapter 2.

The investigated solution aerosols were composed of the following solutes; levoglucosan ( $C_6H_{10}O_5$ ), a monosaccharide anhydride and a major component of biomass burning aerosol, which has been observed to make up as much as 60% of the mass of aerosol from particular types of combusted biomass (Iinuma et al., 2007; Knopf and Rigg, 2011). Raffinose ( $C_{18}H_{32}O_{16}$ ), a trisaccharide that has also been identified as a component of biomass burning aerosol (Decesari et al., 2006; Wan and Yu, 2007). 4-Hydroxy-3-methoxy-mandelic acid (HMMA,  $C_9H_{10}O_5$ ), an aromatic compound that is used as a surrogate for the water soluble organic compounds found in atmospheric aerosol (Decesari et al., 2006). Raffinose/M5AS, which is a multi-component oxidised organic/sulphate mixture that more closely represents internally mixed atmospheric aerosol found in the TTL. The molecular structures and  $T_g$ ' for the species used are shown in Table 5.1.

**Table 5.1** Molecular structures of the glass forming components of the four aqueous aerosols examined in this study with associated  $T_g'$  and uncertainties (Zobrist et al., 2008). The molecular structure and  $T_g'$  of citric acid, a component of the glassy aerosol that was used for the experiments described in Chapter 4 has been included for comparison (note that no uncertainties in  $T_g'$  were available for citric acid). The percentages next to the components of raffinose/M5AS aerosol indicate the individual species contribution by mass to the mixture.

Aerosol	Component(s)	Molecular structure	$T_g' / \text{K}$	$\pm / \text{K}$
HMMA	4-Hydroxy-3-methoxy-DL-mandelic acid		236.5	3.5
Levogluconan	(-)-1,6-Anhydro- $\beta$ -D-glucopyranose		211.7	11.1
Raffinose	D-(+)-Raffinose pentahydrate		240.6	6.1
Raffinose/M5AS	D-(+)-Raffinose pentahydrate (50.00%)	See above	209.6	8.1
	malonic acid (15.35%)			
	DL-Malic acid (7.35%)			
	maleic acid (7.05%)			
	glutaric acid (8.85%)			
	methylsuccinic acid (3.70%)			
	ammonium sulphate (7.70%)	$(\text{NH}_4)_2\text{SO}_4$		
Citric acid	citric acid		211.8	-



## 5.2 Did aerosols crystallise in experiments during ICE02?

At low temperatures, the solution droplets in the AIDA chamber are highly supersaturated with respect to their solutes' crystalline phases. For example, the solubility of raffinose at 273 K is 30 g L<sup>-1</sup> (Hungerford and Nees, 1934) (and will decrease at lower temperatures), whereas the predicted aerosol composition when at ice saturation at 238 K (based on water activity data from (Zobrist et al., 2008)) is 782.5 g L<sup>-1</sup>. Under similarly supersaturated conditions, oxalic acid or ammonium sulphate solution aerosol would be expected to slowly crystallise (Wagner et al., 2010, 2011; Abbatt et al., 2006). This is important because crystalline solid salts are known to catalyse ice nucleation (Wise et al., 2009; Wise et al., 2010; Abbatt et al., 2006; Baustian et al., 2010; Shilling et al., 2006; Eastwood et al., 2009), as are crystalline hydrates (Wise et al., 2012). However, nucleation and crystal growth in highly viscous or glassy aqueous aerosol particles is much slower. For example, none of the species investigated in this study were observed to crystallise during the experiments carried out on droplet in oil emulsions by Zobrist et al. (2008).

In single particle trap experiments at 298 K, 10 µm diameter levoglucosan particles did not crystallise when they were dried to < 5% RH<sub>liq</sub> over the course of minutes (Chan et al., 2005). Similarly, Mikhailov et al. (2009) showed that at 298 K, aqueous levoglucosan droplets of ~100 nm diameters did not crystallise in a differential mobility instrument at low RH<sub>liq</sub> (5%). X-ray diffraction measurements by Chatterjee et al. (2005) show no crystallisation of raffinose from freeze concentrated bulk solutions cooled initially to 203 K at 1 K per minute and then annealed at 241 K ( $T_g'$  for raffinose solution) for 8 hours. This indicates that close to  $T_g'$ , raffinose does not crystallise. At room temperature, Tong et al. (2011) found that amorphous raffinose particles held at ~0% RH<sub>liq</sub> for approximately 6.5 hours did not crystallise. In Chapter 6 the results of freezing experiments conducted using 15 wt% raffinose solution in oil emulsions within a powder X-ray diffractometer showed that homogeneous ice nucleation in the droplets did not catalyse the crystallisation of the raffinose solute at 236 K.

The raffinose/M5AS aerosol used in this study was composed of raffinose, five dicarboxylic acids and ammonium sulphate. Nucleation of one crystalline phase from complex mixtures is likely to be further reduced as the presence of other solutes reduces

the saturation with respect to any single compound. Bodsworth et al. (2010) show that the addition of more than 30% citric acid (by mass) to ammonium sulphate solution droplets inhibits their crystallisation at  $< 250$  K. Even at room temperature, where crystallisation is expected to be more likely, droplets doped with more than 50% citric acid did not crystallise.

The available literature data strongly suggests that the highly viscous solutions used in this study did not crystallise even though they were highly supersaturated. This is supported by the SIMONE depolarisation measurements made during the campaign. This technique was used in previous studies at AIDA to track crystallisation in oxalic acid aerosols with similar size distributions to those in this study (Wagner et al., 2010). Concomitant Fourier transform infrared spectroscopy (FTIR) measurements during experiments with the oxalic acid aerosol confirmed that the entire aerosol population had crystallised.

Liu and Mishchenko (2001) performed T-matrix calculations for polydisperse, randomly orientated spheroidal and cylindrical particles with a refractive index of 1.5. This refractive index is consistent with that of crystalline sucrose (1.558) (Tong et al., 2011) and is likely to be similar to that of the species used in this study. They present  $\delta$  as a function of the effective equal-volume-sphere radius ( $r_{\text{eff}}$ ) (Hansen and Travis, 1974) and the ratio of the spheroids/cylinders largest and smallest semi-axes. The change in  $\delta$  that would be expected to result from the crystallisation of the aerosols used in this study, based on the calculations by Liu and Mishchenko (2001) was assessed. The particle size distributions shown in Figure 5.8 were converted to  $r_{\text{eff}}$  values, which were then adjusted to account for the longer wavelength assumed by Liu and Mishchenko (2001) (603 nm) compared to that used by the SIMONE instrument (488 nm). This gave  $r_{\text{eff}}$  values of between 0.26 and 0.33  $\mu\text{m}$ , with a mean  $r_{\text{eff}}$  of 0.30  $\mu\text{m}$ . For spheroids and cylinders with an  $r_{\text{eff}}$  value of 0.29  $\mu\text{m}$ , Liu and Mishchenko (2001) calculate a depolarisation signal of at least 10%, unless the crystallised particles had a very low degree of asphericity ( $< 1.1 - 1.2$ ). A value of 18% was previously found for crystallisation of oxalic acid aerosols with similar size distributions (Wagner et al., 2010) (Exp. 2 in Figure 4 therein).

The detection limit for a change in depolarisation at AIDA is about 1%. No such change in  $\delta$  was observed during experiments with the aerosols used here or in the

previous work with citric acid aerosol (Chapter 4), strongly suggesting the absence of crystallisation. Assuming that the crystallized particles have the same size and refractive index and a reasonable depolarisation ratio of about 0.2 for these particles then 5% of the aerosol particles in the chamber would need to crystallise in order to produce a detectable change in depolarisation. A similar fraction of crystallites would also be required for detection with FTIR extinction measurements. One might therefore argue that the heterogeneous ice crystal modes observed during both the ICE01 and ICE02 campaigns were due to nucleation on a small subset of particles which had crystallized instead of forming a glassy solid. However, the following experimental data provides strong evidence that this was not the case.

In order to further test if the solution aerosol were crystallising a dedicated experiment was performed with raffinose aerosol in which raffinose solution was injected at ~241 K and the resultant aerosol was cooled to 217.5 K over a period of ~6 hours before warming the chamber to 229 K, at which point an expansion experiment was performed (Figure 5.2A). If raffinose had crystallised during injection of the aerosol or during the subsequent temperature cycling, it would most likely have nucleated ice heterogeneously like other crystalline materials such as ammonium sulphate (Wise et al., 2009; Abbatt et al., 2006) and oxalic acid (Wagner et al., 2010, 2011). During the expansion, no significant heterogeneous ice nucleation was observed, with  $< 1 \text{ cm}^{-3}$  ice particles nucleating prior to a rapid increase in  $N_{\text{ice}}$  when the chamber  $\text{RH}_i$  was within 2% of the predicted homogeneous freezing threshold (based on AIDA freezing data for liquid  $\text{H}_2\text{SO}_4$  solution aerosol (Möhler et al., 2003)) (Figure 5.2B). This offers very strong evidence that the raffinose aerosol did not crystallise at low temperature and that any heterogeneous nucleation observed in other experiments was not due to crystalline raffinose.

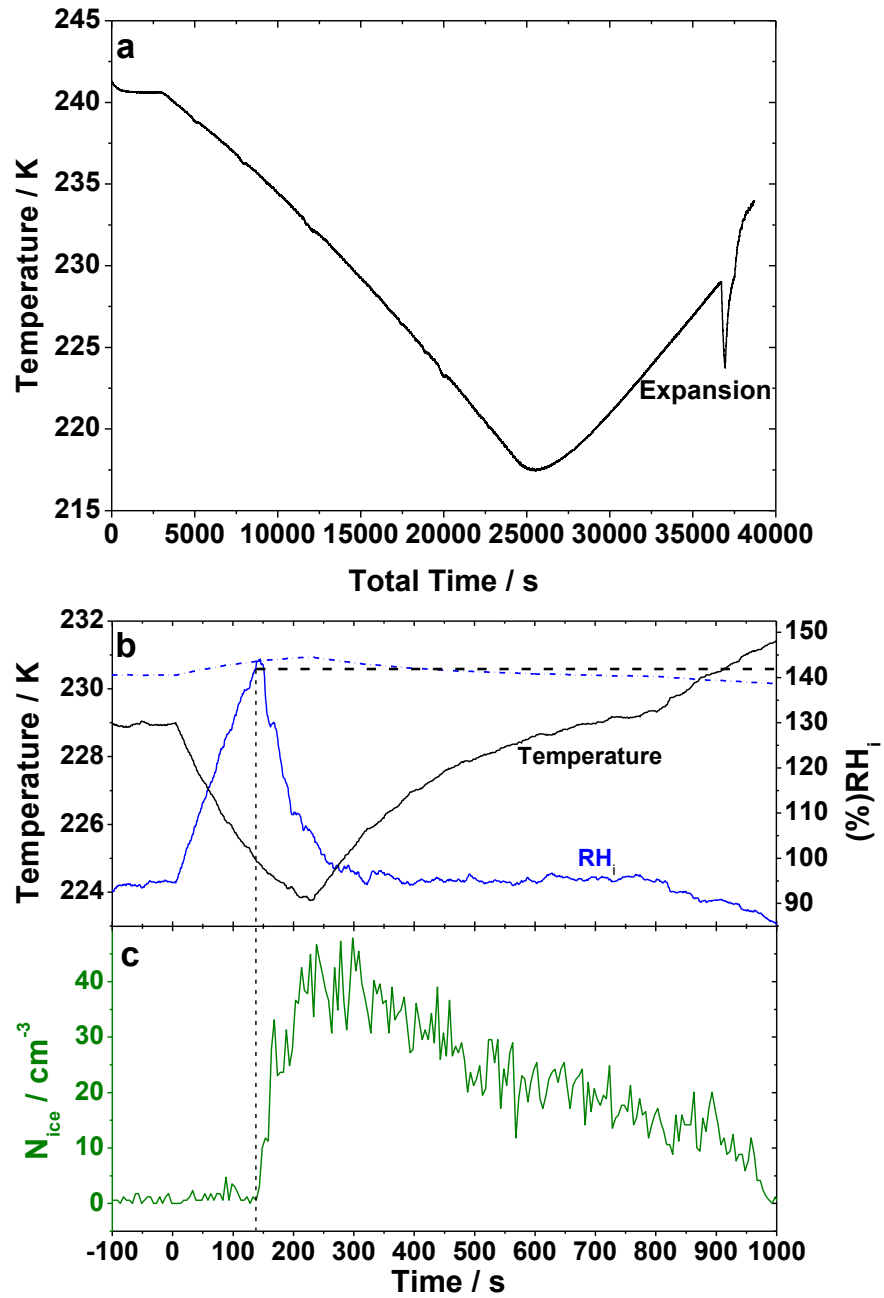


**Figure 5.2** Panel A shows the experimental temperature/time series for raffinose aerosol cooled to 217.5 K then warmed up to 229 K at which point an expansion was performed. The top section of panel B shows the temperature and  $RH_i$  (solid black and blue lines respectively) as well as the temperature dependent threshold humidity at which homogeneous ice nucleation is expected to occur, based on AIDA experiments using liquid aqueous  $H_2SO_4$  aerosol (Möhler et al., 2003) (dotted blue line). Homogeneous ice nucleation was observed at the predicted humidity, indicating that the aerosol had liquefied on exposure to increasing humidity, which would not have occurred had it crystallised.

Further experimental evidence of the lack of crystallisation of the glassy aerosols used in this study can be found in results presented in Chapter 6. In that study, run 3 (Figure 6.1 and Figure 6.2) took place at ~232 K using HMMA aerosol that had previously heterogeneously nucleated ice when in the glassy state at a lower temperature (in run 2). In run 3, only significant homogeneous ice nucleation was observed. This shows that the glassy aerosol had liquefied on warming. Had the aerosol been crystalline it would still have been expected to nucleate ice heterogeneously. Similarly, Chapter 6 also shows the results of an expansion performed on raffinose/M5AS aerosol particles at ~216 K (run 1C, Figure 6.9), that had previously nucleated ice when glassy. Again, after warming into the liquid regime, the only significant ice formation occurred homogeneously. This again strongly indicates that the heterogeneous nucleation at lower temperatures was by glassy particles which were able to liquefy on warming rather than crystallites. In both cases, to ensure that those particles that nucleated ice in the first run were not lost by sedimentation, ice crystals were sublimed quickly by refilling the chamber immediately after pumping had stopped.

These experiments and the literature discussed above strongly suggest that solute crystallisation from the aqueous solution aerosols did not occur and instead the aerosol were in either a liquid, semi-solid glassy state depending on chamber temperature and humidity.

## 5.3 Results and discussion

### 5.3.1 Expansion with a liquid aerosol

The results of an expansion using raffinose/M5AS solution aerosol are shown in Figure 5.3. The aerosol in this experiment was in the liquid state as the chamber gas temperature at the start of the expansion (215.5 K) was well above  $T_g'$  (209.6 K). On expansion, the chamber pressure was reduced (orange line, panel B), resulting in initially adiabatic cooling. As the gas temperature dropped,  $RH_i$  increased (black and blue lines, panel A Figure 5.3). In order for the water activity of the liquid aerosol particles to remain in equilibrium with the surrounding humidity, they must take up water. In the phase diagram shown in Figure 2.3, the arrow from point A to point B is an idealised temperature/water activity trajectory of aerosol during an expansion. Liquid solution aerosol particles become more dilute and freeze when they reach the

homogeneous freezing threshold. The onset of freezing was detected first as an increase in the depolarisation ratio,  $\delta$  (blue line, panel D Figure 5.3). This onset is within ~5% of the humidity of homogeneous ice nucleation in sulphuric acid aerosol at the AIDA chamber (Möhler et al., 2003) (dotted blue line, panel A Figure 5.3). Ice particles grew rapidly into the size range detectable by the WELAS 1 instrument (ice particle number concentration, black line, panel C, Figure 5.3). The fraction of aerosol that froze ( $f_{ice}$ ) is similar to  $f_{ice}$  found for liquid citric acid solution aerosol in an expansion with a similar cooling rate (See Chapter 4). The dilution of liquid aerosol on increasing  $RH_i$  followed by homogeneous freezing is the expected behaviour for liquid aerosol particles (Koop et al., 2000; Möhler et al., 2003).

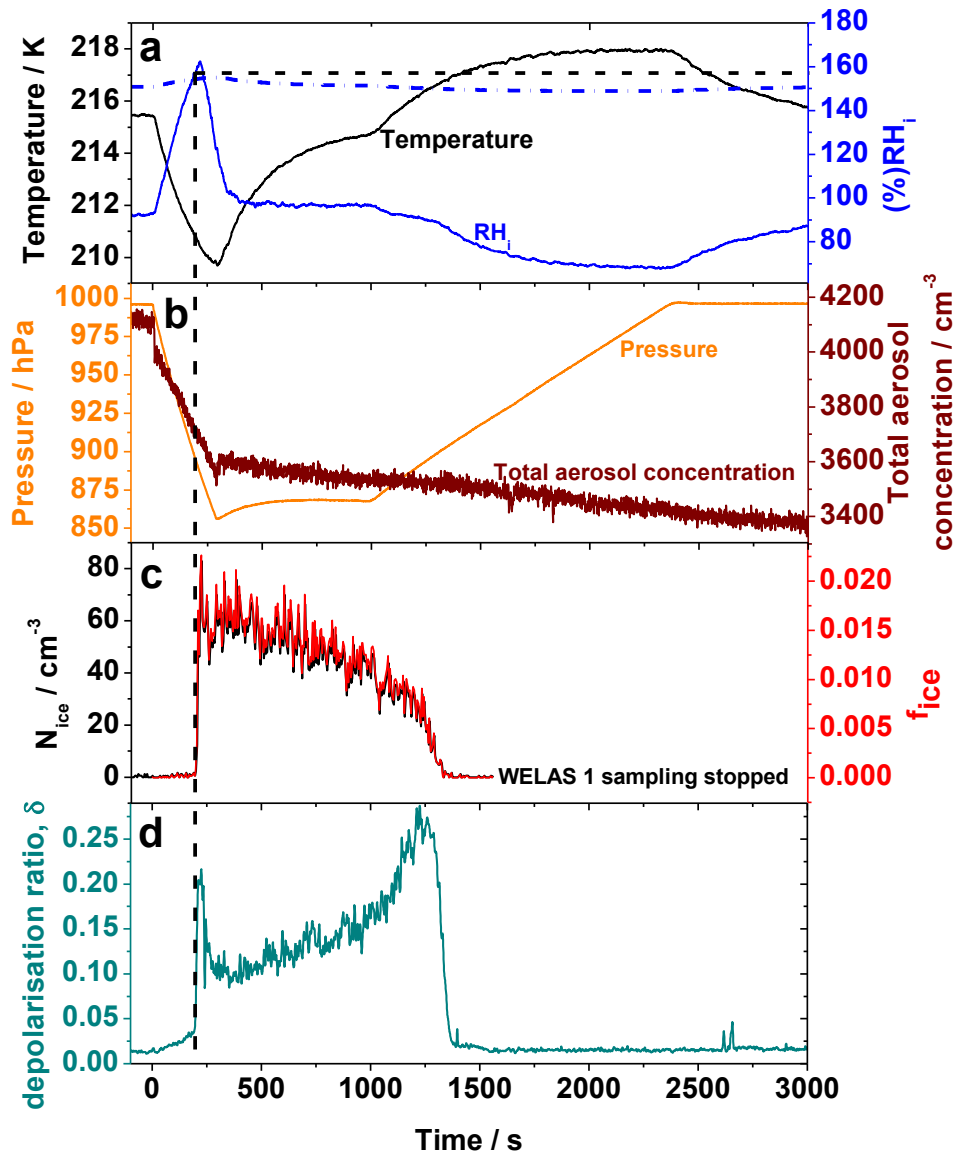


**Figure 5.3** A typical expansion experiment at the AIDA chamber using liquid aqueous raffinose/M5AS aerosol. Panel A shows the temperature and  $RH_i$  (solid black and blue lines) as well as the expected homogeneous freezing  $RH_i$  (dash-dot blue line), based on AIDA homogeneous freezing data from liquid aqueous  $H_2SO_4$  aerosol (Möhler et al., 2003). Panel B shows the pressure and total aerosol concentration (orange and burgundy lines). The ice particle number concentration from WELAS 1 and the fraction of aerosol that froze are shown in Panel C (black and red lines). In panel D, the onset of ice nucleation is seen as the sharp rise in  $\delta$

(cyan line). The time/humidity at the onset of freezing is marked with dashed black lines.

After nucleation, the supersaturation in the chamber was rapidly quenched by the growth of ice particles, lowering  $RH_i$  to well below the homogeneous ice nucleation threshold, preventing any further nucleation. At the end of pumping, heat from the chamber walls (which do not cool significantly during expansions) caused the gas temperature to rise, but the ice cloud persisted. The chamber was returned to its starting pressure by refilling with dry, particulate free synthetic air. This rapidly reduced  $RH_i$  to well below 100% and completed the sublimation of the ice cloud, returning  $\delta$  to its starting value.

### 5.3.2 Expansions with glassy aerosol

Aerosols in the glassy state showed very different behaviour to that of liquid aerosol. This is illustrated by experiments at different temperatures that used the same HMMA solution aerosol. The aerosol was injected at  $\sim 247$  K and then subjected to an initial test expansion at a temperature above the homogeneous freezing limit (*i.e.* no ice was nucleated) and then cooled below  $T_g'$  (the experimental temperature profile is shown in the panel A of Figure 5.4). An expansion was then performed at  $\sim 220$  K in which depolarisation measurements show that the glassy HMMA aerosol nucleated ice at  $120 \pm 5\%$   $RH_i$ , well below the expected homogeneous limit (Figure 5.4 panels B1 and B2). The optical particle counter results show that the fraction of aerosol activated to ice ( $f_{ice}$ ) increased gradually up to  $\sim 0.005$ , a value similar to that found for heterogeneous ice nucleation by glassy citric acid aerosol (See Figure 4.8). This indicates that the glassy HMMA aerosol particles also nucleated ice heterogeneously. The aerosol was then warmed back up to 232 K and underwent another expansion. A concentration of  $200 \text{ cm}^{-3}$  ice particles nucleated at the homogeneous limit, with only  $\sim 1 \text{ cm}^{-3}$  nucleating earlier (Figure 5.4, panels C1 and C2). There was a corresponding rapid increase in  $f_{ice}$ , which reached  $\sim 0.05$ .



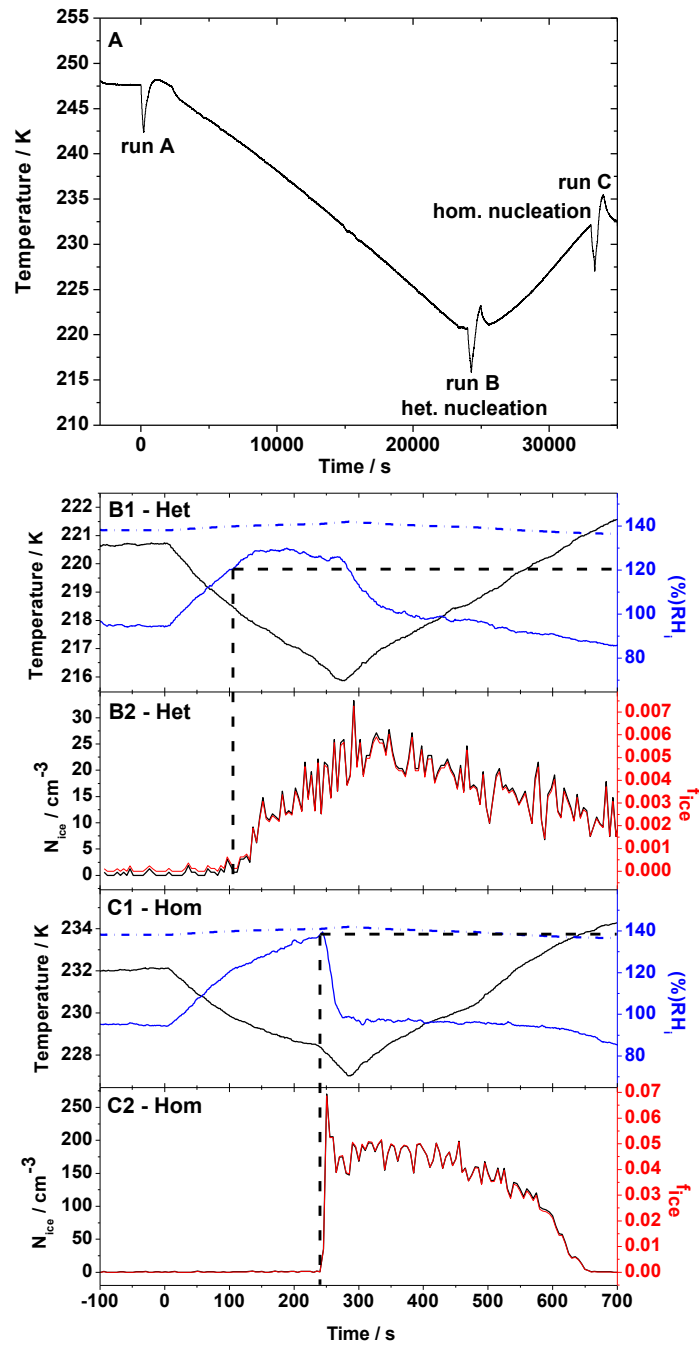


**Figure 5.4** A comparison of the behaviour of aqueous HMMA solution in expansion runs B and C. Panel A shows the temperature profile of the experimental series. The bottom panels show experimental data for runs B (started at 220.7 K) and C (started at 232.1 K). Panels B1 and C1 show in each case the experimental temperature and humidity (black and blue solid lines respectively). Panels B2 and C2 show the ice particle number concentration ( $N_{ice}$ , black line) and the fraction of the aerosol frozen ( $f_{ice}$ , red line). The AIDA homogeneous ice nucleation threshold (Möhler et al., 2003) is indicated in B1 and C1 by dash-dot blue lines. The ice nucleation onsets were observed as an increase of at least 1% in the backscattering linear depolarisation ratio,  $\delta$ , and are marked with dashed black lines.

These experiments also add further weight to the evidence that the aerosol particles acted as IN whilst in the glassy state, rather than nucleating ice having crystallised. Had crystallisation occurred in the aerosol population, it would be expected that heterogeneous nucleation would have also been observed in the run at 232 K. The presence of only the homogeneous freezing mode suggests that the glassy aerosol had liquefied before any heterogeneous nucleation could occur (see Section 5.3.3 for more discussion concerning the liquefaction of aerosol during expansions).

### 5.3.3 Heterogeneous ice nucleation: a general property of glassy aerosols

Expansion experiments were repeated with aerosol of each of the four chosen compositions at a range of temperatures above and below  $T_g'$  (see Table 5.1 for chemical structures and  $T_g'$ ). The results of these experiments are summarised in Figure 5.5. All aerosol types were found to nucleate ice at humidities below the homogeneous freezing threshold at temperatures well below  $T_g'$ , indicating that glassy aerosols of varying chemical composition are capable of heterogeneously nucleating ice.

While nucleation occurred heterogeneously on glassy aerosol well below  $T_g'$ , homogeneous nucleation was observed for raffinose and HMMA aerosols in expansions that started 11.7 K and 4.3 K below  $T_g'$ , respectively. Aerosol particles in expansions that start close to but still below  $T_g'$  may take up water (which serves as a plasticiser) and liquefy on crossing  $RH_g$ . This solid-to-liquid transition is also known as amorphous deliquescence (Mikhailov et al., 2009) and may occur before ice can nucleate heterogeneously. Alternatively, the estimates of  $T_g'$  could be too high and the aerosol particles may have been liquid to begin with. Given the uncertainty in  $RH_g$  it is not possible to categorically rule out either mechanism. However, in Chapter 6 it is shown that aerosol particles become pre-activated after the 232 K HMMA and 229 - 235 K raffinose experiments, which it is argued is related to glass formation and suggests that these runs were indeed below  $T_g'$ . It is most likely therefore that the explanation for homogeneous ice nucleation in the highest temperature HMMA and raffinose runs (despite them starting below  $RH_g$ ) is that the aerosol particles liquefied before ice could nucleate heterogeneously.

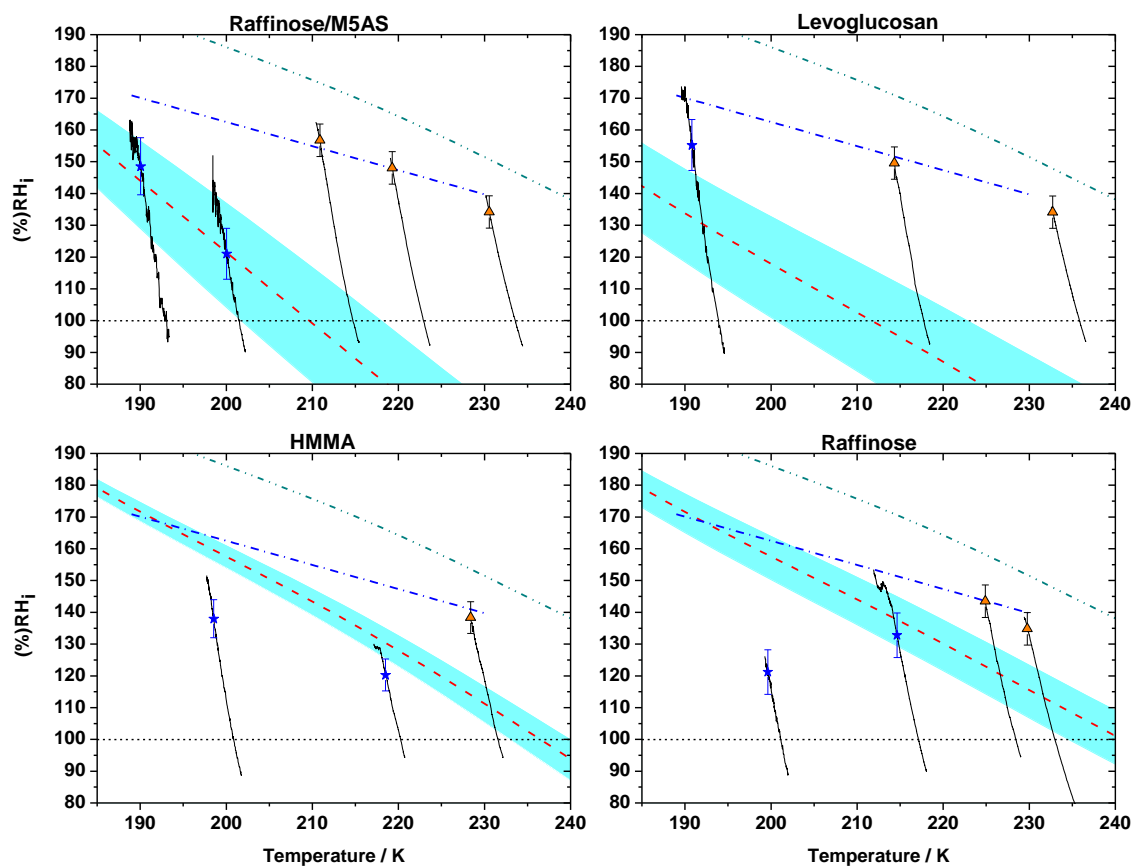


**Figure 5.5** The experimental temperature –  $RH_i$  trajectories for the expansion experiments for each aerosol type (solid black lines). Associated with each trajectory is an ice nucleation onset determined using the depolarisation measurement (defined by a change in the depolarisation ratio of at least 1% – for example see Figure 5.3), with orange triangles representing homogeneous ice nucleation onsets and blue stars representing heterogeneous ice nucleation onsets. The figures also show the aerosol  $RH_g$  thresholds (dashed red lines) and their associated uncertainties (shaded blue areas) based on parameterisations from Zobrist et al. (2008). The point at which  $RH_g$  crosses the marked 100%  $RH_i$  line (dotted black line) is equal to  $T_g'$  for that aerosol type. Also shown is the water saturation line (cyan dot-dot-dash line, shows where  $RH_{liq}$  is equal to 100%) and the expected homogeneous freezing threshold (blue dot-dash line), based on the homogeneous freezing of sulphuric acid solution aerosol in the AIDA chamber (Möhler et al., 2003).

Some differences in the behaviour of aerosols of differing compositions were observed. For example, at  $\sim 200$  K raffinose/M5AS and raffinose particles both nucleated ice at about 121%  $RH_i$  whereas HMMA aerosol was found to nucleate ice at  $138 \pm 6\%$   $RH_i$  at the same temperature. In addition, the two systems with higher  $T_g'$  (raffinose and HMMA) nucleated ice at higher temperatures than levoglucosan and the

raffinose/M5AS mixture. For example, at 218.5 K HMMA nucleated ice heterogeneously at  $120 \pm 5\%$  RH<sub>i</sub>, whereas levoglucosan and raffinose/M5AS only nucleated ice at the homogeneous limit. The impact of changing the aerosols chemical composition (and consequently  $T_g'$ ) on the temperature at which the aerosol nucleate ice heterogeneously is further evidence that the ice nucleation observed in this study is governed by the transition of liquid aerosol into glassy solid aerosol. The findings in this chapter also show that if atmospheric aerosol were to undergo a glass transition then the temperature and humidity at which the aerosol nucleates ice is likely to be dependent upon its chemical composition.

It was, very reasonably, predicted by Zobrist et al. (2008) that glassy aerosols would be unlikely to nucleate ice heterogeneously due to their “smooth convex surface that is disordered on a molecular level”. They surmised that such a surface would lack the characteristics of efficient ice nuclei, such as a crystal lattice match with ice (*e.g.* silver iodide (Vonnegut, 1947)) or surface defects like cracks or pores. This study and the study described in Chapter 4 that used citric acid aerosol show clearly that a small fraction of glassy aerosol particles of varied compositions are able to act as ice nuclei in the deposition mode. The surfaces of this subset of glassy aerosol may therefore possess some ‘active sites’ that are able to stabilise nascent germs of the ice phase. As suggested by Zobrist et al. (2008), the surface of glassy aerosol particles is less likely to host defects such as cracks or pores that might support a critical germ of ice. However, all the aerosols tested in this study are aqueous solutions of species that have numerous hydrogen bonding sites in the form of OH groups and/or carboxylic acid groups. Both water molecules and the solute species will be present at the surface of the aerosol particles and be available to hydrogen bond to adsorbed water molecules, thus fulfilling the chemical bond requirements of an effective ice nucleus (Pruppacher and Klett, 1997). I propose that ice nucleation by the glassy aerosol in this study is catalysed by water and solute molecules that are arranged in a manner that happens to provide a hydrogen bonding site that matches the crystal lattice of ice. Active sites such as these might occur as in any amorphous material and may be related to more ordered regions. Sites capable of nucleating ice may be rare, thus explaining why only small fractions of the glassy aerosols were found to nucleate ice. These active sites may be more or less common in glassy solution aerosol of different chemical composition, which would

explain the observed difference in ice nucleation efficiency of the aerosols tested in this study.

### 5.3.4 Does glassy SOA nucleate ice heterogeneously?

All of the aerosols tested in this study have  $RH_g$  thresholds that fall entirely or mostly in the predicted  $RH_g$  range for SOA (Figure 5.1) which implies that their glass forming properties are comparable to those of atmospheric SOA. In fact, there is mounting evidence that SOA generated in chambers and sampled from the atmosphere can nucleate ice heterogeneously (Knopf et al., 2010; Wang et al., 2012; Möhler et al., 2008). The  $f_{ice}$  values found for  $\alpha$ -pinene SOA particles used by Möhler et al. (2008) are consistent with those observed for citric acid (see Chapter 4) and those for the aerosol investigated in this study (Figure. 5.6). Wang et al. (2012) generated amorphous SOA by the OH radical oxidation of naphthalene and deposited it on a hydrophobic substrate. They observed that the SOA nucleated ice heterogeneously in the deposition mode at temperatures below  $\sim 230$  K and the onset of heterogeneous ice nucleation was observed at between about 135 and 150 %  $RH_i$ . Above  $\sim 230$  K, the aerosol particles were observed to take up water on increasing humidity before freezing heterogeneously. This indicates that a glassy core may have nucleated ice heterogeneously after water condensed to form an aqueous shell in the manner observed by Bones et al. (2012). The change in behaviour of the particles at  $\sim 230$  K was found to be related to the physical state of the aerosol with nucleation occurring when the aerosol were thought to be in an amorphous solid state, which is consistent with findings for glassy aerosols in this project.

There are also a number of contrasting studies in which no ice nucleation was observed on SOA. Wagner et al. (2007) report no significant heterogeneous ice nucleation by the SOA in their study. Instead, the aerosols were found to nucleate ice close to water saturation, indicating that they were not efficient IN. It was found that SOA particles generated by the ozonolysis of a variety of alkenes did not nucleate ice heterogeneously in the deposition mode (Prenni et al., 2009). This may simply be the nature of SOA generated in this experiment or it could be due to the experiments taking place at relatively higher temperatures (243 K), at which the aerosol may have been in a liquid rather than glassy or semi-solid state.

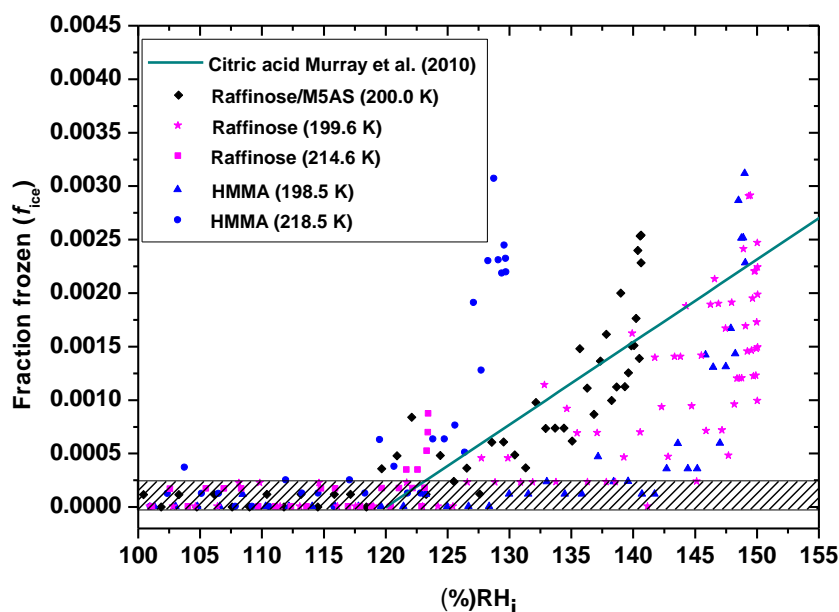


**Figure 5.6** The fraction of aerosol that froze heterogeneously at temperatures above 198 K during the expansion experiments shown in Figure 5.5. At temperatures below 198 K, the ice crystals were too small to allow  $N_{ice}$  to be inferred accurately from the WELAS data using a size threshold, preventing the calculation of  $f_{ice}$  for those experiments. See figure legend for details. Bracketed numbers in legend indicate the temperature at which the onset of ice nucleation occurred in each case. The solid cyan line is the linear fit ( $f_{ice} = 7.7211 \times 10^{-5}(\%RH_i) - 9.2688 \times 10^{-3}$  for  $RH_i = 121 - 170\%$  and  $f_{ice} = 0$  when  $RH_i < 121\%$ ) used to parameterise heterogeneous ice nucleation by glassy citric acid solution aerosol (see Chapter 4). Due to scatter in the ice particle concentration data, a certain amount of noise is present. The shaded region represents a region of uncertainty in which the signal to noise ratio is too low for an accurate estimation of the fraction frozen.

### 5.3.5 Iso-humid experiments to probe ice nucleation above $RH_g$

An interesting observation in this study was the apparent continuation of the heterogeneous nucleation of ice particles above the  $RH_g$  threshold, *i.e.* the point at which glassy aerosol could be expected to liquefy. Ice particle production was observed above  $RH_g$  for levoglucosan, raffinose/M5AS and raffinose aerosol as well as for citric acid (Figure 4.4). The rate at which glassy aerosol take up water and liquefy is kinetically limited by the diffusion of water from the surface of the aerosol droplets into the bulk (Zobrist et al., 2011; Koop et al., 2011). Tong et al. (2011) show that this process was delayed by 10s – 100s of seconds in supermicron sucrose droplets at room temperature, which might be consistent with the observation of ice particle production

above  $RH_g$ . It should be noted however, that the experiments described in this chapter used much smaller droplets and took place at much lower temperatures, and therefore deeper into the glassy regime, both of which may well affect any delay in water uptake. In order to explore this, ‘iso-humid’ experiments were performed in which the pumping speed was controlled to maintain the chamber humidity at close to constant  $RH_i$  ( $\pm 10\%$ ) above  $RH_g$ , but below the homogeneous freezing threshold, for periods on the order of 500 seconds. In separate expansions using raffinose/M5AS and raffinose particles, starting at 202 K and  $\sim 218$  K, respectively (Figure. 5.7), the ice nucleation onsets (vertical dashed black lines) occurred just below or at  $RH_g$  (dot-dot-dash red lines) and then ice particle production continued after  $RH_g$  was crossed. The ice nucleation onset for the expansion using levoglucosan solution aerosol at  $\sim 190$  K occurred well above the  $RH_g$  threshold, with ice particle production continuing as pumping went on (not shown).

There are several potential explanations for the nucleation of ice above  $RH_g$  but below the homogeneous nucleation threshold. Firstly, at the temperatures at which this behaviour was observed, and also at those found in the upper troposphere, the absolute amount of water vapour for a given relative humidity is much smaller than at room temperature. For this reason, the aerosol may take longer to liquefy than the 10s – 100s of seconds found in experiments performed using glassy sucrose droplets at room temperature (Tong et al., 2011). This would also be supported by the observations of Zobrist et al. (2011), who found that sucrose viscosities increased strongly with decreasing temperature and correspondingly that the diffusion of water molecules within the droplets was extremely slow. In the presented iso-humid experiments the aerosol could therefore have persisted in the glassy state for the duration of the experiments, allowing them to be available for heterogeneous ice nucleation.

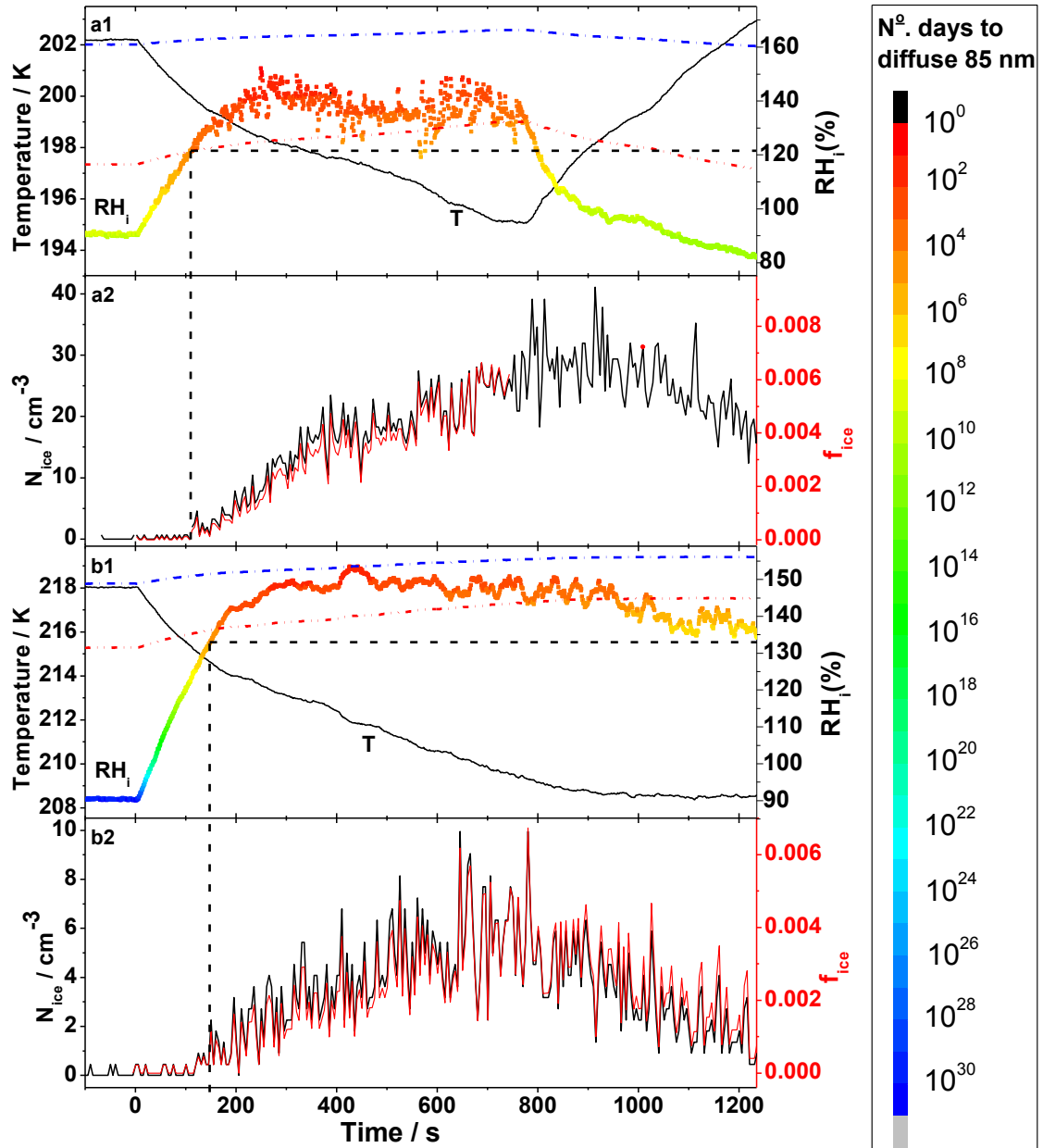


**Figure 5.7** Time series for ice production runs using raffinose/M5AS solution aerosol (Panels A1 and A2) and raffinose solution aerosol (Panels B1 and B2). The temperature trajectories are shown as solid black lines in panels A1 and B1. In these panels the RH<sub>i</sub> trajectories are displayed as colour mapped time series, the colour maps correspond to the estimated time taken for water molecules in the aerosol particles to diffuse 85 nm (the average radius of particles in this study). The humidity at which homogeneous ice nucleation is expected is shown in both cases as a dash-dot blue line. RH<sub>g</sub> is shown as red dot-dot-dash lines. The ice particle number concentration ( $N_{ice}$ ) and fraction frozen ( $f_{ice}$ ) are shown as black and red lines respectively. The onset of ice nucleation is represented in each case by black dashed lines.



To further investigate this possibility, the viscosity of the aerosol during the expansion experiments shown in Figure. 5.7 was estimated using an approach used previously by Murray (Murray, 2008a; Murray, 2008b). The super-Arrhenius dependency of viscosity ( $\eta_T$ ) with temperature above the glass transition temperature ( $T_g$ ) at a RH<sub>i</sub> can be approximated by the Williams-Landel-Ferry (WLF) equation:

$$\log \eta_T = \log \eta_{T_g} \left( \frac{17.44[T - T_g]}{51.6 + [T - T_g]} \right)$$

Equation 5.1

Where viscosity is in cP and  $T$  is the chamber gas temperature. The numerical values are typical for glass forming systems (Debenedetti and Stillinger, 2001). The molecular diffusion coefficient for the water molecules in the aerosol was then estimated based on the viscosity (converted to Pa s) using the Stokes-Einstein equation:

$$D_{\text{H}_2\text{O}} = \frac{kT}{6\pi\eta_T r_{\text{H}_2\text{O}}}$$

Equation 5.2

Where  $k$  is the Boltzmann constant and  $r_{\text{H}_2\text{O}}$  is the hydrodynamic radius of water (0.94 Å; (Murray, 2008a)). Finally, the time,  $t$ , for a water molecule to diffuse a root mean distance ( $x_i$ ) of 85 nm (the average radius of the aerosols used in this study, see Figure 5.8) was estimated using the calculated diffusion coefficients:

$$t = \frac{x_i^2}{6D_{\text{H}_2\text{O}}}$$

Equation 5.3

For both the experiments shown in Figure. 5.7 the time to diffuse 85 nm is displayed as a colour map overlaid on the RH<sub>i</sub> time series in panels a1 and b1. From this it can be seen that at even the highest humidities reached in the two experiments, the predicted time to diffuse 85 nm is estimated at days, much longer than the duration of the experiments, suggesting that the aerosols would not have had time to liquefy. It should be noted that the Stokes-Einstein equation is not expected to hold for liquids close to their glass transitions (Wilson et al., 2012b). The Stokes-Einstein equation is based on the model of a larger spherical molecule travelling through a continuum (Bones et al., 2012; Murray et al., 2012a). This is unlikely to reflect the reality for water

molecules moving through a matrix of much larger solute molecules such as raffinose, and diffusion times calculated here should therefore be considered very approximate. It should also be considered though that predictions made using the Stokes- Einstein equation for water diffusion within viscous sucrose solution droplets (viscosities between 1 and  $10^4$  Pa s) have been found to be consistent with experimental observations (Bones et al., 2012).

In the experiments performed by Bones et al. (2012) it was also found that on humidification an aqueous shell formed on the outside of the highly viscous sucrose and sucrose/NaCl droplets. This liquid shell was in equilibrium with the surrounding humidity. Recently published results found that ice nucleation occurred on highly viscous lab generated SOA particles after they began taking up water (Wang et al., 2012). It is possible therefore that the observed nucleation above  $RH_g$  in this chapter (and in Chapter 4) may be the result of ice nucleation occurring on glassy aerosol cores within aqueous shells of condensed water.

Another possible explanation for the nucleation of ice particles above  $RH_g$  is that all the ice particles nucleated below  $RH_g$  but only grew to a sufficiently large size to be counted as an ice particle by the WELAS instruments on a longer time scale. However, growth of ice particles under these conditions is most likely much more rapid than the duration of the iso-humid experiments; Möhler et al. (2006) estimate that the time taken to grow into the size range of the WELAS instruments after nucleation at the homogeneous threshold is 4 s at 223 K, 8 s at 210 K and 50 s at 196 K. Also, the rapid production of ice crystals in the experiments with liquid aerosol indicate that ice growth is unlikely to be a limiting factor. It is also possible that the estimate of the position of the  $RH_g$  line is inaccurate and the aerosol remained in a glassy state throughout the experiment. While this possibility is difficult to exclude for the data presented in this chapter, experiments with citric acid presented in Chapter 4 show that heterogeneous nucleation continued to a much higher  $RH_i$  above the expected  $RH_g$ . In the citric acid experiments greater pumping speeds were employed which drove the  $RH_i$  to larger values than was possible with the pumping speeds used in this study. Slower pumping speeds were used in the present study to avoid reaching the homogeneous freezing threshold which risked the pre-activation of the aerosol (See Chapter 6). In the citric acid experiments ice particles were produced up to ~40%  $RH_i$  above the best estimate of  $RH_g$  which suggests that the uncertainties in the ice nucleation onset humidity which

were on the order of 15%  $RH_i$  cannot account for the nucleation of ice above the estimated  $RH_g$  line.

Ice production at constant humidity might imply that the time dependence of nucleation on glassy aerosol is significant. Indeed, recent work on ice nucleation in the immersion mode by mineral dusts shows that time dependence may be significant under atmospherically relevant conditions (Murray et al., 2011; Broadley et al., 2012). This may be important in the TTL, because under the weakly forced conditions found in this region a parameterisation neglecting time dependence (*i.e.* a singular parameterisation) may under predict the number of ice nuclei. However, in order to generate iso-humid conditions the temperature was constantly dropping in order to compensate for the loss of water vapour to the growing ice crystals. It is not possible therefore to separate any time dependence from possible temperature dependence in these experiments, despite the  $RH_i$  remaining constant. Further work should be carried out to establish the time dependence of ice nucleation by glassy aerosol and for now a singular description for the parameterisation of ice nucleation by glassy aerosol is provided.

### 5.3.6 Parameterising ice nucleation by glassy aerosol

Modelling studies are required to gauge the importance of glassy aerosol in the nucleation of cirrus ice particles. A modelling study showing the impact of heterogeneous ice nucleation by glassy aerosol on cirrus cloud properties at TTL temperatures was described in Chapter 4, Section 4.3. That study used a one dimensional cloud model and represented glassy aerosol using a parameterisation (Figure 4.7) based on a linear fit to the fraction of glassy citric acid solution aerosol which nucleated ice heterogeneously ( $f_{ice}$ ) during an expansion (run 3, Chapter 4) at  $\sim 200$  K between 121 and 170%  $RH_i$ . The parameter  $f_{ice}$  can only be used accurately if the size distribution in the application is similar to the size distribution of aerosol particles in the experiments. To aid the prediction of the ice nucleation behaviour of aerosols with differing size distributions, the ice active surface site density ( $n_s$ ) (Connolly et al., 2009) was calculated. This parameter takes into consideration the aerosol surface area. Humidity and temperature dependent  $n_s$  values for each glassy system are presented. The values of  $n_s$  for glassy aerosol particles were also compared with those of other materials which have been reported in the literature.

### 5.3.6.1 Parameterisations based on the fraction activated to ice ( $f_{ice}$ )

A comparison of  $f_{ice}$  for aerosols that nucleated ice heterogeneously at temperatures  $\geq \sim 200$  K with the parameterisation for citric acid (for run 3, Chapter 4) is shown in Figure. 5.6. Data are shown up to the point at which the relative humidity reached a maximum. Peak  $RH_i$  in an expansion experiment is determined by the pumping speed and the number of ice crystals nucleated as well as the humidity at which they start nucleating. In general, the greater the pumping speed the higher the peak  $RH_i$ . As mentioned earlier, the peak  $RH_i$  in the citric acid experiments described in Chapter 4 was larger than that achieved here because the pumping speeds used were higher.

### 5.3.6.2 Parameterisations based on the ice active surface site density ( $n_s$ )

Nucleation is a stochastic time dependent process (Vonnegut and Baldwin, 1984; Broadley et al., 2012; Murray et al., 2011), but it has been suggested that the time dependence of nucleation is of secondary importance when compared to particle heterogeneity (Pruppacher and Klett, 1997; Vali, 2008). The assumption of time independence underpins the singular model and provides a simple way to parameterise ice nucleation data. Connolly et al. (2009) define  $n_s$  as  $n_s = -\ln(1-f_{ice})/\sigma$ , where  $\sigma$  is the surface area of the aerosol present during an experiment. This is similar to the volume based cumulative nucleus spectrum defined by Vali (1971),(1994). The ice active surface site density has been applied to a number of other experimental studies of different deposition mode ice nuclei (Connolly et al., 2009; Saunders et al., 2010; Steinke et al., 2011; Niemand et al., 2012a). It is a particularly useful quantity as it provides a surface area independent measurement of a material's ability to nucleate ice. It should be noted that when the singular approximation is applied to conditions of much slower cooling rate than were employed in the experiment upon which the parameterisation was based, the description may lead to an underestimate of the number of ice nuclei (Murray et al., 2011; Vonnegut and Baldwin, 1984).

In order to estimate the ice active surface site density for glassy aerosols it was assumed that the glassy particles were spherical in shape, and the total surface area of the aerosol was then estimated from size distributions taken prior to the start of expansion (Figure 5.8). The loss of aerosol particles during expansion has been

accounted for in the calculation by scaling the total surface area with the total aerosol number.

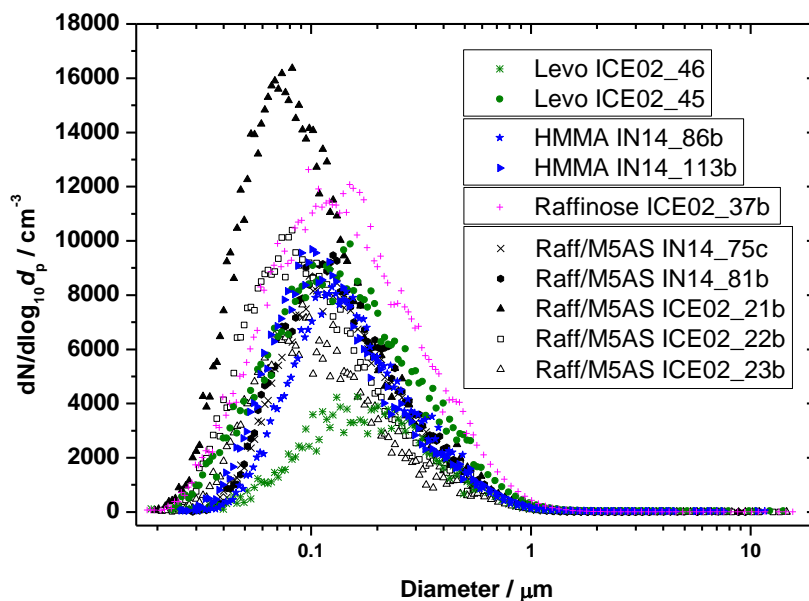


**Figure 5.8** A comparison of combined SMPS and APS size distributions of aerosols taken immediately prior to experiments shown in Figure 5.5. The size distributions of the aerosols used in ICE02 were found to be consistent with size distributions measured for citric acid aerosol during the ICE01 campaign (Figure 4.3). The average of the mean volume-equivalent sphere diameters ( $d_p$ ) of the aerosols was  $0.170 \pm 0.027 \mu\text{m}$ .

The ice active surface site density for expansion experiments with glassy aerosol, including citric acid (based on the parameterisation of  $f_{ice}$  from run 3 of the ICE01 campaign (Figure 4.7) and the aerosol size distribution shown in Figure 4.2), are compared in Figure 5.9. For the glassy aerosols tested in this study,  $n_s$  values at the onset of nucleation were similar ( $\sim 6 \times 10^8 \text{ m}^{-2}$ ). As humidity rose, new ice particles nucleated and there is a corresponding increase in  $n_s$ . Peak  $n_s$  values varied, but for most glassy aerosols the maximum values were in the region of  $\sim 1 \times 10^{10} \text{ m}^{-2}$ . Note that the peak  $n_s$  depended on the maximum supersaturation attained in an experiment; for example, in the experiment with glassy raffinose aerosol at 199.6 K (magenta stars), pumping was discontinued earlier and this resulted in smaller maximum  $n_s$  values ( $\sim 2.5 \times 10^9 \text{ m}^{-2}$ ). The rate of increase of  $n_s$  with  $\text{RH}_i$  and the humidity at which nucleation was first detected were dependent on composition of the aerosol and also the temperature at which the expansion took place. One notable difference is that the expansions with HMMA aerosol had a more rapid rate of increase of  $n_s$  as the humidity

increased than was found for the other glassy systems. Fits to all of the calculated  $n_s$  values shown in Figure 5.9 are given in Table 5.2.

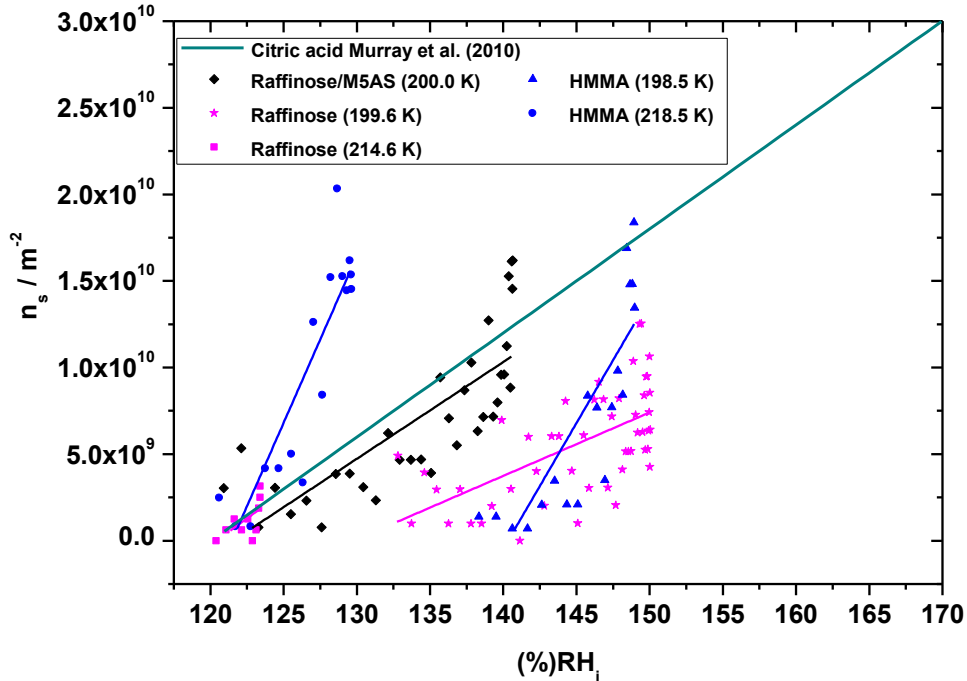


**Figure 5.9** The ice active surface site densities ( $n_s$ ) for glassy aerosols which nucleated ice heterogeneously (see Figure 5.5). Linear fits to each dataset are shown in the corresponding colour. The solid cyan line is  $n_s$  for glassy citric acid aerosol calculated using the fraction frozen parameterisation from Chapter 4 (shown in Figure 5.6 and Figure 4.11) and the size distribution for the aerosol used in the experiment upon which the parameterisation is based. Table 5.2 contains equations for linear fits to  $n_s$  for aerosols from this study and glassy citric acid aerosol.

The range of observed onset humidities makes the parameterisation of glassy aerosol for modelling purposes non-trivial. The atmospheric aerosol particles in a particular location are likely to have a range of compositions and any that are glassy are likely therefore to have a range of ice nucleating abilities. Ice nucleation will be dominated by the ice nuclei in the aerosol that can catalyse ice formation at the lowest humidities. Since citric acid is amongst the materials which nucleate ice at the lowest humidity it seems sensible to use the parameterisation for ice nucleation on aqueous citric acid in cirrus models. In addition, the fit to citric acid is valid over the widest range of relative humidity which also lends itself to use in models.

**Table 5.2** Parameters for the linear fits to  $n_s$  shown in Figure 5.9 and Figure 5.10 as a function of  $RH_i$ . Also included is  $n_s$  for glassy citric acid aerosol, calculated based on the parameterisation of  $f_{ice}$  vs.  $RH_i$  (Figure 4.7). Note that each fit is only valid for the range of  $RH_i$  shown in the rightmost column of the table.

Aerosol	Temperature of ice nucleation onset / K	Linear fit ( $n_s = m \cdot RH_i + c$ )		Valid $RH_i$ range for fit
		$m$	$c$	
Raffinose/M5AS	200.0	$5.5815 \times 10^8$	$-6.7861 \times 10^{10}$	$120.9 \leq RH_i \leq 140.6$
Raffinose	199.6	$6.15127 \times 10^8$	$-7.4095 \times 10^{10}$	$120.4 \leq RH_i \leq 123.4$
Raffinose	214.6	$3.65814 \times 10^8$	$-4.74938 \times 10^{10}$	$132.8 \leq RH_i \leq 150.0$
HMMA	198.5	$1.45114 \times 10^9$	$-2.03713 \times 10^{11}$	$138.3 \leq RH_i \leq 149.0$
HMMA	218.5	$1.92381 \times 10^9$	$-2.33764 \times 10^{11}$	$120.6 \leq RH_i \leq 129.6$
Citric acid	200.5	$6.00235 \times 10^8$	$-7.20796 \times 10^{10}$	$121.0 \leq RH_i \leq 170.0$

For comparison,  $n_s$  data for other atmospherically relevant ice nuclei are shown together with  $n_s$  data for glassy aerosol in Figure 5.10. In general, Arizona Test Dust (ATD, grey triangles) (Connolly et al., 2009), volcanic ash from the Eyjafjallajökull eruption (grey circles) (Steinke et al., 2011) and iron oxide nanoparticles (dashed grey line) (Saunders et al., 2010) have higher  $n_s$  values and are therefore more efficient ice nuclei than glassy aerosol per unit of surface area. While mineral dust is clearly a more effective ice nucleus, the number density (and therefore surface area) of aerosol particles which are potentially glassy far exceeds that of mineral dust in the upper troposphere (Froyd et al., 2010). The implications of this are further discussed in the next section.

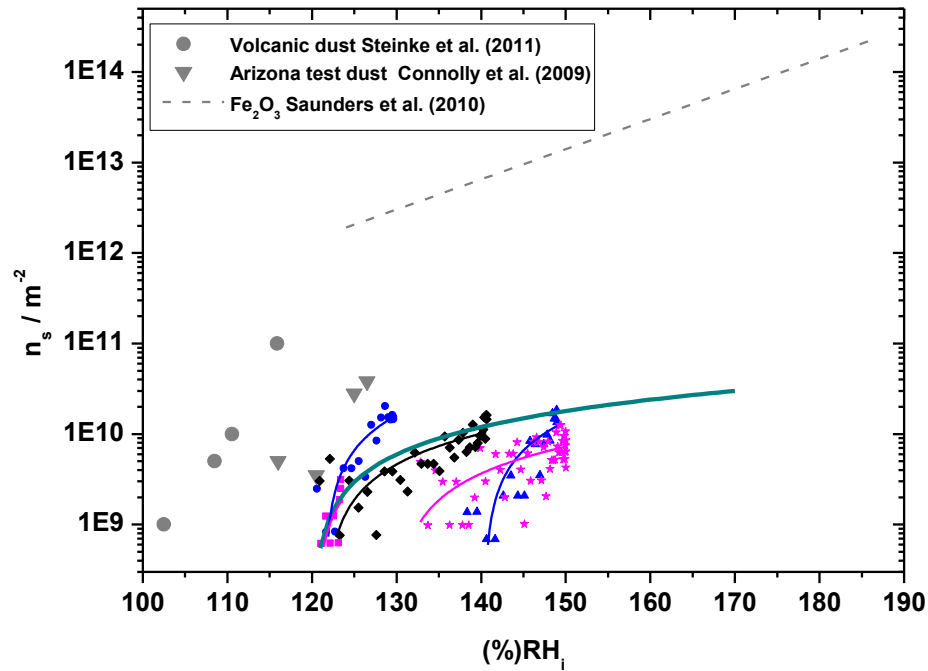


**Figure 5.10** A comparison of  $n_s$  for glassy aerosols from this study and other IN species (see Figure 5.6 legend for symbol details). Glassy citric acid aerosol  $n_s$  is also shown (solid cyan line, see Figure 5.9 caption for details). Linear fits to the data from this study are shown in the corresponding colour. Volcanic dust at  $\sim 225$  K, (grey circles) (Steinke et al., 2011), Arizona test dust (ATD) at 238 – 248 K (grey downwards pointing triangles) (Connolly et al., 2009) (note that these are revised figures for ATD, based on a re-analysis by Niemand et al. (Niemand et al., 2012b)) and a parameterisation of  $n_s$  for iron oxide nanoparticles at 190 K (grey dashed line) (Saunders et al., 2010) are shown. The parameters to the fits to  $n_s$  vs.  $\text{RH}_i$  for all of the glassy aerosols shown in this figure (solid lines) are included in Table 5.2.

### 5.3.7 The impact of glassy aerosol on cirrus formation outside the TTL

The results presented in this chapter show that glassy aerosol can nucleate ice under conditions relevant for ice cloud formation in parts of the atmosphere which are warmer than the very cold TTL. The possibility that ice nucleation on glassy aerosol might compete with ice nucleation on mineral dusts at warmer cirrus temperatures is now explored. Starting with a total of  $300 \text{ cm}^{-3}$  aerosol particles and based on the measurements of DeMott et al. (2003) it is taken that 1% of these were mineral dust particles and 86% were organic sulphate particles. It is assumed that mineral dust



particles have a diameter of 500 nm and the organic-sulphate particles have a diameter of 150 nm. It is also assumed that only 50% of the organic-sulphate aerosol particles are glassy and that 50% of the mineral dust particles have been deactivated by coatings. Using an  $n_s$  value for mineral dust of  $3 \times 10^{10} \text{ m}^{-2}$  and a value of  $3 \times 10^9 \text{ m}^{-2}$  for sulphate-organic aerosol at 125% RH<sub>i</sub> (Figure. 5.10), it is estimated that mineral dust and organic-sulphate particles would nucleate comparable numbers of ice particles ( $0.033$  vs.  $0.027 \text{ cm}^{-3}$ ). The total number of ice particles nucleated would be  $\sim 0.060 \text{ cm}^{-3}$ , which is consistent with the observed mean ice particle number density in mid-latitude cirrus (Krämer et al., 2009). This estimation suggests amorphous solid organic aerosol could play a role in mid-latitude cirrus formation.

## 5.4 Summary and conclusions

The main aim of this study was to compare the ice nucleating properties of a range of atmospherically relevant glass forming compounds under conditions relevant for cirrus cloud formation. During the ICE01 campaign (Chapter 4) glassy citric acid solution aerosol particles were found to nucleate ice heterogeneously at temperatures below  $T_g'$  (the glass transition temperature at ice saturation, 100% RH<sub>i</sub>). This study tested the ice nucleation efficiency of atmospherically relevant aerosol species with  $T_g'$  close to that of citric acid (raffinose/M5AS and levoglucosan solution aerosols) and species with much higher  $T_g'$  (raffinose and HMMA solution aerosols). At temperatures  $\leq 200 \text{ K}$  all the aerosol types acted as heterogeneous ice nuclei, catalysing ice production below the homogeneous freezing threshold (Figure. 5.5). The higher temperature glass formers raffinose and HMMA were also found to nucleate ice heterogeneously at higher temperatures (214.6 K and 218.5 K respectively). These results suggest that heterogeneous ice nucleation is a general property of glassy aerosols and that the temperature at which they are able to nucleate ice is strongly related to their glass transition temperature.

In a very recent study Baustian et al. (2011) used Raman microscopy in conjunction with a humidity controlled cold stage to investigate the ice nucleation properties of aqueous super-micron sized glassy particles. It was found that glassy sucrose, dextrose and citric acid solution particles also nucleate ice heterogeneously in the deposition mode. It has also been found recently by Wang et al. (2012) that SOA particles in a glassy state generated by the oxidation of naphthalene by OH radicals

heterogeneously nucleate ice . These results support the conclusion that heterogeneous ice nucleation is a general property of aqueous glassy aerosol particles.

The onset humidity of heterogeneous ice formation was found to be dependent on both the temperature and the chemical composition of the aerosol used. With the exception of raffinose aerosol, the heterogeneous ice nucleation onsets increased at lower temperatures. A wide range of onset humidities were observed; for instance glassy levoglucosan aerosol nucleated ice at  $155 \pm 8\%$  RH<sub>i</sub> at 190.8 K whereas glassy HMMA aerosol nucleated ice heterogeneously at  $120 \pm 5\%$  RH<sub>i</sub> at 218.5 K.

The range of observed onset humidities makes the parameterisation of glassy aerosol for modelling purposes non-trivial. Aerosol particles that nucleate ice at lower humidities are likely to be the dominant source of ice particles in a cloud, as early nucleation is likely to prevent the humidity rising significantly. The lowest humidity onsets for ice nucleation were found for Raffinose, HMMA and the raffinose/M5AS aerosol which were all found to nucleate ice at humidities as low as  $\sim 120\%$  RH<sub>i</sub>, which is consistent with the onsets found for glassy citric acid aerosol (Chapter 4). For modelling ice nucleation by glassy aerosol it is recommended that the parameterisation of the ice active surface site density,  $n_s$ , of glassy citric acid aerosol as a function of RH<sub>i</sub> (Table 5.2), which is based on data from the ICE01 campaign (Chapter 4), is used. It is a general representation of the properties found in this study and it should be used as a basis for ice nucleation by the most 'ice active' glassy aerosol.

In a study of ice nuclei composition in free tropospheric air, DeMott et al. (2003) found that 25% of ice nuclei were composed of sulphate-organic mixtures compared to 33% which were mineral dust and fly ash. It is shown using an  $n_s$  value for glassy aerosol based on data from this study that glassy sulphate-organic aerosol might account for the fraction of sulphate-organic ice nuclei observed by DeMott et al. (2003). This indicates that heterogeneous ice nucleation by glassy aerosol particles may be of importance at warmer temperatures and outside of the TTL.

## Chapter 6: ICE02 campaign: Enhanced ice nucleation by ice processed glassy aerosols

Aerosol particles found in the upper troposphere are likely to undergo repeated cloud formation cycles. The deposition mode ice nucleating ability of insoluble particles such as mineral dusts has been observed to become enhanced in repeated ice nucleation experiments. This chapter describes the enhancement of the ice nucleation properties of glassy/ultra viscous aerosols that was observed when aerosols of four different compositions were exposed to repeated homogeneous cloud formation cycles at the AIDA cloud simulation Chamber.

*Experiments took place as part of the ICE02 campaign and data from this chapter plus additional data collected by the Robert Wagner and the AIDA team were published in Atmospheric Chemistry and Physics Discussions (Wagner, R., Möhler, O., Saathoff, H., Schnaiter, M., Skrotzki, J., Leisner, T., Wilson, T. W., Malkin, T. L., and Murray, B. J., Ice cloud processing of ultra-viscous/glassy aerosol particles leads to enhanced ice nucleation ability, Atmospheric Chemistry and Physics, 12, 8589-8610, 2012, doi:10.5194/acp-12-8589-2012). TWW directed experiments and analysed results in collaboration with RW and BJM. TWW also helped write a successful proposal to EUROCHAMP 2 to fund this work. RW oversaw the operation of the AIDA chamber, directed experiments and processed and analysed data and wrote the manuscript in collaboration with TWW and BJM. TLM provided additional x-ray diffraction data in collaboration with TWW. BJM oversaw the study and sought financial support. OM and TL led the AIDA team, which included HS, MS, JS and who operated the AIDA chamber and associated equipment.*

### 6.1 Aerosols chosen for study

Repeat expansion cycles were performed using aqueous raffinose, HMMA and raffinose/M5AS aerosols. For more information including molecular structures,  $RH_g$  thresholds and information regarding the atmospheric relevance of the chosen aerosols please see Chapter 5, Section 5.1. For size distributions of the aerosols used in the experiments in this chapter, see Figure 5.8

## 6.2 Results

The results presented in the following sections are from experiments directed by TWW in collaboration with RW and BJM. Some further experiments were performed by RW and the AIDA team for which data is not shown, but the results of which are summarised. Full details of those experiments are available in Wagner et al. (2012b). The experimental results in this chapter have been separated depending on the aerosol composition that was used. The first section shows the results of a set of experiments that used HMMA aerosol and which illustrate clearly the circumstances under which the enhancement of ice nucleation occurred.

### 6.2.1 HMMA

The temperature/time profile shown in Figure 6.1, panel A, is for a set of expansion experiments (runs 1 – 5) that used HMMA solution aerosol. Panel B of Figure 6.1 shows the state diagram for HMMA solution aerosol, including the homogeneous freezing threshold (red dashed line) (Koop et al., 2000), the ice-liquid equilibrium (black solid line), the HMMA solution aerosol  $RH_g$  threshold (green solid line) and its associated upper and lower uncertainty limits (green dotted lines) (Zobrist et al., 2008). Also shown are the approximate starting points of expansion in runs 1 – 5 (green dots), which are shown on the ice-liquid line but which in reality would be to the right of the line, due to the chamber humidity being 90-95%  $RH_{liq}$  at equilibrium.

The aerosol was injected into the chamber at  $\sim 248$  K, and an expansion (run 1) was then performed. At this temperature the aerosol was well above  $T_g'$  and also above the maximum temperature at which homogeneous ice nucleation can occur in aqueous aerosol droplets of the size used in the experiment. No heterogeneous ice nucleation was observed indicating that the aerosol was liquid. After refilling the chamber with dry air, it was cooled to  $\sim 220$  K, well into the glassy regime, and an expansion was performed (run 2). At this temperature the now glassy aerosol particles were found to nucleate ice heterogeneously. The results of this expansion have been detailed already in Chapter 5, (Figure. 5.5). Hence briefly, ice nucleated at 116%  $RH_i$ , well below the AIDA homogeneous threshold (based on homogeneous nucleation in sulphuric acid droplets at AIDA (Möhler et al., 2003)) and also below  $RH_g$ . Pumping was stopped before  $RH_g$  was crossed and consequently before any homogeneous ice nucleation could occur. At the end of pumping the ice particle concentration had reached  $\sim 25$   $cm^{-3}$ . The ice

particles were sublimed after 200 s by refilling the chamber. This avoided substantial sedimentation of ice particles, ensuring that the aerosol from which they nucleated was still present in the chamber for the following run.

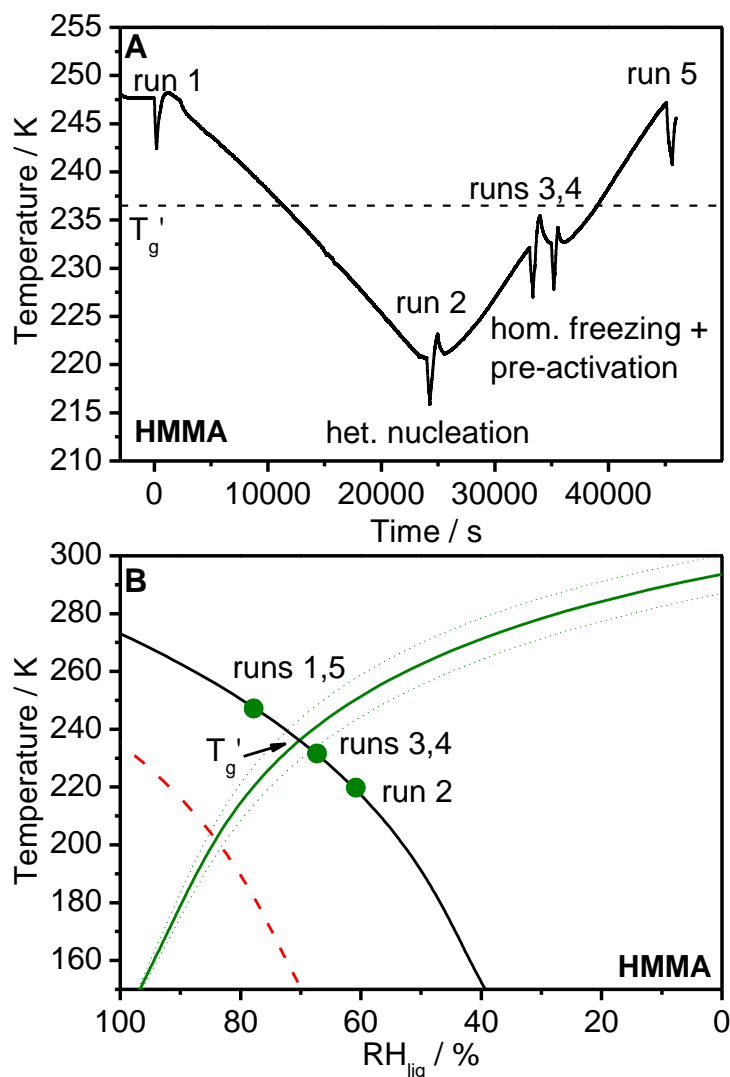


**Figure 6.1** Panel A shows the experimental temperature time series for expansion runs (1 – 5) that used HMMA aerosol. Panel B shows the approximate starting points for expansions 1 – 5 in the HMMA solution state diagram. See text for details.

The temperature of the chamber was increased to  $\sim 232$  K, close to the lower uncertainty limit of  $T_g'$ . At this temperature two expansion experiments were performed in succession (runs 3 and 4), the results of which are shown in detail in Figure 6.2. In run 3, the aerosol froze homogeneously with only  $\sim 1 \text{ cm}^{-3}$  ice particles nucleated prior to the homogeneous nucleation threshold being reached, despite the experimental temperature/humidity trajectory starting below  $RH_g$ . This indicates that the ice nucleation properties of the aerosols were not affected by the previous heterogeneous

ice nucleation and that they liquefied on crossing the  $RH_g$  threshold, allowing water uptake and homogeneous freezing. After homogeneous ice nucleation occurred, the chamber humidity fell rapidly (within  $\sim 20$  s) to below  $RH_g$ . After pumping finished, the nucleated ice particles were sublimated as the chamber humidity dropped to  $\sim 72\%$   $RH_i$  during refilling. The following expansion (run 4) was started about 30 mins after the start of run 3.

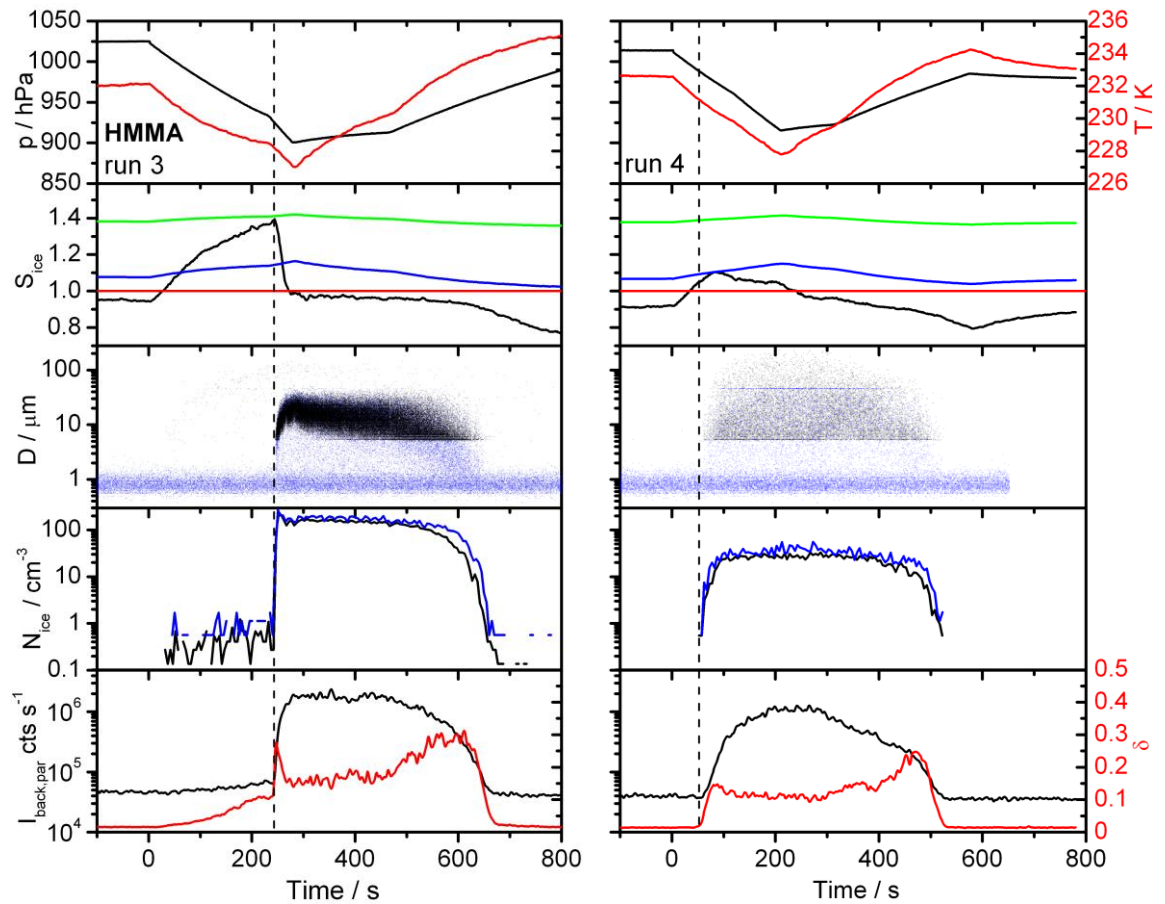


**Figure 6.2** Experimental results for runs 3 and 4 (Figure 6.1A) that used HMMA aerosol. In run 3, homogeneous nucleation occurred at the AIDA homogeneous nucleation threshold (Green solid line). This caused enhancement of the aerosol’s ice nucleation ability in the following run in which ice nucleated very close to ice saturation (red horizontal line second panel down) at 105%  $RH_i$ . The  $RH_g$  threshold is also shown (solid blue line, second panel down) (Zobrist et al. (2008)) and in each panel data colour is coordinated to the colour of the corresponding axis label. Particle diameter (third panel down) and  $N_{ice}$  (fourth panel down) data from the WELAS 1 and WELAS 2 OPC’s are displayed in blue and black respectively. Vertical black dashed lines indicate the onset of ice nucleation based on the change in the backscattering linear depolarisation ratio  $\delta$  in the bottom panel, which also shows the backscattered intensity parallel to the incident polarisation state of the laser light,  $I_{back,par}$ .

In run 4 (right hand panel, Figure 6.2), instead of freezing homogeneously, around  $30 \text{ cm}^{-3}$  ice particles nucleated at 105% RH<sub>i</sub>. This is a much lower onset humidity than was observed for heterogeneous ice nucleation by glassy HMMA aerosol and other glassy aerosol compositions used in ICE01 and ICE02. It should also be noted that unlike in run 3, the chamber humidity in run 4 did not reach high enough levels to cross the RH<sub>g</sub> threshold. The observed change in behaviour is particularly striking as runs 3 and 4 started at such similar temperatures. After the expansion, the nucleated ice particles were again sublimed after only a short observational period to prevent their sedimentation. The final expansion (run 5) took place after the chamber was warmed back up to 247 K, close to the temperature of run 1. In this expansion no pre-activation behaviour was observed, with only  $0.1 \text{ cm}^{-3}$  ice particles nucleating ice heterogeneously.

The phenomenon of aerosol ice nucleation ability enhancement after having nucleated ice homogeneously outlined above was also observed for the other aerosols studied in ICE02. This behaviour was dubbed aerosol ‘pre-activation’ due to its apparent similarity to the pre-activation observed for other IN such as mineral dust.

## **6.2.2 Raffinose**

### **6.2.2.1 Pre-activation in a repetitive series of expansions**

The set of experiments shown in Figure 6.3 was designed to test the effect of repeated expansions on glassy aerosol particles. They were preceded by a long cooling and heating cycle to test for crystallisation of the raffinose solute (for a detailed discussion about the likelihood of aerosol crystallisation during ICE02 see Chapter 5, Section 5.2).

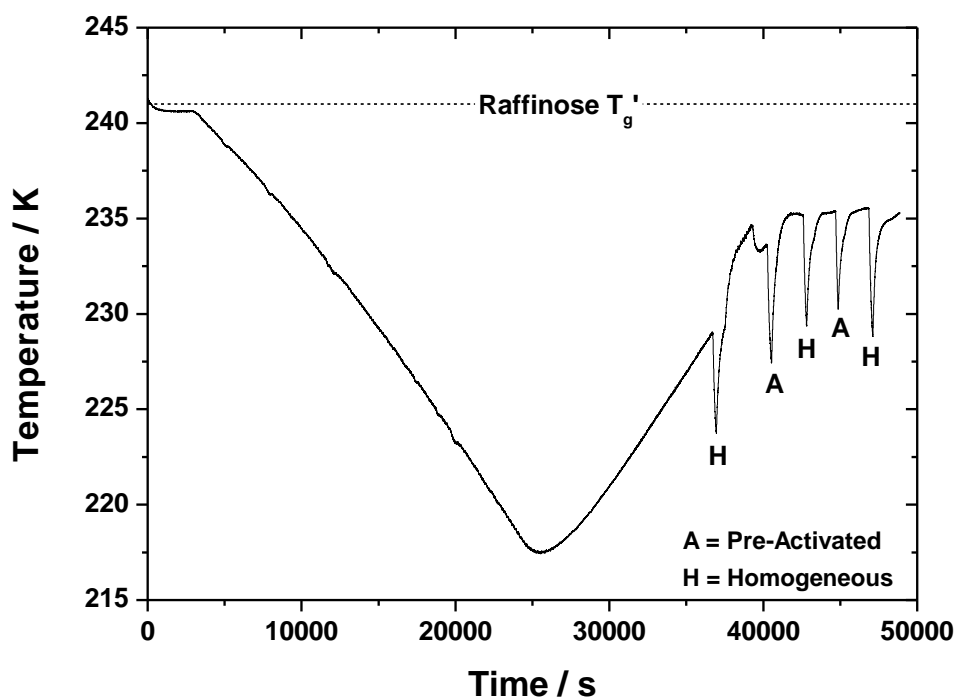


**Figure 6.3** Temperature profile for an expansion series using raffinose aerosol. The four expansion experiments are labelled ‘H’ or ‘A’ to indicate the presence of homogeneous ice nucleation or pre-activation behaviour during the expansion.

The temperature, humidity,  $N_{ice}$  and depolarisation profiles of the expansion experiments are shown in Figure 6.4, along with the AIDA homogeneous freezing threshold and the  $RH_g$  threshold for raffinose solution aerosol (Zobrist et al., 2008). During the first expansion after cooling to 217 K and warming back up to 229 K homogeneous ice nucleation was observed, with no significant heterogeneous mode ( $< 1 \text{ cm}^{-1}$  particles nucleated before the homogeneous threshold). The experimental humidity trajectory in this expansion crossed the  $RH_g$  threshold into the liquid region of the state diagram, before crossing it in the reverse direction after homogeneous nucleation occurred. This was also the case for the homogeneous experiments using HMMA that resulted in pre-activation (Figure 6.2). The resulting ice cloud was observed for a longer period of time (750 s) than was the case for the HMMA experiments.

In the second expansion, which took place at a slightly higher temperature ( $\sim 233 \text{ K}$ ), a large change in  $\delta$  and a rapid increase in  $N_{ice}$  to  $\sim 9 \text{ cm}^{-3}$  was observed just above ice saturation. This is consistent with the enhancement in the ice nucleation



efficiency of the HMMA aerosol, in the run following homogeneous ice nucleation. This indicates that the raffinose aerosol had also become ‘pre-activated’, apparently by the same mechanism as the HMMA aerosol. After refilling the chamber,  $< 1 \text{ cm}^{-3}$  ice particles nucleated prior to nucleation at the homogeneous threshold in run 3. This was despite the run taking place at almost the same temperature as run 2. At the same temperature, early ice nucleation very similar to that observed in run 2 occurred in run 4, presumably the result of the homogeneous ice nucleation in run 3. In the final run, again homogeneous ice nucleation was observed with only  $\sim 1 \text{ cm}^{-3}$  ice particles nucleating heterogeneously.

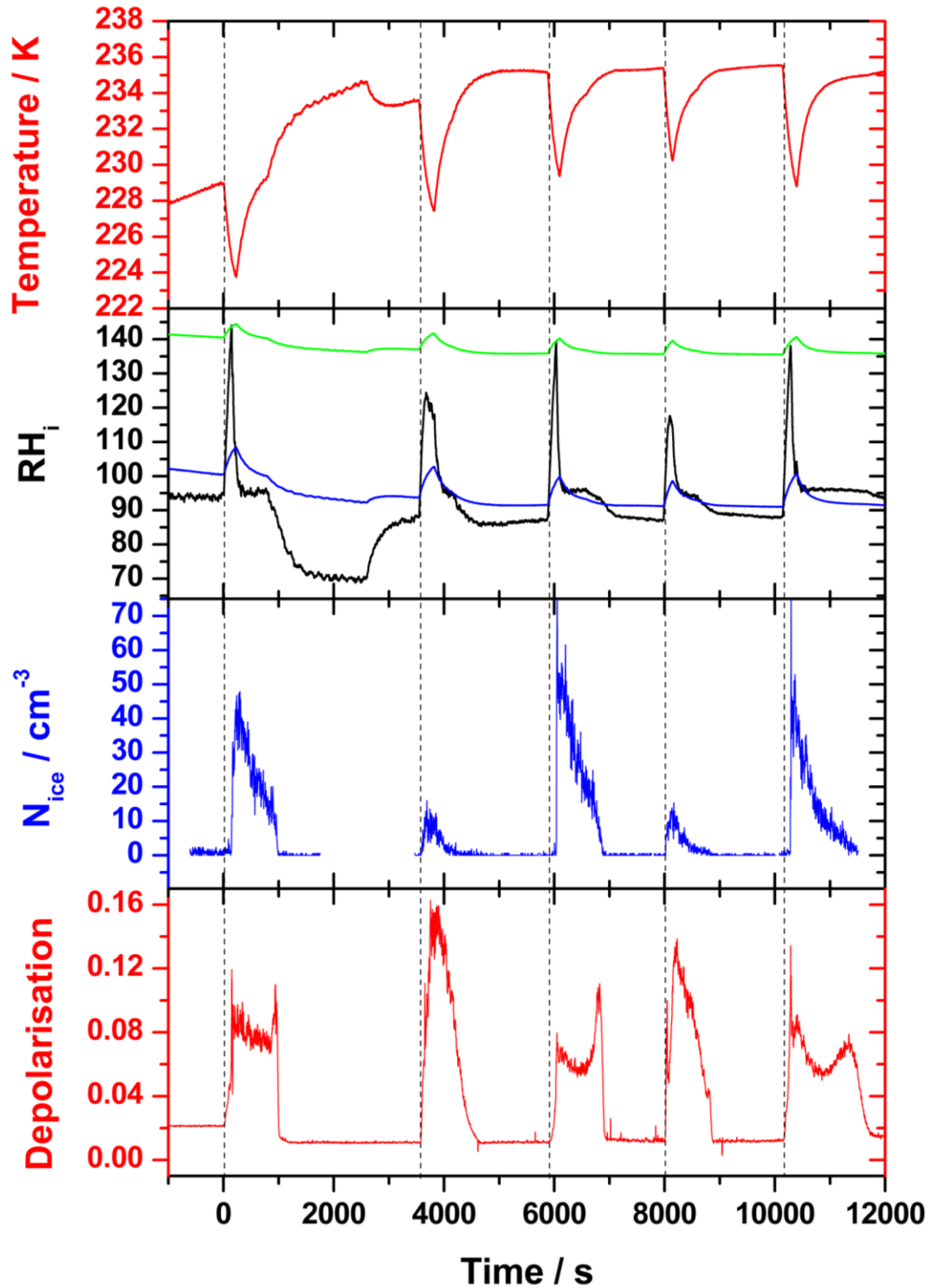


**Figure 6.4** Results for the experimental series of expansions shown in Figure 6.3 after  $\sim 35000$  s. Note that the second panel down which shows the chamber humidity (black solid line) also includes the AIDA homogeneous ice nucleation threshold (green line) and the  $RH_g$  threshold (blue line) (Zobrist et al., 2008). The vertical black dashed lines mark the time at which the chamber humidity passed 100%  $RH_i$ .

It appeared from the experiments shown in Figure 6.4 that the pre-activation behaviour was switching off in the runs that came immediately after runs in which pre-activated aerosols nucleated ice. A further series of experiments using raffinose solution aerosol at a similar temperature were performed separately by RW and the AIDA team. In that experimental series, the chamber was refilled at the end of pumping after a much shorter period of time than the experiments shown in Figure 6.4 (10s of seconds rather than 100s of seconds). Rather than the previously observed switching off of pre-activation in a succeeding run, there remained a comparable number of pre-activated particles in repeated expansion experiments. This strongly suggests that the switching off was the result of ice particles growing very large and sedimenting out, thus permanently removing the pre-activated IN from the chamber (Wagner et al., 2012b). A gradual decrease in  $N_{ice}$  and increase in the ice nucleation onset humidity for repeat expansions with a pre-activated aerosol was observed by Wagner et al. (2012), which is consistent with the loss of a few particles during each expansion.

#### **6.2.2.2 Conservation of pre-activation for long time periods under subsaturated conditions**

The examples shown of pre-activation in glassy aerosol have thus far been in expansions that followed homogeneous freezing within a relatively short period of time (at most 1 hour). During this time the particles were exposed to significant subsaturations with respect to ice (up to 20 minutes at  $\sim 70\%$  RH<sub>i</sub>). The experimental series presented in this section tested the effect of leaving raffinose aerosol for  $\sim 2.5$  hours at humidities between 70 and 80% RH<sub>i</sub>.

The temperature profile of the experimental series is shown in Figure 6.5. After injection at 256 K and an expansion was performed in the liquid regime to test for water uptake by the aerosol (no significant heterogeneous ice nucleation occurred). After refilling the aerosol was then cooled to below  $T_g'$  and an expansion was performed at 235 K (run 2). The chamber humidity crossed RH<sub>g</sub> and only  $0.5\text{ cm}^{-3}$  ice particles nucleated prior to  $\sim 100\text{ cm}^{-3}$  nucleating at the homogeneous threshold (Figure 6.6). The ice particles were sublimed by refilling the chamber, during which the humidity reached a minimum of  $\sim 70\%$  RH<sub>i</sub>. The chamber was then cooled to 224 K, during which RH<sub>i</sub> remained at  $\sim 80\%$  (this is unusually low for AIDA whilst cooling at equilibrium, and

may have been due to there being only a partial covering of ice on the chamber walls). This took approximately two and a half hours.

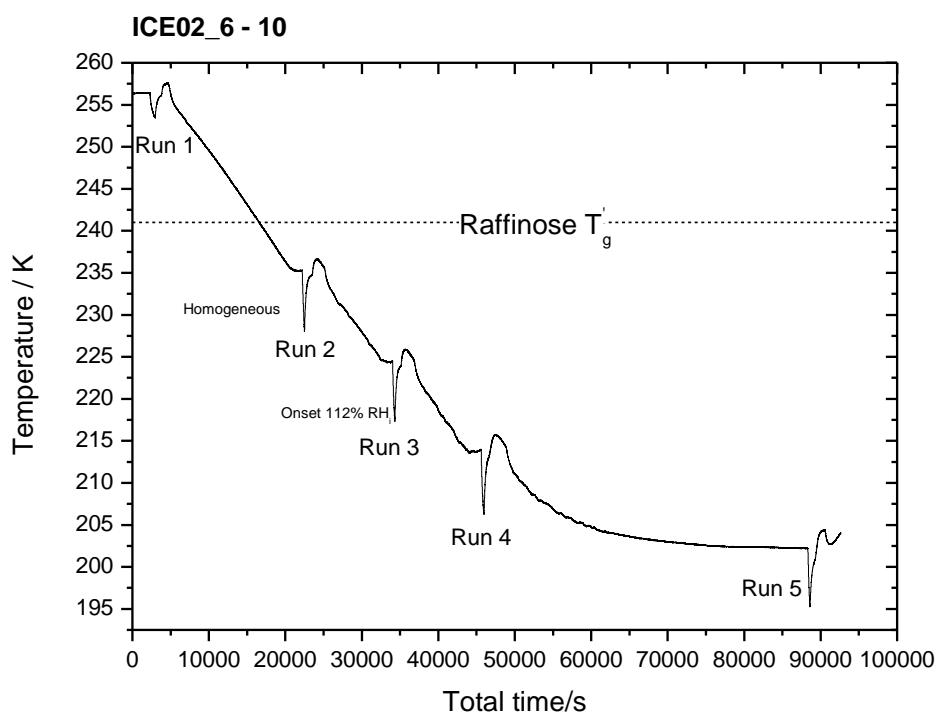


**Figure 6.5** Temperature profile experiments using raffinose aerosol. Pre-activation was observed in run 3 after homogeneous nucleation in run 2, despite  $\sim 2.5$  hours at  $\sim 70\%$  RH<sub>i</sub>.

In the expansion started at 224 K (run 3),  $10 \text{ cm}^{-3}$  ice particles nucleated with an onset at 112% RH<sub>i</sub> (Figure 6.6). The homogeneous ice nucleation that took place in run 2 was at the same temperature at which homogeneous ice nucleation caused pre-activation of raffinose aerosol in the expansions Figure 6.4 ( $\sim 230 \text{ K}$ ) indicating that the aerosol in run 3 might be pre-activated. It is possible that the early nucleation observed in run 3 was the result of heterogeneous ice nucleation on glassy aerosol, as the nucleation occurred well below  $T'_g$ . Heterogeneous nucleation on glassy aerosol is less likely than ice nucleation by pre-activated aerosol however, as it would be in contradiction of the experiment described in Chapter 5 (Figure 5.2) that used raffinose aerosol and started at only a slightly higher temperature than run 3. No significant heterogeneous ice nucleation was observed in that experiment, instead ice nucleated at the homogeneous threshold. The run was not preceded by any expansions. The available evidence suggests that the same aerosol pre-activation behaviour that was observed in the experiments shown in Figure 6.4 and for HMMA aerosol was responsible for the

early ice nucleation observed in run 3. It also indicates therefore that aerosol is able to remain pre-activated for periods of up to ~2.5 hours at between 70 and 80% RH<sub>i</sub>.

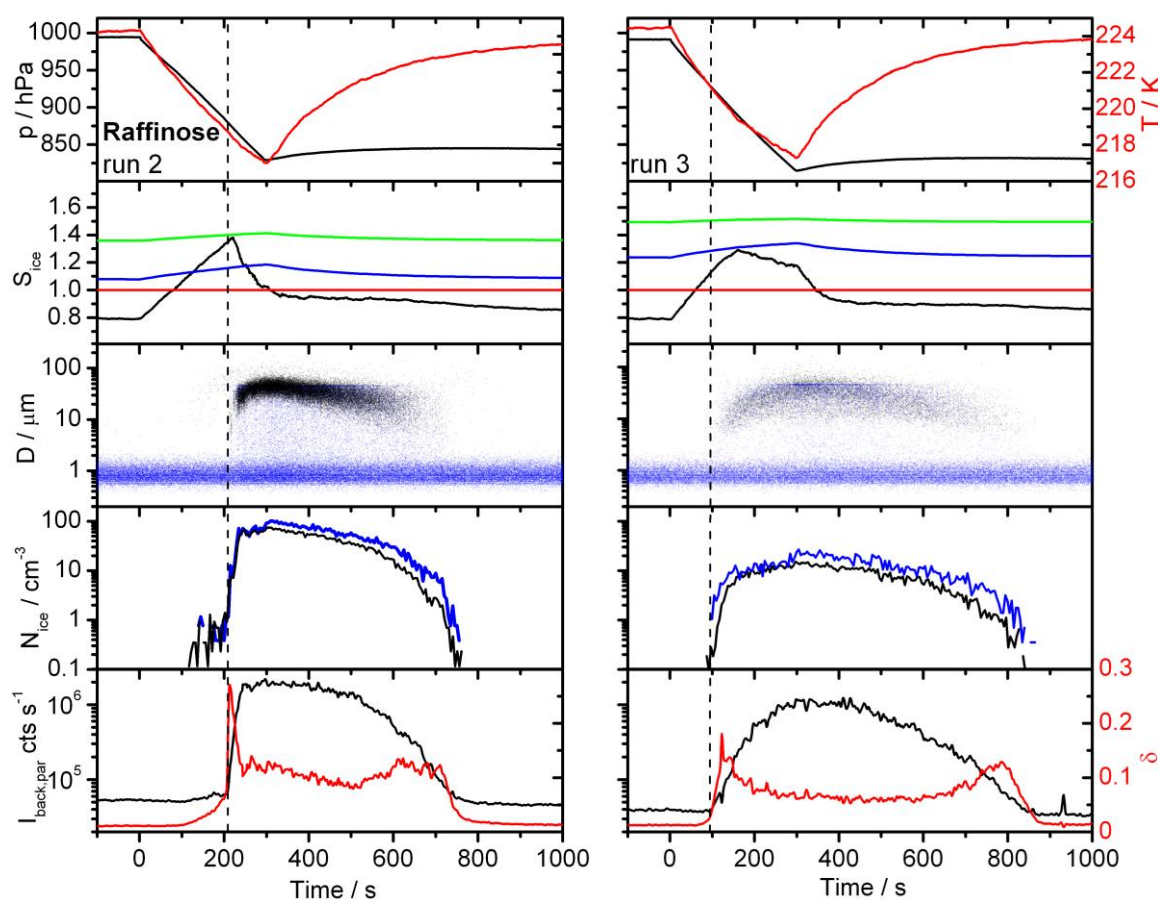


**Figure 6.6** Experimental data for runs 2 and 3 which used raffinose aerosol. Early onset ice nucleation consistent with pre-activation was observed in run 3 after homogeneous ice nucleation in run 2. This was despite the aerosol being exposed to humidities between 70 and 80% RH<sub>i</sub> for 2.5 hours between the two runs. See Figure 6.2 caption for full details of each panels contents.

Ice nucleation was also observed below the homogeneous freezing threshold in the runs that occurred later in the experimental series at lower temperatures (runs 4 and 5). These expansions started below 217 K, the highest temperature at which expansions were started in which raffinose aerosol was found to nucleate ice heterogeneously (Figure. 5.5). It is therefore impossible to tell from the experimental data (not shown) whether this nucleation was the result of some aerosol particles remaining pre-activated or whether standard heterogeneous ice nucleation occurred on glassy aerosol. Ice particles could also have resulted from a mixture of both pre-activated and heterogeneous nucleation.

### 6.2.3 Raffinose/M5AS

In this section two contrasting experimental series which used raffinose/M5AS aerosol are discussed in which the pre-activation aerosol is shown to be very sensitive to temperature. In the first series (temperature profile shown in Figure 6.7) aerosol was injected at 236 K, the chamber was cooled to 193 K and then an expansion was performed (run 1A, not shown). At this temperature the aerosol were well into the glassy region and heterogeneous ice nucleation was observed. Pumping was stopped before the humidity reached the homogeneous threshold.

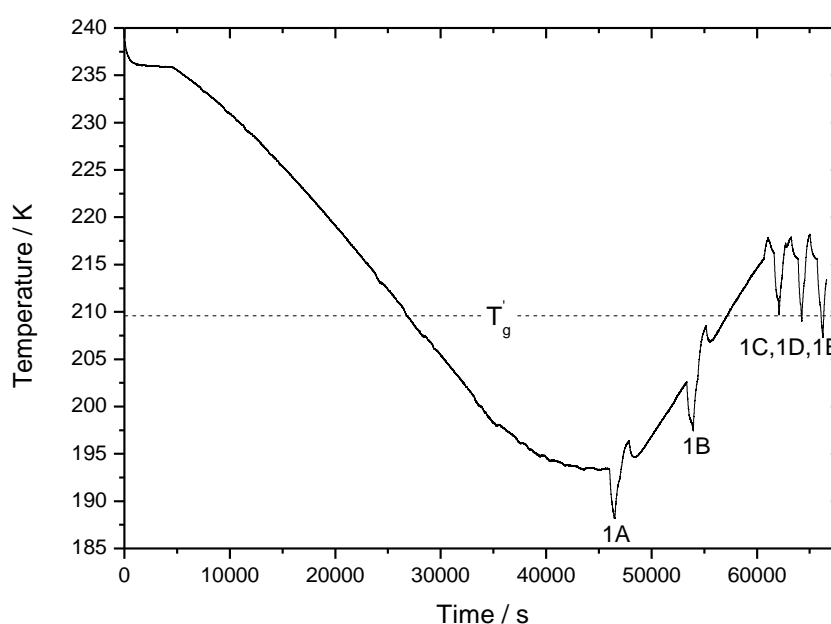


**Figure 6.7** Temperature profile for an experimental series using raffinose/M5AS aerosol. Early onset ice nucleation consistent with pre-activation was observed in runs 1D and 1E after homogeneous ice nucleation in the run 1C.

Once refilling was complete, the chamber was warmed to 202 K and another expansion was performed (run 1B, Figure 6.8). Ice nucleation was again observed below the homogeneous threshold, with an onset at around 120%  $RH_i$  and  $\sim 10 \text{ cm}^{-3}$  ice particles nucleating by the end of pumping. The ice onset humidity and  $N_{ice}$  for 1B are in very good agreement with an expansion that was performed at the same temperature with raffinose/M5AS aerosol which had not been exposed previously to heterogeneous (or any other) ice nucleation (See Figure. 5.5). This suggests that the heterogeneous ice nucleation that occurred in run 1A did not stimulate aerosol pre-activation in run 1B.

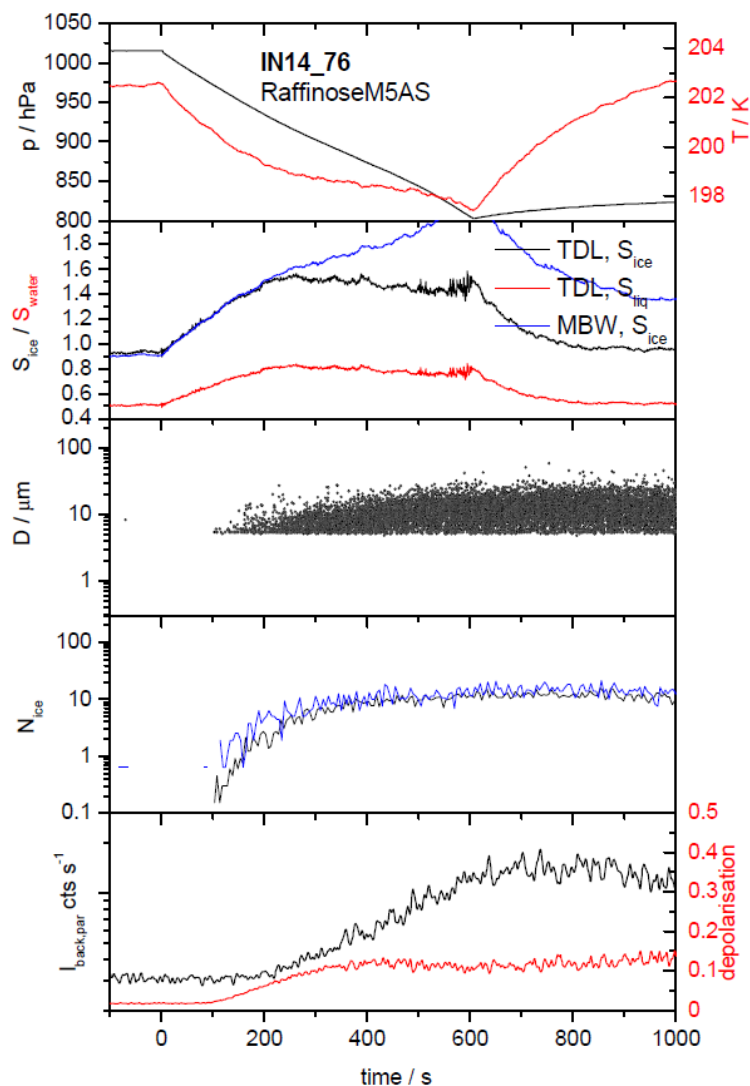


**Figure 6.8** Run 1B of the series of expansions shown in the temperature profile in Figure 6.7. Ice nucleation starting at 120%  $RH_i$  is most likely heterogeneous. See Figure 6.2 caption for details of the contents of each panel.

Run 1C was performed once the chamber had been refilled and then warmed to 216 K. Ice nucleation occurred at the homogeneous threshold with very few ice particles ( $< 0.5 \text{ cm}^{-3}$ ) nucleating at lower humidities (Figure 6.9, left hand panel). This was followed at the same temperature by run 1D (right hand panel, Figure 6.9), in which  $3 \text{ cm}^{-3}$  ice particles nucleated with an onset at 130%  $RH_i$ . Pumping continued until the homogeneous threshold was reached and  $\sim 60 \text{ cm}^{-3}$  ice particles were nucleated. A third expansion was performed at this temperature (1E, not shown), which exhibited very similar behaviour to 1D, with a heterogeneous ice mode followed by homogeneous freezing.

The enhancement in ice nucleating efficiency after homogeneous ice nucleation that was observed in these experiments appears similar to that observed for HMMA and raffinose aerosols, only with higher onset humidity and somewhat fewer ice particles nucleating. The expansions in which homogeneous nucleation occurred that caused HMMA and raffinose aerosol pre-activation had humidity trajectories that crossed the  $RH_g$  threshold. In the runs that followed, the pre-activated nucleation mode started before the experimental trajectories had crossed  $RH_g$ . In this case, the trajectory in 1C began just above  $RH_g$  and then dropped just below it after homogeneous ice nucleation. Again the trajectory began above  $RH_g$  in 1D and so did the early onset of ice nucleation. It is possible that the early onset mode found in these experiments is caused by the same mechanism as that observed in HMMA and raffinose, despite the trajectories being above  $RH_g$ . There is a substantial uncertainty in the raffinose/M5AS  $RH_g$  threshold (See  $RH_g$  in Figure. 5.5) that is related to the extrapolation of solution water activity measurements to lower temperatures ( $< 289$  K). It is therefore possible that  $RH_g$  actually exists at a higher humidity at this temperature, and that the aerosol in these experiments was in the glassy state at the start of the expansions. It is also possible that whatever mechanism causes pre-activation is able to work when aerosol particles are in an ultra-viscous rather than a glassy state.



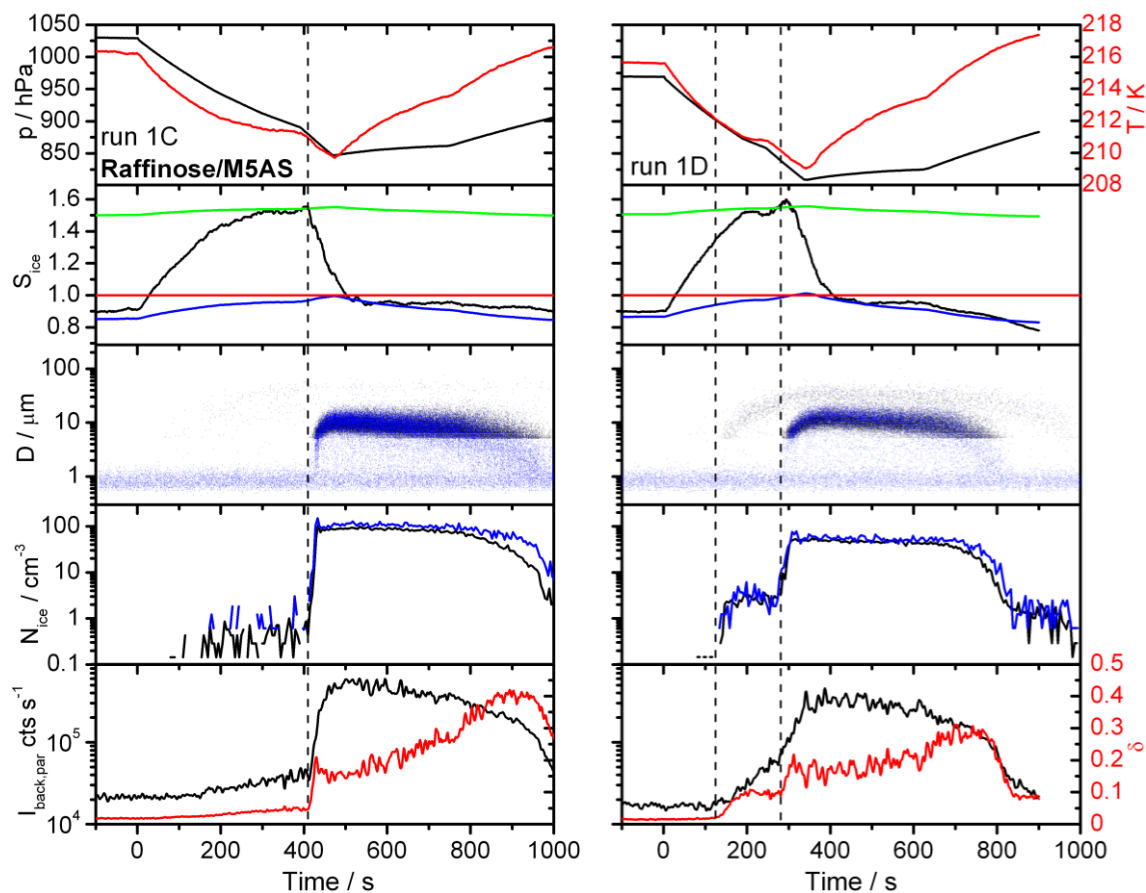


**Figure 6.9** Experimental data for runs 1C and 1D from the expansion series shown in Figure 6.7. An early ice mode at with an onset at 130% RH<sub>i</sub> was observed in 1D (first vertical dashed black line right hand panel, second vertical line marks start of homogeneous mode). This followed homogeneous ice nucleation in run 1C. See caption of Figure 6.2 for details of the measurements shown in each panel.

The series of experiments (2A – 2C) shown in the temperature profile in Figure 6.10 also used raffinose/M5AS aerosol. The aerosol in this experiment was injected at  $\sim 236$  K and an expansion was performed (2A). As would be expected for virgin liquid solution aerosol of this type and at this temperature, ice nucleation was observed at the AIDA homogeneous ice nucleation threshold with no significant early ice formation. The following expansion 2B was started after cooling the chamber to 223.5 K and once again the aerosol froze at the homogeneous threshold with no sign of pre-activation behaviour resulting from the homogeneous ice nucleation in 2A (left panel, Figure 6.11). Again the chamber was refilled, cooled and an expansion (2C) was performed at 215.5 K, very close in temperature to expansions 1D in which early ice nucleation was observed after homogeneous ice nucleation at the same temperature in run 1C. It is clear from the results of expansion 2C shown in the right hand panel of Figure 6.11 that very

little ice ( $< 0.5 \text{ cm}^{-3}$ ) nucleated before the humidity reached the homogeneous threshold, at which point  $\sim 60 \text{ cm}^{-3}$  ice particles nucleated.

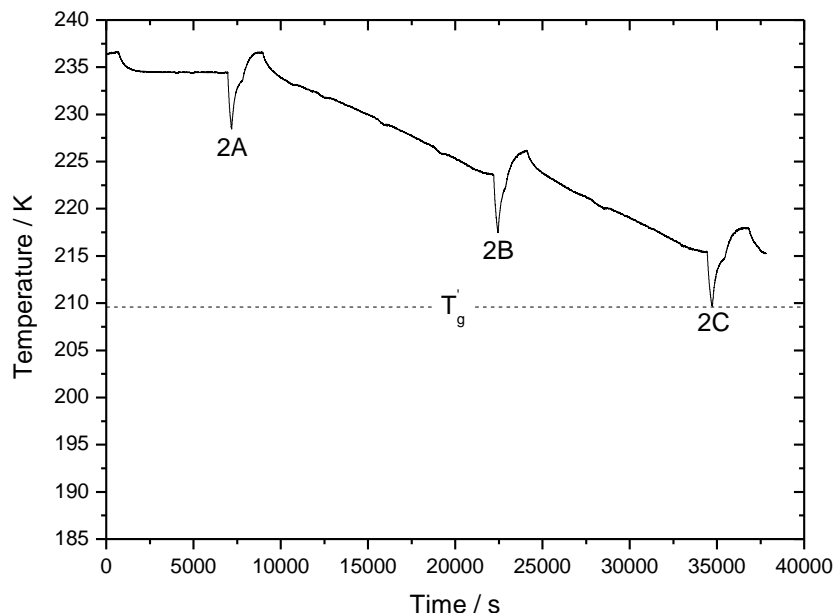


**Figure 6.10** Experimental temperature profile for another series of expansions using raffinose/M5AS aerosol.

The lack of early mode ice nucleation in run 2C strongly indicates that the aerosol was not affected by the homogeneous ice nucleation at a higher temperature in run 2B in a way similar to that observed for HMMA, raffinose or runs 1C and 1D that used raffinose/M5AS aerosol. It is possible that this is because expansion 2B took place at a higher temperature (2B started  $\sim 7 \text{ K}$  higher than 1C), causing the aerosol to be in a less viscous state. There was also a much longer time delay between 2B and 2C ( $\sim 200$  minutes) than there was between 1C and 1D ( $\sim 20$  minutes) which could also have influenced the result. This seems relatively unlikely however as raffinose aerosol remained pre-activated after a delay of also about 200 minutes after the initial run in which homogeneous nucleation occurred (see Section 6.2.2.2).

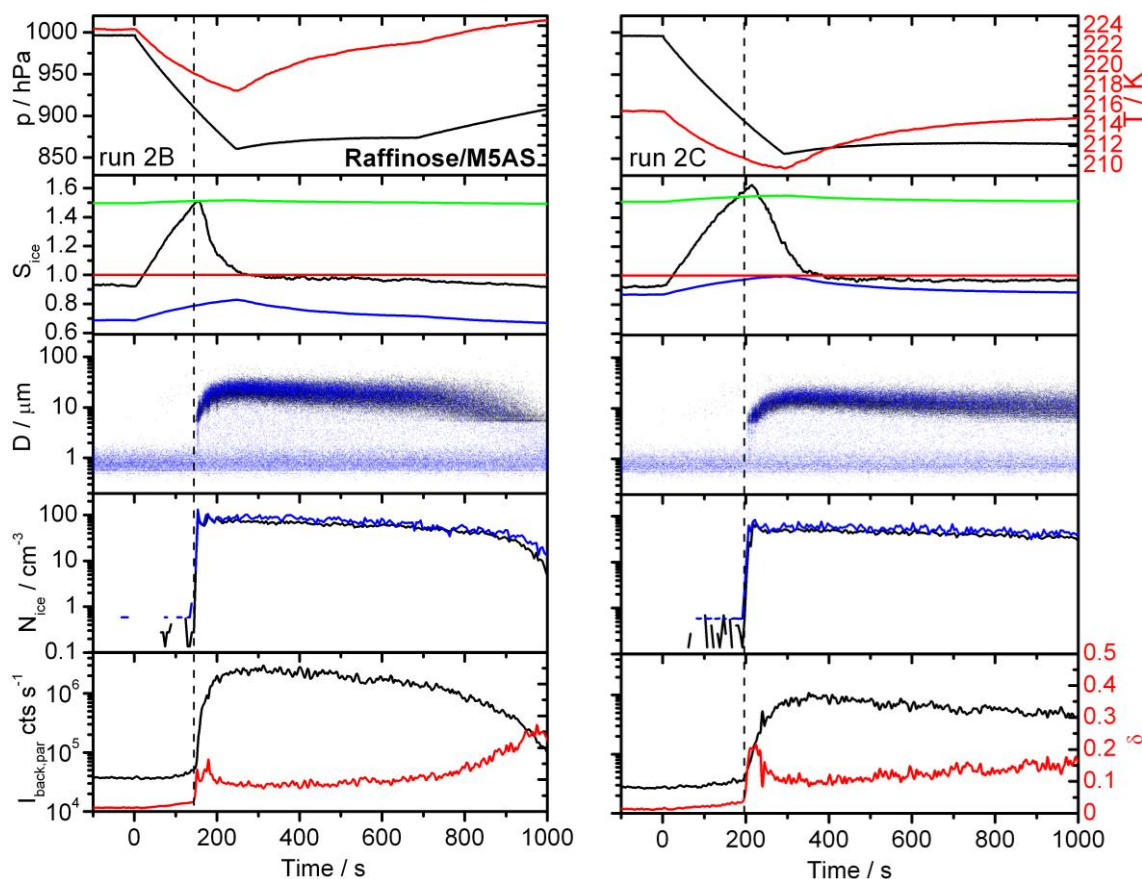


**Figure 6.11** Experimental data for expansion runs 2B and 2C of the experimental series shown in Figure 6.10. No early ice mode was observed in run 2C despite homogeneous freezing in the preceding expansion (run 2B) and the expansion starting at a temperature close to run 1D in which an early mode was observed. This appears to be due to 2B taking place at a higher temperature. For details of the measurements shown in each panel see Figure 6.2.

### 6.3 Summary of results

The glassy aerosols used in the ICE02 campaign were found to become much better ice nuclei after having frozen homogeneously in a preceding expansion run, for a limited range of temperatures. This occurred at different temperatures in aerosols of different composition. It was found to occur close to  $T_g'$ , but at temperatures above those at which standard heterogeneous ice nucleation was observed (see Chapter 5). This was in contrast to homogeneous freezing runs which started well above  $T_g'$  which did not alter the ice nucleation ability of the aerosol in the following run.

The onset of ice nucleation for pre-activated aerosols occurred at as low as 105% RH<sub>i</sub> but was found to be significantly higher for raffinose/M5AS aerosol, for which pre-activated onset humidities of up to 130% RH<sub>i</sub> were observed. Pre-activation of aerosol was conserved despite being exposed to humidities well below ice saturation (~70% RH<sub>i</sub>) whilst in the glassy regime for a period of hours. However, aerosol pre-activation was lost when the aerosol was warmed above  $T_g'$  at ice saturation.

Further experiments and analysis by RW (for details see Wagner et al. (2012b)) show that the number of ice crystals nucleated by pre-activated aerosol was only a fraction of the total number that froze homogeneously in the preceding run. Analysis of all the conducted pre-activation experiments found that the number of ice crystals that formed from pre-activated aerosol was generally between 10 and 35% of the number that had frozen homogeneously in the preceding run, except for raffinose/M5AS aerosol where a smaller fraction was observed. Further experiments by RW found that aerosol remained pre-activated in repeat expansions in which ice crystals were sublimed very soon after nucleation by refilling the chamber. This prevented ice crystals growing large enough to sediment. It was also found during that series of experiments that when pre-activated aerosol were exposed to supersaturations above RH<sub>g</sub>, the number of ice crystals that nucleated early was reduced, suggesting a loss of activity on liquefaction.

## **6.4 Discussion**

There are two likely causes of the observed enhancement in ice nucleation ability of glassy aerosols after homogeneous nucleation: i) the surface of homogeneously nucleated ice crystals nucleates the crystallisation of the solute in the aerosol particles, which are then able to catalyse ice formation; ii) The observed behaviour is related to the re-vitrification of the aerosol solution after ice has nucleated homogeneously. These explanations for pre-activation are discussed in this section.

### **6.4.1 Could homogeneously nucleated ice catalyse the crystallisation of solute crystals that then nucleate ice heterogeneously?**

Soluble salt crystals of ammonium sulphate, sodium chloride and oxalic acid have all been shown to nucleate ice heterogeneously in the deposition mode (Abbatt et al., 2006; Kanji et al., 2008; Wise et al., 2012; Wagner et al., 2010). If solutes in the aerosol used

in this study were to crystallise then a change or enhancement in the aerosol particles' ability as IN might be expected. When ice nucleates inside a liquefied solution droplet during an expansion with a trajectory that crosses  $RH_g$ , the composition of the unfrozen solution around the ice crystal will return to the water activity defined by the ice-liquid equilibrium threshold. As the  $RH_g$  threshold is higher than the ice-liquid threshold, the freeze concentrated solution in contact with the ice crystal is likely to vitrify or at least become ultra-viscous before the solute is able to crystallise. This was found for citric acid solutions and would be expected as nucleation rates in viscous mediums are reduced (Murray, 2008b). To test whether crystallisation might have occurred under conditions relevant to the ICE02 campaign, an experiment was performed (in collaboration with Tamsin Malkin (School of Earth and Environment, University of Leeds) on raffinose solution droplets in a powder X-ray diffractometer (Bruker, D8 Advance) with a temperature controlled stage.

An emulsion of  $\sim 10 \mu\text{m}$ , 15 wt% raffinose solution droplets in oil was introduced to the diffractometer's cold stage using the same procedure detailed by Malkin et al (2012). The emulsion was cooled at  $30 \text{ K min}^{-1}$  and ice nucleated in the droplets at  $236 \pm 1 \text{ K}$  (as predicted by the Koop line (Koop et al. 2000)). Cooling continued down to 223 K, at which point a diffraction pattern was collected (pattern A, Figure 6.12). The pattern is very close to that found for stacking disordered ice ( $I_{sd}$ ) nucleated in pure water droplets (pattern E) (Malkin et al., 2012). This metastable form of ice was formerly referred to as cubic ice but it actually lacks both cubic or hexagonal symmetry (Malkin et al., 2012). The peaks shown in Pattern F, that would be expected from crystalline raffinose, are absent from pattern A. No crystallisation of raffinose was observed when the emulsion was warmed up to 239 K (patterns B – D). The sensitivity of the technique was tested by suspending crystalline raffinose pentahydrate in oil. Pattern F shows the clear signal observed from 2 wt% crystalline raffinose pentahydrate. It should also be noted that the emulsion droplets used in this experiment were at least an order of magnitude larger than those used in the AIDA chamber experiments and that the catalysis of solute crystallisation less likely in smaller droplets (Murray and Bertram, 2008).

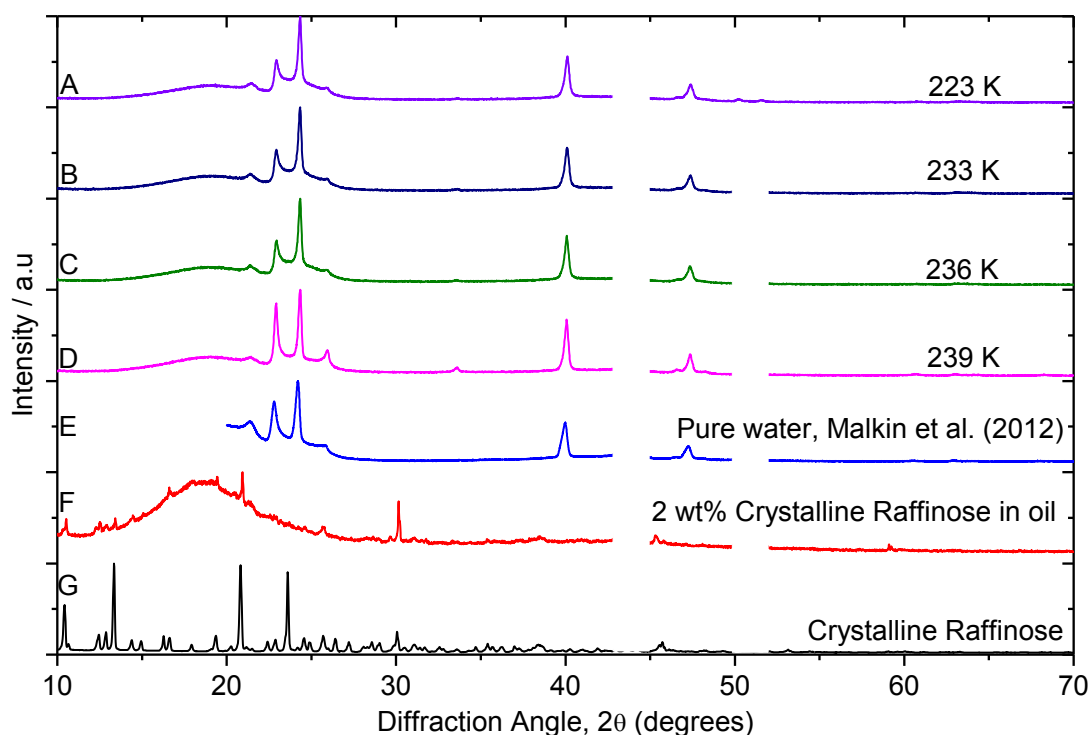


**Figure 6.12** Powder X-ray diffraction patterns captured during a freezing experiment using an emulsion of 15 wt% aqueous raffinose solution in oil (A – D). These patterns are consistent with those of stacking disordered ice (Isd) found by Malkin et al. (2012) (E). Also shown are the diffraction patterns for 2 wt% crystalline raffinose pentahydrate in oil (F) and crystalline raffinose pentahydrate.

The presented experiments show that the crystallisation of raffinose did not result from homogeneous ice nucleation in the AIDA chamber experiments. It is also therefore unlikely that the other species of aerosol studied at AIDA crystallised as they would have also formed glassy or ultra-viscous solutions as a result of freeze concentration (Zobrist et al., 2008).

Evidence from the X-ray diffraction experiment is supported by the lack of any increase in the depolarisation ratio ( $\delta$ ) after the sublimation of ice crystals nucleated during the homogeneous runs that preceded pre-activation. It should be noted that certain crystal habits result in only a small increase in  $\delta$  (Zakharova and Mishchenko, 2000) and during homogeneous freezing only a fraction of the aerosol freeze. The SIMONE instrument may therefore not be sensitive enough to always observe solute crystallisation. There is however more supportive evidence available that shows solute crystallisation was not involved.

In Section 6.2.3 it was shown that pre-activation was observed in run 1D (Figure 6.7 and right hand panel of Figure 6.9) but not in run 2C (Figure 6.10 and right hand panel of Figure 6.11). Both experiments took place at roughly 216 K and used raffinose/M5AS aerosol. However, in each case the temperature at which the preceding homogeneous freezing took place was different. The expansion before run 1D started close to  $T_g'$  at ~216 K; pre-activation was then observed in 1D. The homogeneous run preceding 2C was started well above  $T_g'$  at ~224 K; no pre-activation was observed in 2C. These results strongly suggest that the observed pre-activation in run 1D was not the result of solute crystallisation as this would also have been expected to occur in the run preceding 2C at 224 K.

In Section 6.2.1 a series of experiments that used HMMA aerosol were shown. In run 4 (Figure 6.1, right hand panel Figure 6.2) pre-activation was observed and the chamber was refilled rapidly to prevent the sedimentation of ice crystals. Had the pre-activation been the result of crystalline particles, pre-activation would also have been expected to occur in run 5. This assumes that the increase in temperature of 15 K prior to run 5 would not change the ability of any crystals to nucleate ice.

A recent study at the AIDA chamber by Wagner (2011) showed that the efficiency of nucleation of oxalic acid crystals by ice in aqueous oxalic acid/sulphuric acid droplets was low. No more than 1% of homogeneously nucleated ice crystals catalysed the production of an ice active oxalic acid crystal. This is much lower than the fraction of homogeneously frozen aerosol particles that became pre-activated in a succeeding expansion in this study, which was found to be between 10 and 35% after further experiments performed by Robert Wagner (Wagner et al., 2012b).

#### **6.4.2 The relationship between pre-activation and glass formation**

The presented evidence strongly suggests that solute crystallisation is not involved in the pre-activation of glassy aerosols. The observed behaviour does however have similarities to the well established phenomenon of pre-activation in mineral dusts (Pruppacher and Klett, 1997) (more information on and evidence for pre-activation in mineral dusts is presented in Chapter 7). Mineral dust may become pre-activated as the result of embryonic ice crystals surviving in small cracks or pores at the surface of the dust, even at humidities well below ice saturation. It is also hypothesised that it is the

result of sublimed ice crystals leaving an ice active ‘molecular footprint’ in the surface of the dust (Vali, 2008; Zuberi et al., 2001).

The pre-activation mechanism for glassy aerosols may be similar to those proposed for mineral dusts. When ice nucleates in a viscous medium and is then sublimed, the remaining glassy freeze concentrated solution that was in contact with the ice crystal could retain an ice active ‘footprint’ that might nucleate ice in a succeeding expansion run.

In addition to this, the growth of ice in the potentially viscous solutions will, after sublimation, leave the remaining vitrified solution with a more complex and potentially porous structure. Aerosol particles of this type would have a larger surface area for ice nucleation and would also be more likely to have surface defects that could catalyse ice formation. This argument was proposed by Zuberi et al. (2001) to explain the difference in ice nucleation efficiency of ammonium sulphate crystals with different morphologies. Cracks or pores might also harbour ice embryos which could survive below ice saturation (due to the ‘reverse Kelvin effect’) and then go on to form macroscopic ice crystals at low supersaturations.

The proposed mechanisms for pre-activation provide good explanations for the results summarised in Section 6.3. In particular, a relationship between pre-activation and vitrification would explain why the pre-activation behaviour was not observed after homogeneous freezing in the liquid regime. It also provides an excellent explanation for the loss of pre-activation of the aerosol in run 5 from Section 6.2.1. In this case any surface modification or ice embryos present in the vitrified pre-activated aerosol would have been lost when the chamber was warmed above  $T_g$ , due to liquefaction of the aerosol.

The higher onsets observed for pre-activated raffinose/M5AS aerosol could also be the result of the aerosol particles proximity to their glass transition. Runs 1C and 1D (see Section 6.2.3) took place just above  $RH_g$  and consequently the aerosol may have been in an ultra-viscous rather than a solid state. This would result in a ‘softer’, less viscous aerosol that might not retain ice crystal footprints or embryos as effectively as glassy material which would have been present in experiments that used the higher temperature glass formers raffinose and HMMA.



### 6.4.3 Atmospheric implications

Pre-activation is an additional way in which high viscosity amorphous aerosols could catalyse ice formation in the atmosphere. Chapters 4 and 5 describe deposition mode ice nucleation by glassy aerosols. Pre-activation could extend the temperature range in which glassy aerosols might be expected to heterogeneously nucleate ice. Pre-activated aerosol was also found to have generally much lower ice onsets than were observed for standard deposition mode nucleation by glassy aerosol, increasing the likelihood of them being involved in cirrus cloud formation.

Aerosol in the atmosphere will not have uniform composition like the aerosols used at AIDA. Aerosol particles that form TTL cirrus have been shown to be mostly potentially glass-forming mixtures of organic material and sulphate rather than traditional IN such as mineral dusts. There will still be a range of aerosol composition however, so it would be expected that the aerosol would have a distribution of  $T_g'$  values. It is likely therefore that when homogeneous ice nucleation occurs, a subset of the aerosol would be in the right phase regime to become pre-activated. In order to go on to nucleate ice however, an activated aerosol would have to not be exposed to temperatures above its own  $T_g'$ , as this would result in a loss of surface activity or ice embryos.

Assuming only a small fraction of aerosol might become pre-activated (for the reasons outlined above), any cloud forming from pre-activated aerosol would be likely to have a low number concentration of ice crystals, which would impact its optical density and potentially result in high in-cloud humidity (Krämer et al., 2009). It is also possible that aerosol that has frozen homogeneously and become pre-activated could sediment, impacting ice clouds at lower altitudes. The impact and importance of glassy aerosol pre-activation on widespread cloud properties needs to be assessed computationally using cirrus cloud models.

## 6.5 Summary and Conclusions

This chapter presents measurements made during the ICE02 campaign at the AIDA chamber which used glass forming aerosol. It was found that the homogeneous nucleation of ice in expansions starting slightly below or very close to  $T_g'$  resulted in a fraction of the aerosol nucleating ice at humidities as low as 105% RH<sub>i</sub> in succeeding expansions at the same temperature. This behaviour was termed ‘pre-activation’ due to

its similarities to pre-activation behaviour observed in mineral dusts (Pruppacher and Klett). Pre-activation was observed in aerosols with atmospherically relevant compositions (raffinose, HMMA and raffinose/M5AS) with  $T_g'$  values between 209.6 and 240.6 K

It was proposed that the observed behaviour was related to the vitrification of the freeze concentrated solution resulting from the growth of ice in the aerosol. This could lead to ice active 'footprints' on the surface of the re-vitrified aerosol left by sublimed ice crystals. It could also leave aerosol with a porous structure of surface defects that could promote ice nucleation due to increased surface area or active sites. Pores could also potentially support embryonic ice crystals that could survive at  $< 100\%$  RH<sub>i</sub> and then grow rapidly under supersaturated conditions.

It was shown using powder X-ray diffraction measurements that pre-activation was unlikely to be due to solute crystallisation catalysed by ice crystals. Crystalline material could act as heterogeneous IN at low supersaturations but it would not explain the observed loss of aerosol pre-activation on crossing  $T_g'$ .

Pre-activated aerosol may impact the formation and properties of cirrus clouds by providing highly active IN for ice production. Cloud formed by a small subset of an aerosol is likely to result in a cloud with low ice particle number concentration, which could lead to persistent in cloud supersaturation. To take part in ice formation, a pre-activated aerosol would have to remain at temperatures below  $T_g'$ . The potential impact of pre-activated aerosol needs to be assessed using quantitative cloud models that use realistic temperature/humidity trajectories for the upper troposphere. It would also be necessary to represent aerosol with a distribution of  $T_g'$  prime values as atmospheric aerosol will have a range of compositions.

## Chapter 7: Characterisation and first results from the DMC

This chapter details the characterisation of the supersaturation with respect to ice generated in the chamber and the results of deposition mode ice nucleation experiments using natural kaolinite dust. Experiments were also performed to test whether ice nucleation by the kaolinite dust became enhanced in repeated freezing runs and to investigate the dependence of the heterogeneous ice onset  $RH_i$  on dust surface area. The development of and the experimental methodology for the deposition mode chamber (DMC) is described in Chapter 3.

### 7.1 Chamber humidity characterisation

The relative humidity experienced by the particles in the chamber is determined by the temperature of the sample and also the temperature of the ice film which serves as a water source. When a sample is at a lower temperature than the ice film, it experiences supersaturation ( $> 100\% RH_i$ ) with respect to ice. When the sample temperature is higher than that of the ice, it is exposed to a subsaturation with respect to ice ( $< 100\% RH_i$ ). Validation of the generated  $RH_i$  was achieved by observing two well characterised phase transitions; the sublimation of ice particles as the ice saturation point was crossed and the deliquescence of ammonium sulphate crystals.

#### 7.1.1 The ice sublimation point

At ice saturation ( $100\% RH_i$ ) an ice crystal will neither grow nor sublimate. By measuring the point at which ice crystals began to sublime, the offset between the  $RH_i$  calculated using Equation 3.1 and the actual humidity experienced by a sample in the chamber could be estimated. Ice crystals were observed as they were warmed at a rate of  $0.1 \text{ K min}^{-1}$  which corresponds to a calculated rate of change in  $RH_i$  when crossing the ice saturation threshold of between  $1.4\% \text{ min}^{-1}$  (at 210 K) and  $1.1\% \text{ min}^{-1}$  (at 240 K) (Figure 7.1).

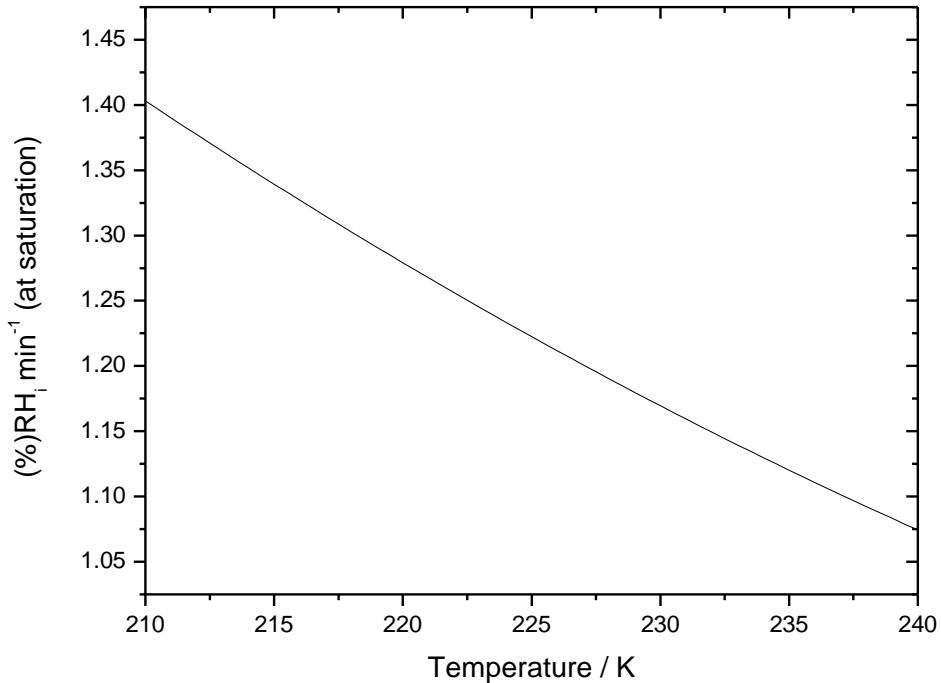


**Figure 7.1** The rate of change in  $RH_i$  at ice saturation for a sample changing in temperature at  $0.1 \text{ K min}^{-1}$ .

Due to the subtlety of the process being observed, it was difficult to exactly pinpoint the start of sublimation in the recorded experimental videos. Instead it was necessary to take the range of frames in which sublimation could have begun. From each range the mid-point was taken as the sublimation onset. The onset ranges were between 0.5 and 5 minutes long, giving a maximum potential change in  $RH_i$  during that time of 7% (at 210 K) during the 5 minute period. This was less than the calculated uncertainty in the onset humidities (displayed as error bars), which were estimated based on the upper and lower limits of the quoted temperature error ( $\pm 0.5 \text{ K}$ ) for the ice film and sample thermocouples.

The size of ice crystals was found to affect the observed onset of sublimation. Some parts of larger crystals, like those shown in Figure 7.2A were found to start sublimating earlier than other parts. This was due to the upper parts of such crystals not being in good thermal contact with the slide surface. Smaller crystals, like those shown in Figure 7.2B were found to sublimate uniformly. Experiments in which crystals grew too large to provide an accurate sublimation onset were excluded from the analysis.

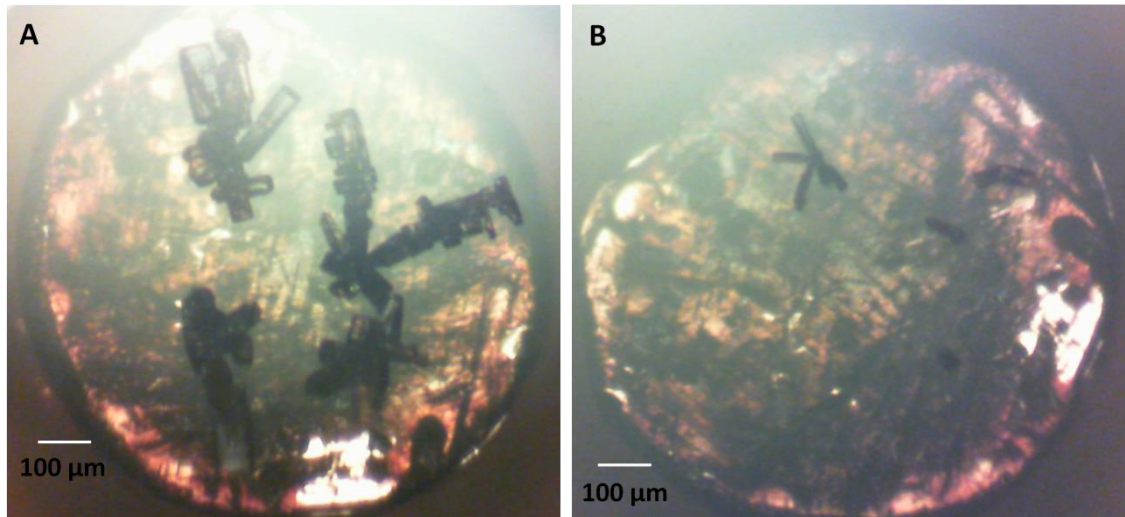


**Figure 7.2** Parts of large ice crystals (panel A) which were not in good thermal contact with the glass substrate were found to sublime at higher calculated humidities. Smaller crystals like those shown in panel B sublimated uniformly.

Sublimation experiments were performed at temperatures between 213 and 240 K (Figure 7.3). Most experiments used the same thermocouple to measure the sample temperature (TC 1, light blue triangles) but some experiments were also performed that used a different thermocouple (TC 2, red squares). Sublimation experiments performed using TC 1 gave humidities calculated using Equation 3.1 that were offset from the actual humidity ( $100\% RH_i$ ) by between 8 and 20%  $RH_i$ . The offset in sublimation humidity in experiments using TC 1 appeared to increase as temperature decreased. Experiments that used TC 2 showed offsets from ice saturation of between 1 and 3%  $RH_i$ .

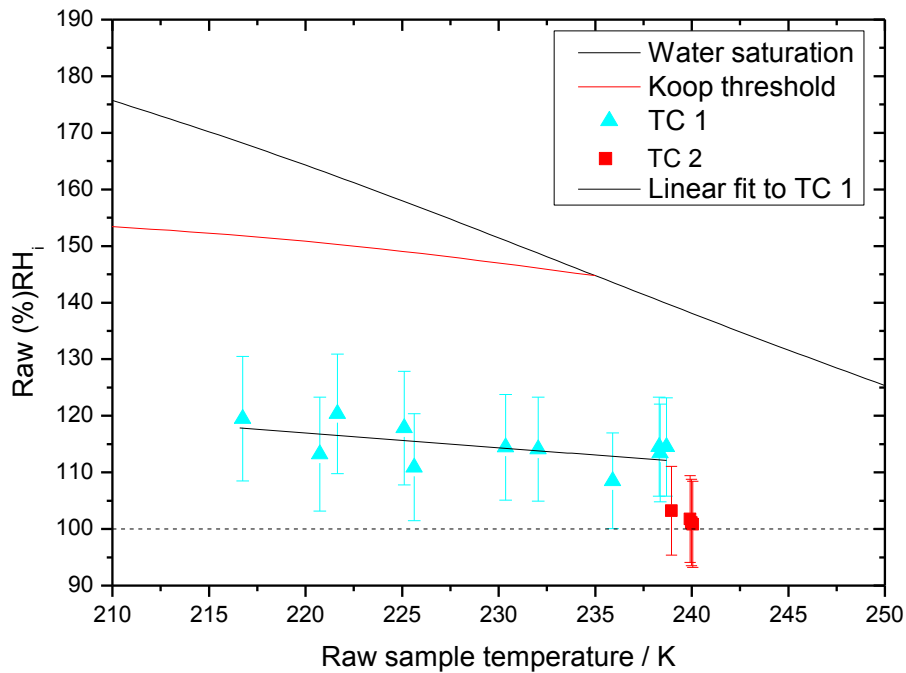


**Figure 7.3** The humidities generated by the DMC were tested by observing the point at which ice crystals began sublimating as they were heated at  $0.1 \text{ K min}^{-1}$ . There was found to be an offset between  $\text{RH}_i$  calculated using Equation 3.1, based on the temperatures of the sample support and the ice film, and the actual chamber  $\text{RH}_i$  at saturation. The offset was significantly larger for thermocouple 1 (TC 1, blue triangle) than it was for thermocouple 2 (TC 2, red squares)

The observed sublimation humidity offsets are related to error in the temperature measurements made for the sample and the ice film. In each case there is a small physical separation between the thermocouple junction and what it is measuring the temperature of. The large difference in the sublimation humidity offsets measured using sample thermocouples TC 1 and TC 2 indicates that the main source of error was related to the sample thermocouple rather than the ice film measurement. The difference in the offset measured when using TC 1 and TC 2 was probably the result of different positioning of the thermocouple junctions inside the sample rod. TC 2 was made with slightly heavier gauge thermocouple wire, which allowed its insertion into the rod without it becoming bent over, leading to a smaller separation between the junction and the sample. This consequently resulted in a smaller temperature and therefore  $\text{RH}_i$  offsets.

To parameterise the change in sublimation offset at lower temperatures, a linear curve of best fit was calculated for the TC 1 sublimation onsets (slope = -0.237, intercept = 168.882). Equation 3.1 uses the parameterisation for the saturation vapour pressure over a flat hexagonal ice surface provided by Murphy and Koop, (2005). As this parameterisation is a function of temperature it was straightforward to convert the observed humidity offset into a temperature offset (Figure 7.4), based on the linear fit to the TC 1 sublimation onsets. The offset represents the estimated difference in temperature between that measured by TC 1 and the temperature actually experienced by the sample. It assumes that the difference in the temperature of the sample and the temperature measured by the thermocouple in the sample rod is much greater than the difference in the temperature between the ice film and the thermocouple used to measure it. The TC 1 temperature offset was found to increase from just under 1.05 K at a measured temperature of 242 K to 1.26 K at 213 K. This small increase in the temperature offset may be due to the larger difference in temperature between the chamber's top and bottom plates during experiments which take place at lower temperatures. The temperature offset for TC 2 was calculated based on an average offset from ice saturation of 1.6% RH<sub>i</sub> at 240 K. This works out as a temperature offset between TC2 and the sample of 0.16 K

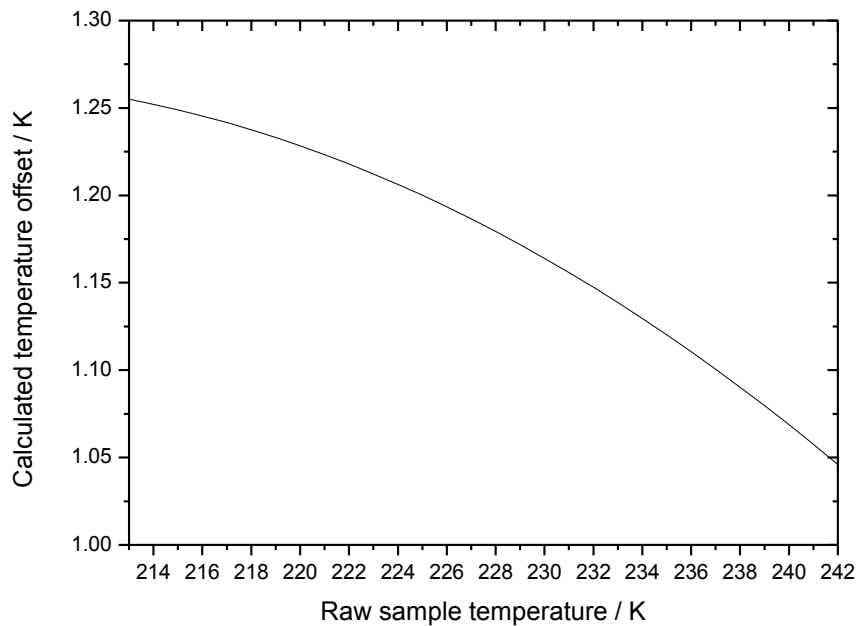


**Figure 7.4** The calculated temperature offset for the TC1 thermocouple based on the linear fit to the sublimation offsets shown in Figure 7.3. The fit was converted from a RH<sub>i</sub> offset to a

temperature offset and re-fitted using a second order polynomial - (Offset =  $-0.00015448918T^2 + 0.063085882T - 5.1732499$ ).

The temperature offsets found for TC 1 and TC 2 were used to correct the measured sample temperature, which was then used with the raw ice surface temperature to re-calculate  $RH_i$ . Corrections were applied to all the experimental data that follows.

### 7.1.2 Deliquescence point of ammonium sulphate

The deliquescence point of crystalline ammonium sulphate ( $(NH_4)_2SO_4$ ) has been extensively studied and has been well characterised experimentally at temperatures down to  $\sim 230$  K (Kulkarni et al., 2009; Onasch et al., 1999; Kanji and Abbatt, 2006; Braban et al., 2001). The deliquescence humidity of  $(NH_4)_2SO_4$  particles was tested in a series of experiments using the DMC. The onset of water uptake by ammonium sulphate particles cooled at  $0.1$  K  $min^{-1}$  was observed as re-structuring of the particles (A – D, Figure 7.5). When cooling was continued, particles deliquesced almost completely leaving some entirely liquid solution droplets and some droplets still containing crystalline  $(NH_4)_2SO_4$  (E and F, Figure 7.5).

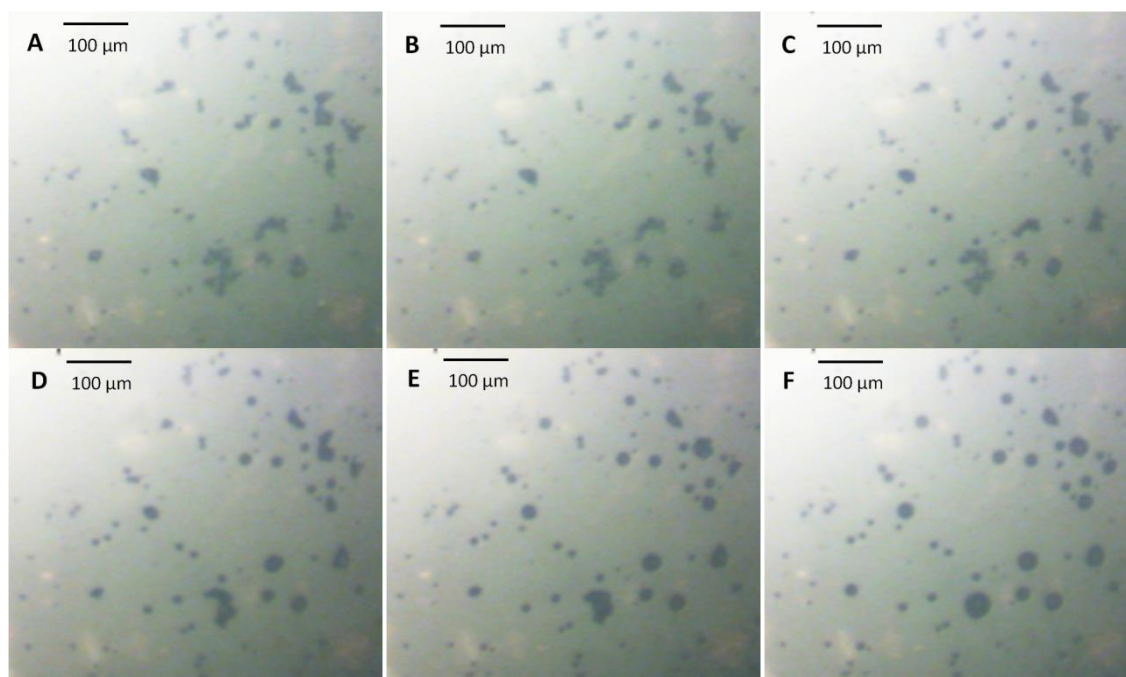




**Figure 7.5** Still images taken from a DMC experimental video which show the initial restructuring and then dissolution of ammonium sulphate crystals on crossing the deliquescence threshold.

The deliquescence experiments were conducted using TC 1 so the onset temperatures and humidities were corrected applying the temperature offset calculated using the curve shown in Figure 7.4. The corrected deliquescence onsets are in good agreement with the available literature data and also with the deliquescence point for  $(\text{NH}_4)_2\text{SO}_4$  aerosol modelled using the Extended Aerosol Inorganics Model (E-AIM) (Wexler and Clegg, 2002; Friese and Ebel, 2010) (Figure 7.6).

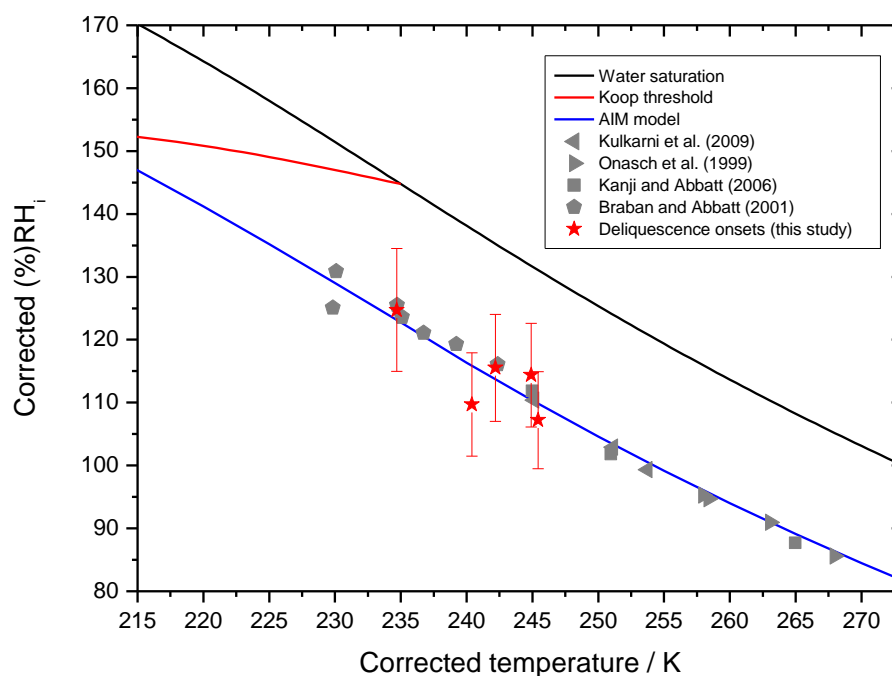


**Figure 7.6** Deliquescence  $\text{RH}_i$  onsets for ammonium sulphate crystals tested in the DMC at a range of temperatures (red stars). Also shown are experimentally derived deliquescence onsets from the literature (grey symbols, see figure legend and text for details) and the deliquescence threshold predicted using the E-AIM model (Wexler and Clegg, 2002).

## 7.2 Does the hydrophobic sample substrate nucleate ice?

In order to investigate deposition mode ice nucleation using the DMC samples are supported by a carefully cleaned hydrophobic glass surface. It was therefore important to investigate the ice nucleating properties of the glass surface. Repeated experimental

runs using two different glass slides were performed at temperatures between 215 and 238 K. As the experiments used TC 1, the temperature and humidity of the resulting ice nucleation onsets were corrected according to the temperature offset curve shown in Figure 7.4. No nucleation was observed below 137% RH<sub>i</sub> and there appears to be a slight upwards trend in the ice nucleation onsets at lower temperatures. These experiments provide a humidity limit below which ice nucleation onsets are attributable to particles placed on silanised glass slides.

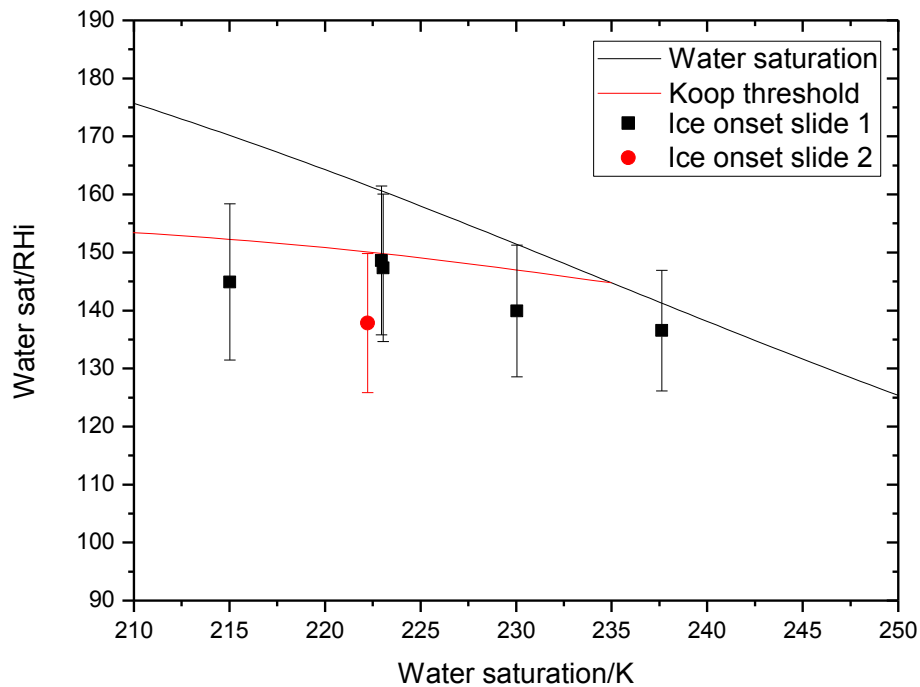


**Figure 7.7** Ice nucleation onsets for two cleaned, silanised glass slides of the type used to support samples in the DMC.

### 7.3 Deposition mode ice nucleation by kaolinite (KGa-1b)

Between 1000 and 3000 Tg of mineral dust is emitted into the atmosphere per year from arid and semi-arid regions such as the Sahara desert in North Africa (Goudie and Middleton, 2006). Measurements made *in situ* on Storm Peak, Colorado by DeMott et al. (2003) showed that 33% of ice particles nucleated in the deposition mode by natural aerosols contained either mineral dust or fly ash. This was despite mineral dusts and fly ash making up no more than 1% of the background aerosol. Mineral dust is found to make up a significant fraction of aerosol throughout the troposphere, with

concentrations falling at higher altitudes (Froyd et al., 2009b). Ice particle residues from cirrus associated with the anvils of clouds in large convective systems are found to be disproportionately enriched in mineral dust compared to the background aerosol (Cziczo et al., 2004; Froyd et al., 2010).

The mineralogy of dust particles that are found in the atmosphere varies depending on the geology of the source region and on the period of time dust aerosols have been transported for (Glaccum and Prospero, 1980). The IN ability of mineral dusts of different composition has been shown to vary considerably in the deposition mode (Kanji et al., 2008; Zimmermann et al., 2008). Clay species make up on average 63% of all atmospheric mineral dusts. On average kaolinite clay alone makes up 13% of the total (Atkinson and Murray, 2012). In this section, results are presented for deposition mode ice nucleation experiments using a well characterised natural kaolinite ( $\text{Al}_4(\text{OH})_8\text{Si}_4\text{O}_{10}$ ) clay dust (KGa-1b). The sample was supplied ground by the Clay Minerals Society, who provide clay minerals which have not been acid washed or subject to any other chemical treatment (Costanzo and Guggenheim, 2001). In order to test the ice nucleation properties of kaolinite particles using the DMC, samples were deposited by evaporating droplets or a single droplet of KGa-1b aqueous suspensions on the surface of silanised glass slides. The slides were then placed in the DMC sample holder prior to being exposed to supersaturations with respect to ice. For more details of the experimental methodology used, please refer to Chapter 3.

### **7.3.1 Does repeated ice nucleation by KGa-1b particles enhance their ability to act as IN?**

Some mineral dusts have been found to become more active ice nuclei after having previously nucleated ice in the deposition mode (Pruppacher and Klett, 1997; Fournier D'albe, 1949; Mason, 1950; Mossop, 1956; Mason and Maybank, 1958; Mossop, 1963; Knopf and Koop, 2006). The enhancement in ice nucleation ability is observed as a decrease in the  $\text{RH}_i$  at which the particles nucleate ice, compared to the onset humidity at which they nucleated ice previously. Particles that have been enhanced as IN are commonly referred to as 'pre-activated'. The precise molecular cause of pre-activation in mineral dusts is unknown. One hypothesis is that embryonic ice crystals might survive in small cracks or pores at the surface of the IN (Volmer, 1945; Turnbull, 1950; Mossop, 1956; Mason and Maybank, 1958; Mossop, 1963; Fukuta, 1966; Roberts and

Hallett, 1968). Pre-activation is observed despite the dust particles being exposed to humidities below ice saturation. This does not rule out the possibility of ice being retained in cracks or pores. Ice in a hydrophilic capillary or pore is likely to have a negative curvature at its surface. This results in a ‘reverse Kelvin effect’, decreasing the retained ice’s equilibrium vapour pressure (Fukuta, 1966; Pruppacher and Klett, 1997). Pre-activation in mineral dusts may also be the result of nucleated ice crystals modifying the surface of the dust. An ice crystal may leave what could be termed a ‘molecular footprint’ in the dust’s surface. This footprint could then act as a highly efficient active site for ice nucleation, causing the observed increase in activity (Roberts and Hallett, 1968).

It should also be noted that similar enhancement of ice nucleation ability was observed for glassy or ultra-viscous aerosols (Chapter 6). In that system, the aerosol particles become more active ice nuclei after nucleating ice homogeneously rather than after nucleating ice heterogeneously in the deposition mode. To check for ice nucleation enhancement, sample 110929-KGa1b (Figure 7.8, the 6-digit prefix corresponds to the date on which the sample was deposited onto a silanised glass slide) was exposed in the DMC to repeated nucleation experiments at the same temperature ( $\sim 238$  K) and cooling rate ( $0.1 \text{ K min}^{-1}$ ).

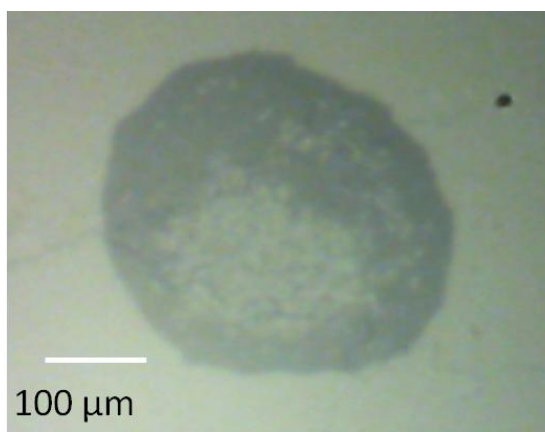


**Figure 7.8** Sample 110929-KGa1b (pictured) was deposited by evaporating a single large droplet of an aqueous suspension of Kga-1b. Rather than one big particle, this image shows a collection of smaller particles.

Figure 7.9 shows temperature (top panel) and  $\text{RH}_i$  (bottom panel) profiles that the sample was subject to. The chamber was allowed to equilibrate for a period of at least 30 minutes, during which the temperature of the ice surface was maintained at

240 K. The sample was then cooled at a rate of  $0.1 \text{ K min}^{-1}$ , raising the humidity the sample was exposed to. The KGa-1b particles were found to nucleate ice at  $135 \pm 10\% \text{ RH}_i$ . The nucleated ice crystals were clearly associated with the deposited sample (Panel A, Figure 7.10) rather than the supporting substrate. The ice particles were then sublimated by reducing the chamber  $\text{RH}_i$  to no less than 75%. After sublimation of all the visible ice particles (marked in each run by a vertical dashed red line in Figure 7.9), the chamber was maintained at between 80 and 95%  $\text{RH}_i$  for  $\sim 40$  minutes. To test for a change in the ice nucleation onset, the sample was then cooled. In run 2, the onset of ice nucleation was observed at  $114 \pm 9\%$ , considerably lower than the onset observed in run 1. A 21.% change in the ice nucleation onset is outside of the range of uncertainties of the onsets, suggesting that the ice nucleation ability of the KGa-1b particles had been enhanced by the ice nucleation in run 1.

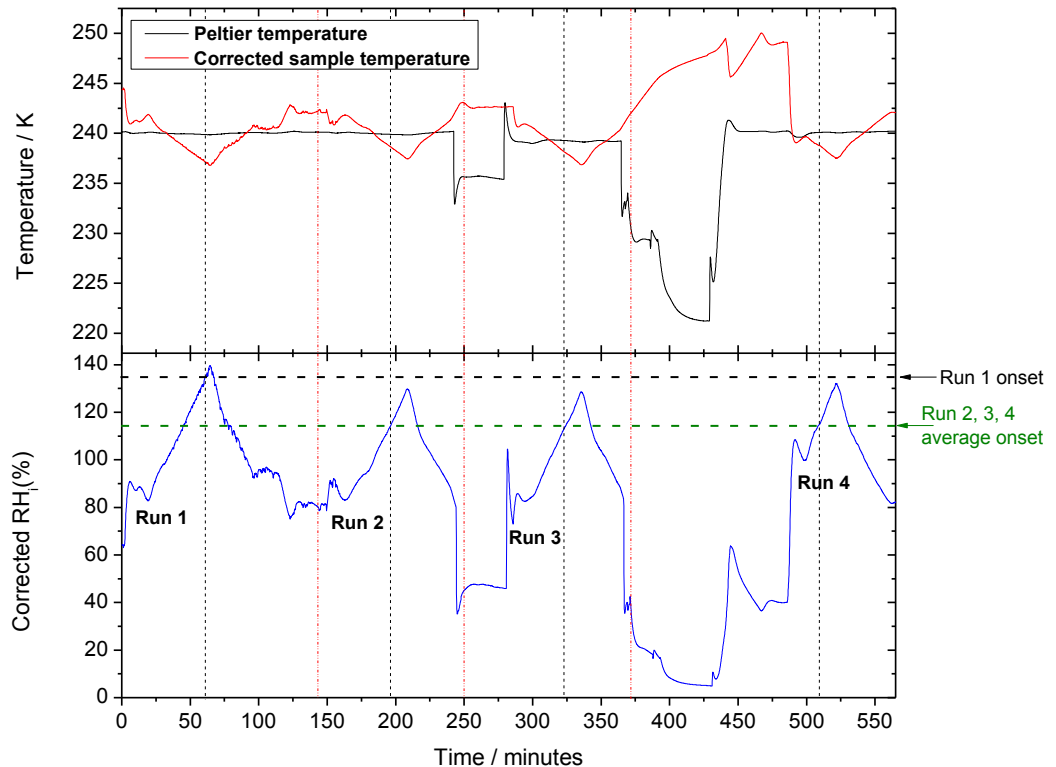


**Figure 7.9** Time series for experimental runs 1- 4 which used sample 110929-KGa1b. The top panel shows the measured Peltier temperature and the sample temperature corrected based on the temperature offset for TC 2 at 240 K. The bottom panel shows  $\text{RH}_i$  calculated with the corrected sample temperature using Equation 3.1. For each experiment, the onset time of ice nucleation is marked with a vertical dashed black line and the time at which all visible ice particles had sublimated is marked with a vertical dash-dot-dot red line. The run 1  $\text{RH}_i$  ice onset and the average onset found in runs 2 – 4 are shown as black and green horizontal dashed lines

respectively.

Other studies into the enhancement of ice nucleation in mineral dusts have found that the behaviour was retained even after IN were exposed to humidities below ice saturation (Volmer, 1945; Turnbull, 1950; Mossop, 1956; Mossop, 1963; Mason and Maybank, 1958; Fukuta, 1966; Roberts and Hallett, 1968). To test whether this was the case for KGa-1b, the particles which nucleated ice in runs 2 and 3 were exposed to lower  $RH_i$  during and after ice sublimation than those in run 1. In run 2, the ice particles were sublimed more quickly than those nucleated in run 1. This was achieved by simultaneously warming the sample and lowering the temperature of the ice surface. This briefly dropped the chamber  $RH_i$  to ~35%, subliming the ice, before an increase in the ice surface temperature stabilised the chamber at about 46%  $RH_i$ . The particles were then left at that humidity for ~35 minutes. No significant change was observed in run 3, with ice nucleating at  $113 \pm 9\%$ . The crystals in run 3 were again sublimed quickly by reducing the chamber  $RH_i$  to ~40%. The  $RH_i$  was also then further reduced to between 22 and 5%  $RH_i$  for ~60 minutes before the Peltier and rod temperatures were re-stabilised prior to the following run. Again in run 4 no significant change in the ice onset  $RH_i$  was observed, with crystals nucleating at  $115 \pm 9\%$ .

An interesting feature of the observed ice nucleation enhancement is visible in the experimental videos for runs 1 – 4. In the initial experiment that used particles that had not nucleated ice before (run 1), numerous ice particles nucleated all over the deposited sample (Panel A, Figure 7.10) at roughly the same humidity (for comparison the ice free sample is pictured in Figure 7.8). In run 2, enhanced ice nucleation occurred at a lower supersaturation and gave apparently fewer ice crystals, concentrated in the upper left hand quarter of the sample (Panel B, Figure 7.10). This behaviour was more pronounced in runs 3 and 4 (Panels C and D, Figure 7.10), where ice particles clearly nucleated at a few specific positions on the samples.

The change in the number and distribution of ice particles that nucleated in runs 1 – 4 indicates that only a subset of the deposited KGa-1b particles became enhanced or ‘pre-activated’ IN. The pre-activated particles were able to nucleate ice at lower humidities than the surrounding non-pre-activated dust. This would have depleted water vapour locally and prevented the nearby dust reaching humidities high enough for it to nucleate ice, resulting in fewer and localised ice particles.

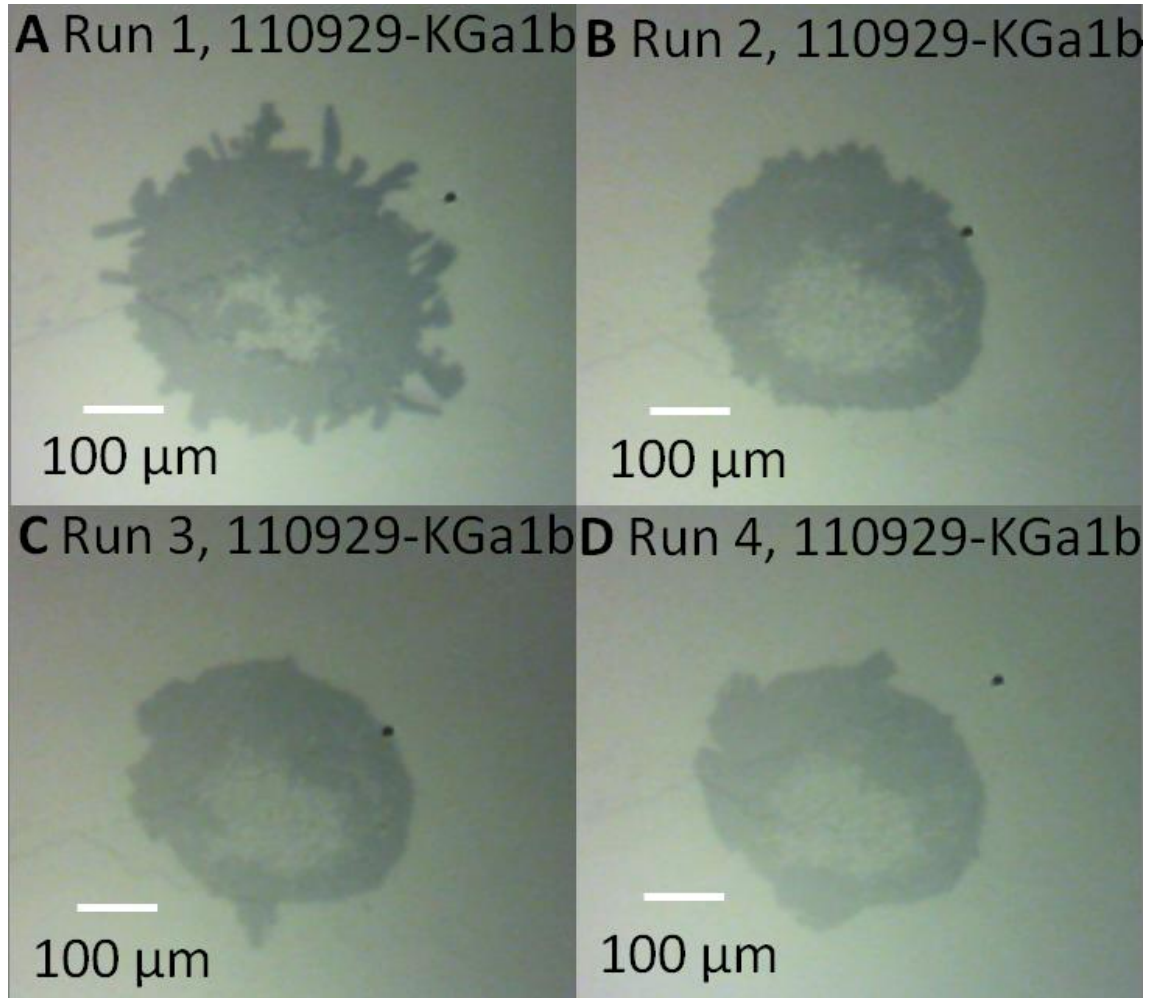


**Figure 7.10** Stills from the videos of runs 1 – 4 taken after ice nucleation had occurred. The distribution and number of ice particles that nucleated on the sample was greatly reduced in runs 2 and 4 (Panels C and D), in which ice nucleation was enhanced.

The increase in IN activity ( $\Delta RH_i$ ) can be expressed by measuring the difference in the ice nucleation onsets of runs 1 and 2. (*i.e.*  $\Delta RH_i = RH_i(\text{run 1}) - RH_i(\text{run 2})$ ). The uncertainty in  $\Delta RH_i$  ( $\sigma_{\Delta RH_i}$ ) was calculated by combining the errors in the two onsets using the formula  $\sigma_{\Delta RH_i} = \sqrt{\sigma_{RH_i(\text{run 1})}^2 - \sigma_{RH_i(\text{run 2})}^2}$ . For runs 1 and 2,  $\Delta RH_i$  was  $21 \pm 14\%$ . For comparison this is plotted in Figure 7.11 with  $\Delta RH_i$  for a different kaolinite sample (observed in a chamber with a very similar concept to the DMC (Roberts and Hallett, 1968)) and Arizona Test Dust (ATD) (Knopf and Koop, 2006). The  $\Delta RH_i$  for KGa-1b is somewhat larger than that for kaolinite by Roberts and Hallett (1968), although their experiments did take place about 10 K higher in temperature. Literature results for ATD show substantial variation of  $\Delta RH_i$  (from 3 to 30%).

The ice nucleation onsets in runs 3 and 4 were very similar to that observed in run 2 despite the low humidities the samples were exposed to after sublimation. This suggests that the enhancement of nucleation was unlikely to be the result of ice trapped in surface defects such as cracks or pores. It might therefore be considered more likely to have been due to the nucleation and growth of ice particles modifying the surface of the dust and making it a more efficient IN. However, Knopf and Koop (2006), who observed pre-activation of ATD particles in repeated ice nucleation experiments, found that pre-activation of the dust was eliminated when particles were exposed  $< \sim 5\% \text{ RH}_i$ . It is possible therefore that the humidities reached between runs 3 and 4 were not quite low enough to eliminate the pre-activation of the deposited KGa-1b sample. This does not agree with the findings of Roberts and Hallett (1968) however, who found that pre-activation ceased when kaolinite particles were exposed to lower than  $35\% \text{ RH}_i$ . It should be noted though that in that case, particles were left for substantially longer periods of time (weeks). Temperature may also play an important role, in experiments by Kanji et al. (2008) samples of ATD were heated to room temperature in between repeated ice nucleation experiments and it was found that no pre-activation of the dust occurred.

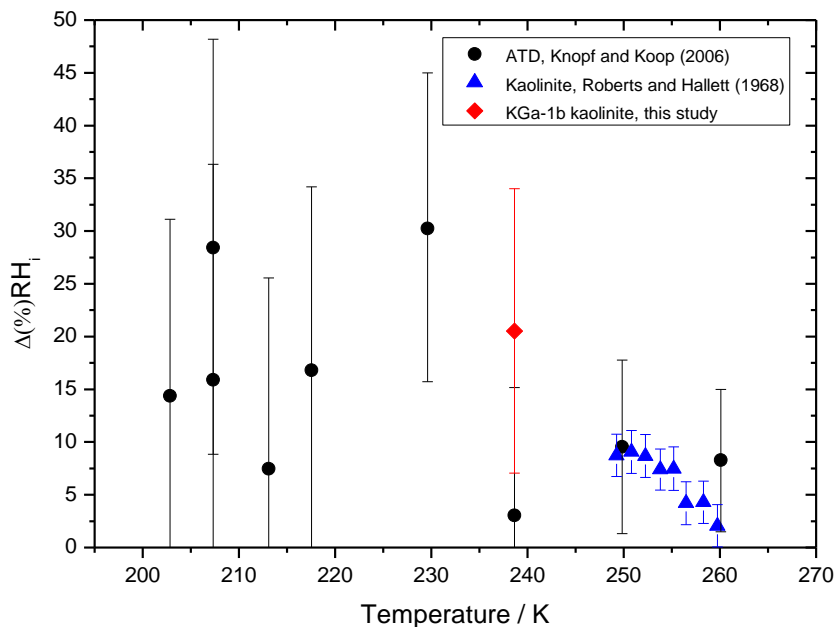


**Figure 7.11** A comparison of  $\Delta \text{RH}_i$  for KGa-1b calculated from the ice onsets for runs 1 and 2 with  $\Delta \text{RH}_i$  for a different kaolinite sample (Roberts and Hallett, 1968) and Arizona Test Dust (ATD) (Knopf and Koop, 2006).



### 7.3.2 Effect of KGa-1b surface area on ice onset RH<sub>i</sub>

The onset RH<sub>i</sub> of deposition mode ice nucleation by mineral dusts varies with the surface area of dust available for nucleation (Wheeler and Bertram, 2012; Kanji et al., 2008; Kanji and Abbatt, 2010). This effect was investigated for KGa-1b dust using the DMC. As described in Chapter 3, known surface areas of kaolinite (KGa-1b, Clay Minerals Society) were deposited onto hydrophobic glass slides, prior to the deposited dust's IN behaviour being tested using the DMC. Samples with three different total surface areas were investigated (Table 7.1) at temperatures between 237 and 240 K. Due to the observed enhancement in IN ability of KGa-1b particles after having nucleated ice once, the results shown in Table 7.1 are for KGa-1b samples that had not previously nucleated ice (See Section 7.3.1 for pre-activation experiments using KGa-1b, Chapter 6 for a similar phenomenon found for glassy aerosols)

**Table 7.1** Temperature and RH<sub>i</sub> at the onset of ice nucleation for experiments with varying surface areas of KGa-1b present. Note that the ice onset for the 110927-KGa1b experiment (marked in red) is for an ice crystal that could have nucleated either on the glass substrate or on a clay particle.

KGa-1b sample	KGa-1b surface area / cm <sup>2</sup>	± / cm <sup>2</sup>	Corrected ice onset temperature / K	Corrected ice onset RH <sub>i</sub>	±
110921-KGa1b	3.89 × 10 <sup>-3</sup>	7.23 × 10 <sup>-4</sup>	238.9 K	106%	8%
110929-KGa1b	3.82 × 10 <sup>-4</sup>	3.67 × 10 <sup>-5</sup>	237.1 K	135%	10%
110927-KGa1b	2.70 × 10 <sup>-5</sup>	3.68 × 10 <sup>-6</sup>	239.8 K	133%	10%

In the experiment with 110921-KGa1b sample, which had the highest surface area, ice nucleated at 106 ± 8% RH<sub>i</sub>. The available surface area was one order of magnitude less for sample 110929-KGa1b. As described in Section 7.3.1 it was found to nucleate ice at 135 ± 10% RH<sub>i</sub>. In both cases, the nucleated ice crystals were clearly associated with the deposited KGa-1b particles and it did not appear that the hydrophobic glass substrate had induced crystallisation based on the microscope images (Figure 7.12, panels A - D). The surface area of kaolinite was again an order of magnitude smaller for sample 110927-KGa1b and it was found to nucleate ice at 133 ± 10% RH<sub>i</sub>. However, in the associated experimental video it appeared that the ice

crystal that formed may have nucleated on the supporting glass substrate, rather than on the deposited clay particles (Figure 7.12, panels E and F). The clay particles in this experiment were deposited by placing a single,  $\sim 440 \mu\text{m}$  diameter KGa-1b suspension droplet of known concentration onto the glass substrate and then allowing it to evaporate, leaving dry particles on the surface. During this process the evaporating droplet could have potentially left behind particles too small to be visible at the magnification used, but which could have nucleated the observed ice particle. Due to the ice onset  $\text{RH}_i$  for this experiment being similar to that observed for sample 110929-KGa1b, but also only slightly lower than the onsets observed for clean glass slides shown in Figure 7.7 it is not possible to rule out either the clay particles or the glass surface as the source of the nucleation.

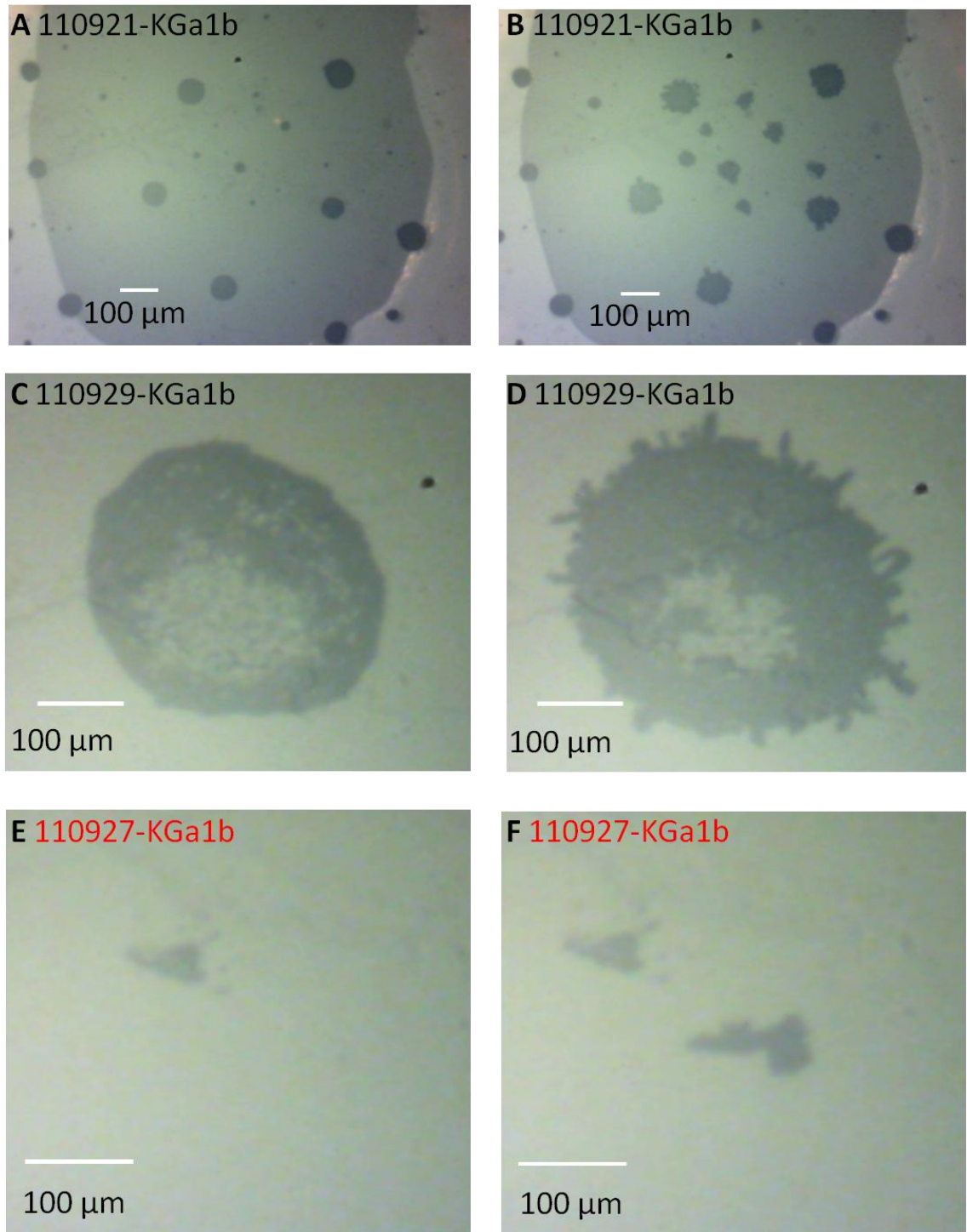


**Figure 7.12** Images before (left hand column) and after (right hand column) ice nucleation in experiments using KGa-1b kaolinite (clay minerals society) particles of known surface area. For a summary of results see Table 7.1.

A number of other studies have shown kaolinite particles to act as heterogeneous IN in the deposition mode (Kanji et al., 2008; Wheeler and Bertram, 2012; Salam et al., 2006; Zimmermann et al., 2007; Chernoff and Bertram, 2010; Wang and Knopf, 2011;

Eastwood et al., 2008; Eastwood et al., 2009; Zimmermann et al., 2008; Bailey and Hallett, 2002; Roberts and Hallett, 1968; Schaller and Fukuta, 1979). Unfortunately, the studies often do not quote the origin of their kaolinite dust or the surface area of the sample used, making direct comparison with the results from the DMC impossible in most cases. However, two recent studies do provide both an origin and a surface area for the kaolinite used. Kanji et al. (2008) show the onset  $RH_i$  of ice nucleation as a function of surface area for a range of mineral dusts including KGa-1b kaolinite from the Clay Minerals Society at 233 K. Wheeler and Bertram (2012) investigated the effect of changing surface area of Fluka brand kaolinite (product ID: 03584) on the  $RH_i$  at which it nucleated ice at temperatures between 239 and 242 K. A comparison of the ice onset  $RH_i$  from these studies with the onsets for KGa-1b collected using the DMC is shown in Figure 7.13.

The ice onset  $RH_i$  for KGa-1b from Kanji et al. (2008) is in good agreement with those found using the DMC, especially given the magnitude of the error in  $RH_i$  associated with the DMC onsets. Wheeler and Bertram (2012) show average ice onsets for the Fluka brand kaolinite that are significantly lower than those for KGa-1b. The averaged onsets increased from ~100% to 108% as surface area decreased from  $3.3 \times 10^{-3}$  to  $1.8 \times 10^{-5} \text{ cm}^2$  (Figure 7.13). The increase in ice onset humidity with decreasing surface area for KGa-1b is steeper than that observed for the Fluka kaolinite. The Fluka kaolinite appears from the data to be better at nucleating ice ‘per unit of surface area’ than the KGa-1b. This suggests that there are significant differences in the composition or surface properties of the two kaolinite samples, possibly relating to the local geology of their respective source regions or processing of sample prior to sale. It may also be due to the difference in methods by which the particles were deposited onto their supporting substrates. The method used by Wheeler and Bertram (2012) provides discrete particles with surfaces exposed to the surrounding gases. The ‘droplet evaporation’ method of depositing particles used in this study may lead to particles clumping together as droplets dry out, reducing the actual surface area of the clay particles exposed to the chamber’s atmosphere.

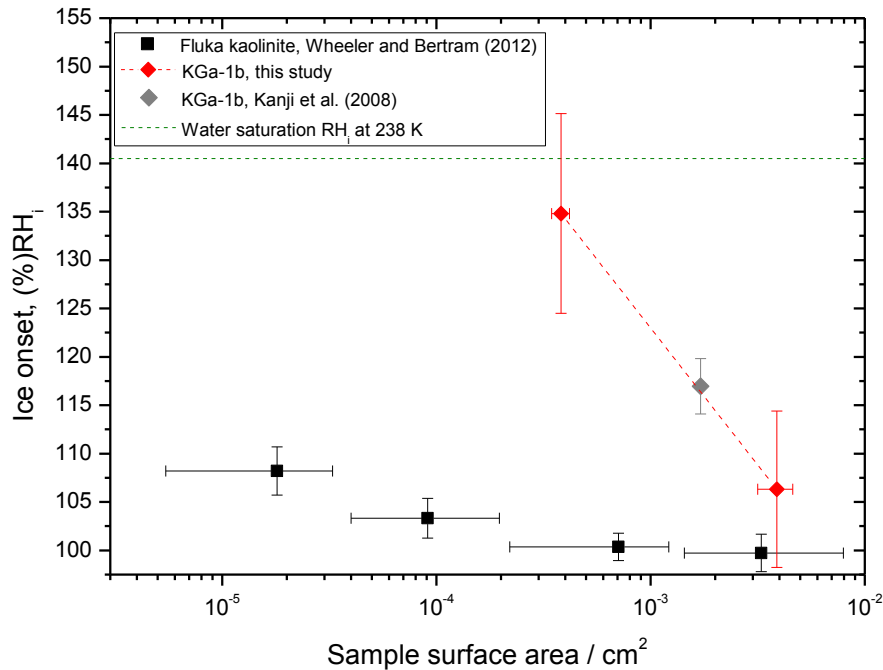


**Figure 7.13** The variation of ice onset  $RH_i$  with the surface area of kaolinite mineral dust. Ice onsets from DMC experiments at  $\sim 238$  K which used KGA-1b kaolinite (red diamonds) are shown. They are compared with an ice onset for KGA-1b at 233 K (Kanji et al., 2008) (grey diamond) and average ice onsets for Fluka kaolinite at temperatures between 242 and 239 K (Wheeler and Bertram, 2012) (black squares).

Mineral dust with a range of compositions is found in the atmosphere. Different source regions have different abundances of minerals to start with and as the dust is transported, the lofted dust compositions change with time (Glaccum and Prospero, 1980) (See mineral dusts section in Chapter 1). It is therefore necessary to compare the IN efficiency of different mineral dusts. As well as KGA-1b, Kanji et al. (2008) investigated the ice onset humidities of a selection of atmospherically relevant dusts as a function of surface area. The ice onsets of those dusts are compared in Figure 7.14 along with the ice onsets found for KGA-1b using the DMC and with ice onsets for kaolinite (Fluka) and illite (IMt-1, Clay minerals society) (Wheeler and Bertram, 2012). From this comparison it appears that the onset for the sample with a larger surface area (110921-KGa1b) is very close to that found for Saharan dust by Kanji et al. (2008) and in good general agreement with the other mineral types. The onset for the lower surface area sample (110929-KGa1b) was substantially higher than those found for kaolinite and other minerals at this surface area. This difference may simply be due to KGA-1b

being a less efficient IN. It could also be due to the method by which the dust was deposited onto the slide, the 110929-KGa1b sample was deposited by evaporating a single larger (~1 mm) droplet. On evaporation the particles contained in the droplet become more clumped together (Figure 7.12, panel C), potentially reducing their total surface area. This may have been less of an issue for the 110921-KGa1b sample as it was deposited as a collection of smaller droplets (Figure 7.12, panel A).

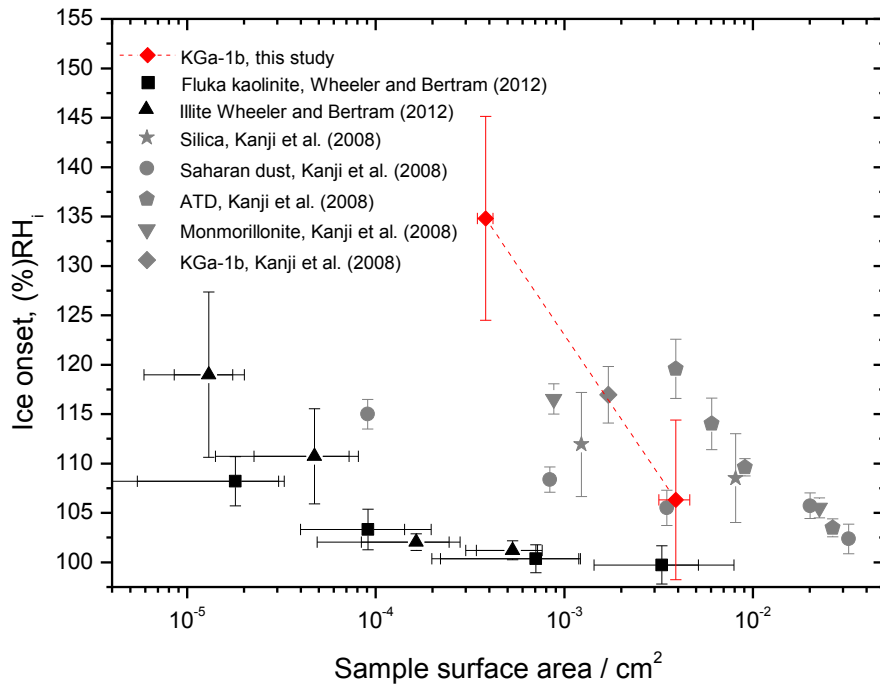


**Figure 7.14** A comparison of ice onset  $RH_i$  as a function of sample surface area for a variety of atmospherically relevant mineral dusts. Ice nucleation onsets are shown for KGa-1b sample tested in the DMC at ~238 K alongside ice onsets for kaolinite (Fluka) and Illite (IMt-1, Clay Minerals Society) at 242 and 239 K and a selection of mineral dusts (including KGa-1b) tested by Kanji et al. (2008) at 233 K.

### 7.3.3 Nucleation rates and contact angles

To provide a more general parameterisation for the data collected for KGa-1b, the heterogeneous ice nucleation rate coefficients ( $J_{\text{het}}$ ) at the onset of ice nucleation were calculated for experiments 110921-KGa1b and 110929-KGa1b. The calculation used Equation 1.22, a time interval ( $\Delta t$ ) of 6 seconds (the time between frames in the experimental videos) and the surface areas given in Table 7.2. As the particles in the samples used in both experiments were quite tightly packed on the surface of the glass slide (due to the evaporation of droplets, see above), it was not possible to accurately determine how many nucleation events occurred at the ice onset humidity. The number of nucleation events at the onset ( $\Delta N_{\text{ice}}$ ) was therefore set at the limiting value of 1; hence the calculated nucleation rates are lower limits. Contact angles were then calculated for experiments 110921-KGa1b and 110929-KGa1b based on the lower limit of  $J_{\text{het}}$  using Equations 1.13 – 1.15 (Table 7.2).

For comparison, Table 7.2 contains contact angles found for kaolinite from other studies (Wheeler and Bertram, 2012; Chernoff and Bertram, 2010; Wang and Knopf, 2011). The literature values vary between  $9^\circ$  and  $14^\circ$  and are from experiments that took place at temperatures close to that of the experiments from this study. The contact angle for experiment 110921-KGa1b ( $11.85^\circ$ ) falls within the range of the literature values, which might indicate that the KGa-1b dust is a comparable IN to the commercial Fluka kaolinite used in the other studies. However, the contact angle for experiment 110929-KGa1b ( $26.14^\circ$ ), was substantially higher than the upper limit of the literature values. This was largely due to the considerably higher ice onset  $\text{RH}_i$  that was observed in the 110929-KGa1b experiment. As previously discussed, this may be related to KGa-1b being a less efficient IN or the reduction of available particle surface area caused by agglomeration during the deposition of particles by evaporating suspension droplets.

**Table 7.2** The heterogeneous nucleation rate ( $J_{\text{het}}$ ) and contact angles at the onset of ice nucleation for experiments 110921-KGa1b and 110929-KGa1b.

Study	Kaolinite source	Corrected ice onset $T / \text{K}$	Corrected ice onset $\text{RH}_i$	$J_{\text{het}} / \text{cm}^{-2} \text{s}^{-1}$	$\pm / \text{cm}^{-2} \text{s}^{-1}$	$\alpha / ^\circ$	$\pm / ^\circ$
This study (110921-KGa1b)	KGa-1b	238.9	106%	43	8	12	6
This study (110929-KGa1b)	KGa-1b	237.12	135%	436	42	26	4
Wheeler and Bertram (2012)	Fluka	239 – 242	100 - 108%	-	-	3 – 14	-
Chernoff and Bertram (2010)	Fluka	236	104%	281	-	9	-
Wang and Knopf (2011)	Fluka	238	110 – 120%	-	-	11	



## 7.4 Summary and conclusions

In this chapter the results of characterisation experiments for the DMC were presented along with the results of ice nucleation experiments performed using natural kaolinite dust samples. The purpose of the chamber characterisation was to gauge the how the experimental humidities in the DMC (calculated using Equation 3.1 and the measured temperatures) compared to the actual conditions experienced by samples in the chamber. This was achieved by observing the point at which ice crystals began to sublime when the chamber humidity was reduced at around  $1\% \text{ RH}_i \text{ min}^{-1}$ . This provided a measure of the ice saturation point (*i.e.* the point at which the sample was exposed to 100%  $\text{RH}_i$ ). For both thermocouples used in this study it was found that the ice particles sublimed at calculated  $\text{RH}_i$  above 100%. The magnitude of the  $\text{RH}_i$  offsets was different and it is thought that this was due to differences in the positioning of TC 1 and TC 2 in the sample rod. The  $\text{RH}_i$  offsets were converted to sample temperature offsets that were used to correct the measured experimental sample temperature, which was then used to re-calculate the chamber  $\text{RH}_i$ . Experiments were performed in which the deliquescence of crystalline ammonium sulphate particles was observed. This provided deliquescence onset  $\text{RH}_i$  values at temperatures between 235 and 245 K, which when corrected in the way described above agreed well with literature values and the ammonium sulphate deliquescence threshold calculated using the E-AIM model.

Ice nucleation experiments using natural kaolinite dust (KGa-1b, Clay minerals Society) samples were also performed using the DMC. Experiments investigated whether the ice nucleation ability of the mineral dust became enhanced after having nucleated ice in repeated experimental runs. It was found that KGa-1b was able to nucleate ice at  $\sim 20\%$  lower  $\text{RH}_i$  in experiments repeated after an initial freezing run. This is very similar to results from previous studies which observed enhancement in mineral dust IN ability after an initial freezing experiment. The behaviour is described as pre-activation. Sublimating nucleated ice crystals and exposing the sample to  $\text{RH}_i$  as low as  $\sim 5\%$  for extended periods of time between experiments did not prevent pre-activation of the dust in a subsequent run. Further work is required to investigate the exact conditions under which KGa-1b ceases to be pre-activated.

The effect of KGa-1b surface area on the ice nucleation onset  $\text{RH}_i$  was also investigated. It was found that higher surface areas of the clay resulted in lower onset

$RH_i$ . The measured onsets results were in agreement with another study that used KGa-1b, though it was found that the ice onset for lowest surface area experiment was somewhat high. This could be due to KGa-1b being a less efficient IN or to the loss of particle surface area during the deposition of particles by evaporating suspension droplets. Nucleation rates and contact angles were calculated using classical nucleation theory. At higher surface areas the contact angles calculated for KGa-1b were in the range of angles calculated for Fluka kaolinite dust. The lower surface area experiment had a considerably larger contact angle, which was the result of the higher ice onset humidity that was observed in that experiment.

## Chapter 8: Summary and conclusions

This thesis presented the results of experimental studies into ice nucleation under cirrus cloud conditions. Cirrus clouds are formed in the upper troposphere and are entirely composed of ice particles. They are known to have a significant impact on the Earth's radiation budget. A better understanding of cirrus, including the mechanisms by which they form, is required fully assess that impact (Lynch et al., 2002). The results from two experimental campaigns (ICE01 and ICE02) which took place at the AIDA cloud simulation chamber (KIT, Germany), were described. In these campaigns, the ice nucleation behaviour of glassy aqueous solution aerosols was investigated. Also presented were details of the development, characterisation and the first results from the Deposition Mode Chamber (DMC); a new benchtop chamber for the study of deposition mode ice nucleation.

### 8.1 Ice nucleation by glassy aerosols under cirrus conditions

Recent experimental studies in the laboratory and in-situ have shown that organic aerosol particles often exist in an amorphous solid state (Mikhailov et al., 2009; Virtanen et al., 2010). Unlike crystalline materials, amorphous solids do not have regular, repeating molecular arrangements. Droplets with a range of atmospherically relevant compositions have been shown to form glasses (Zobrist et al., 2008; Murray et al., 2012b), which are amorphous solids with a viscosity that exceeds  $10^{12}$  Pa s (Angell, 1995; Debenedetti and Stillinger, 2001). The aim of the ICE01 and ICE02 campaigns was to study the ice nucleation properties of five different glass forming aerosols at the AIDA chamber. AIDA is a highly instrumented cloud simulation chamber capable of accessing temperatures as low as 180 K. All of the aerosols studied had compositions relevant to the atmosphere and had glass transition temperatures low enough to be of importance under cirrus cloud conditions. In ICE01, citric acid aerosol was studied. In ICE02, raffinose, HMMA, levoglucosan and raffinose/M5AS (a mixture of raffinose with five dicarboxylic acids and ammonium sulphate) aerosols were tested. The glass transition temperature at ice saturation ( $T_g'$ ) was different for each aerosol. Citric acid, levoglucosan and raffinose M5AS have  $T_g'$  of between 209.6 and 211.8 K. Raffinose

and HMMA solutions form glasses at significantly higher temperatures (240.6 and 236.5 K respectively).

It was found that all of the aerosols nucleated ice both heterogeneously or homogeneously depending upon their physical state – *i.e.* whether they were in the solid glassy or the liquid state. In all cases it was found that a small fraction of the aerosol particles nucleated ice heterogeneously (at  $RH_i$  below the homogeneous freezing threshold) at  $< 200$  K; a temperature at which aerosols of all compositions were in the glassy state. Levoglucosan, raffinose/M5AS and citric acid aerosol particles all nucleated ice homogeneously in experimental runs that started above their respective  $T_g'$ . Raffinose and HMMA aerosol particles remained glassy at higher temperatures and were found to also nucleate ice heterogeneously at higher temperatures (214.6 and 218.5 K respectively). However, during experimental runs for both raffinose and HMMA aerosols above these temperatures but still below the expected  $T_g'$  ice only nucleated at the homogeneous threshold. In both cases, the experimental temperature/humidity trajectories crossed the relative predicted humidity induced glass transition ( $RH_g$ ). This indicates that although probably initially glassy, the aerosol liquefied on crossing  $RH_g$  before the aerosol could nucleate ice heterogeneously. This resulted in only homogeneous ice nucleation being observed.

Heterogeneous ice nucleation was observed above  $RH_g$  for citric acid, levoglucosan, raffinose and raffinose/M5AS aerosols. In the latter two cases 'isohumid' experiments were performed in which the chamber humidity was maintained above  $RH_g$  but kept below the homogeneous threshold for at least 500 seconds. In both cases, ice particles continued to nucleate at humidities higher than  $RH_g$  - *i.e.* humidities at which the aerosol particles might be expected to have liquefied. In order to heterogeneously nucleate ice, it is most likely that the aerosol particles remained in a glassy or perhaps ultra-viscous state. An estimation of aerosol viscosity using and subsequent calculation of the diffusion time for water molecules to the centre of aerosol particles suggested that even at the highest humidities reached in the two experiments, the diffusion time was on the order of days. This was much longer than the duration of the experiments, suggesting that the aerosols would not have had time to liquefy.

In experiments in which ice was nucleated heterogeneously, it was observed that only a small fraction of the total aerosol population nucleated ice. For all of the

compositions investigated, the fraction frozen heterogeneously was of the order of  $10^{-3}$ . The maximum fraction depended on pumping speed and the peak  $RH_i$  reached in the experiment. By estimating the total surface area of each of the aerosols used, it was possible to use the fraction frozen data to calculate the ice active surface site density ( $n_s$ ) of the aerosols. The  $n_s$  parameter is used in the time independent, deterministic model of ice nucleation (Connolly et al., 2009), which assumes that ice forms immediately on an ice active surface site when a specific  $RH_i$  is reached.

A 1D cirrus cloud model was used to simulate and compare the properties of a cirrus cloud nucleated by glassy aerosol with a cirrus cloud formed homogeneously from liquid aerosol particles. A simple parameterisation of the fraction of citric acid glassy aerosols that nucleated ice heterogeneously as a function of  $RH_i$  in the AIDA chamber was used to control the nucleation of ice by glassy aerosols in the model. It was found that cirrus cloud nucleated heterogeneously in runs that contained a 1:1 ratio of glassy and liquid particles were made up of fewer, larger ice particles than cirrus which was nucleated homogeneously in runs that used only liquid aerosol. The ice particle number concentration of cirrus nucleated by glassy particles was found to be consistent with concentrations measured *in situ* for TTL cirrus (Jensen et al., 2010) for model runs that used cooling rates between 0.5 and 3.8 K hr<sup>-1</sup>. It was also observed that the humidity within cirrus clouds nucleated by glassy aerosols did not return to ice saturation but instead remained significantly supersaturated with respect to ice for prolonged periods of time (100s minutes). This ‘dynamic equilibrium’ was the result of the decreased surface area of ice to take up water vapour in cirrus nucleated by glassy aerosols compared to that in homogeneously nucleated cirrus. This finding may provide an explanation for the observed high in cloud humidities observed particularly in cirrus at temperatures below 200 K (Krämer et al., 2009) (Gao, 2004). It was also consistent with other model studies that show heterogeneous ice nucleation by non-specified IN leads to cirrus with high in cloud humidities (Krämer et al., 2009; Gensch et al., 2008; Khvorostyanov et al., 2006; Spichtinger and Gierens, 2009; Spichtinger and Cziczo, 2010; Jensen et al., 2010; Ren and Mackenzie, 2005).

In a study of ice nuclei composition in free tropospheric air, DeMott et al. (2003) found that 25% of ice nuclei were composed of sulphate-organic mixtures compared to 33% which were mineral dust and fly ash. Using an  $n_s$  value for glassy consistent with data from the ICE campaigns it was shown that glassy sulphate-organic

aerosol might potentially account for the fraction of sulphate-organic ice nuclei observed by DeMott et al. (2003) at temperatures relevant to mid-latitude cirrus. This indicates that heterogeneous ice nucleation by glassy aerosol may be of importance outside of the TTL.

In the ICE02 campaign it was found that under certain conditions, the ice nucleation ability of glassy aerosol particles was enhanced by ice cloud processing. Aerosol was found to nucleate ice at lower  $RH_i$  in runs that followed a run in which the aerosol nucleated ice homogeneously. It was found to occur close to  $T_g'$ , but at temperatures above those at which non pre-activated heterogeneous ice nucleation was observed. It was proposed that the observed behaviour was related to the vitrification of the freeze concentrated solution that resulted from the growth of ice inside liquid aerosol. Ice crystals could have left behind ice active 'footprints' on the surface of the re-vitrified aerosol after they had sublimed. They may also have left aerosol with a porous structure with surface defects that could promote ice nucleation due to increased surface area or active sites. Pores could also potentially support embryonic ice crystals that could survive at  $< 100\%$   $RH_i$  and then grow rapidly under supersaturated conditions. The behaviour was termed 'pre-activation' due to its similarities to the observed phenomenon of pre-activation in mineral dusts. Further experimental work is required to fully understand the mechanism by which pre-activation occurred. The observed behaviour may also impact the formation and properties of cirrus clouds by providing highly active IN for ice particle production. Cloud formed by a small subset of an aerosol is likely to result in a cloud with low ice particle number concentration, which could lead to persistent in cloud supersaturation. Modelling work is required to better assess the impact of aerosol pre-activation on cirrus clouds.

The results from the AIDA chamber provide conclusive evidence that glassy aqueous solution aerosols with a range of compositions can nucleate ice heterogeneously. The aerosol compositions used were atmospherically relevant; however they are not as chemically complex as organic aerosols found in the atmosphere. Secondary organic aerosol (SOA) has been shown to behave in a manner consistent with it being in a solid amorphous (possibly glassy) state (Virtanen et al., 2010) and is likely to have a glass transition temperature higher than the temperatures at which cirrus form (Koop et al., 2011).

Studies which have investigated whether SOA particles nucleate ice have found conflicting results. Like the glassy aerosol tested in this project, heterogeneous ice nucleation by SOA particles has been observed at the AIDA chamber (Möhler et al., 2008) and also in recent experiments performed by Wang et al. (2012). In others, no significant heterogeneous ice nucleation was observed (Wagner et al., 2007; Prenni et al., 2009). *In situ* measurements show that ice particle residues from TTL cirrus are overwhelmingly composed of internally mixed sulphate and organic species (Froyd et al., 2010). The ice particle number concentrations found in TTL cirrus suggest that they are nucleated heterogeneously. As discussed, 25% of ice particles that were heterogeneously nucleated from sampled background aerosol at lower altitudes were also composed of sulphate and organic species (DeMott et al., 2003). In both cases heterogeneous ice nucleation by glassy aerosol composed of organic and sulphate species could explain the observed ice particle residues. The available experimental and *in situ* observations strongly suggest that more IN experiments should be attempted with SOA particles of varied composition, both *in situ* and with lab generated SOA. The effect on IN ability of incorporating sulphate into the organic aerosol should also be tested.

The AIDA chamber provides an excellent tool to observe the ‘bulk’ ice nucleation properties of aerosols. It generates supersaturations with respect to ice by rapidly reducing the pressure inside its ice coated vessel. Unfortunately, expansion experiments do not allow the time dependent aspects of water uptake and ice nucleation to be investigated, as it is impossible to maintain both a constant temperature and  $RH_i$  within the chamber during expansion. Time dependence appears to be of particular importance when considering ice nucleation by glassy aerosols, as experiments performed at AIDA show that nucleation may occur on glassy aerosol above their  $RH_g$  threshold. This is an important avenue for future research.

Finally, atmospheric aerosol could well exist in other amorphous solid forms such as rubbers or gels. Work is needed to ascertain whether such phases are able to act as IN under atmospheric conditions.

## **8.2 The deposition mode chamber**

A major part of this PhD project was the development of a benchtop chamber for the investigation of deposition mode ice nucleation on a variety of aerosol particles.

The deposition mode chamber (DMC) generates partial pressures of water vapour using a temperature controlled ice surface. Particles were exposed to supersaturations with respect to ice by placing samples on a hydrophobic glass substrate which was cooled independently to temperatures below that of the ice surface. This design allowed particles to be observed for extended periods of time and over repeated RH<sub>i</sub> and temperature cycles. It also provides a more cost effective method for conducting deposition mode ice nucleation experiments.

After characterisation of the chamber, ice nucleation experiments were performed with the DMC using a natural kaolinite dust sample (KGa-1b, Clay Minerals Society). The effect of KGa-1b surface area on the ice nucleation onset RH<sub>i</sub> was investigated. It was found that higher surface areas of the clay resulted in lower onset RH<sub>i</sub>. The measured onsets were in agreement with those found by Kanji et al. (2008) for KGa-1b. Contact angles were calculated using classical nucleation theory and were found to be in agreement with literature values for Fluka kaolinite dust, at the higher investigated surface area. The measured contact angle at the lowest surface area was considerably higher than that for Fluka kaolinite, which was related to the higher ice onset humidity found in that experiment.

Evidence was also found that suggests KGa-1b becomes 'pre-activated' after having nucleated ice in an initial experiment. The dust was able to nucleate ice at ~20% lower RH<sub>i</sub> in following experiments. Sublimating nucleated ice crystals and exposing the sample to RH<sub>i</sub> as low as ~5% for extended periods of time between experiments did not prevent pre-activation of the dust in a subsequent run. Further work is required to investigate the exact conditions under which KGa-1b ceases to be pre-activated.



## **Appendix – Pictures from the ICE campaigns**



BJM inside the AIDA chamber chilled housing.



TWW enters the AIDA chamber.





TWW inside the AIDA chamber.



TLM and BJM in front of one of the many liquid N<sub>2</sub> tankers consumed during the ICE campaigns.

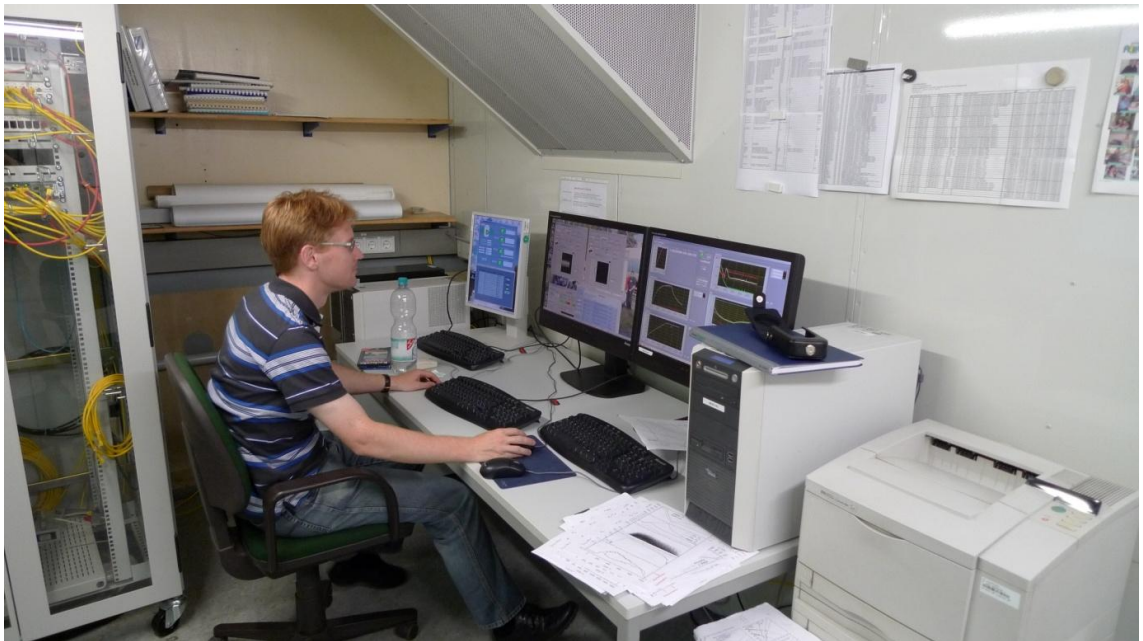


The AIDA synthetic air supply.





TLM in front of the AIDA facility.



RW starts another expansion in the AIDA control room.

## References

Abbatt, J. P. D., Benz, S., Cziczo, D. J., Kanji, Z., Lohmann, U., and Mohler, O.: Solid ammonium sulfate aerosols as ice nuclei: A pathway for cirrus cloud formation, *Science*, 313, 1770-1773, 10.1126/science.1129726, 2006.

Adachi, K., and Buseck, P. R.: Atmospheric tar balls from biomass burning in Mexico, *Journal of Geophysical Research-Atmospheres*, 116, D05204

10.1029/2010jd015102, 2011.

Albrecht, B. A.: Aerosols, cloud microphysics, and fractional cloudiness, *Science*, 245, 1227-1230, 10.1126/science.245.4923.1227, 1989.

Alexander, D. T. L., Crozier, P. A., and Anderson, J. R.: Brown carbon spheres in East Asian outflow and their optical properties, *Science*, 321, 833-836, 10.1126/science.1155296, 2008.

Alpert, P. A., Aller, J. Y., and Knopf, D. A.: Ice nucleation from aqueous NaCl droplets with and without marine diatoms, *Atmospheric Chemistry and Physics*, 11, 5539-5555, 10.5194/acp-11-5539-2011, 2011.

Angell, C. A.: Formation of glasses from liquids and biopolymers, *Science*, 267, 1924-1935, 10.1126/science.267.5206.1924, 1995.

Angell, C. A.: Liquid fragility and the glass transition in water and aqueous solutions, *Chemical Reviews*, 102, 2627-2649, 10.1021/cr000689q, 2002.

Archuleta, C. M., DeMott, P. J., and Kreidenweis, S. M.: Ice nucleation by surrogates for atmospheric mineral dust and mineral dust/sulfate particles at cirrus temperatures, *Atmospheric Chemistry and Physics*, 5, 2617-2634, 2005.

Arnold, E., Merrill, J., Leinen, M., and King, J.: The effect of source area and atmospheric transport on mineral aerosol collected over the North Pacific Ocean, *Global and Planetary Change*, 18, 137-159, 10.1016/s0921-8181(98)00013-7, 1998.

Atkins, P. W., and De Paula, J.: *Atkins' Physical chemistry*, 8th ed., Oxford University Press, Oxford ; New York, xxx, 1064 p. pp., 2006.

Atkinson, J. D., and Murray, B. J.: Ice nucleation by atmospheric mineral dusts – do a few minerals dominate?, EGU General Assembly, Vienna, 2012.

Bailey, M., and Hallett, J.: Nucleation effects on the habit of vapour grown ice crystals from -18 to -42 degrees C, *Quarterly Journal of the Royal Meteorological Society*, 128, 1461-1483, 2002.

Baker, M. B.: Cloud microphysics and climate, *Science*, 276, 1072-1078, 10.1126/science.276.5315.1072, 1997.

Baker, M. B., and Peter, T.: Small-scale cloud processes and climate, *Nature*, 451, 299-300, 10.1038/nature06594, 2008.

Barahona, D., and Nenes, A.: Dynamical states of low temperature cirrus, *Atmospheric Chemistry and Physics*, 11, 3757-3771, 10.5194/acp-11-3757-2011, 2011.

Baran, A. J.: A review of the light scattering properties of cirrus, *Journal of Quantitative Spectroscopy and Radiative Transfer*, 110, 1239-1260, 10.1016/j.jqsrt.2009.02.026, 2009.

Baustian, K. J., Wise, M. E., and Tolbert, M. A.: Depositional ice nucleation on solid ammonium sulfate and glutaric acid particles, *Atmospheric Chemistry and Physics*, 10, 2307-2317, 10.5194/acp-10-2307-2010, 2010.

Baustian, K. J., Wise, M. E., and Tolbert, M. A.: Influence of Glassy Organic Species on Ice Nucleation and Water Uptake of Single Micron-sized Aerosol Particles, American Geophysical Union Fall Meeting, 2011.

Baustian, K. J., Cziczo, D. J., Wise, M. E., Pratt, K. A., Kulkarni, G., Hallar, A. G., and Tolbert, M. A.: Importance of aerosol composition, mixing state, and morphology for heterogeneous ice nucleation: A combined field and laboratory approach, *Journal of Geophysical Research-Atmospheres*, 117, 10.1029/2011jd016784, 2012.

Benz, S., Megahed, K., Möhler, O., Saathoff, H., Wagner, R., and Schurath, U.: T-dependent rate measurements of homogeneous ice nucleation in cloud droplets using a large atmospheric simulation chamber, *Journal of Photochemistry and Photobiology a-Chemistry*, 176, 208-217, 10.1016/j.jphotochem.2005.08.026, 2005.

Bereznitski, Y., Jaroniec, M., and Maurice, P.: Adsorption Characterization of Two Clay Minerals Society Standard Kaolinites, *Journal of Colloid and Interface Science*, 205, 528-530, 1998.

Bickmore, B. R., Nagy, K. L., Sandlin, P. E., and Crater, T. S.: Quantifying surface areas of clays by atomic force microscopy, *American Mineralogist*, 87, 780-783, 2002.

Bingemer, H., Klein, H., Ebert, M., Haunold, W., Bundke, U., Herrmann, T., Kandler, K., Müller-Ebert, D., Weinbruch, S., Judt, A., Weber, A., Nillius, B., Ardon-Dryer, K., Levin, Z., and Curtius, J.: Atmospheric ice nuclei in the Eyjafjallajökull volcanic ash plume, *Atmospheric Chemistry and Physics*, 12, 857-867, 10.5194/acp-12-857-2012, 2012.

Bodsworth, A., Zobrist, B., and Bertram, A. K.: Inhibition of efflorescence in mixed organic-inorganic particles at temperatures less than 250 K, *Physical Chemistry Chemical Physics*, 12, 12259-12266, 2010.



Bones, D. L., Reid, J. P., Lienhard, D. M., and Krieger, U. K.: Comparing the mechanism of water condensation and evaporation in glassy aerosol, *Proceedings of the National Academy of Sciences of the United States of America*, 109, 11613-11618, 10.1073/pnas.1200691109, 2012.

Braban, C. F., Abbatt, J. P. D., and Cziczo, D. J.: Deliquescence of ammonium sulfate particles at sub-eutectic temperatures, *Geophysical Research Letters*, 28, 3879-3882, 10.1029/2001gl013175, 2001.

Brasseur, G. P., Orlando, J. J., Tyndall, G. S., and Research, N. C. f. A.: *Atmospheric Chemistry and Global Change*, Oxford University Press, 1999.

Broadley, S. L., Murray, B. J., Herbert, R. J., Atkinson, J. D., Dobbie, S., Malkin, T. L., Condliffe, E., and Neve, L.: Immersion mode heterogeneous ice nucleation by an illite rich powder representative of atmospheric mineral dust, *Atmospheric Chemistry and Physics*, 12, 287-307, 10.5194/acp-12-287-2012, 2012.

Bryant, G. W., Hallett, J., and Mason, B. J.: The epitaxial growth of ice on single-crystalline substrates, *Journal of Physics and Chemistry of Solids*, 12, 189-&, 1959.

Bundke, U., Nillius, B., Jaenicke, R., Wetter, T., Klein, H., and Bingemer, H.: The fast Ice Nucleus chamber FINCH, *Atmospheric Research*, 90, 180-186, 10.1016/j.atmosres.2008.02.008, 2008.

Cantrell, W., and Heymsfield, A.: Production of Ice in Tropospheric Clouds: A Review, *Bulletin of the American Meteorological Society*, 86, 795-807, 10.1175/bams-86-6-795, 2005.

Cappa, C. D., and Wilson, K. R.: Evolution of organic aerosol mass spectra upon heating: implications for OA phase and partitioning behavior, *Atmospheric Chemistry and Physics*, 11, 1895-1911, 10.5194/acp-11-1895-2011, 2011.

Chan, M. N., Choi, M. Y., Ng, N. L., and Chan, C. K.: Hygroscopicity of water-soluble organic compounds in atmospheric aerosols: Amino acids and biomass burning derived organic species, *Environmental Science & Technology*, 39, 1555-1562, 10.1021/es049584l, 2005.

Chatterjee, K., Shalaev, E. Y., and Suryanarayanan, R.: Raffinose crystallization during freeze-drying and its impact on recovery of protein activity, *Pharmaceutical Research*, 22, 303-309, 10.1007/s11095-004-1198-y, 2005.

Chen, Y. L., Kreidenweis, S. M., McInnes, L. M., Rogers, D. C., and DeMott, P. J.: Single particle analyses of ice nucleating aerosols in the upper troposphere and lower stratosphere, *Geophysical Research Letters*, 25, 1391-1394, 10.1029/97gl03261, 1998.

Chernoff, D. I., and Bertram, A. K.: Effects of sulfate coatings on the ice nucleation properties of a biological ice nucleus and several types of minerals, *Journal of Geophysical Research-Atmospheres*, 115, D2020510.1029/2010jd014254, 2010.

Comstock, J. M., Ackerman, T. P., and Turner, D. D.: Evidence of high ice supersaturation in cirrus clouds using ARM Raman lidar measurements, *Geophysical Research Letters*, 31, 10.1029/2004gl019705, 2004.

Connolly, P. J., Möhler, O., Field, P. R., Saathoff, H., Burgess, R., Choulaton, T., and Gallagher, M.: Studies of heterogeneous freezing by three different desert dust samples, *Atmospheric Chemistry and Physics*, 9, 2805-2824, 2009.

Costanzo, P. A., and Guggenheim, S.: Baseline studies of The Clay Minerals Society Source Clays: Preface, *Clays and Clay Minerals*, 49, 371-371, 10.1346/ccmn.2001.0490501, 2001.

Cziczo, D. J., DeMott, P. J., Brock, C., Hudson, P. K., Jesse, B., Kreidenweis, S. M., Prenni, A. J., Schreiner, J., Thomson, D. S., and Murphy, D. M.: A method for single

particle mass spectrometry of ice nuclei, *Aerosol Science and Technology*, 37, 460-470, 10.1080/02786820390112687, 2003.

Cziczo, D. J., Murphy, D. M., Hudson, P. K., and Thomson, D. S.: Single particle measurements of the chemical composition of cirrus ice residue during CRYSTAL-FACE, *Journal of Geophysical Research-Atmospheres*, 109, 10.1029/2003jd004032, 2004.

Cziczo, D. J., Stetzer, O., Worringen, A., Ebert, M., Weinbruch, S., Kamphus, M., Gallavardin, S. J., Curtius, J., Borrmann, S., Froyd, K. D., Mertes, S., Mohler, O., and Lohmann, U.: Inadvertent climate modification due to anthropogenic lead, *Nature Geosci*, 2, 333-336, 2009.

Debenedetti, P. G.: *Metastable liquids : concepts and principles*, Princeton University Press, Princeton, N.J., xiv, 411 p pp., 1996.

Debenedetti, P. G., and Stillinger, F. H.: Supercooled liquids and the glass transition, *Nature*, 410, 259-267, 2001.

Decesari, S., Fuzzi, S., Facchini, M. C., Mircea, M., Emblico, L., Cavalli, F., Maenhaut, W., Chi, X., Schkolnik, G., Falkovich, A., Rudich, Y., Claeys, M., Pashynska, V., Vas, G., Kourtchev, I., Vermeylen, R., Hoffer, A., Andreae, M. O., Tagliavini, E., Moretti, F., and Artaxo, P.: Characterization of the organic composition of aerosols from Rondonia, Brazil, during the LBA-SMOCC 2002 experiment and its representation through model compounds, *Atmospheric Chemistry and Physics*, 6, 375-402, 2006.

Delany, A. C., Parkin, D. W., Griffin, J. J., Goldberg, E. D., and Reimann, B. E. F.: Airborne dust collected at Barbados, *Geochimica Et Cosmochimica Acta*, 31, 885-&, 10.1016/s0016-7037(67)80037-1, 1967.

Demott, P. J., and Rogers, D. C.: Freezing nucleation rates of dilute solution droplets measured between -30°C and -40°C in laboratory simulations of natural clouds, *Journal*

of the Atmospheric Sciences, 47, 1056-1064, 10.1175/1520-0469(1990)047<1056:fnrods>2.0.co;2, 1990.

Demott, P. J.: Quantitative descriptions of ice formation mechanisms of silver iodide-type aerosols, *Atmospheric Research*, 38, 63-99, 10.1016/0169-8095(94)00088-u, 1995.

DeMott, P. J., Chen, Y., Kreidenweis, S. M., Rogers, D. C., and Sherman, D. E.: Ice formation by black carbon particles, *Geophysical Research Letters*, 26, 2429-2432, 10.1029/1999gl900580, 1999.

DeMott, P. J., Cziczo, D. J., Prenni, A. J., Murphy, D. M., Kreidenweis, S. M., Thomson, D. S., Borys, R., and Rogers, D. C.: Measurements of the concentration and composition of nuclei for cirrus formation, *Proceedings of the National Academy of Sciences of the United States of America*, 100, 14655-14660, 10.1073/pnas.2532677100, 2003.

DeMott, P. J., Prenni, A. J., Liu, X., Kreidenweis, S. M., Petters, M. D., Twohy, C. H., Richardson, M. S., Eidhammer, T., and Rogers, D. C.: Predicting global atmospheric ice nuclei distributions and their impacts on climate, *Proceedings of the National Academy of Sciences of the United States of America*, 107, 11217-11222, 10.1073/pnas.0910818107, 2010.

Despres, V. R., Huffman, J. A., Burrows, S. M., Hoose, C., Safatov, A. S., Buryak, G., Froehlich-Nowoisky, J., Elbert, W., Andreae, M. O., Poeschl, U., and Jaenicke, R.: Primary biological aerosol particles in the atmosphere: a review, *Tellus Series B-Chemical and Physical Meteorology*, 64, 10.3402/tellusb.v64i0.15598, 2012.

Dogan, A. U., Dogan, M., Onal, M., Sarikaya, Y., Aburub, A., and Wurster, D. E.: Baseline studies of the Clay Minerals Society Source Clays: specific surface area by the Brunauer Emmett Teller (BET) method, *Clay and Clay Minerals*, 54, 62-66, 2006.

Dymarska, M., Murray, B. J., Sun, L. M., Eastwood, M. L., Knopf, D. A., and Bertram, A. K.: Deposition ice nucleation on soot at temperatures relevant for the lower troposphere, *Journal of Geophysical Research-Atmospheres*, 111, D04204

10.1029/2005jd006627, 2006.

Eastwood, M. L., Cremel, S., Gehrke, C., Girard, E., and Bertram, A. K.: Ice nucleation on mineral dust particles: Onset conditions, nucleation rates and contact angles, *Journal of Geophysical Research-Atmospheres*, 113, 10.1029/2008jd010639, 2008.

Eastwood, M. L., Cremel, S., Wheeler, M., Murray, B. J., Girard, E., and Bertram, A. K.: Effects of sulfuric acid and ammonium sulfate coatings on the ice nucleation properties of kaolinite particles, *Geophysical Research Letters*, 36, L0281110.1029/2008gl035997, 2009.

Fahey, D. W., Gao, R. S., and Möhler, O.: Summary of the AquaVIT Water Vapor Intercomparison: Static Experiments, Available online at <https://aquavit.icg.kfa-juelich.de/AquaVit/>, 2009.

Fletcher, N. H.: Size effect in heterogeneous nucleation, *Journal of Chemical Physics*, 29, 572-576, 10.1063/1.1744540, 1958.

Forster, P., Ramaswamy, V., Artaxo, P., Berntsen, T., Betts, R., Fahey, D. W., Haywood, J., Lean, J., Lowe, D. C., Myhre, G., Nganga, J., Prinn, R., Raga, G., Schulz, M., and Van Dorland, R.: Changes in Atmospheric Constituents and in Radiative Forcing in: *Climate Change 2007: The Physical Science Basis. Contribution of Working Group I to the Fourth Assessment Report of the Intergovernmental Panel on Climate Change* edited by: Solomon, S., D. Qin, M. Manning, Z. Chen, M. Marquis, K.B. Averyt, M. Tignor and H.L. Miller Cambridge University Press, United Kingdom and New York, NY, USA, 131 - 234, 2007.

Foster, A. L., Brown Jr, G. E., and Parks, G. A.: X-ray Absorption Fine-Structure Spectroscopy of Photocatalyzed, heterogeneous As(III) Oxidation on Kaolin and Anatase, *Environmental Science and Technology*, 32, 1444-1452, 1998.

Fournier D'albe, E. M.: Some experiments on the condensation of water vapour at temperatures below 0°C, *Quarterly Journal of the Royal Meteorological Society*, 75, 1-16, 10.1002/qj.49707532302, 1949.

Friedman, B., Kulkarni, G., Beranek, J., Zelenyuk, A., Thornton, J. A., and Cziczo, D. J.: Ice nucleation and droplet formation by bare and coated soot particles, *Journal of Geophysical Research-Atmospheres*, 116, 10.1029/2011jd015999, 2011.

Friese, E., and Ebel, A.: Temperature Dependent Thermodynamic Model of the System H(+)-NH<sub>4</sub>(+)-Na(+)-SO<sub>4</sub>(<sup>2-</sup>)-NO<sub>3</sub>(-)-Cl(-)-H<sub>2</sub>O, *J. Phys. Chem. A*, 114, 11595-11631, 10.1021/jp101041j, 2010.

Froyd, K. D., Murphy, D. M., Jensen, E. J., Murray, B. J., and Möhler, O.: Ice Nucleation at the Tropical Tropopause: Insights from *in situ* Measurements, Simulations and Laboratory Studies, ICNAA, Prague, Czech Republic, 2009a,

Froyd, K. D., Murphy, D. M., Sanford, T. J., Thomson, D. S., Wilson, J. C., Pfister, L., and Lait, L.: Aerosol composition of the tropical upper troposphere, *Atmospheric Chemistry and Physics*, 9, 4363-4385, 2009b.

Froyd, K. D., Murphy, D. M., Lawson, P., Baumgardner, D., and Herman, R. L.: Aerosols that form subvisible cirrus at the tropical tropopause, *Atmospheric Chemistry and Physics*, 10, 209-218, 2010.

Fu, Q.: A New Parameterization of an Asymmetry Factor of Cirrus Clouds for Climate Models, *Journal of the Atmospheric Sciences*, 64, 4140-4150, 10.1175/2007jas2289.1, 2007.

Fueglistaler, S., Dessler, A. E., Dunkerton, T. J., Folkins, I., Fu, Q., and Mote, P. W.: Tropical Tropopause Layer, *Reviews of Geophysics*, 47, 10.1029/2008rg000267, 2009.

Fukuta, N.: Activation of atmospheric particles as ice nuclei in cold and dry air, *Journal of the Atmospheric Sciences*, 23, 741-&, 10.1175/1520-0469(1966)023<0741:aoapai>2.0.co;2, 1966.

Gao, R. S., Popp, P. J., Fahey, D. W., Marcy, T. P., Herman, R. L., Weinstock, E. M., Baumgardner, D. G., Garrett, T. J., Rosenlof, K. H., Thompson, T. L., Bui, P. T., Ridley, B. A., Wofsy, S. C., Toon, O. B., Tolbert, M. A., Karcher, B., Peter, T., Hudson, P. K., Weinheimer, A. J., and Heymsfield, A. J.: Evidence that nitric acid increases relative humidity in low-temperature cirrus clouds, *Science*, 303, 516-520, 10.1126/science.1091255, 2004.

Gayet, J. F., Ovarlez, J., Shcherbakov, V., Strom, J., Schumann, U., Minikin, A., Auriol, F., Petzold, A., and Monier, M.: Cirrus cloud microphysical and optical properties at southern and northern midlatitudes during the INCA experiment, *Journal of Geophysical Research-Atmospheres*, 109, 10.1029/2004jd004803, 2004.

Gayet, J. F., Shcherbakov, V., Mannstein, H., Minikin, A., Schumann, U., Strom, J., Petzold, A., Ovarlez, J., and Immler, F.: Microphysical and optical properties of midlatitude cirrus clouds observed in the southern hemisphere during INCA, *Quarterly Journal of the Royal Meteorological Society*, 132, 2719-2748, 10.1256/qj.05.162, 2006.

Gensch, I. V., Bunz, H., Baumgardner, D. G., Christensen, L. E., Fahey, D. W., Herman, R. L., Popp, P. J., Smith, J. B., Troy, R. F., Webster, C. R., Weinstock, E. M., Wilson, J. C., Peter, T., and Kramer, M.: Supersaturations, microphysics and nitric acid partitioning in a cold cirrus cloud observed during CR-AVE 2006: an observation-modelling intercomparison study, *Environmental Research Letters*, 3, 9, 10.1088/1748-9326/3/3/035003, 2008.

Gettelman, A., Fetzer, E. J., Eldering, A., and Irion, F. W.: The global distribution of supersaturation in the upper troposphere from the Atmospheric Infrared Sounder, *Journal of Climate*, 19, 6089-6103, 2006.

Gierens, K., Schumann, U., Helten, M., Smit, H., and Marenco, A.: A distribution law for relative humidity in the upper troposphere and lower stratosphere derived from three years of MOZAIC measurements, *Annales Geophysicae-Atmospheres Hydrospheres and Space Sciences*, 17, 1218-1226, 1999.

Gierens, K., Schumann, U., Helten, M., Smit, H., and Wang, P. H.: Ice-supersaturated regions and subvisible cirrus in the northern midlatitude upper troposphere, *Journal of Geophysical Research-Atmospheres*, 105, 22743-22753, 2000.

Glaccum, R. A., and Prospero, J. M.: Saharan aerosols over the tropical north-atlantic - mineralogy, *Marine Geology*, 37, 295-321, 10.1016/0025-3227(80)90107-3, 1980.

Gordon, M., and Taylor, J. S.: Ideal copolymers and the 2nd-order transitions of synthetic rubbers 1. Non-crystalline copolymers, *Journal of Applied Chemistry*, 2, 493-500, 1952.

Goudie, A. S., and Middleton, N. J.: Desert dust in the global system, *Desert Dust in the Global System*, 1 pp., 2006.

Graber, E. R., and Rudich, Y.: Atmospheric HULIS: How humic-like are they? A comprehensive and critical review, *Atmospheric Chemistry and Physics*, 6, 729-753, 2006.

Gunthe, S. S., King, S. M., Rose, D., Chen, Q., Roldin, P., Farmer, D. K., Jimenez, J. L., Artaxo, P., Andreae, M. O., Martin, S. T., and Poeschl, U.: Cloud condensation nuclei in pristine tropical rainforest air of Amazonia: size-resolved measurements and modeling of atmospheric aerosol composition and CCN activity, *Atmospheric Chemistry and Physics*, 9, 7551-7575, 2009.



Haag, W., Karcher, B., Strom, J., Minikin, A., Lohmann, U., Ovarlez, J., and Stohl, A.: Freezing thresholds and cirrus cloud formation mechanisms inferred from in situ measurements of relative humidity, *Atmospheric Chemistry and Physics*, 3, 1791-1806, 2003.

Hansen, J. E., and Travis, L. D.: Light-scattering in planetary atmospheres, *Space Science Reviews*, 16, 527-610, 10.1007/bf00168069, 1974.

Heintzenberg, J., Okada, K., and Strom, J.: On the composition of non-volatile material in upper tropospheric aerosols and cirrus crystals, *Atmospheric Research*, 41, 81-88, 10.1016/0169-8095(95)00042-9, 1996.

Heintzenberg, J., and Charlson, R. J.: *Clouds in the Perturbed Climate System: Their Relationship to Energy Balance, Atmospheric Dynamics, and Precipitation*, MIT Press, 2009.

Heymsfield, A. J., and LM, M.: Relative Humidity and Temperature Influences on Cirrus Formation and Evolution: Observations from Wave Clouds and FIRE II, *Journal of Atmospheric Science*, 52, 1995.

Heymsfield, A. J., Miloshevich, L. M., Twohy, C., Sachse, G., and Oltmans, S.: Upper-tropospheric relative humidity observations and implications for cirrus ice nucleation, *Geophysical Research Letters*, 25, 1343-1346, 1998.

Hinds, W. C.: *Aerosol technology: properties, behavior, and measurement of airborne particles*, Wiley, 1999.

Holton, J. R., and Gettelman, A.: Horizontal transport and the dehydration of the stratosphere, *Geophysical Research Letters*, 28, 2799-2802, 2001.

Hoose, C., Kristjansson, J. E., and Burrows, S. M.: How important is biological ice nucleation in clouds on a global scale?, *Environmental Research Letters*, 5, 10.1088/1748-9326/5/2/024009, 2010a.

Hoose, C., Kristjansson, J. E., Chen, J.-P., and Hazra, A.: A Classical-Theory-Based Parameterization of Heterogeneous Ice Nucleation by Mineral Dust, Soot, and Biological Particles in a Global Climate Model, *Journal of the Atmospheric Sciences*, 67, 2483-2503, 10.1175/2010jas3425.1, 2010b.

Hoose, C., and Möhler, O.: Heterogeneous ice nucleation on atmospheric aerosols: a review of results from laboratory experiments, *Atmospheric Chemistry and Physics*, 12, 9817-9854, 10.5194/acp-12-9817-2012, 2012.

Hoyle, C. R., Pinti, V., Welti, A., Zobrist, B., Marcolli, C., Luo, B., Hoeskuldsson, A., Mattsson, H. B., Stetzer, O., Thorsteinsson, T., Larsen, G., and Peter, T.: Ice nucleation properties of volcanic ash from Eyjafjallajökull, *Atmospheric Chemistry and Physics*, 11, 9911-9926, 10.5194/acp-11-9911-2011, 2011.

Hungerford, E. H., and Nees, A. R.: Raffinose - Preparation and properties, *Industrial and Engineering Chemistry*, 26, 462-464, 1934.

Iinuma, Y., Brüeggemann, E., Gnauk, T., Mueller, K., Andreae, M. O., Helas, G., Parmar, R., and Herrmann, H.: Source characterization of biomass burning particles: The combustion of selected European conifers, African hardwood, savanna grass, and German and Indonesian peat, *Journal of Geophysical Research-Atmospheres*, 112, D08209 10.1029/2006jd007120, 2007.

Immler, F., Treffeisen, R., Engelbart, D., Krüger, K., and Schrems, O.: Cirrus, contrails, and ice supersaturated regions in high pressure systems at northern mid latitudes, *Atmospheric Chemistry and Physics*, 8, 1689-1699, 2008.

Isono, K.: On ice-crystal nuclei and other substances found in snow crystals, *Journal of Meteorology*, 12, 456-462, 10.1175/1520-0469(1955)012<0456:oicnao>2.0.co;2, 1955.

Jaynes, W. F., Zartman, R. E., Green, C. J., San Francisco, M. J., and Zak, J. C.: Castor toxin adsorption to clay minerals, *Clay and Clay Minerals*, 53, 268-277, 2005.

Jensen, E., and Pfister, L.: Transport and freeze-drying in the tropical tropopause layer, *Journal of Geophysical Research-Atmospheres*, 109, 10.1029/2003jd004022, 2004.

Jensen, E., Pfister, L., Bui, T., Weinheimer, A., Weinstock, E., Smith, J., Pittman, J., Baumgardner, D., Lawson, P., and McGill, M. J.: Formation of a tropopause cirrus layer observed over Florida during CRYSTAL-FACE, *Journal of Geophysical Research-Atmospheres*, 110, 10.1029/2004jd004671, 2005a.

Jensen, E. J., Toon, O. B., Pfister, L., and Selkirk, H. B.: Dehydration of the upper troposphere and lower stratosphere by subvisible cirrus clouds near the tropical tropopause, *Geophysical Research Letters*, 23, 825-828, 1996.

Jensen, E. J., and Toon, O. B.: The potential impact of soot particles from aircraft exhaust on cirrus clouds, *Geophysical Research Letters*, 24, 249-252, 10.1029/96gl03235, 1997.

Jensen, E. J., Toon, O. B., Pueschel, R. F., Goodman, J., Sachse, G. W., Anderson, B. E., Chan, K. R., Baumgardner, D., and Miake-Lye, R. C.: Ice crystal nucleation and growth in contrails forming at low ambient temperatures, *Geophysical Research Letters*, 25, 1371-1374, 10.1029/97gl03592, 1998.

Jensen, E. J., Toon, O. B., Vay, S. A., Ovarlez, J., May, R., Bui, T. P., Twohy, C. H., Gandrud, B. W., Pueschel, R. F., and Schumann, U.: Prevalence of ice-supersaturated regions in the upper troposphere: Implications for optically thin ice cloud formation, *Journal of Geophysical Research-Atmospheres*, 106, 17253-17266, 2001.

Jensen, E. J., Smith, J. B., Pfister, L., Pittman, J. V., Weinstock, E. M., Sayres, D. S., Herman, R. L., Troy, R. F., Rosenlof, K., Thompson, T. L., Fridlind, A. M., Hudson, P. K., Cziczo, D. J., Heymsfield, A. J., Schmitt, C., and Wilson, J. C.: Ice supersaturations exceeding 100% at the cold tropical tropopause: implications for cirrus formation and dehydration, *Atmospheric Chemistry and Physics*, 5, 851-862, 2005b.

Jensen, E. J., Pfister, L., Bui, T. V., Lawson, P., Baker, B., Mo, Q., Baumgardner, D., Weinstock, E. M., Smith, J. B., Moyer, E. J., Hanisco, T. F., Sayres, D. S., St Clair, J. M., Alexander, M. J., Toon, O. B., and Smith, J. A.: Formation of large (similar or equal to 100  $\mu$  m) ice crystals near the tropical tropopause, *Atmospheric Chemistry and Physics*, 8, 1621-1633, 2008.

Jensen, E. J., Pfister, L., Bui, T. P., Lawson, P., and Baumgardner, D.: Ice nucleation and cloud microphysical properties in tropical tropopause layer cirrus, *Atmospheric Chemistry and Physics*, 10, 1369-1384, 2010.

Johari, G. P., Hallbrucker, A., and Mayer, E.: The glass liquid transition of hyperquenched water, *Nature*, 330, 552-553, 10.1038/330552a0, 1987.

Kandler, K., Schuetz, L., Deutscher, C., Ebert, M., Hofmann, H., Jaeckel, S., Jaenicke, R., Knippertz, P., Lieke, K., Massling, A., Petzold, A., Schladitz, A., Weinzierl, B., Wiedensohler, A., Zorn, S., and Weinbruch, S.: Size distribution, mass concentration, chemical and mineralogical composition and derived optical parameters of the boundary layer aerosol at Tinfou, Morocco, during SAMUM 2006, *Tellus Series B-Chemical and Physical Meteorology*, 61, 32-50, 10.1111/j.1600-0889.2008.00385.x, 2009.

Kandler, K., Schuetz, L., Jaeckel, S., Lieke, K., Emmel, C., Mueller-Ebert, D., Ebert, M., Scheuven, D., Schladitz, A., Segvic, B., Wiedensohler, A., and Weinbruch, S.: Ground-based off-line aerosol measurements at Praia, Cape Verde, during the Saharan Mineral Dust Experiment: microphysical properties and mineralogy, *Tellus Series B-Chemical and Physical Meteorology*, 63, 459-474, 10.1111/j.1600-0889.2011.00546.x, 2011.

Kanji, Z. A., and Abbatt, J. P. D.: Laboratory studies of ice formation via deposition mode nucleation onto mineral dust and n-hexane soot samples, *Journal of Geophysical Research-Atmospheres*, 111, D16204 10.1029/2005jd006766, 2006.

Kanji, Z. A., Florea, O., and Abbatt, J. P. D.: Ice formation via deposition nucleation on mineral dust and organics: dependence of onset relative humidity on total particulate surface area, *Environmental Research Letters*, 3, 025004 10.1088/1748-9326/3/2/025004, 2008.

Kanji, Z. A., and Abbatt, J. P. D.: Ice Nucleation onto Arizona Test Dust at Cirrus Temperatures: Effect of Temperature and Aerosol Size on Onset Relative Humidity, *J. Phys. Chem. A*, 114, 935-941, 10.1021/jp908661m, 2010.

Kanji, Z. A., DeMott, P. J., Moehler, O., and Abbatt, J. P. D.: Results from the University of Toronto continuous flow diffusion chamber at ICIS 2007: instrument intercomparison and ice onsets for different aerosol types, *Atmospheric Chemistry and Physics*, 11, 31-41, 10.5194/acp-11-31-2011, 2011.

Kärcher, B.: Aircraft-generated aerosols and visible contrails, *Geophysical Research Letters*, 23, 1933-1936, 10.1029/96gl01853, 1996.

Kärcher, B.: Supersaturation, dehydration, and denitrification in Arctic cirrus, *Atmospheric Chemistry and Physics*, 5, 1757-1772, 2005.

Katkov, II, and Levine, F.: Prediction of the glass transition temperature of water solutions: comparison of different models, *Cryobiology*, 49, 62-82, 10.1016/j.cryobiol.2004.05.004, 2004.

Kelly, K. K., Proffitt, M. H., Chan, K. R., Loewenstein, M., Podolske, J. R., Strahan, S. E., Wilson, J. C., and Kley, D.: Water-Vapor and Cloud Water Measurements Over Darwin During the STEP 1987 Tropical Mission, *Journal of Geophysical Research-Atmospheres*, 98, 8713-8723, 1993.

Khvorostyanov, V. I., Morrison, H., Curry, J. A., Baumgardner, D., and Lawson, P.: High supersaturation and modes of ice nucleation in thin tropopause cirrus: Simulation of the 13 July 2002 Cirrus Regional Study of Tropical Anvils and Cirrus Layers case, *Journal of Geophysical Research-Atmospheres*, 111, 10.1029/2004jd005235, 2006.

Klein, H., Haunold, W., Bundke, U., Nillius, B., Wetter, T., Schallenberg, S., and Bingemer, H.: A new method for sampling of atmospheric ice nuclei with subsequent analysis in a static diffusion chamber, *Atmospheric Research*, 96, 218-224, 10.1016/j.atmosres.2009.08.002, 2010.

Knopf, D. A., and Koop, T.: Heterogeneous nucleation of ice on surrogates of mineral dust, *Journal of Geophysical Research-Atmospheres*, 111, 10, D12201 10.1029/2005jd006894, 2006.

Knopf, D. A., Wang, B., Laskin, A., Moffet, R. C., and Gilles, M. K.: Heterogeneous nucleation of ice on anthropogenic organic particles collected in Mexico City, *Geophysical Research Letters*, 37, L11803, 10.1029/2010gl043362, 2010.

Knopf, D. A., and Rigg, Y. J.: Homogeneous Ice Nucleation From Aqueous Inorganic/Organic Particles Representative of Biomass Burning: Water Activity, Freezing Temperatures, Nucleation Rates, *J. Phys. Chem. A*, 115, 762-773, 10.1021/jp109171g, 2011.

Koehler, K. A., DeMott, P. J., Kreidenweis, S. M., Popovicheva, O. B., Petters, M. D., Carrico, C. M., Kireeva, E. D., Khokhlova, T. D., and Shonija, N. K.: Cloud condensation nuclei and ice nucleation activity of hydrophobic and hydrophilic soot particles, *Physical Chemistry Chemical Physics*, 11, 7906-7920, 10.1039/b905334b, 2009.

Kohl, I., Bachmann, L., Hallbrucker, A., Mayer, E., and Loerting, T.: Liquid-like relaxation in hyperquenched water at  $\leq 140$  K, *Physical Chemistry Chemical Physics*, 7, 3210-3220, 10.1039/b507651j, 2005.

Koop, T., Luo, B. P., Tsias, A., and Peter, T.: Water activity as the determinant for homogeneous ice nucleation in aqueous solutions, *Nature*, 406, 611-614, 2000.

Koop, T., Bookhold, J., Shiraiwa, M., and Poeschl, U.: Glass transition and phase state of organic compounds: dependency on molecular properties and implications for secondary organic aerosols in the atmosphere, *Physical Chemistry Chemical Physics*, 13, 19238-19255, 10.1039/c1cp22617g, 2011.

Koren, I., Kaufman, Y. J., Washington, R., Todd, M. C., Rudich, Y., Martins, J. V., and Rosenfeld, D.: The Bodele depression: a single spot in the Sahara that provides most of the mineral dust to the Amazon forest, *Environmental Research Letters*, 1, 10.1088/1748-9326/1/1/014005, 2006.

Korolev, A., and Isaac, G. A.: Relative humidity in liquid, mixed-phase, and ice clouds, *Journal of the Atmospheric Sciences*, 63, 2865-2880, 2006.

Kramer, B., Hubner, O., Vortisch, H., Woste, L., Leisner, T., Schwell, M., Ruhl, E., and Baumgartel, H.: Homogeneous nucleation rates of supercooled water measured in single levitated microdroplets, *Journal of Chemical Physics*, 111, 6521-6527, 1999.

Krämer, M., Schiller, C., Afchine, A., Bauer, R., Gensch, I., Mangold, A., Schlicht, S., Spelten, N., Sitnikov, N., Borrmann, S., de Reus, M., and Spichtinger, P.: Ice supersaturations and cirrus cloud crystal numbers, *Atmospheric Chemistry and Physics*, 9, 3505-3522, 2009.

Kulkarni, G., Dobbie, S., and McQuaid, J. B.: A new thermal gradient ice nucleation diffusion chamber instrument: design, development and first results using Saharan mineral dust, *Atmospheric Measurement Techniques*, 2, 221-229, 2009.

Kulkarni, G., and Dobbie, S.: Ice nucleation properties of mineral dust particles: determination of onset RH(i), IN active fraction, nucleation time-lag, and the effect of active sites on contact angles, *Atmospheric Chemistry and Physics*, 10, 95-105, 2010.

Kulkarni , G. R.: Development and application of a new thermal gradient diffusion chamber to study the ice nucleation properties of inhomogeneous dust aerosols, Doctor of Philosophy, School of Earth and Environment, University of Leeds, 2007.

Kumai, M.: Electron-microscope study of snow-crystal nuclei, *Journal of Meteorology*, 8, 151-156, 10.1175/1520-0469(1951)008<0151:emsosc>2.0.co;2, 1951.

Kumai, M.: Snow crystals and the identification of the nuclei in the northern United-States of America, *Journal of Meteorology*, 18, 139-150, 10.1175/1520-0469(1961)018<0139:scatio>2.0.co;2, 1961.

Kumai, M., and Francis, K. E.: Nuclei in snow and ice crystals on the Greenland ice cap under natural and artificially stimulated conditions, *Journal of the Atmospheric Sciences*, 19, 474-481, 10.1175/1520-0469(1962)019<0474:nisaic>2.0.co;2, 1962.

Kumai, M.: Identification of nuclei and concentrations of chemical species in snow crystals sampled at south-pole, *Journal of the Atmospheric Sciences*, 33, 833-841, 10.1175/1520-0469(1976)033<0833:ionaco>2.0.co;2, 1976.

Latham, J., Rasch, P., Chen, C. C., Kettles, L., Gadian, A., Gettelman, A., Morrison, H., Bower, K., and Choulaton, T.: Global temperature stabilization via controlled albedo enhancement of low-level maritime clouds, *Philosophical Transactions of the Royal Society a-Mathematical Physical and Engineering Sciences*, 366, 3969-3987, 10.1098/rsta.2008.0137, 2008.

Lavanchy, V. M. H., Gaggeler, H. W., Schotterer, U., Schwikowski, M., and Baltensperger, U.: Historical record of carbonaceous particle concentrations from a European high-alpine glacier (Colle Gnifetti, Switzerland), *Journal of Geophysical Research-Atmospheres*, 104, 21227-21236, 10.1029/1999jd900408, 1999.



Lawson, R. P., Pilson, B., Baker, B., Mo, Q., Jensen, E., Pfister, L., and Bui, P.: Aircraft measurements of microphysical properties of subvisible cirrus in the tropical tropopause layer, *Atmospheric Chemistry and Physics*, 8, 1609-1620, 2008.

Lee, S. H., Wilson, J. C., Baumgardner, D., Herman, R. L., Weinstock, E. M., LaFleur, B. G., Kok, G., Anderson, B., Lawson, P., Baker, B., Strawa, A., Pittman, J. V., Reeves, J. M., and Bui, T. P.: New particle formation observed in the tropical/subtropical cirrus clouds, *Journal of Geophysical Research-Atmospheres*, 109, 7, D20209 10.1029/2004jd005033, 2004.

Leinen, M., Prospero, J. M., Arnold, E., and Blank, M.: Mineralogy of aeolian dust reaching the North Pacific-ocean. 1.Sampling and analysis, *Journal of Geophysical Research-Atmospheres*, 99, 21017-21023, 10.1029/94jd01735, 1994.

Liou, K. N.: Influence of cirrus clouds on weather and climate processes - a global perspective, *Monthly Weather Review*, 114, 1167-1199, 10.1175/1520-0493(1986)114<1167:ioccow>2.0.co;2, 1986.

Liou, K. N., and Takano, Y.: Light scattering by nonspherical particles: Remote sensing and climatic implications, *Atmospheric Research*, 31, 271-298, 10.1016/0169-8095(94)90004-3, 1994.

Liu, L., and Mishchenko, M. I.: Constraints on PSC particle microphysics derived from lidar observations, *Journal of Quantitative Spectroscopy & Radiative Transfer*, 70, 817-831, 10.1016/s0022-4073(01)00048-6, 2001.

Lohmann, U., and Feichter, J.: Global indirect aerosol effects: a review, *Atmospheric Chemistry and Physics*, 5, 715-737, 2005.

Lüönd, F., Stetzer, O., Welti, A., and Lohmann, U.: Experimental study on the ice nucleation ability of size-selected kaolinite particles in the immersion mode, *Journal of Geophysical Research-Atmospheres*, 115, 10.1029/2009jd012959, 2010.

Lynch, D. K.: Cirrus clouds: Their role in climate and global change, *Acta Astronautica*, 38, 859-863, 10.1016/s0094-5765(96)00098-7, 1996.

Lynch, D. K., Sassen, K., Starr, D. O. C., and Stephens, G.: *Cirrus*, Oxford University Press, Cambridge ; New York, xvii, 480 p. pp., 2002.

MacKenzie, A. R., Schiller, C., Peter, T., Adriani, A., Beuermann, J., Bujok, O., Cairo, F., Corti, T., DiDonfrancesco, G., Gensch, I., Kiemle, C., Kramer, M., Kroger, C., Merkulov, S., Oulanovsky, A., Ravegnani, F., Rohs, S., Rudakov, V., Salter, P., Santacesaria, V., Stefanutti, L., and Yushkov, V.: Tropopause and hygropause variability over the equatorial Indian Ocean during February and March 1999, *Journal of Geophysical Research-Atmospheres*, 111, 10.1029/2005jd006639, 2006.

Magee, N., Moyle, A. M., and Lamb, D.: Experimental determination of the deposition coefficient of small cirrus-like ice crystals near -50 degrees C, *Geophysical Research Letters*, 33, 10.1029/2006gl026665, 2006.

Maki, L. R., Galyan, E. L., Changchi.Mm, and Caldwell, D. R.: Ice nucleation induced by *psuedomonas syringae*, *Applied Microbiology*, 28, 456-459, 1974.

Malkin, T. L., Murray, B. J., Brukhno, A. V., Anwar, J., and Salzmann, C. G.: Structure of ice crystallized from supercooled water, *Proceedings of the National Academy of Sciences*, 10.1073/pnas.1113059109, 2012.

Maltini, E., Anese, M., and Shtylla, I.: State diagrams of some organic acid-water systems of interest in food, *Cryo-Letters*, 18, 263-268, 1997.

Marculli, C., Gedamke, S., Peter, T., and Zobrist, B.: Efficiency of immersion mode ice nucleation on surrogates of mineral dust, *Atmospheric Chemistry and Physics*, 7, 5081-5091, 2007.

Mason, B. J.: The nature of ice-forming nuclei in the atmosphere, *Quarterly Journal of the Royal Meteorological Society*, 76, 59-74, 10.1002/qj.49707632707, 1950.

Mason, B. J., and Maybank, J.: Ice-nucleating properties of some natural mineral dusts, *Quarterly Journal of the Royal Meteorological Society*, 84, 235-241, 10.1002/qj.49708436104, 1958.

McFarquhar, G. M., Heymsfield, A. J., Spinhirne, J., and Hart, B.: Thin and subvisual tropopause tropical cirrus: Observations and radiative impacts, *Journal of the Atmospheric Sciences*, 57, 1841-1853, 10.1175/1520-0469(2000)057<1841:tasttc>2.0.co;2, 2000.

McFiggans, G., Alfarra, M. R., Allan, J., Bower, K., Coe, H., Cubison, M., Topping, D., Williams, P., Decesari, S., Facchini, C., and Fuzzi, S.: Simplification of the representation of the organic component of atmospheric particulates, *Faraday Discussions*, 130, 341-362, 10.1039/b419435g, 2005.

McFiggans, G., Artaxo, P., Baltensperger, U., Coe, H., Facchini, M. C., Feingold, G., Fuzzi, S., Gysel, M., Laaksonen, A., Lohmann, U., Mentel, T. F., Murphy, D. M., O'Dowd, C. D., Snider, J. R., and Weingartner, E.: The effect of physical and chemical aerosol properties on warm cloud droplet activation, *Atmospheric Chemistry and Physics*, 6, 2593-2649, 2006.

Mikhailov, E., Vlasenko, S., Martin, S. T., Koop, T., and Pöschl, U.: Amorphous and crystalline aerosol particles interacting with water vapor: conceptual framework and experimental evidence for restructuring, phase transitions and kinetic limitations, *Atmospheric Chemistry and Physics*, 9, 9491-9522, 2009.

Mitchell, D. L., and Finnegan, W.: Modification of cirrus clouds to reduce global warming, *Environmental Research Letters*, 4, 10.1088/1748-9326/4/4/045102, 2009.

Mitchell, J. F. B., Senior, C. A., and Ingram, W. J.: CO<sub>2</sub> and climate: a missing feedback?, *Nature*, 341, 132-134, 1989.

Möhler, O., Stetzer, O., Schaefers, S., Linke, C., Schnaiter, M., Tiede, R., Saathoff, H., Kramer, M., Mangold, A., Budz, P., Zink, P., Schreiner, J., Mauersberger, K., Haag, W., Karcher, B., and Schurath, U.: Experimental investigation of homogeneous freezing of sulphuric acid particles in the aerosol chamber AIDA, *Atmospheric Chemistry and Physics*, 3, 211-223, 2003.

Möhler, O., Field, P. R., Connolly, P., Benz, S., Saathoff, H., Schnaiter, M., Wagner, R., Cotton, R., Kraemer, M., Mangold, A., and Heymsfield, A. J.: Efficiency of the deposition mode ice nucleation on mineral dust particles, *Atmospheric Chemistry and Physics*, 6, 3007-3021, 2006.

Möhler, O., Benz, S., Saathoff, H., Schnaiter, M., Wagner, R., Schneider, J., Walter, S., Ebert, V., and Wagner, S.: The effect of organic coating on the heterogeneous ice nucleation efficiency of mineral dust aerosols, *Environmental Research Letters*, 3, 10.1088/1748-9326/3/2/025007, 2008.

Mossop, S. C.: Sublimation Nuclei, *Proceedings of the Physical Society. Section B*, 69, 161, 1956.

Mossop, S. C.: Atmospheric ice nuclei, *Zeitschrift für Angewandte Mathematik und Physik (ZAMP)*, 14, 456-486, 10.1007/bf01601253, 1963.

Mullin, J. W.: *Crystallization*, Butterworth-Heinemann, 2001.

Murphy, D. M., Thomson, D. S., and Mahoney, T. M. J.: In situ measurements of organics, meteoritic material, mercury, and other elements in aerosols at 5 to 19 kilometers, *Science*, 282, 1664-1669, 1998.

Murphy, D. M., and Koop, T.: Review of the vapour pressures of ice and supercooled water for atmospheric applications, *Quarterly Journal of the Royal Meteorological Society*, 131, 1539-1565, 10.1256/qj.04.94, 2005.

Murphy, D. M., Cziczo, D. J., Froyd, K. D., Hudson, P. K., Matthew, B. M., Middlebrook, A. M., Peltier, R. E., Sullivan, A., Thomson, D. S., and Weber, R. J.: Single-particle mass spectrometry of tropospheric aerosol particles, *Journal of Geophysical Research-Atmospheres*, 111, D23s32 10.1029/2006jd007340, 2006.

Murray, B. J., Knopf, D. A., and Bertram, A. K.: The formation of cubic ice under conditions relevant to Earth's atmosphere, *Nature*, 434, 202-205, 10.1038/nature03403, 2005.

Murray, B. J., and Bertram, A. K.: Strong dependence of cubic ice formation on droplet ammonium to sulfate ratio, *Geophysical Research Letters*, 34, L16810 10.1029/2007gl030471, 2007.

Murray, B. J.: Enhanced formation of cubic ice in aqueous organic acid droplets, *Environmental Research Letters*, 3, 025008 10.1088/1748-9326/3/2/025008, 2008a.

Murray, B. J.: Inhibition of ice crystallisation in highly viscous aqueous organic acid droplets, *Atmospheric Chemistry and Physics*, 8, 5423-5433, 2008b.

Murray, B. J., and Bertram, A. K.: Inhibition of solute crystallisation in aqueous H(+)-NH<sub>4</sub>(+)-SO<sub>4</sub>(<sup>2-</sup>)-H<sub>2</sub>O droplets, *Physical Chemistry Chemical Physics*, 10, 3287-3301, 10.1039/b802216j, 2008.

Murray, B. J., Broadley, S. L., Wilson, T. W., Bull, S. J., Wills, R. H., Christenson, H. K., and Murray, E. J.: Kinetics of the homogeneous freezing of water, *Physical Chemistry Chemical Physics*, -, 2010a.

Murray, B. J., and Jensen, E. J.: Homogeneous nucleation of amorphous solid water particles in the upper mesosphere, *Journal of Atmospheric and Solar-Terrestrial Physics*, 72, 51-61, 2010.

Murray, B. J., Wilson, T. W., Dobbie, S., Cui, Z. Q., Al-Jumur, S., Möhler, O., Schnaiter, M., Wagner, R., Benz, S., Niemand, M., Saathoff, H., Ebert, V., Wagner, S., and Karcher, B.: Heterogeneous nucleation of ice particles on glassy aerosols under cirrus conditions, *Nature Geoscience*, 3, 233-237, 10.1038/ngeo817, 2010b.

Murray, B. J., Broadley, S. L., Wilson, T. W., Atkinson, J. D., and Wills, R. H.: Heterogeneous freezing of water droplets containing kaolinite particles, *Atmospheric Chemistry and Physics*, 11, 4191-4207, 10.5194/acp-11-4191-2011, 2011.

Murray, B. J., Haddrell, A. E., Peppe, S., Davies, J. F., Reid, J. P., O'Sullivan, D., Price, H. C., Kumar, R., Saunders, R. W., Plane, J. M. C., Umo, N. S., and Wilson, T. W.: Glass formation and unusual hygroscopic growth of iodic acid solution droplets with relevance for iodine mediated particle formation in the marine boundary layer, *Atmos. Chem. Phys.*, 12, 8575-8587, 10.5194/acp-12-8575-2012, 2012a.

Murray, B. J., Haddrell, A. E., Peppe, S., Davies, J. F., Reid, J. P., O'Sullivan, D., Price, H. C., Kumar, R., Saunders, R. W., Plane, J. M. C., Umo, N. S., and Wilson, T. W.: Glass formation and unusual hygroscopic growth of iodic acid solution droplets with relevance for iodine oxide particles in the coastal marine boundary layer, *Atmospheric Chemistry and Physics Discussions*, 12, 7879-7908, 10.5194/acpd-12-7879-2012, 2012b.

Nazaryan, H., McCormick, M. P., and Menzel, W. P.: Global characterization of cirrus clouds using CALIPSO data, *J. Geophys. Res.*, 113, D16211, 10.1029/2007jd009481, 2008.

Niemand, M., Möhler, M., Vogel, B., Vogel, H., Hoose, C., Connolly, P., Klein, H., Bingemer, H., DeMott, P., Skrotzki, J., and Leisner, T.: A particle-surface-area-based

parameterization of immersion freezing on mineral dust particles, Under review for Journal of Atmospheric Science 2012a.

Niemand, M., Möhler, O., Vogel, B., Vogel, H., Hoose, C., Connolly, P., Klein, H., Bingemer, H., DeMott, P., Skrotzki, J., and Leisner, T.: A particle-surface-area-based parameterization of immersion freezing on desert dust particles, Journal of the Atmospheric Sciences, 10.1175/jas-d-11-0249.1, 2012b.

Onasch, T. B., Siefert, R. L., Brooks, S. D., Prenni, A. J., Murray, B., Wilson, M. A., and Tolbert, M. A.: Infrared spectroscopic study of the deliquescence and efflorescence of ammonium sulfate aerosol as a function of temperature, Journal of Geophysical Research-Atmospheres, 104, 21317-21326, 10.1029/1999jd900384, 1999.

Ovarlez, J., Gayet, J. F., Gierens, K., Strom, J., Ovarlez, H., Auriol, F., Busen, R., and Schumann, U.: Water vapour measurements inside cirrus clouds in Northern and Southern hemispheres during INCA, Geophysical Research Letters, 29, 10.1029/2001gl014440, 2002.

Peter, T., Luo, B. P., Wirth, M., Kiemle, C., Flentje, H., Yushkov, V. A., Khattatov, V., Rudakov, V., Thomas, A., Borrmann, S., Toci, G., Mazzinghi, P., Beuermann, J., Schiller, C., Cairo, F., Di Donfrancesco, G., Adriani, A., Volk, C. M., Strom, J., Noone, K., Mitev, V., MacKenzie, R. A., Carslaw, K. S., Trautmann, T., Santacesaria, V., and Stefanutti, L.: Ultrathin Tropical Tropopause Clouds (UTTCS): I. Cloud morphology and occurrence, Atmospheric Chemistry and Physics, 3, 1083-1091, 2003.

Peter, T., Marcolli, C., Spichtinger, P., Corti, T., Baker, M. B., and Koop, T.: When dry air is too humid, Science, 314, 1399+, 10.1126/science.1135199, 2006.

Popp, P. J., Marcy, T. P., Watts, L. A., Gao, R. S., Fahey, D. W., Weinstock, E. M., Smith, J. B., Herman, R. L., Troy, R. F., Webster, C. R., Christensen, L. E., Baumgardner, D. G., Voigt, C., Karcher, B., Wilson, J. C., Mahoney, M. J., Jensen, E. J., and Bui, T. P.: Condensed-phase nitric acid in a tropical subvisible cirrus cloud, Geophysical Research Letters, 34, 10.1029/2007gl031832, 2007.

Posfai, M., Gelencser, A., Simonics, R., Arato, K., Li, J., Hobbs, P. V., and Buseck, P. R.: Atmospheric tar balls: Particles from biomass and biofuel burning, *Journal of Geophysical Research-Atmospheres*, 109, D06213 10.1029/2003jd004169, 2004.

Prenni, A. J., Petters, M. D., Faulhaber, A., Carrico, C. M., Ziemann, P. J., Kreidenweis, S. M., and DeMott, P. J.: Heterogeneous ice nucleation measurements of secondary organic aerosol generated from ozonolysis of alkenes, *Geophysical Research Letters*, 36, L06808 10.1029/2008gl036957, 2009.

Prospero, J. M., Glaccum, R. A., and Nees, R. T.: Atmospheric transport of soil dust from Africa to South-America, *Nature*, 289, 570-572, 10.1038/289570a0, 1981.

Pruppacher, H. R., and Klett, J. D.: *Microphysics of clouds and precipitation*, 2nd rev. and enl. ed., *Atmospheric and oceanographic sciences library* ;, v. 18, Kluwer Academic Publishers, Dordrecht ; Boston, xx, 954 p. pp., 1997.

Ramanathan, V., and Collins, W.: Thermodynamic regulation of ocean warming by cirrus clouds deduced from observations of the 1987 El-Nino, *Nature*, 351, 27-32, 10.1038/351027a0, 1991.

Ramanathan, V., Crutzen, P. J., Kiehl, J. T., and Rosenfeld, D.: Atmosphere - Aerosols, climate, and the hydrological cycle, *Science*, 294, 2119-2124, 10.1126/science.1064034, 2001.

Ren, C., and Mackenzie, A. R.: Cirrus parametrization and the role of ice nuclei, *Quarterly Journal of the Royal Meteorological Society*, 131, 1585-1605, 10.1256/qj.04.126, 2005.

Roberts, P., and Hallett, J.: A laboratory study of the ice nucleating properties of some mineral particulates, *Quarterly Journal of the Royal Meteorological Society*, 94, 25-&, 10.1002/qj.49709439904, 1968.



Rosenfeld, D.: Suppression of rain and snow by urban and industrial air pollution, *Science*, 287, 1793-1796, 10.1126/science.287.5459.1793, 2000.

Roth, C. M., Goss, K. U., and Schwarzenbach, R. P.: Sorption of a diverse set of organic vapors to urban aerosols, *Environmental Science & Technology*, 39, 6638-6643, 10.1021/es0503837, 2005.

Rucklidge, J.: Examination by electron microscope of ice crystal nuclei from cloud chamber experiments, *Journal of the Atmospheric Sciences*, 22, 301-&, 10.1175/1520-0469(1965)022<0301:tebemo>2.0.co;2, 1965.

Salam, A., Lohmann, U., Crenna, B., Lesins, G., Klages, P., Rogers, D., Irani, R., MacGillivray, A., and Coffin, M.: Ice nucleation studies of mineral dust particles with a new continuous flow diffusion chamber, *Aerosol Science and Technology*, 40, 134-143, 10.1080/02786820500444853, 2006.

Sassen, K., and Comstock, J. M.: A Midlatitude Cirrus Cloud Climatology from the Facility for Atmospheric Remote Sensing. Part III: Radiative Properties, *Journal of the Atmospheric Sciences*, 58, 2113-2127, 10.1175/1520-0469(2001)058<2113:amcccf>2.0.co;2, 2001.

Sassen, K., Wang, Z., and Liu, D.: Global distribution of cirrus clouds from CloudSat/Cloud-Aerosol Lidar and Infrared Pathfinder Satellite Observations (CALIPSO) measurements, *Journal of Geophysical Research-Atmospheres*, 113, 10.1029/2008jd009972, 2008.

Saukko, E., Lambe, A. T., Massoli, P., Koop, T., Wright, J. P., Croasdale, D. R., Pedernera, D. A., Onasch, T. B., Laaksonen, A., Davidovits, P., Worsnop, D. R., and Virtanen, A.: Humidity-dependent phase state of SOA particles from biogenic and anthropogenic precursors, *Atmospheric Chemistry and Physics Discussions*, 12, 4447-4476, 10.5194/acpd-12-4447-2012, 2012.

Saunders, R. W., Möhler, O., Schnaiter, M., Benz, S., Wagner, R., Saathoff, H., Connolly, P. J., Burgess, R., Murray, B. J., Gallagher, M., Wills, R., and Plane, J. M. C.: An aerosol chamber investigation of the heterogeneous ice nucleating potential of refractory nanoparticles, *Atmospheric Chemistry and Physics*, 10, 1227-1247, 10.5194/acp-10-1227-2010, 2010.

Saxena, P., and Hildemann, L. M.: Water-soluble organics in atmospheric particles: A critical review of the literature and application of thermodynamics to identify candidate compounds, *Journal of Atmospheric Chemistry*, 24, 57-109, 1996.

Schaller, R. C., and Fukuta, N.: Ice nucleation by aerosol particles - Experimental studies using a wedge-shaped ice thermal-diffusion chamber, *Journal of the Atmospheric Sciences*, 36, 1788-1802, 1979.

Schnaiter, M., Büttner, S., Möhler, O., Skrotzki, J., Vragel, M., and Wagner, R.: Influence of particle size and shape on the backscattering linear depolarization ratio of small ice crystals - Cloud chamber measurements in the context of contrail and cirrus microphysics, To be submitted to *Atmos. Chem. Phys. Discuss.*, 2012.

Seinfeld, J. H., and Pandis, S. N.: *Atmospheric chemistry and physics : from air pollution to climate change*, 2nd ed., Wiley, Hoboken N.J., 1420 p. pp., 2006.

Shaw, D., and Mason, B. J.: The growth of ice crystals from the vapour, *Philosophical Magazine*, 46, 249-&, 1955.

Shen, T. L., Woolridge, P. J., and Molina, M. J.: *Stratospheric pollution and ozone depletion, Composition, chemistry, and climate of the atmosphere*, New York, 1995, xii, 527 p.,

Shilling, J. E., Fortin, T. J., and Tolbert, M. A.: Depositional ice nucleation on crystalline organic and inorganic solids, *Journal of Geophysical Research-Atmospheres*, 111, 10.1029/2005jd006664, 2006.

Shilling, J. E., Tolbert, M. A., Toon, O. B., Jensen, E. J., Murray, B. J., and Bertram, A. K.: Measurements of the vapor pressure of cubic ice and their implications for atmospheric ice clouds, *Geophysical Research Letters*, 33, 10.1029/2006gl026671, 2006a.

Shiraiwa, M., Ammann, M., Koop, T., and Poeschl, U.: Gas uptake and chemical aging of semisolid organic aerosol particles, *Proceedings of the National Academy of Sciences of the United States of America*, 108, 11003-11008, 10.1073/pnas.1103045108, 2011.

Skrotzki, J.: High-accuracy multiphase humidity measurements using TDLAS: application to the investigation of ice growth in simulated cirrus clouds, Doctor of Natural Sciences, Combined Faculties for the Natural Sciences and for Mathematics, Ruperto-Carola University of Heidelberg, Heidelberg, 140 pp., 2012.

Solomon, S., Intergovernmental Panel on Climate Change., and Intergovernmental Panel on Climate Change. Working Group I.: *Climate Change 2007 : the physical science basis : contribution of Working Group I to the Fourth Assessment Report of the Intergovernmental Panel on Climate Change*, Cambridge University Press, Cambridge ; New York, viii, 996 p. pp., 2007.

Spichtinger, P., Gierens, K., and Read, W.: The global distribution of ice-supersaturated regions as seen by the Microwave Limb Sounder, *Quarterly Journal of the Royal Meteorological Society*, 129, 3391-3410, 10.1256/qj.02.141, 2003.

Spichtinger, P., Gierens, K., Smit, H. G. J., Ovarlez, J., and Gayet, J. F.: On the distribution of relative humidity in cirrus clouds, *Atmospheric Chemistry and Physics*, 4, 639-647, 2004.

Spichtinger, P., and Gierens, K. M.: Modelling of cirrus clouds - Part 2: Competition of different nucleation mechanisms, *Atmospheric Chemistry and Physics*, 9, 2319-2334, 2009.

Spichtinger, P., and Cziczo, D. J.: Impact of heterogeneous ice nuclei on homogeneous freezing events in cirrus clouds, *Journal of Geophysical Research-Atmospheres*, 115, 22, D14208 10.1029/2009jd012168, 2010.

Stan, C. A., Schneider, G. F., Shevkoplyas, S. S., Hashimoto, M., Ibanescu, M., Wiley, B. J., and Whitesides, G. M.: A microfluidic apparatus for the study of ice nucleation in supercooled water drops, *Lab on a Chip*, 9, 2293-2305, 10.1039/b906198c, 2009.

Steinke, I., Möhler, O., Kiselev, A., Niemand, M., Saathoff, H., Schnaiter, M., Skrotzki, J., Hoose, C., and Leisner, T.: Ice nucleation properties of fine ash particles from the Eyjafjallajökull eruption in April 2010, *Atmospheric Chemistry and Physics*, 11, 12945-12958, 10.5194/acp-11-12945-2011, 2011.

Stubenrauch, C. J., Chédin, A., Rädcl, G., Scott, N. A., and Serrar, S.: Cloud Properties and Their Seasonal and Diurnal Variability from TOVS Path-B, *Journal of Climate*, 19, 5531-5553, 10.1175/jcli3929.1, 2006.

Szyrmer, W., and Zawadzki, I.: Biogenic and anthropogenic sources of ice-forming nuclei: A review, *Bulletin of the American Meteorological Society*, 78, 209-228, 10.1175/1520-0477(1997)078<0209:baasoi>2.0.co;2, 1997.

Thompson, H. A., Parks, G. A., and Brown Jr, G. E.: Dynamic interactions of dissolution, surface adsorption, and precipitation in an ageing cobalt(II)-clay-water system, *Geochimica et Cosmochimica Acta*, 63, 1767-1779, 1999.

Tivanski, A. V., Hopkins, R. J., Tyliczszak, T., and Gilles, M. K.: Oxygenated interface on biomass burn tar balls determined by single particle scanning transmission X-ray microscopy, *J. Phys. Chem. A*, 111, 5448-5458, 10.1021/jp070155u, 2007.

Tong, H. J., Reid, J. P., Bones, D. L., Luo, B. P., and Krieger, U. K.: Measurements of the timescales for the mass transfer of water in glassy aerosol at low relative humidity

and ambient temperature, *Atmospheric Chemistry and Physics*, 11, 4739-4754, 10.5194/acp-11-4739-2011, 2011.

Turnbull, D.: Kinetics of Heterogeneous Nucleation, *The Journal of Chemical Physics*, 18, 198-203, 1950.

Twomey, S.: Pollution and planetary albedo, *Atmospheric Environment*, 8, 1251-1256, 10.1016/0004-6981(74)90004-3, 1974.

Vaden, T. D., Imre, D., Beranek, J., Shrivastava, M., and Zelenyuk, A.: Evaporation kinetics and phase of laboratory and ambient secondary organic aerosol, *Proceedings of the National Academy of Sciences of the United States of America*, 108, 2190-2195, 10.1073/pnas.1013391108, 2011.

Vali, G.: Supercooling of water and nucleation of ice (drop freezer), *American Journal of Physics*, 39, 1125-&, 10.1119/1.1976585, 1971.

Vali, G.: Nucleation terminology, *Bulletin of the American Meteorological Society*, 66, 1426-1427, 1985.

Vali, G.: Freezing rate due to heterogeneous nucleation, *Journal of the Atmospheric Sciences*, 51, 2683-2683, 1994.

Vali, G.: Repeatability and randomness in heterogeneous freezing nucleation, *Atmospheric Chemistry and Physics*, 8, 5017-5031, 2008.

Vargaftik, N. B., Volkov, B. N., and Voljak, L. D.: International tables of the surface-tension of water, *Journal of Physical and Chemical Reference Data*, 12, 817-820, 1983.

Virtanen, A., Joutsensaari, J., Koop, T., Kannosto, J., Yli-Pirila, P., Leskinen, J., Makela, J. M., Holopainen, J. K., Poschl, U., Kulmala, M., Worsnop, D. R., and

Laaksonen, A.: An amorphous solid state of biogenic secondary organic aerosol particles, *Nature*, 467, 824-827, 10.1038/nature09455, 2010.

Volmer, M.: *Kinetik der Phasenbildung*, J. W. Edwards, 1945.

Vonnegut, B.: The nucleation of ice formation by silver iodide, *Journal of Applied Physics*, 18, 593-595, 10.1063/1.1697813, 1947.

Vonnegut, B., and Baldwin, M.: Repeated Nucleation of a Supercooled Water Sample that Contains Silver Iodide Particles, *Journal of Climate and Applied Meteorology*, 23, 486-490, 10.1175/1520-0450(1984)023<0486:rnoasw>2.0.co;2, 1984.

Wagner, R., Benz, S., Möhler, O., Saathoff, H., and Schurath, U.: Probing ice clouds by broadband mid-infrared extinction spectroscopy: case studies from ice nucleation experiments in the AIDA aerosol and cloud chamber, *Atmospheric Chemistry and Physics*, 6, 4775-4800, 10.5194/acp-6-4775-2006, 2006.

Wagner, R., Benz, S., Möhler, O., Saathoff, H., Schnaiter, M., and Leisner, T.: Influence of particle aspect ratio on the midinfrared extinction spectra of wavelength-sized ice crystals, *J. Phys. Chem. A*, 111, 13003-13022, 10.1021/jp0741713, 2007.

Wagner, R., Benz, S., Bunz, H., Möhler, O., Saathoff, H., Schnaiter, M., Leisner, T., and Ebert, V.: Infrared Optical Constants of Highly Diluted Sulfuric Acid Solution Droplets at Cirrus Temperatures, *The Journal of Physical Chemistry A*, 112, 11661-11676, 10.1021/jp8066102, 2008.

Wagner, R., Linke, C., Naumann, K. H., Schnaiter, M., Vragel, M., Gangl, M., and Horvath, H.: A review of optical measurements at the aerosol and cloud chamber AIDA, *Journal of Quantitative Spectroscopy & Radiative Transfer*, 110, 930-949, 10.1016/j.jqsrt.2009.01.026, 2009.

Wagner, R., Möhler, O., Saathoff, H., Schnaiter, M., and Leisner, T.: High variability of the heterogeneous ice nucleation potential of oxalic acid dihydrate and sodium oxalate, *Atmospheric Chemistry and Physics*, 10, 7617-7641, 10.5194/acp-10-7617-2010, 2010.

Wagner, R., Möhler, O., Saathoff, H., Schnaiter, M., and Leisner, T.: New cloud chamber experiments on the heterogeneous ice nucleation ability of oxalic acid in the immersion mode, *Atmospheric Chemistry and Physics*, 11, 2083-2110, 10.5194/acp-11-2083-2011, 2011.

Wagner, R., Möhler, O., Saathoff, H., Schnaiter, M., Skrotzki, J., Leisner, T., Wilson, T. W., Malkin, T. L., and Murray, B. J.: Ice cloud processing of ultra-viscous/glassy aerosol particles leads to enhanced ice nucleation ability, *Atmos. Chem. Phys.*, 12, 8589-8610, 10.5194/acp-12-8589-2012, 2012a.

Wagner, R., Möhler, O., Saathoff, H., Schnaiter, M., Skrotzki, J., Leisner, T., Wilson, T. W., and Murray, B. J.: Ice cloud processing of ultra-viscous/glassy aerosol particles leads to enhanced ice nucleation ability, *Atmospheric Chemistry and Physics Discussions*, this issue, 2012b.

Wagner, W., and Pruss, A.: The IAPWS formulation 1995 for the thermodynamic properties of ordinary water substance for general and scientific use, *Journal of Physical and Chemical Reference Data*, 31, 387-535, 2002.

Wan, E. C. H., and Yu, J. Z.: Analysis of sugars and sugar polyols in atmospheric aerosols by chloride attachment in liquid chromatography/negative ion electrospray mass spectrometry, *Environmental Science & Technology*, 41, 2459-2466, 10.1021/es062390g, 2007.

Wang, B., and Knopf, D. A.: Heterogeneous ice nucleation on particles composed of humic-like substances impacted by O<sub>3</sub>, *Journal of Geophysical Research-Atmospheres*, 116, D03205

10.1029/2010jd014964, 2011.

Wang, B., Lambe, A. T., Massoli, P., Onasch, T. B., Davidovits, P., Worsnop, D. R., and Knopf, D. A.: The Deposition Ice Nucleation and Immersion Freezing Potential of Amorphous Secondary Organic Aerosol: Pathways for Ice and Mixed Phase Cloud Formation, *Journal of Geophysical Research*, Accepted, 2012.

Wayne, R. P.: *Chemistry of atmospheres : an introduction to the chemistry of the atmospheres of Earth, the planets, and their satellites*, 3rd ed., Oxford University Press, Oxford, xxix, 775 p pp., 2000.

Wexler, A. S., and Clegg, S. L.: Atmospheric aerosol models for systems including the ions  $H^+$ ,  $NH_4^+$ ,  $Na^+$ ,  $SO_4^{2-}$ ,  $NO_3^-$ ,  $Cl^-$ ,  $Br^-$ , and  $H_2O$ , *Journal of Geophysical Research-Atmospheres*, 107, 4207 10.1029/2001jd000451, 2002.

Wheeler, M. J., and Bertram, A. K.: Deposition nucleation on mineral dust particles: a case against classical nucleation theory with the assumption of a single contact angle, *Atmospheric Chemistry and Physics*, 12, 1189-1201, 10.5194/acp-12-1189-2012, 2012.

Wilson, T. W., Murray, B. J., Wagner, R., Möhler, O., Saathoff, H., Schnaiter, M., Skrotzki, J., Price, H. C., Malkin, T. L., Dobbie, S., and Al-Jumur, S. M. R. K.: Glassy aerosols with a range of compositions nucleate ice heterogeneously at cirrus temperature, *ACPD*, 2012a.

Wilson, T. W., Murray, B. J., Wagner, R., Möhler, O., Saathoff, H., Schnaiter, M., Skrotzki, J., Price, H. C., Malkin, T. L., Dobbie, S., and Al-Jumur, S. M. R. K.: Glassy aerosols with a range of compositions nucleate ice heterogeneously at cirrus temperatures, *Atmos. Chem. Phys.*, 12, 8611-8632, 10.5194/acp-12-8611-2012, 2012b.

Wise, M. E., Baustian, K. J., and Tolbert, M. A.: Laboratory studies of ice formation pathways from ammonium sulfate particles, *Atmospheric Chemistry and Physics*, 9, 1639-1646, 2009.



Wise, M. E., Baustian, K. J., and Tolbert, M. A.: Internally mixed sulfate and organic particles as potential ice nuclei in the tropical tropopause region, *Proceedings of the National Academy of Sciences of the United States of America*, 107, 6693-6698, 10.1073/pnas.0913018107, 2010.

Wise, M. E., Baustian, K. J., Koop, T., Freedman, M. A., Jensen, E. J., and Tolbert, M. A.: Depositional ice nucleation onto crystalline hydrated NaCl particles: a new mechanism for ice formation in the troposphere, *Atmospheric Chemistry and Physics*, 12, 1121-1134, 10.5194/acp-12-1121-2012, 2012.

Wylie, D. P., and Menzel, W. P.: Eight Years of High Cloud Statistics Using HIRS, *Journal of Climate*, 12, 170-184, 10.1175/1520-0442-12.1.170, 1999.

Young, K. D., and Leboeuf, E. J.: Glass transition behavior in a peat humic acid and an aquatic fulvic acid, *Environmental Science & Technology*, 34, 4549-4553, 10.1021/es00889j, 2000.

Zakharova, N. T., and Mishchenko, M. I.: Scattering properties of needlelike and platelike ice spheroids with moderate size parameters, *Applied Optics*, 39, 5052-5057, 10.1364/ao.39.005052, 2000.

Zhang, Y., Macke, A., and Albers, F.: Effect of crystal size spectrum and crystal shape on stratiform cirrus radiative forcing, *Atmospheric Research*, 52, 59-75, 10.1016/s0169-8095(99)00026-5, 1999.

Zimmermann, F., Ebert, M., Worringer, A., Schuetz, L., and Weinbruch, S.: Environmental scanning electron microscopy (ESEM) as a new technique to determine the ice nucleation capability of individual atmospheric aerosol particles, *Atmospheric Environment*, 41, 8219-8227, 10.1016/j.atmosenv.2007.06.023, 2007.

Zimmermann, F., Weinbruch, S., Schuetz, L., Hofmann, H., Ebert, M., Kandler, K., and Worringer, A.: Ice nucleation properties of the most abundant mineral dust phases,

Journal of Geophysical Research-Atmospheres, 113, D23204 10.1029/2008jd010655, 2008.

Zobrist, B., Marcolli, C., Pedernera, D. A., and Koop, T.: Do atmospheric aerosols form glasses?, Atmos. Chem. Phys., 8, 5221-5244, 2008.

Zobrist, B., Soonsin, V., Luo, B. P., Krieger, U. K., Marcolli, C., Peter, T., and Koop, T.: Ultra-slow water diffusion in aqueous sucrose glasses, Physical Chemistry Chemical Physics, 13, 3514-3526, 10.1039/c0cp01273d, 2011.

Zuberi, B., Bertram, A. K., Koop, T., Molina, L. T., and Molina, M. J.: Heterogeneous freezing of aqueous particles induced by crystallized  $(\text{NH}_4)_2\text{SO}_4$ , ice, and letovicite, J. Phys. Chem. A, 105, 6458-6464, 10.1021/jp010094e, 2001.